Searching for hot Jupiter transits around cool stars

Christian Obermeier

Searching for hot Jupiter transits around cool stars

The search for extrasolar planets with the Pan-Planets data

Dissertation an der Fakultät für Physik
der Ludwig-Maximilians-Universität München

PhD thesis at the faculty of physics
of the Ludwig-Maximilians-University Munich

Vorgelegt von Christian Obermeier
München, 29. Juli 2016

Erstgutachter: Priv. Doz. Dr. Roberto P. Saglia
Zweitgutachter: Prof. Dr. Thomas K. Henning

Datum der mündlichen Prüfung: 20. September, 2016

Contents

List of Figures

List of Tables

Zusammenfassung

Die Suche nach extrasolaren Planeten und deren Charakterisierung ist ein Forschungsgebiet, welches sich so rasant entwickelt wie kaum ein anderes im Bereich der Astronomie. Über das letzte Jahrzehnt wurden große Fortschritte bezüglich der Anzahl der Planetenentdeckungen und der Vermessung ihrer Eigenschaften gemacht. Die bislang bei weitem erfolgreichste Methode, die Transitmethode, trug mehr als 2000 bestätigte Planeten zur Gesamtzahl von 2900 Entdeckungen bei. Aufgrund dieser großen Anzahl an entdeckten Planeten sind nun statistische Analysen von Planeteneigenschaften möglich. Das Hauptziel des Pan-Planets Projektes und dieser Doktorarbeit ist die Berechnung der Häufigkeit von sogenannten heißen Jupitern um M-Zwerge, auch rote Zwerge genannt. Wie in Abschnitten 1.4 und 1.6.2 beschrieben, scheinen M-Zwerge auf theoretischen Modellen basierend eine andere Verteilung von Planetentypen zu besitzen als größere FGK-Zwerge. Transitprojekte wie Kepler konnten bereits große Erfolge aufweisen und ermöglichten es, die Häufigkeit von Felsplaneten um verschiedene Sterntypen genau abzuschätzen. Allerdings waren diese Projekte bei M-Zwergen aufgrund ihrer geringen Anzahl im Sichtfeld (< 3000) für die Studie von heißen Jupitern aufgrund ihrer intrinsischen niedrigen Häufigkeit weniger erfolgreich. Das Pan-Planets Projekt beobachtete mehr als 65000 M-Zwerge, was eine im Vergleich bedeutend größere Anzahl darstellt.

In Kapitel 1 gebe ich zunächst einen Überblick über alle für diese Doktorarbeit relevanten Themen. Ich beschreibe die Geschichte der Exoplanetenwissenschaft, diskutiere die Definition von Planeten, definiere verschiedene Planetentypen und fasse die derzeitigen Erkenntnisse zur Planetenentstehung, M-Zwergen und Methoden zur Planetenentdeckung zusammen. Anschließend gebe ich einen Überblick über die derzeitigen Planetenentdeckungen, diskutiere das Konzept von habitablen Planeten und schließe das Kapitel mit einer Beschreibung ab, wie Planeten mit beobachtbaren Transits bestätigt und nachbeobachtet werden können.

In Kapitel 2 beschreibe ich zunächst das Pan-Planets Projekt und die Verarbeitung der Beobachtungsdaten. Diese ist eine aufwendige Aufgabe, die das Entwerfen von automatischen Verarbeitungsroutinen, Bildverarbeitungsprogrammen für das automatische Maskieren von systematischen Fehlern, Lichtkurvengenerierung und Signalerkennung beinhaltet. Um eine Analyse der statistischen Häufigkeit von Exoplaneten durchführen zu können, müssen zunächst die M-Zwerge im Sichtfeld von Pan-Planets identifiziert werden. Dieser Punkt ist essentiell: je genauer die M-Zwerge in den Daten identifiziert sind, desto besser können die Planetenhäufigkeiten abgeschätzt werden. Im Sichtfeld von Pan-Planets gibt es Bereiche mit starker interstellarer Extinktion, die zu einer Rötung der Sterne führt. Daher ist es nötig, die Sterne möglichst genau zu charakterisieren und hierfür auch die Extinktionseffekte zu entfernen. Ich demonstriere die Genauigkeit unserer Methode der M-Zwerg Klassifizierung und führe verschiedene Konsistenzchecks durch. Ein Konzept für Monte-Carlo-Simulationen wird von mir erarbeitet und durchgeführt, um die Erfolgsrate von Pan-Planets bezüglich der Entdeckung von Planeten abzuschätzen. Ich führe diese Analyse für verschiedene Stern- und Planetenradien durch.

In Kapitel 3 diskutiere ich die Nachbeobachtungen, die für unsere Pan-Planets Kandidaten mit dem Fraunhofer Teleskop Wendelstein Wide Field Imager (FTW WFI) und dem Mc-

Donald Otto Struve ES2 Spektrograf durchgeführt wurden. Alle Planeten werden durch Parameterabschätzung der Transitkurve charakterisiert und anschließend mit Photometrie und Spektroskopie genauer überprüft, um den Sterntyp und das Transitmodel zu verbessern. Mit diesen Daten erstelle ich eine Falschpositiv-Analyse für alle Planetenkandidaten und beschreibe die finale Liste an geprüften Kandidaten in vier Kategorien: Planeten um M- und FGK-Zwerge, bedeckungsveränderliche M-Zwerg Doppelsterne und veränderliche Sternsysteme. Anschließend beurteile ich die Implikationen unserer Entdeckungen im Kontext der Planetenhäufigkeiten mit Hilfe der Monte-Carlo-Simulationen. Für die Häufigkeit von heißen Jupitern um M-Zwerge berechne ich einen Wert von $0.11^{+0.37}_{-0.02}\%$ bei einer Konfidenz von 95%. Für den Fall, dass sich unsere M-Zwerg Kandidaten als Falschpositive herausstellen, berechne ich ein Oberlimit von 0.34% für die Häufigkeit. Diese Ergebnisse sind wesentlich niedriger als die der bisherigen Transit- und Radialgeschwindigkeitsprojekte, welche nur Oberlimits von etwa 1% berechnen konnten. Während dies noch nicht die Vorhersage bestätigt, dass heiße Jupiter um M-Zwerge wesentlich seltener sind, kann nun bereits festgestellt werden, dass diese zumindest ebenso selten sind wie um heißere FGK-Zwerge, bei denen Häufigkeiten zwischen 0.3%-0.6% festgestellt wurden.

In Kapitel 4 beschreibe ich die Entdeckung eines ungewöhnlich großen, neptunartigen Planeten mit einem Radius von $\mathrm{R_p} = 3.47^{+0.78}_{-0.53}\,\mathrm{R_\oplus}$, der im offenen Cluster Praesepe (M44) in der K2 Kampagne 5 entdeckt wurde. Planetenentdeckungen in offenen Clustern sind bislang eine Seltenheit mit derzeit 14 bestätigten Entdeckungen und sind von großer Relevanz aufgrund der bekannten Alter, Entfernungen und Metallizitäten ihrer Zentralgestirne. Offene Cluster sind außerdem oftmals jung ($< 1\,Gyr$) und die Planetenentstehung könnte anders ablaufen aufgrund der häufigeren gravitativen Wechselwirkungen mit benachtbarten Sternen. Die Beobachtung von Clustersternen, die Planeten beherbergen, könnte deshalb zu neuen Einblicken in die Unterschiede der Planetenentstehung führen. Ich gebe einen Überblick über unsere Nachbeobachtungen, charakterisiere das Zentralgestirn des Planeten, validiere den Planeten statistisch und diskutiere eine Anomalie, die ich bei dem Planetenradius festgestellt habe. Nur wenige Planeten um M-Zwerge außerhalb von offenen Clustern besitzen Radien oberhalb von $3\,R_\oplus$. Die wenigen bekannten Planeten sind außerdem größer als unsere Entdeckung und wesentlich stärkerer Strahlung ausgesetzt, was vermutlich zu einer Vergrößerung des Planetenradius führt. Unsere Entdeckung ist bereits der zweite Planet in einem offenen Cluster mit einer derartigen Anomalie und wir diskutieren verschiedene Erklärungsansätze für diesen Effekt.

Meine Schlussbemerkungen und eine Zusammenfassung der Doktorarbeit finden sich abschließend in Kapitel 5.

Summary

Planet studies are one of the fastest-growing branches in astronomy. Over the past decade, advances have been made with a continually rising number of exoplanet discoveries and the more accurate study of their properties. The by far most successful detection technique is the transit method which contributes more than 2000 exoplanets to the total number of 2900 discoveries. Due to this large sample, the statistical assessment of planet populations has become possible. The primary goal of the Pan-Planets survey and this thesis is the determination of the hot-Jupiter occurrence rate around M-dwarfs. As described in sections 1.4 and 1.6.2, M-dwarfs seem to be peculiar in that their planet distributions appear to be different to that of FGK-dwarfs based on theoretical models. While transit surveys such as Kepler are very successful in discovering planets and estimating the occurrence rates of rocky planets, the small M-dwarf samples (< 3000) of those surveys have limited the statistical study of the M-dwarf hot Jupiter occurrence rate. The Pan-Planets survey observed a substantially larger number of M-dwarfs compared to other projects with more than 65000 M-dwarf targets.

In chapter 1, I provide an overview of all topics that are relevant to this thesis. I describe the history of exoplanet science, define the status of a planet, list different planetary types and summarize planet formation, M-dwarfs and planet detection methods. After this, I provide an overview of planet discoveries, briefly discuss the concept of planet habitability and conclude this chapter with a discussion of how to follow up transiting planets.

In chapter 2, I first describe the Pan-Planets survey and data reduction. The data reduction of Pan-Planets is a challenging task that encompasses writing automatic pipelines, creating image-processing scripts for automatic masking of systematics, light curve creation and signal detection. In order to perform the statistical occurrence-rate analysis, one first has to identify the M-dwarf target sample. This is a critical point: the more robustly M-dwarfs are identified, the more stringent occurrence rate limits can be established. The Pan-Planets field has a high amount of interstellar extinction which reddens the individual stars. Therefore, a significant task is the proper stellar characterization of the target stars which incorporates extinction fitting. I demonstrate the accuracy of our M-dwarf selection method and perform various consistency checks. Next, a concept for Monte Carlo simulations has to be planned and executed in order to estimate the detection efficiency based on the data. I estimate the detection efficiency of Pan-Planets for various planet and star radii based on these data.

In chapter 3, I detail the follow-up efforts of our Pan-Planets targets with the Fraunhofer Telescope Wendelstein Wide Field Imager and the McDonald observatory Otto Struve telescope with the ES2 spectrograph. All planet candidates are characterized by transit-shape fitting and followed up with photometry and spectroscopy in order to determine the stellar type of their host stars and improve the transit model. Using all of the obtained data, I perform a false-positive probability analysis on all planet candidates. I detail the final list of vetted candidates in our target categories, planet candidates around FGKM-dwarfs, M-dwarf binaries and variable systems, and give a summary of the current status. Finally, I determine the impact of our discoveries by providing a new upper limit for the occurrence rate for M-dwarf hot Jupiters based on our candidate set and the results from our Monte

Carlo simulations. Assuming one confirmed detection, I estimate the occurrence rate to be $0.11^{+0.37}_{-0.02}\%$ at a 95% confidence limit. In case of a null detection, I estimate an upper limit of 0.34%. These results are more constrained than the previous occurrence rate estimates based on radial velocity surveys and transit surveys which placed upper limits down to 1%. While this does not yet confirm the prediction that M-dwarf hot Jupiters are more rare, it can already be established that hot Jupiters are at least as rare as around hotter FGK-dwarfs.

In chapter 4, I describe the discovery of an unusually large Neptunian planet with a radius of $\mathrm{R_p} = 3.47^{+0.78}_{-0.53}\,\mathrm{R_\oplus}$ that was found in the Praesepe cluster (M44) during the K2 campaign 5 survey. Planet discoveries in clusters are quite rare with 14 confirmed detections so far and are of great interest for follow-up characterization due to the known age, distance and metallicity of their host stars. Furthermore, many open clusters are young ($< 1\,Gyr$) and planet formation might be different to the more frequent gravitational interaction with neighbouring stars. Studying planet-hosting cluster members might therefore gain further insight into this difference in formation. I provide an overview of our follow-up layout, characterize the host star, validate the planet statistically and discuss an anomaly which I detected in the planet's radius. There are very few known M-dwarf field stars that host planets with radii above $3\,R_\oplus$ and those receive significantly more stellar flux and are much larger than this planet. It is the second cluster planet with such an anomaly, hence we provide possible explanations for this effect.

Finally, I provide concluding remarks and a summary in chapter 5.

Chapter 1

Theory

My God, it's full of planets! They should have sent a poet.

Mixture of quotes from the movies Contact and 2001: A Space Odyssey

Note: Unless indicated otherwise by providing a source, figures were created by me.

1.1 History

Already very early on in the history of humanity, ancient scientists and philosophers discussed the nature of the stars that we can see in the night sky. Our own Solar System consists of a single star, rocky planets and gas giants in various sizes, several dwarf planets and dozens of moons. This lead to the century-spanning discussion of whether other stars also possessed their own planets or not - if our Solar System was a unique exception and whether other types of stellar systems would be possible. Greek astronomers and philosophers already hypothesized that the stars we see in the sky are just like the Sun and each represents a miniature system[1]. However, with no data to base actual theories on, it was nothing more than a philosophical discourse. The idea got picked up again by Giordano Bruno in the Renaissance era, stating: "Innumerable Suns exist. Innumerable earths revolve around these - Living beings inhabit these worlds"[2]. Swedenborg (1734) first proposed concrete ideas on planet formation, the so-called nebular hypothesis, stating that interstellar gaseous nebulae and clouds could collapse under their own gravitational forces and compress into stars and planets. This was further expanded on and published by Immanuel Kant in his "Universal Natural History and Theory of the Heavens" (Kant, 1755).
The first indication for the existence of a planetary companion was found by Campbell et al. (1988) who detected a periodic signal in the radial velocity curve of Gamma Cephei. Due to a low signal to noise (S/N) ratio, the publication was eventually retracted but the existence of that planet was finally confirmed by Hatzes et al. (2003).

[1]Epicurus: "There are infinite worlds both like and unlike this world of ours. We have to think of living creatures in all of these worlds" (Epicurus - The Extant Remains, Cyril Bailey, 1926).

[2]Sadly, Giordano Brunos ideas proved to be quite unpopular with the clergy and he got burned alive by the inquisition in 1600 for heresy. Charges included "claiming the existence of a plurality of worlds" (Luigi Firpo, *Il processo di Giordano Bruno*, 1993).

The year 1992 marked the first discovery of a confirmed exoplanet. Wolszczan and Frail (1992) detected two large rocky planets, so-called super-Earths, in orbit around a pulsar. This was an early indication that the variety of planets in the galaxy is much greater than in our own Solar System. The first exoplanet orbiting around a main-sequence star was discovered in 1995, a Hot Jupiter (HJ) exoplanet around the main-sequence star 51 Pegasi (Mayor and Queloz, 1995). It was detected by measurements of the radial velocity over time, as were most confirmed planets in the first years thereafter. Again, this planet - a gas giant larger than Jupiter, orbiting its star on an orbit closer than that of Mercury - was entirely unexpected in its type with no analogy in our Solar System. The first successfully confirmed exoplanet with the transit method was HD 209458 b, published by Charbonneau et al. (2000) and Henry et al. (2000). This method proved to be the most effective both in number of detections and ways to subsequently characterize the star and planet.
The search for extrasolar planets has seen extremely rapid growth over the past years. With dedicated telescopes, instruments and surveys being deployed over the last decade, every year leads to more discoveries than the previous. As of July 2016, more than 2900 exoplanets[3] have been discovered, the majority of them with the transit method.

1.2 Planets: Introduction

1.2.1 Definition

With the rising number of exoplanet detections year by year, it became a necessity to improve upon the definition on what actually makes up a planet and, subsequently, an exoplanet. Hence, after the IAU general assembly in 2006, the following criteria[4] for a planet in our Solar System were set:

- *"is in orbit around the Sun"*
- *"has sufficient mass for its self-gravity to overcome rigid body forces so that it assumes a hydrostatic equilibrium (nearly round) shape"*
- *"has cleared the neighbourhood around its orbit".*

Slightly confusing, the working definition of an exoplanet was set several years earlier, before the proper redefinition of a planet took place. For such a celestial body, there are additional criteria to be considered[5]:

- *"Objects with true masses below the limiting mass for thermonuclear fusion of deuterium (currently calculated to be 13 Jupiter masses for objects of solar metallicity) that orbit stars or stellar remnants are 'planets' (no matter how they formed). The minimum mass/size required for an extrasolar object to be considered a planet should be the same as that used in our Solar System."*
- *"Substellar objects with true masses above the limiting mass for thermonuclear fusion of deuterium are 'brown dwarfs', no matter how they formed nor where they are located."*

[3]Based on data collected by www.exoplanets.org (Han et al., 2014).
[4]http://www.iau.org/news/pressreleases/detail/iau0603/
[5]http://w.astro.berkeley.edu/ basri/defineplanet/IAU-WGExSP.htm

- *"Free-floating objects*[6] *in young star clusters with masses below the limiting mass for thermonuclear fusion of deuterium are not 'planets', but are 'sub-brown dwarfs'."*

Hence, one should keep both definitions in mind for the status of a true exoplanet, although they are not precise in several areas. There is no proper quantification of what constitutes "clearing the neighbourhood": Pluto's orbital path overlaps with Neptune's, so has Neptune cleared its orbit? What constitutes a "nearly round" shape? Several suggestions have been put forward to improve the definition (Soter, 2006; Margot, 2015) but so far, none have been accepted by the IAU.
In case of an exoplanet detection, the naming procedure is as follows: the first detection ends with the suffix "b" to the name of the star[7] with all further detected planets being named chronologically in alphabetical order. The order of detection determines the suffix, not the orbital distance to the star, which has the (usually not used) suffix "a".

1.2.2 Planet types

There is a variety of planets and planet-like objects, both in our Solar System and beyond. The first-order distinction has to be made between terrestrial, i.e. rocky, and gas planets.

Rocky planet: Rocky (or terrestrial) planets are small in size. They consist mostly of either iron, silicates or ice depending on where their formation took place. Mercury is an example for an iron-rich planet which formed very close to the Sun. Most planets and moons in our Solar System, including Earth, consist mainly of silicates. Ice- or water-based planets do not exist in our Solar System and formed farther away from the Sun, however, several moons around Jupiter and Saturn like Europa and Enceladus fit into that group.
One kind of rocky planet that does not exist in the Solar System is the so-called super-Earth. This is a group of planets with masses larger than Earth's but with a density much greater than that of gas giants. Super-Earths have been discovered to be quite common (Dressing and Charbonneau, 2013; Silburt et al., 2015) with some systems consisting mostly of such planets (Crossfield et al., 2015).

Gas planet: Gas planets make up the largest planets. It is assumed that they consist of an outer gas layer, mostly molecular hydrogen, a middle layer of liquid metallic hydrogen - due to the enormous pressure - and a molten rocky core (see section 1.3.2). Generally, gas planets can be divided into two categories, Neptune-sized and Jupiter-sized[8] planets. The larger gas planets in our Solar System, Jupiter and Saturn, are also called gas giants and consist mainly of hydrogen and helium. The smaller gas planets Neptune and Uranus, are so-called ice giants and their mass is mostly made up by large quantities of heavier elements like oxygen or nitrogen. Their density is therefore higher which makes it difficult to distinguish between low-density super-Earths and ice giants.
There are methods to characterize gas giants by their outer atmosphere and albedo, for

[6] See sections 1.2.2 and 1.3.5 for further information.

[7] The name of the star is usually determined through the catalogue with which it was identified. In case of larger surveys like Kepler or Super-WASP, the name is instead assigned based on the project name and a number in order of detections.

[8] Some further distinguish Saturn-sized planets, i.e. gas planets having about $0.7\,R_J$.

example the Sudarsky classification (Sudarsky et al., 2000, 2003). The model differentiates between 5 classes of atmospheric models which are sorted by their equilibrium temperature, starting with the coolest:

Class I: Ammonia These planets are found in the outer regions of planetary systems with low temperatures of less than 150 K and a high albedo of about 0.57. Both Jupiter and Saturn belong to this group.

Class II: Water vapor Planets with higher temperatures than class I whose atmospheres are dominated by water clouds. They have the highest albedo of all classes at about 0.81 and temperatures of less than 350 K.

Class III: Cloudless With equilibrium temperatures between 350 K and 800 K, planets of this class do not form clouds. Too hot to form water clouds and too cold for silicate or iron grains, they appear clear with a slightly blue colour due to Rayleigh scattering and have a low albedo of 0.12.

Class IV: Alkali metals and CO The orbits of these very hot planets (>1000 K) are closer than Mercury and their atmospheres are dominated by alkali metals, with strong Potassium and Sodium lines. CO-molecule absorption is also very strong in the infrared and the overall albedo of this class is the lowest at 0.03.

Class V: Silicates Nowadays being called hot Jupiters, these planets have the highest equilibrium temperatures of > 1400 K. Their atmospheres are mostly dominated by silicates and they have a relatively high albedo of 0.55.

This method is only applicable to the subset of gas giants, e.g. Neptune and Uranus cannot be classified with it.
There is a kind of gas planet that was not expected to exist and is unknown in our Solar System, the so-called Hot Jupiters[9]. They are class V planets according to the Sudarsky classification and have very short planetary periods of less than ten days. The very first discovered planet with a measured radius, HD 209458 b, is such a hot Jupiter (Charbonneau et al., 2000; Henry et al., 2000). They likely formed through migration processes (see section 1.3.5) which leads to the question of whether they still occur around the smallest stars, M-dwarfs (see chapter 2).

Free-floating planet: Free floating planets[10] are planetary-mass objects that do not orbit a star. Based on gravitational microlensing surveys (see section 1.5.2), they seem to be quite common in the Milky Way, possibly numbering in the billions. They most likely form through two different processes: during the planetary migrations phase in the formation of a stellar system, planets may get ejected. An alternative process is that the collapsing dust cloud that does not contain enough matter for the formation of a star and instead ends in the birth of a brown dwarf or planet-sized object. This process - or another unknown process - has to occur since the amount of free-floating planets is too high to be explained by ejection alone (Veras and Raymond, 2012).

[9] Called Hot Neptunes for smaller radii.
[10] Also called rogue planets or starless planets.

1.3 Formation

The development of a theory of stellar and planetary formation has been an ongoing process. The number of exoplanet discoveries over the last years has progressed to a point where statistical analysis is now possible. At the same time, more and more powerful computers have enabled simulations of this formation process to a more precise degree. The established working theory is at least capable of describing the full time-scale of the development from dust grains to planets.

1.3.1 Star formation

The formation of a planet is closely linked to the formation of its host star. Vast clouds of dust, chemically enriched with small amounts of metals[11] from previous stellar life-cycles, are in hydrostatic equilibrium, e.g. the kinetic energy from the gas pressure balances the gravitational attraction (Prialnik, 2000). Stars usually do not form isolated but rather in large star-forming regions[12]. One such region is shown in Figure 1.1.

Figure 1.1: Hubble image of the horsehead nebula, a star-forming region located in the Orion constellation. One can see thin wisps of gas and dust which are only visible in this false-colour infrared image. (Source: http://hubblesite.org/newscenter/archive/releases/2013/12/image/a/)

At some point, possibly by external perturbation, a part of the cloud contracts. Initially, it collapses isothermally but once a threshold in the central density is reached, the core becomes optically thick, i.e. photons get absorbed before leaving the core. This leads to strong heating and the contraction slows considerably. At about 1000 K, molecular hydrogen becomes dissociated which subsequently cools the core. This accelerates the contraction of

[11] In astronomy, any element heavier than helium is considered a "metal".
[12] Also called stellar nurseries.

the cloud and heats the centre again to central temperatures of about 10000 K, at which point the core stabilizes.
The angular momentum of the cloud is conserved, leading to rotation of the floating dust and gas around the centre of mass. In most cases, this leads to the subsequent formation of a disk (Haisch et al., 2001). The centre keeps accreting mass from the surrounding disc. After about 10000 years, the protostar reaches $1\,M_\odot$ and further contracts on a Kelvin-Helmholtz timescale[13], converting the gain in potential energy from contraction into heat and radiation. In this state, it is fully convective and in hydrostatic equilibrium and moves on the so-called Hayashi track (Beccari and Carraro, 2015). Finally, the star contracts and temperatures in the core rise until the star is able to burn hydrogen in nuclear fusion. At this point, the star reaches the Zero Age Main Sequence (ZAMS) and starts its life on the main sequence track.

1.3.2 Planet formation

In-fall of gas from the surrounding cloud and viscous dissipation leads to a heating up of the disc. Most lighter elements and molecules evaporate and migrate outwards, leaving only heavier elements like iron behind. Eventually, the disc compresses into a very thin layer and reveals the star to the observer.
Figure 1.2 shows an image taken with the Hubble Space Telescope (HST), displaying an active starforming region where at least two protoplanetary discs are located. One can see the surrounding clouds of dust and gas that are illuminated by the newly born stars, the protoplanetary discs and, in the case of HH 30, two jets of material that are ejected by the star during its accretion process. Further overlaid is an image of HL Tau, upper left quadrant, taken with ALMA which is presumably proof for the existence of three exoplanets with masses between $0.2\,M_J$ and $0.55\,M_J$ and distances between 13.2 and 68.8 AU (ALMA Partnership et al., 2015; Dipierro et al., 2015). However, there is some doubt whether all gaps were formed by planets (Gonzalez et al., 2015). One of the two current theories on how most planets form is the core-accretion/gas-capture model (Pollack et al., 1996; Perryman, 2000).

1.3.3 Core-accretion/gas-capture

The core-accretion/gas-capture (CA-GC) model is, as the name indicates, a two step process (Hubickyj et al., 2004). The first step consists of solid matter coagulation/accretion. While the star is being born in the centre, small dust molecules in the disc may collide randomly and sometimes stick together due to Van der Waals forces (Scheeres et al., 2010). This process takes place over the first 100.000 years of the disc's lifetime. During this time, a few bodies - called planetesimals - may form and reach diameters of more than 1 km. Their mass gain is slowly increasing as their cross-section is growing, not only due to their rising size but further due to their starting gravitational pull. Their masses become high enough to decouple from the surrounding disc gas and dust and enter Keplerian orbits around the star. Since their gravitational pull allows them to attract more material, those planetesimals are growing faster and faster. When their masses and radii become equivalent to that of the Moon, those so-called protoplanets sometimes collide with each other which further increases their mass.
After about 1 Myr, a few protoplanets are massive enough (about 10 M_E) to enter the second phase of planet formation. They bind and accumulate the surrounding gas from the disc.

[13] I.e. the approximate time it takes a star to radiate away its kinetic energy based on its current luminosity rate.

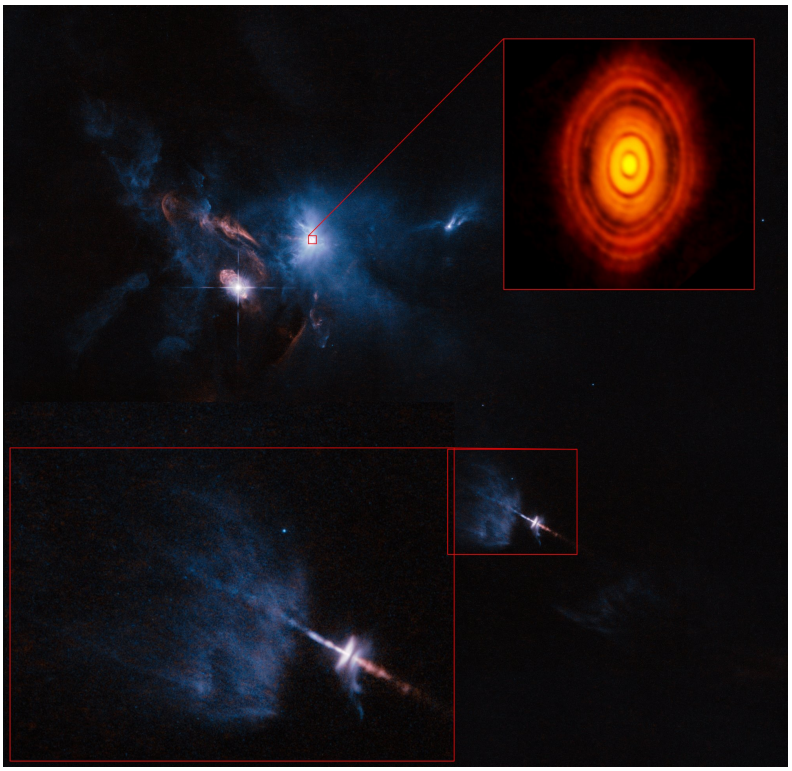

Figure 1.2: Superimposition of the star HL Tauri and its surroundings (upper half) with data taken with the ALMA telescope. Another protoplanetary disc, HH 30, is visible in the lower half of the figure, adapted with enlargement of the relevant region (lower left quadrant). The red regions mark the magnified areas. Data from ALMA (upper red quadrant) lead to the conclusion that there are already fully-developed planets in the disc, although there is an ongoing discussion about the actual number of detected planets (Gonzalez et al., 2015). (Source: http://www.eso.org/public/images/eso1436b/ and http://www.eso.org/public/news/eso1436/)

Since this creates a new source of matter flow, the following mass growth is rising exponentially. At the same time, the protoplanets exert an even stronger gravitational pull on other nearby bodies, leading to migration or, in other cases, orbit destabilization which can send protoplanets into the star or throw them out of the stellar system. The accretion ends when either all gas has been absorbed or the star is shining bright enough to push the remaining gas out of the stellar system due to radiation pressure. The typical timescale for the lifetime of a disc is 10 Myr and the mass development of a planet during that time is illustrated in Figure 1.3.
The CA-GC model is capable of describing the whole process from small dust molecules to gas giants. However, accretion by Van der Waals forces becomes rather inefficient for larger sizes (cm and mm-size), so-called pebbles, before gravity starts having an effect. Ice cannot be formed closer to the star and the remaining silicates[14] cannot pass several millimetres in size (Youdin and Shu, 2002), therefore it is not entirely clear how planetesimals can form in such a short time span (Youdin and Shu, 2002). Although it seems plausible that massive

[14]Iron and other metals are still liquid close to the star.

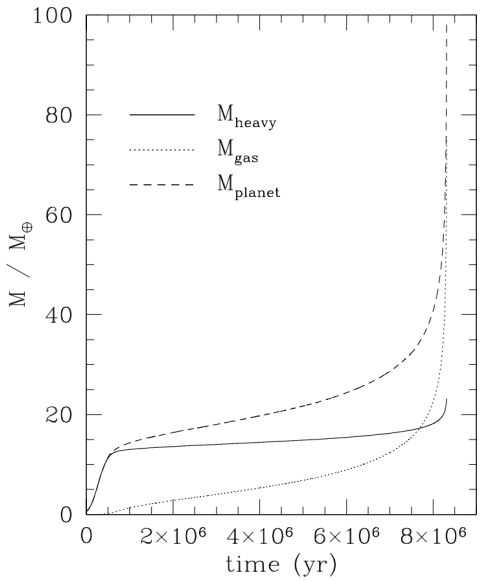

Figure 1.3: Timescale for the mass developement of a planet in the core-accretion/gas-capture model with masses of accreted planetesimals (solid line) and gas (dotted line). One can see the initial phase of pure solid matter accretion (first Myr) and the runaway accretion of gas and matter in the final phase (8 Myr and onwards). (Taken from Alibert et al. (2005))

gas planets like Saturn could still be created in time (Dodson-Robinson et al., 2008), general consensus is that another mechanism should at least add to this process.
The Pebble-accretion model attempts to resolve this issue (Chambers, 2016). Ice-rich pebbles that form outside of the snow line can form if they are more "sticky" than the silicate-based counterparts. They drift inward due to gas drag and may aid in creating larger-sized planetesimals in a short timescale.
In addition, the formation of the terrestrial planets (Mercury, Venus, Earth, Mars) together with the asteroid belt cannot be modelled sufficiently as of now (Izidoro et al., 2015). However, the CA-GC model has made strides over the last 10 years and managed to close many of the open questions concerning timescales.

1.3.4 Gravitational instability

Gravitational instability (GI) seems to be a plausible alternative formation mechanism at least for massive planets. A strong indication that GI seems to contribute in the formation is the analysis of chondrites[15] (Youdin and Shu, 2002). While they have sizes of several centimetres and more, they consist of many small millimetre-sized particles that seemed to have been molten together in only one or several events. Therefore, they cannot have formed through small accretion of silicates.
Massive particles, as large as they could get by accretion, tend to gather in the middle of the disc plane. This creates a very thin layer with a high density that can become unstable when

[15]Meteorites that were formed at the early phases of the Solar System.

the following criterion is fulfilled (Youdin and Shu, 2002):

$$Q_p \equiv \frac{\Omega \cdot c_p}{\pi \cdot G \cdot \sum_p} < 1 \quad , \tag{1.1}$$

where Ω denotes the Keplerian rotation rate, c_p the velocity dispersion and $\sum_p$ the surface density. Since there is a direct relation with the rotation rate Ω, the outer region of the disc has a higher possibility of fulfilling this criterion and fragmenting into a planet. Further, cooling time scales have a direct effect on whether or not disc fragmentation occurs (Gammie, 2001) and the outer area of the disc has both less stability and lower cooling times. Therefore, it is assumed that GI dominates the formation mechanisms for distances larger than 50 AU (Kley and Nelson, 2012; Rice et al., 2015) and up to 100 AU (Boley, 2009).
Although this process is generating a planet very fast, a rare combination of further factors have to add up, including tidal shearing and internal pressure (Kratter and Murray-Clay, 2011). GI seems to contribute only a minor fraction of formed planets which is backed up by observational evidence (Rice et al., 2015). However, some of the exoplanets observed with direct imaging (see section 1.5.3) may have formed that way (Kratter and Murray-Clay, 2011). Since GI can only work at larger distances and migration seems to occur only very rarely at those distances (Forgan and Rice, 2013), planets of the inner zone have to be formed by other processes. There are constraints for the frequency of planet formation by the GI model: Less than 8% are thought to have formed by GI for stars of stellar types FGKM (Janson et al., 2012).

1.3.5 Migration/orbital evolution

The existence of Hot Jupiters, discovered by transit and radial velocity surveys (see below), brought forth questions that need to be addressed by formation models. As it turns out, model calculations in the core-accretion/gas-capture already predicted the existence of such planets before they were discovered (Lin and Papaloizou, 1979; Goldreich and Tremaine, 1980). Since the amount of material close to the star is not sufficient to create gas giants and temperatures are too high for matter to solidify, they must have either formed elsewhere and then moved inwards or collected the material on their way closer to the star. Generally, there are three different migration processes.

Type I Migration

This is the earliest type of migration that can occur. A protoplanet that has gathered enough mass to influence its surroundings can excite density waves in the disc due to its gravitational pull. This happens when the protoplanet's epicyclic frequency κ

$$\kappa^2 \equiv \frac{2\Omega}{r}\frac{d}{dr}(r^2\Omega) \quad , \tag{1.2}$$

where Ω is the differential rotation frequency and r the distance to the star, is a multiple of another forcing frequency, for example the disc's rotation period; in this case, $k \equiv \Omega$ (Armitage and Rice, 2005). Depending on the characteristics of the system, the resonance - a so-called Linblad resonance - occurs inside or outside of the orbital radius. This leads to matter flow and a subsequent torque that affects the protoplanet's orbit due to the increase or decrease in angular momentum. Most of the time, protoplanets undergo this migration

on an inward-going spiral (Lubow and Ida, 2010). A simulation of this process is shown in Figure 1.4 in the left panel.

Type II Migration

Planets that undergo the type I process with a mass higher than that of Jupiter can have a different outcome: they further clear a large gap around their orbital radius. The torques generated by the planet cause material on the inside of the orbital radius to loose angular momentum (Kley and Nelson, 2012) while material on the outside is gaining angular momentum, feeding the planet further. This pulls the planet inwards, likely the way Hot Jupiters are being formed. The timescale for this process is rather long with about $\sim 10^5$ years (Lubow and Ida, 2010), but short enough to happen before the disc dissipates. A simulation of this process is shown in Figure 1.4 in the right panel.

Type III Migration

There are different definitions of type III migration. Lubow and Ida (2010) describe it as a runaway coorbital migration. The coorbital torque saturates with low viscosity (Masset, 2002). If the migration of the planet is fast enough and therefore its movement through the disc creates turbulent viscosity, the coorbital torque starts exerting an effect and increases or decreases the rate of migration. An alternative interpretation of type III migration, discussed in Cloutier and Lin (2013), occurs when gravitationally unstable gaps are being created by a massive planet. This creates negative pressure that can quickly move the planet outwards to twice the previous orbital radius.

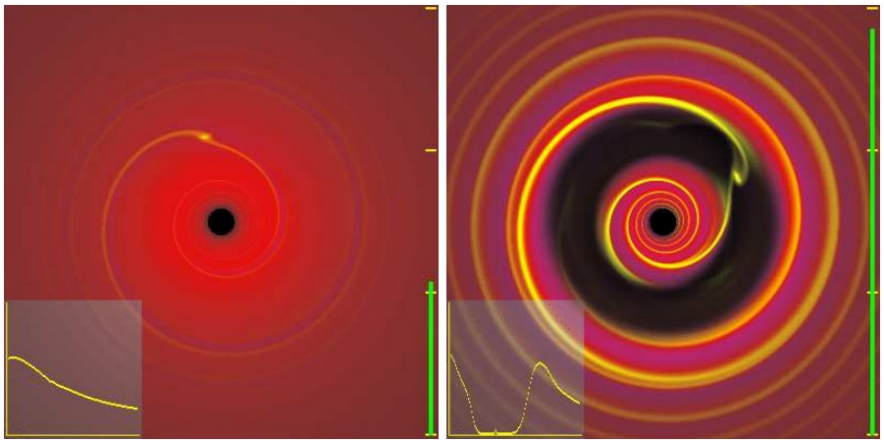

Figure 1.4: Illustration of type I (left) and type II (right) migration. In this simulation, a 2-dimensional hydrodynamic model with a planet on a fixed radius was created. On the left-hand panel, a low-mass protoplanet excites a resonance in the disc, leading it inwards with the torque clearly visible in the matter stream. In the right panel, a $10\,M_J$ body was simulated which clears a large gap in the disc (taken from Armitage and Rice (2005)).

Orbital evolution

Planetary bodies interact with each other and their star. A classic example for this effect is the orbital evolution of Uranus and Neptune, which probably got scattered by the more massive giants Jupiter and Saturn during their formation and therefore migrated outwards (Thommes et al., 2002). It is presumed that there was not enough building material to allow for those planets to form at their current orbits which further strengthens that assumption.

Orbit circularization

Tidal interaction between a star and its planet is strongly dependent on the orbital distance r, even more so for the timescale of orbit circularization ($t \sim r^6$, Heath and Doyle, 2004). Planets that are close to their star, such as Hot Jupiters and Hot Neptunes, are therefore affected by very strong tidal forces which lead to circularization on short timescales. Most planets closer than 0.1 AU have been shown to possess circular orbits (Matsumura et al., 2008) as a consequence.

Tidal locking

As described above, the tidal interaction between a star and a planet is rapidly decreasing with the orbital distance r. After a certain timescale t, the planet is in synchronous rotation with the star, i.e. one side of the planet is constantly facing the star just as the Moon is facing the Earth. For a given initial rotation period P_0, stellar mass M and planetary friction parameter Q[16], the timescale for tidal locking is entirely dependent on r (Heath and Doyle, 2004):

$$t = \frac{Q}{P_0 M^2} \left(\frac{r}{0.027}\right)^6 \quad . \tag{1.3}$$

A planet's orbit will therefore circularize faster the closer it is to its host star and the more massive the star is. Different planet compositions (and subsequently the friction parameter Q) can further affect the timescale. For Hot Jupiters, this process takes place in the order of 10^5 yr, meaning that any Hot Jupiter should be tidally locked. This leads to a variety of effects. The magnetic dynamo of the planet, generated by its rotation, is significantly weakened which leads to a weaker magnetosphere and subsequently higher rate of particle loss due to stellar winds. The flux difference between the star-facing and the opposite side of the planet creates a temperature gradient. However, there is a redistribution of thermal energy across the planet as several measured Hot Jupiter thermal maps show (Knutson et al., 2007; Stevenson et al., 2014). For the case of HD189733b, temperatures differ by only 25% between the bright and dark side.

Resonant orbits

In systems with multiple planets, there is frequent gravitational interaction. Orbital migration or planet-disc interaction can lead to resonances where the planets periodically come close to each other in time intervals close to integer ratios of their orbital periods. This significantly increases the effect of the mutual gravitational interactions which either ends in destabilized orbits due to oscillation or, in other cases, stabilized orbits. Such unstable resonances have

[16] For an Earth-like planet with oceans one assumes $Q = 13$, higher values for gaseous planets.

created gaps in the Saturn rings while the Galilean moons Ganymede, Europa and Io developed a 1:2:4 resonance which stabilizes their orbits, shown in Figure 1.5. Resonant orbits

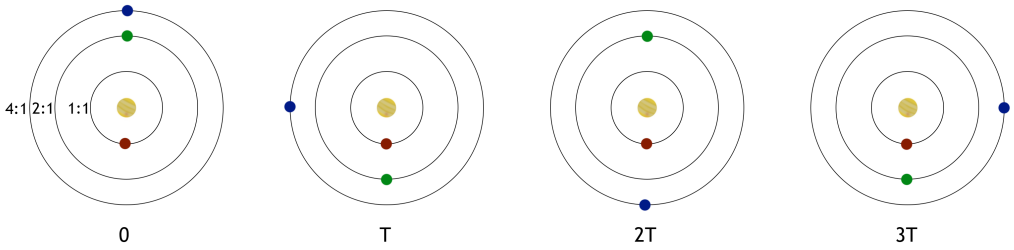

Figure 1.5: Illustration of orbital resonance between the three Galilean moons Ganymede (blue), Europa (green) and Io (red) which orbit Jupiter. The ratios given in the figure correspond to their orbital period ratios.

can create systems that otherwise would destabilize quickly, such as Kepler-11 with its 5 interior planets[17] that are packed closely to the star with minimal deviations in their orbital inclination. Planets b, c and d, e, f orbit in resonance (Lissauer et al., 2011).

1.4 M-dwarfs

M-dwarfs, the smallest and lowest-mass main-sequence stars with the spectral type M, are the most common stars in the Milky Way. They make up 70% of all stars (Henry et al., 1994) but due to their low luminosity and effective temperature, most are only visible at fainter magnitudes and in the infrared. Average values for effective temperature T_{eff}, stellar radius $R_\star$, mass $M_\star$, luminosity $L_\star$ and absolute magnitude M_V are given in Table 1.1.

Type	T_{eff} [K]	$R_\star$ [$R_\odot$]	$M_\star$ [$M_\odot$]	$L_\star$ [$L_\odot$]	M_V [mag]
M0	3800	0.62	0.60	7.2	9.34
M1	3600	0.49	0.49	3.5	9.65
M2	3400	0.44	0.44	2.3	10.1
M3	3250	0.39	0.39	1.5	11.2
M4	3100	0.26	0.20	0.55	12.1
M5	2800	0.20	0.14	0.22	16.0
M6	2600	0.15	0.10	0.090	16.6
M7	2500	0.12	0.090	0.050	17.4
M8	2400	0.11	0.080	0.030	18.8
M9	2300	0.08	0.075	0.015	19.8

Table 1.1: Properties of different M-dwarf subclasses (Kaltenegger and Traub, 2009).

[17] Kepler-11 also has a 6th planet that is orbiting farther away and does not interact with the interior planets.

M-dwarfs are of particular interest to the scientific community for a variety of reasons. The S/N of transits and radial velocity shifts are stronger for smaller stellar radii and stellar masses, respectively. This makes them ideal targets to search for small planets and M-dwarfs have been the focus of several RV surveys (Bonfils et al., 2005, 2007, 2013). However, those surveys focused on the brightest M-dwarfs in the sky and were limited by low sample sizes, making some statistical assessments difficult.
Furthermore, M-dwarfs may be the easiest route towards detecting habitable planets (Scalo et al., 2007). The Liquid-Water Habitable Zone (LWHZ) is much closer to the star (see section 1.7.2) and, due to the stronger S/N of a transit, smaller, Earth-sized planets can be discovered more easily. Also, atmosphere spectroscopy during the planet's transit has a larger signal strength due to the more favourable radius ratio between planet and star compared to larger main-sequence stars. It should be further pointed out that, since M-dwarfs are fainter and therefore the observed stars are closer to Earth, those worlds might be the best-suited targets for interstellar visits.
There are still open questions surrounding planet formation in planetary systems. M-dwarfs have the lowest masses of all main-sequence stars and there is growing evidence that their planetary systems may be different to those of higher-mass FGK-dwarfs. Various studies and theoretical models (Laughlin et al., 2004; Ida and Lin, 2005; Johnson et al., 2010; Mordasini et al., 2012) have lead to the conclusion that the frequency of hot Jupiter planets may be much lower in M-dwarf systems.
There are several different theories on how such planets may form, e.g. in situ (Hansen and Murray, 2013) like in our Solar System, inward-migration after formation in the outer regions (Swift et al., 2013) or a combination of both processes (Hansen and Murray, 2012; Alibert et al., 2013; Cossou et al., 2014). However, none can explain this observed difference to a sufficient degree. Redistributing the available planet mass of a planetary disc into several smaller planets does not solve this since the total heavy-element mass contained in M-dwarf planetary systems appears to be *higher* than in FGK-dwarfs. This is very puzzling, considering that the total disc mass of young M-dwarf systems is lower, based on measurements with imaging (Mulders et al., 2015b).

1.5 Planet detection methods

There are a variety of different detection methods, each having strengths and weaknesses. In order to create a comprehensive view of planets, their properties and distribution, each technique therefore has to be utilized.

1.5.1 Timing

The category timing encompasses four distinctly different techniques, each of them having led to several successful planet detections.

Pulsars

The first detection of extrasolar planets by Wolszczan and Frail (1992) was made with the timing method by measuring the extremely regular radio signals of pulsar[18] PSR B1257+12. It is a so-called millisecond pulsar which, as the name implies, emits a signal in the kHz range at an extremely time-constant period with changes of less than $10^{-19}\mathrm{s\,s^{-1}}$ (Perryman, 2000). Perturbations from orbiting planets therefore create detectable signal deviations with timing amplitudes of

$$\tau = 1.2 \left(\frac{M_P}{M_\oplus}\right) \left(\frac{P}{1yr}\right)^{2/3} ms \quad , \tag{1.4}$$

assuming a pulsar mass of $1.35\,M_\odot$ and a circular planet orbit. The three planets detected in PSR B1257+12 came as a big surprise to the science community for various reasons. Not only were they the first discovered extrasolar planets, two of them have super-Earth dimensions[19] with masses of 3.9 and 4.3 $\mathrm{M_\oplus}$. Somehow, those planets survived the violent transformation of a massive star into a pulsar without being swallowed or thrown out of the system. The fact that the pulsar is further located in a globular cluster just added to the scientist's bafflement.

Pulsations

Many stars, notably subdwarf B stars[20] show periodical luminosity variations due to pulsations (Heber, 2009; Lutz et al., 2009). Those variations usually occur at short-period or long-period timescales, but in some cases, stars can exhibit both variabilities at the same time while having very low perturbations in their timings. Silvotti et al. (2007) used this to detect the first exoplanet with pulsation timing around the star V391 Pegasi. By comparing the observed to the calculated pulsation timings in an O-C diagram (Sterken, 2005), they could determine that a planet with a minimum mass of 3.2 $\mathrm{M_J}$[21] is orbiting the star with a period of 3.2 yr.

[18] A pulsar is a rapidly spinning neutron star which emits strong radio signals along a narrow cone due to its very strong magnetic fields.

[19] Hence, the first planet detection was already of a planet type that does not exist in our Solar System.

[20] Small, low-mass ($0.5\,\mathrm{M_\odot}$) stars that consist almost entirely out of helium, have very high effective temperatures of around 30000 K and are positioned at the extreme horizontal branch of the Hertzsprung Russel Diagram.

[21] More precisely, dependent on the inclination of the system, the mass is $\frac{3.2\mathrm{M_J}}{\sin i}$.

Eclipsing binaries

The process of star formation leads to a high fraction of stars that are gravitationally bound to at least one other star. Raghavan et al. (2010) estimate the multiplicity of binary systems to be $33\% \pm 2\%$. In the case where the system's inclination is edge-on from Earth's point of view, the stars eclipse each other and periodically decrease the overall brightness while doing so. In a 2-body system, this process is very time-stable which means that perturbations by a third body can be visible in an Observed-Calculated (O-C) diagram where it will lead to a periodic change between slightly too late and too early eclipses. Lee et al. (2009) detected such a perturbation in the eclipsing binary system HW Vir. It consists of an M-dwarf and a B subdwarf that orbit each other very closely with a period of 2.8 hours. Over the course of 20 years, they measured variations that are consistent with two massive planets with minimum masses of $8.5\,M_J$ and $19.2\,M_J$[22]. However, the existence of planets in this system has been disputed by Horner et al. (2012). It is therefore still unclear whether eclipsing binary timing has yielded a successful planet detection or not.

Transit timing variations (TTV)

Not only eclipsing binaries or pulsating planets can be used for photometric timing analysis, transiting planets themselves can give clues to the existence of further planets orbiting the same system. The high-cadence, high-precision and long-term data collected by the Kepler space telescope yielded an unprecedented amount of transiting planets that were suggested to be used for such a study even before the launch of the telescope (Holman and Murray, 2005). The first claimed detection was an additional planet around WASP-3 (Maciejewski et al., 2010), but it had to be retracted later on after a publication by Montalto et al. (2012). However, the method has proven to be extremely successful in confirming exoplanets and/or characterizing planet's masses in multiple systems (see section 1.8.3).

Timing methods are very effective in their respective fields with 23 detections as of July 2016[23]. Their distribution in semi-major axis and planetary mass are shown in Figure 1.6. Although other techniques have higher detection rates, timing is very well-suited to complement other methods such as radial velocity and transit.

1.5.2 Gravitational microlensing

The thought that gravitation could even bend the path of light has been around for several centuries. Isaac Newton proposed this idea in the early 1700s[24] (Soares, 2005). However, with Einstein's theory of General Relativity, the effect of gravitational interaction with light could finally be described accurately in 1915 and was essential in proving the validity of this theory for the first time. Gravitational lensing effects can happen in various ways. For distant galaxies, this can lead to double or quadruple images[25] and many other kinds of distortions. For stars and planets, however, the angular separation is so small that only one source of

[22] This body is therefore a brown dwarf although the initial publication stated that it is supposedly a planet.

[23] Based on www.exoplanets.eu (Schneider et al., 2011).

[24] "Do not Bodies act upon Light at a distance, and by their action bend its Rays, and is not this action (caeteris paribus) strongest at the least distance?", *Opticks*

[25] So-called Einstein's cross.

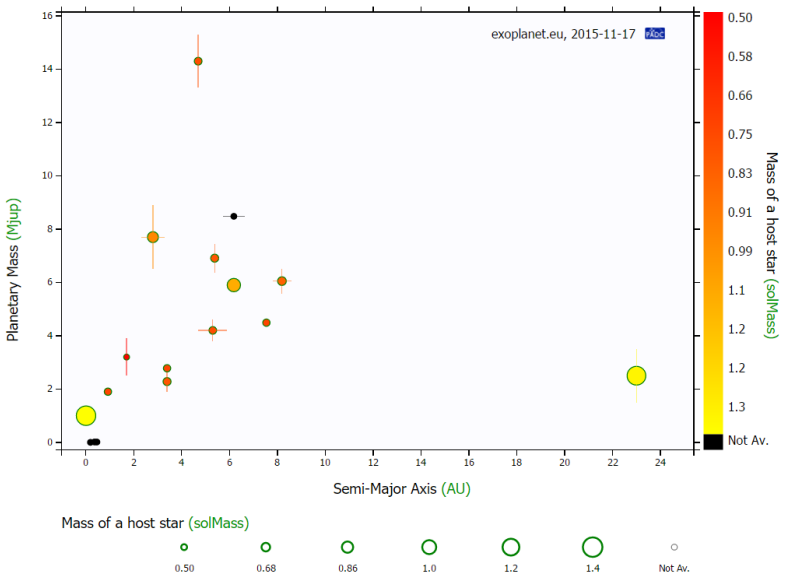

Figure 1.6: Semi-major axis over planetary mass for all 18 detected exoplanets with the timing method that have measured masses (extracted from www.exoplanet.eu (Schneider et al., 2011)).

light can be resolved. If the constellation is just right, light from a background star[26] can be deflected by a passing-by foreground star, shown in Figure 1.7. This foreground star acts like a lens to the background star and bends its light to some degree. Depending on the strength of this effect, the angular separation from the observer's point of view can be so small that there is an apparent brightness increase and subsequent dimming of the source instead of separate actual images. The whole process is well-characterized with the lensing event taking place over tens of days with a magnification of several magnitudes. The simplest case of a uniform rectilinear motion with a lens star of mass M for a time-dependent angular separation u(t) can be parametrized (Gaudi, 2010) by

$$u(t) = \left(u_0^2 + (\frac{t - t_0}{t_E})^2 \right)^{1/2} \quad , \tag{1.5}$$

where the constant u_0 denotes the minimum separation in Einstein radii[27]. The factors t_E and t_0 normalize the equation to the point of the largest magnification (t_0) and the timescale of the event (t_E). The time-dependent magnification $A(t)$ and timescale t_E can be characterized by:

$$A(t) = \frac{u(t)^2 + 2}{u(t)\sqrt{u(t)^2 + 4}} \quad \text{and} \tag{1.6}$$

$$t_E = 19d \left(\frac{M}{0.3 M_\odot} \right)^{1/2} \left(\frac{\pi_{rel}}{123 \mu as} \right)^{1/2} \left(\frac{\mu_{rel}}{10.5 mas/yr} \right)^{-1} \quad . \tag{1.7}$$

[26]Located in the distant region of the Milky Way, e.g. the Galactic bulge, one of the Magellanic Clouds or in the M31 Andromeda galaxy.

[27]The Einstein radius is defined as $\theta_E = 550\, mas \left(\frac{M}{0.3\, M_\odot} \right)^{1/2} \left(\frac{\pi_{rel}}{125\, \mu as} \right)$, π_{rel} being the relative parallax between both sources.

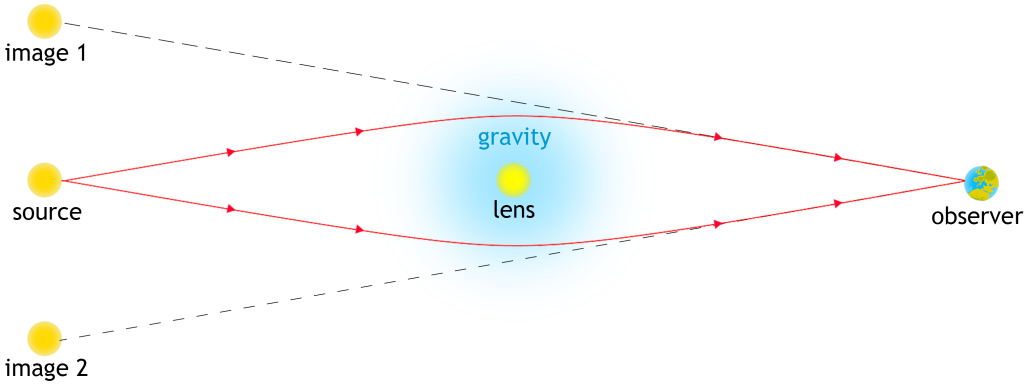

Figure 1.7: Illustration of light paths from a distant light source that is deflected by a lens, in this case a star.

Note that $A(t)$ converges to 1 with rising $u(t)$ which means that the magnification decreases. The factor π_{rel} denotes the relative parallax between both sources and μ_{rel} the relative proper motion of the stars. However, if a planet is orbiting around the lens star, it can also create a much shorter microlensing effect during this event:

$$t_{E,p} = \sqrt{\frac{m_P}{M}} t_E \quad . \tag{1.8}$$

The mass m_P of the planet is therefore significant for the duration of the planet magnification. Depending on the geometry of the event, the magnification caused by the planet can be higher than the star's. An example case for a microlensing event with a planet is shown in Figure 1.8 (Udalski et al., 2005) which consist of a star and a massive Jovian planet that creates a light magnification of the same magnitude.
Gravitational microlensing is an effective method to detect exoplanets and, compared to other methods, very effective in detecting low-mass planets even at far-out orbits. However, this technique does have several drawbacks: the recorded event is a one-time occurrence. No further information about the planet besides distance and mass can be gained and the frequency of microlensing events is very low. However, since a typical microlens with a star takes several days and has a very high amplification, this technique is well-suited to large-scale statistical surveys and has been quite successful with so far 47 detections as of July 2016[28]. The distribution of planetary masses and semi-major axes is shown in Figure 1.9.

[28] Based on www.exoplanet.eu (Schneider et al., 2011).

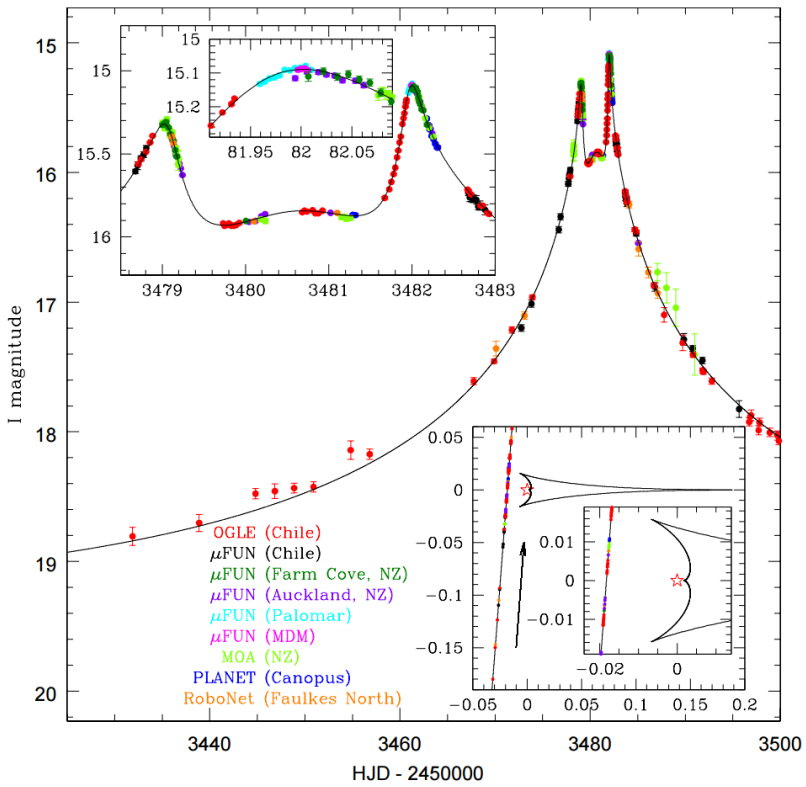

Figure 1.8: Light curve of microlensing event OGLE-2005-BLG-071, showing a double-peak structure which is created by a Jupiter-sized companion (second peak) to the lens star (left peak). The peaks are about 3 days apart, having allowed various telescopes to record this data in cooperation. (Taken from Udalski et al. (2005))

1.5.3 Imaging

Direct imaging of planets - i.e. detecting planetary light either directly emitted or reflected - is very challenging for a variety of reasons. Nevertheless, the first discovery was made already early on by Chauvin et al. (2004) and was just the first of many. In some cases, even multiple planets could be detected (Marois et al., 2008). The angular separation of a planet and its star is extremely low. Considering the definition of a parsec (pc) shows the scale of this separation: 1 pc is the distance at which an orbit of 1 AU has a parallax of 1 arcsec. Stars are usually much farther away than 1 pc and many planets orbit closer than 1 AU. This means that the majority of the planets are separated less than 1 arcsec from their host star, an angular distance that is extremely difficult to resolve from the ground. Besides the issue of angular separation, the contrast ratio[29] $\frac{L_p}{L_\star}$ is very low (Perryman, 2000):

$$\frac{L_p}{L_\star} = p(\lambda, \alpha) \left(\frac{R_p}{a}\right)^2, \tag{1.9}$$

with semi-major axis a and planetary radius R_p. The factor $p(\lambda, \alpha)$ encompasses the geometric albedo for given wavelength λ and phase α. This formula does not include self-illumination

[29] i.e. the ratio between the flux of both sources.

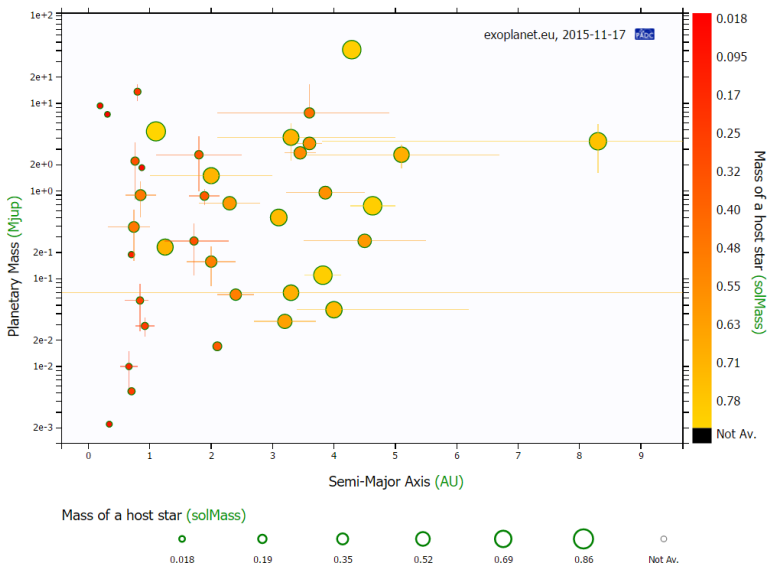

Figure 1.9: Semi-major axis over planetary mass for all 47 detected exoplanets with microlensing. Note that only 43 out of 47 detections are shown, 2 being discarded since the orbital distance is missing, 2 for masses higher than 13 M_J. (extracted from www.exoplanet.eu (Schneider et al., 2011))

for a planet with a significant thermal emission (Perryman, 2011).
In case of Jupiter, the contrast ratio is about 10^{-9} in the optical with an angular separation of 0.5 arcsec at 10 pc but this would improve to 10^{-4} in the infrared.
Earth's turbulent atmosphere smears any object that is being observed by a mixing of different layers which creates a variable optical path length over time. This effect, called seeing, creates a point spread function (PSF) that makes such a detection quite challenging. Locating the telescope in space or utilizing adaptive optics are therefore highly effective ways for this detection technique, since they improve the PSF considerably. A coronagraph is further needed for imaging to succeed. This instrument was originally used in daylight astronomy for studying the Sun's corona by blocking out direct sunlight but has seen a renaissance with the observations of discs and planets. New coronagraphs being constructed right now (Jovanovic et al., 2015) will allow to observe less angularly separated planets in the future, even with a lower contrast ratio. In order to maximize the target selection for imaging, one should focus on (Perryman, 2011):

- Nearby stars (d $<$ 5 pc),
- Young systems (10-100 Myr, d $<$ 100 pc) for a lower contrast ratio in the infrared,
- Stars with known planets (from radial velocity or transit studies),

while the use of large apertures[30], coronagraphs[31], adaptive optics[32] (Beckers, 1993) and nulling interferometry (Monnier, 2003) provide a better signal to noise.

[30] In order to improve resolution and signal to noise.
[31] As described in the text above, for minimizing the stellar light.
[32] For reducing the atmospheric effects, not needed for space-based telescopes.

In addition to the difficulty of imaging a planet, this method is ill-suited for measuring the planetary mass. The only way - as of now - is a modelling of the planet based on spectroscopic and photometric information which has a large intrinsic uncertainty. Imaging is, however, an important tool in studying the different phases of planet formation. In the future, spectroscopic characterization of the planet's atmosphere might be feasible with space telescopes like the James Webb Space Telescope (Gardner et al., 2006).

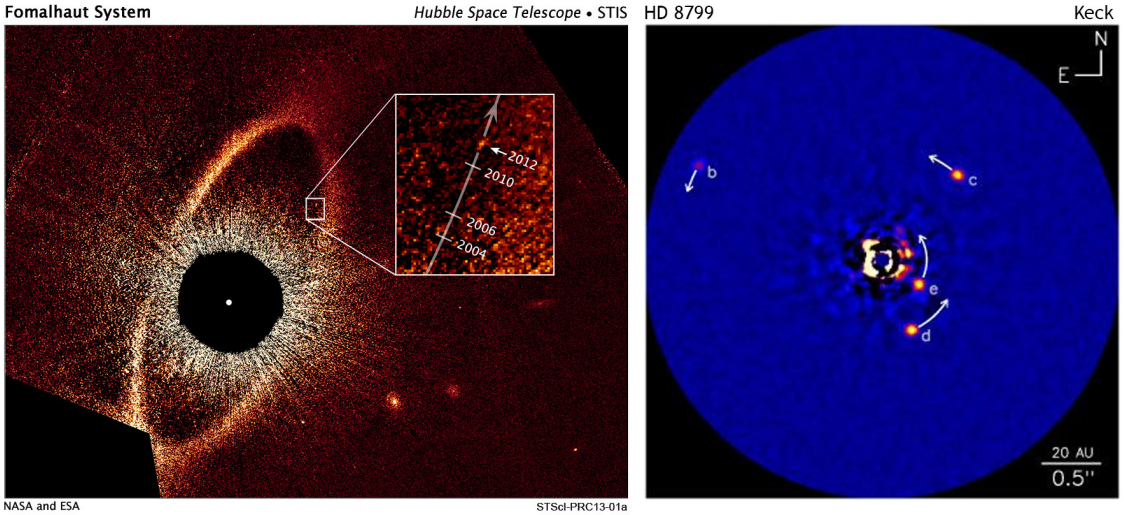

Figure 1.10: Planets detected with the imaging method: Fomalhaut b (left), recorded with the Hubble Space Telescope and HD8799 b-e (right), recorded with the Keck observatory. The curved arrows show the estimated orbital motion of the planets over the next 10 years (taken from http://hubblesite.org/newscenter/archive/releases/2013/01 and http://newsroom.ucla.edu/releases/astronomers-discover-and-image-186446, respectively).

As of July 2016, 27 planets have been directly imaged[33]. However, this number should be taken with a certain amount of scrutiny since the existence of several targets is still debated. Fomalhaut b, shown in Figure 1.10 on the left, was once thought to be one of the clearest cases of an imaged planet (Kalas et al., 2008). It is now being contested with an alternative theory being put forward that the signal might actually be a circumplanetary disc around a planet that cannot be seen directly or the remnants of a planetary collision event (Galicher et al., 2013). Multiple planets have been discovered in several systems with one of the most famous systems being HR 8799 (Marois et al., 2008), shown in Figure 4.4 on the right.
Figure 1.11 shows the mass of all imaged planets over their semi-major axis. It is noteworthy that several planets have been detected around brown dwarfs, shown as small red dots. Since the contrast ratio is much better for such a host body, planets can be detected at much closer semi-major axes around brown dwarfs. The current planet definition does only state that a planet must orbit a stellar object - which may or may not include a brown dwarf. Hence, the number of discovered planets might be further reduced to 18.

[33]Based on www.exoplanet.eu (Schneider et al., 2011) with the omission of falsely classified planets Kepler-70b and Kepler-70c and objects that should be classified as brown dwarfs since their masses are higher than $13\,M_J$.

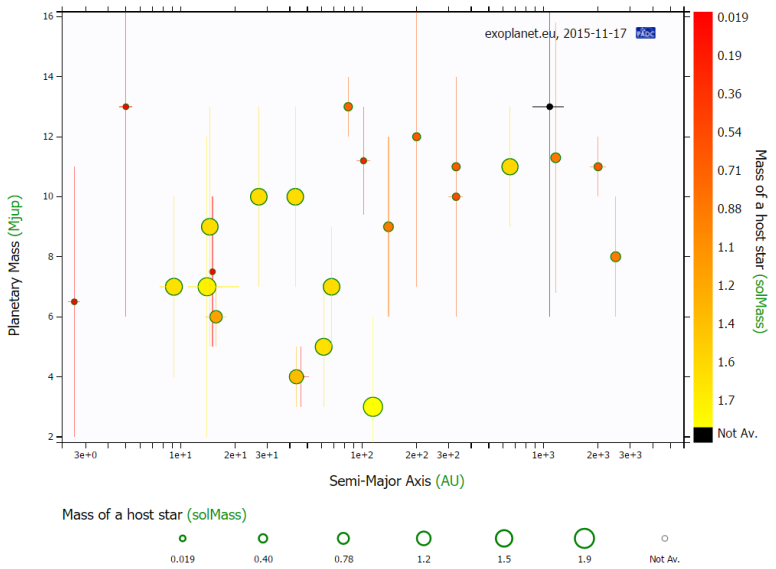

Figure 1.11: Semi-major axis over planetary mass for all planets detected with imaging. Note that only 27 out of 64 detections are shown, 37 being discarded for masses higher than 13 M_J (extracted from www.exoplanet.eu (Schneider et al., 2011)).

1.5.4 Radial velocity

Radial velocity (RV) has been the most successful detection method for a long time. Originally proposed by Struve (1952), technical restrictions made it difficult to implement until the arrival of digital detectors and high-resolution spectrographs. Although it would have been possible to detect planetary signals already in the beginning of the digital age, there was widespread initial doubt (Walker, 2012)[34]. This changed completely when the first exoplanet around a solar-type main sequence star was identified and published by Mayor and Queloz (1995)[35], a Hot Jupiter with a period of 4.2 days. The radial velocity method can be credited with jump-starting the ongoing revolution of exoplanet research.

A star is moving in conjunction with the planet as a reflex motion around the combined barycentre, i.e. the centre of mass. As with microlensing, the radial velocity method is based on the theory of General Relativity. Since the speed of light is constant, any motion towards or away from the observer results in a blue-shift or red-shift of the light, respectively, the so-called Doppler effect. Depending on the inclination of a planet-star system, some component of the star's motion vector is oriented towards the observer - the radial velocity of a star.

This mechanism is illustrated in Figure 1.12. A continuous survey can reveal periodic radial velocity shifts if a planet is present and its inclination allows for this effect to become detectable.

In mathematical terms (Hilditch, 2001), the barycentric semi-major axis of the star in a two-

[34]Walker (2012): *"It is quite hard nowadays to realise the atmosphere of scepticism and indifference in the 1980s to proposed searches for extra-solar planets. Some people felt that such an undertaking was not even a legitimate part of astronomy."*

[35]There was a previous detection by Campbell et al. (1988), however, this publication was later retracted due to the doubts about the uncertainties of the measurements. It was finally reconfirmed by Hatzes et al. (2003).

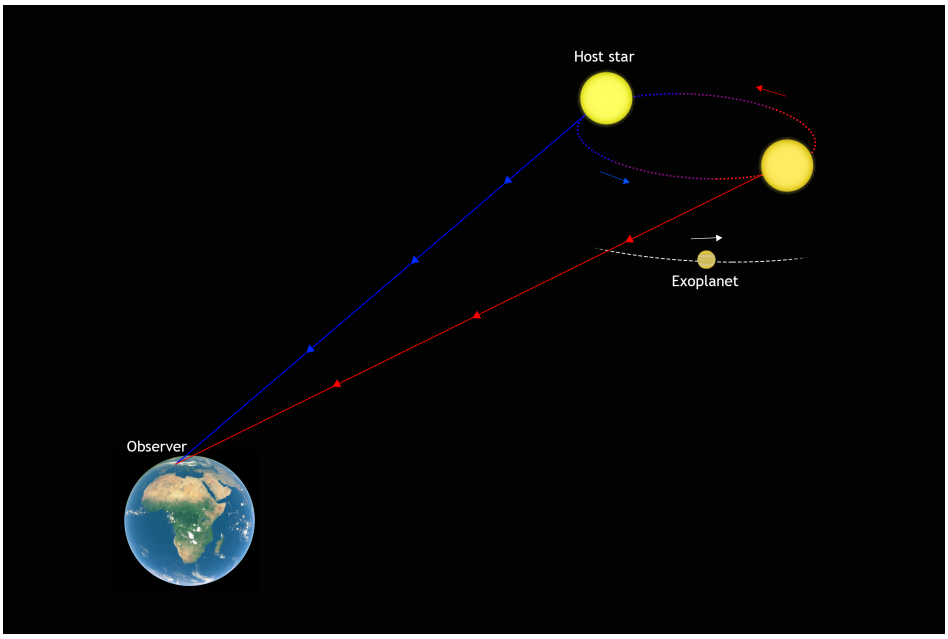

Figure 1.12: Depiction of blue/redshifting in a star system created by an orbiting exoplanet. This in turn leads to a detectable radial velocity change when observed from Earth.

body system can be determined by the relation between semi-major axes a_i and the respective masses m_i of both bodies:

$$\mathrm{a}_\star \cdot \mathrm{m}_\star = \mathrm{a_P} \cdot \mathrm{m_{planet}} \quad . \tag{1.10}$$

Smaller stellar masses or higher planetary masses therefore lead to a larger motion of the star. For the case of a circular orbit, the orbital velocity of the star can be determined easily:

$$\mathrm{v}_\star = \frac{2\pi \mathrm{a}_\star}{\mathrm{P}} \quad . \tag{1.11}$$

Equations 1.10 and 1.11 can be combined. Further using Kepler's Third Law[36] leads to:

$$\frac{\mathrm{P}^2}{(\mathrm{a}_\star + \mathrm{a_P})^3} = \frac{4\pi^2}{\mathrm{G}(\mathrm{m}_\star + \mathrm{m_P})} \quad , \tag{1.12}$$

which can be simplified to[37]:

$$\frac{\mathrm{P}^2}{\mathrm{a_P^3}} = \frac{4\pi^2}{\mathrm{G} \cdot \mathrm{m}_\star} \quad , \tag{1.13}$$

this leads to an equation for the visible radial velocity amplitude K for an observer at inclination angle i:

$$\mathrm{K} = \mathrm{v}_\star \sin \mathrm{i} = \left(\frac{2\pi \mathrm{G}}{\mathrm{P}}\right)^{1/3} \cdot \frac{\mathrm{M_P}}{\mathrm{M}_\star^{2/3}} \cdot \sin \mathrm{i} \quad . \tag{1.14}$$

[36] The square of the orbital period of a planet is proportional to the cube of the semi-major axis of its orbit.
[37] Planetary mass and stellar semi-major axes are much smaller than their counterparts and do not contribute significantly.

Using Kepler's Second Law[38], the orbital velocity can further be determined for elliptical orbits. The amplitude K changes slightly with the introduction of the eccentricity value e:

$$\mathrm{K} = \mathrm{v}_\star \sin \mathrm{i} = \left(\frac{2\pi \mathrm{G}}{\mathrm{P}}\right)^{1/3} \cdot \frac{\mathrm{M_P}}{\mathrm{M}_\star^{2/3}} \cdot \sin \mathrm{i} \cdot \frac{1}{\sqrt{1-\mathrm{e}^2}} \quad . \tag{1.15}$$

Note that the shape of the RV curve is further affected by the orientation angle ω which expresses the orientation of the system from the observer's point of view. In eq. 1.15, it is assumed that the periastron is oriented towards the observer. For other angles, the RV amplitude is lower.
The inclination acts as a constant factor. A value other than 90° scales down the radial velocity function by a factor of $\sin i$. The eccentricity of a system influences both the amplitude and the shape of the RV curve. Three examples of different RV curves, the first case being nearly sinusoidal, are shown in Figure 1.13.

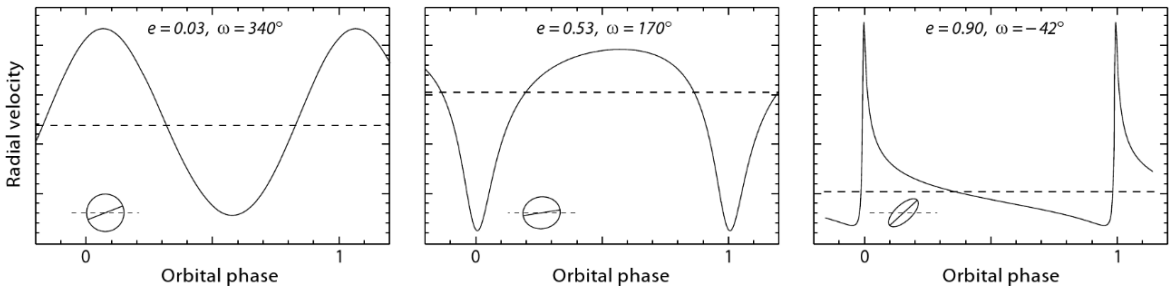

Figure 1.13: Example radial velocity curves with different eccentricities and orientation angles (Perryman, 2011).

Figure 1.14 shows the minimum mass of all RV-detected planets over their semi-major axis. It is immediately clear that the RV method is immensely successful with 618 confirmed detections as of July 2016[39]. Only the transit method (see section 1.5.6) has a higher success rate. As for all of its advantages, there are severe limitations of the radial velocity method. The planetary mass cannot be determined precisely since the actual inclination is unknown. Only a minimum mass can be given, furthermore, only a small sample of bright stars can be observed in a survey due to the constraints of spectroscopy. No measurement of the planet's radius, density or atmosphere is possible. However, it is the perfect complementary technique to the transit method, as there the RV and subsequently the planet's mass can be determined more precisely due to the known inclination. A description of how to obtain high resolution spectra can be found in section 1.8.6.

1.5.5 Astrometry

Astrometry is a branch of astronomy that concerns itself with the measurement of positions and motions of stellar bodies, both in the Solar System and beyond. Stellar parallax and proper motion measurements are the most common subsections of this. Repeated high-accuracy measurements can reveal the existence of a planet that slightly influences the orbital

[38] A line segment joining a planet and the Sun sweeps out equal areas during equal intervals of time.
[39] Based on www.exoplanet.eu (Schneider et al., 2011)

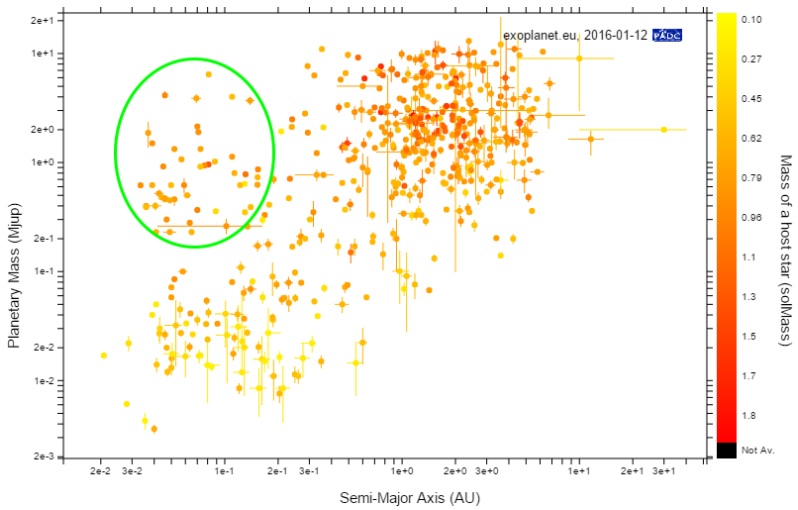

Figure 1.14: Semi-major axis over planetary mass for all 618 exoplanets that were detected with the RV method. Note that detections with masses higher than 13 M_J were discarded. One can see the hot Jupiter population (marked green) in the upper left corner. (extracted from www.exoplanet.eu (Schneider et al., 2011))

path of its host star. While the RV method measures the radial component of orbits, astrometry measures the transverse. Two-dimensional measurements mean that the $\sin i$ ambiguity of the one-dimensional radial velocity method is not an issue with this technique. Both the planetary mass and a precise orbit can be determined with astrometry. This process is illustrated in Figure 1.15 for a hypothetical system, located 50 pc from Earth. High-precision astrometry from the HST or large-diameter telescopes with narrow-field imagers, for example the Hale Telescope in Palomar or the VLT in Paranal, could already detect such a system with precisions down to 100-300μas (Perryman, 2011).
However, only one such system has been discovered so far (Muterspaugh et al., 2010), illustrating why a dedicated high-precision instrument, ideally located in space for higher accuracy[40], is needed to make effective use of this technique.
Thankfully, this is already the case with the ongoing GAIA mission (Eyer et al., 2013) which will measure parallaxes for a billion stars with an accuracy of down to 9 μm (Eyer et al., 2015). Located in a Lissajous-type orbit around the L2 Lagrange point, the satellite telescope utilizes two 1.45 x 0.5 m mirrors to map a 1.0 x 0.5 m focal area with a resolution of 1 gigapixel and will continually cycle through the entire sky over a course of 5 years. This will enable GAIA to detect up to 20000 hot Jupiter systems alone (Eyer et al., 2015).

1.5.6 The transit method

The transit method is by far the most successful technique with more active surveys than for any other detection method. Rosenblatt (1971) suggested this method for the first time, although his method was slightly different: by using several colour channels at once, one might detect a planetary transit by small colour-changes which get induced by the position of the planet in front of the star and its limb darkening. This bears a strong resemblance

[40] As with imaging, atmospheric turbulences that smear the PSF decrease the precision of astrometry from the ground.

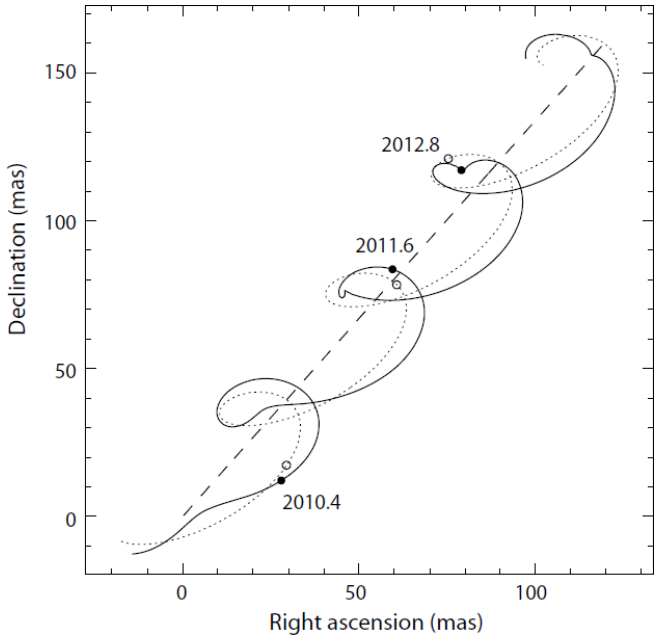

Figure 1.15: Path schematic for a hypothetical star at a distance of 50 pc, orbited by a planet with 15 M_J at 0.6 AU and an eccentricity of 0.2. The dotted line shows the parallax motion from Earth, the dashed line the system's barycentric motion. The solid line shows the effect that the planet would have on this system (Taken from Perryman (2011)).

to the Rossiter-McLaughlin effect which will be introduced later on in this section. Having started off slowly with the first discovered transit (Charbonneau et al., 2000), this method has overtaken the radial velocity method as the most successful planet detection technique with many dedicated surveys and telescopes.
The premise is rather simple: for an inclination i that is close to 90°, a planet might transit[41] its host star and periodically dim the measured flux. This effect can be observed in our own Solar System as Mercury and Venus transit our Sun every few years and decades, respectively. The most recent occurrence, a Mercury transit that happened on May 9th 2016, is shown in Figure 1.16.
The geometric details of this effect are illustrated in Figure 1.17. If the separation d is smaller than the stellar radius R, the planet creates an observable transit. If d is even smaller than R − r, the planet fully transits the star. The effect's amplitude varies with two parameters: the radius ratio between planet and star and the inclination. The probability Ω (Charbonneau et al., 2007) for being able to observe this effect is very small and further depends on eccentricity:

$$\Omega = 0.0045 \left(\frac{1\mathrm{AU}}{\mathrm{a}}\right) \left(\frac{\mathrm{R}_\star + \mathrm{R}_\mathrm{P}}{\mathrm{R}_\odot}\right) \left(\frac{1 + \mathrm{e}\cos(\pi/2 - \omega)}{1 - \mathrm{e}^2}\right), \tag{1.16}$$

where ω is the argument of periastron. One would therefore only be able to observe 0.45% of all Earths that are orbiting around a Sun. This probability increases significantly for larger planets and/or larger stars and for smaller semi-major axes, going as high as 10% for hot

[41] I.e. periodically move in front of.

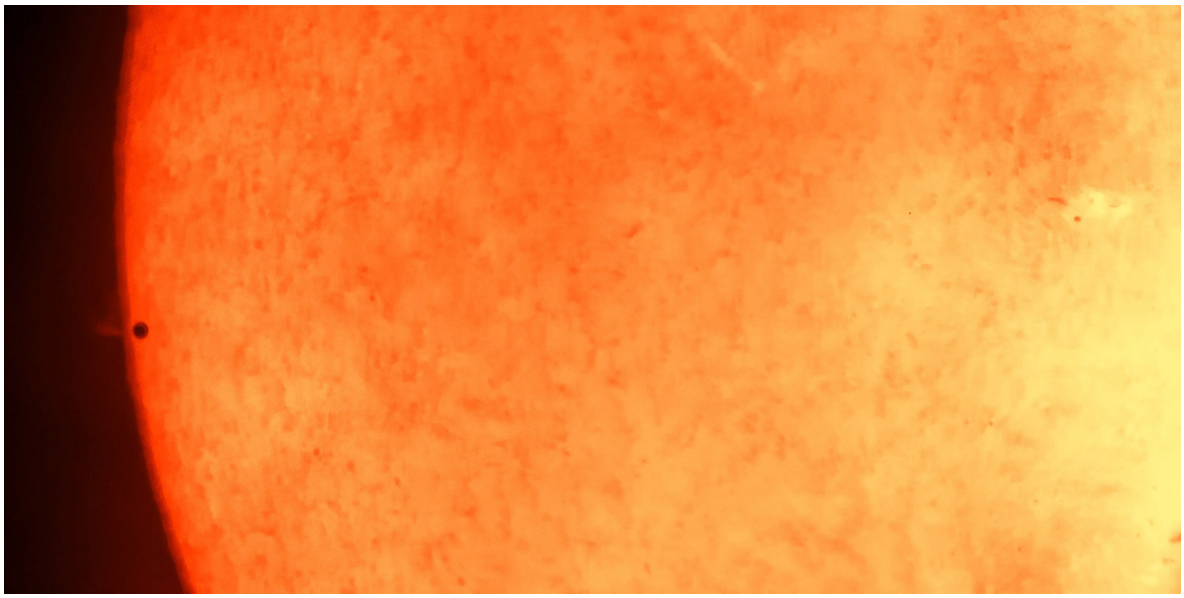

Figure 1.16: Transit of Mercury in front of the Sun, captured on May 9th 2016 at the Wendelstein observatory, using a coronagraph and a camera with an adapted H_α filter. The colours were added by remapping the luminance channel onto a heatmap for better visual clarity. There is no actual colour information in the photo.

Figure 1.17: Illustration of the transit effect for a stellar system with given stellar radius R, planetary radius r, inclination angle i, separation d and planet-star angle δ.

Jupiters. Simple geometry leads from the flux ratio $\frac{\Delta L}{L_\star}$ to the radii (Perryman, 2000):

$$\frac{\Delta L}{L_\star} \approx \left(\frac{R_P}{R_\star}\right)^2. \tag{1.17}$$

Jupiter-sized planets produce a light drop of about 1% for Sun-like stars while for Earth, this reduces to 0.08%. It should be noted that the inclination has also an effect on the flux ratio. A transit that happens at inclinations smaller than 90° results in a lower flux ratio, so Equation 1.17 should only be taken as a reference point. The transit duration τ can be described by the Keplerian laws of motion, the radii of star and planet and the angle δ of the transit (Perryman, 2000):

$$\tau = \frac{P}{\pi}\left(\frac{R_\star \cos(\delta) + R_P}{a}\right) \approx 13\left(\frac{M_\star}{M_\odot}\right)^{-1/2}\left(\frac{a}{1AU}\right)^{1/2}\left(\frac{R_\star}{R_\odot}\right) \text{ h} \tag{1.18}$$

A transit of Earth would therefore take over 13 h, assuming an inclination of 90°. In units of orbital periods, the so-called fractional transit time depends on the semi-major axis:

$$\tau_{\text{frac}} = \frac{\tau}{\text{P}} \propto \text{a}^{-1}, \tag{1.19}$$

meaning that τ_{frac} decreases also with longer periods since both parameters are linked by $\text{P}^2 \propto \text{a}^3$.

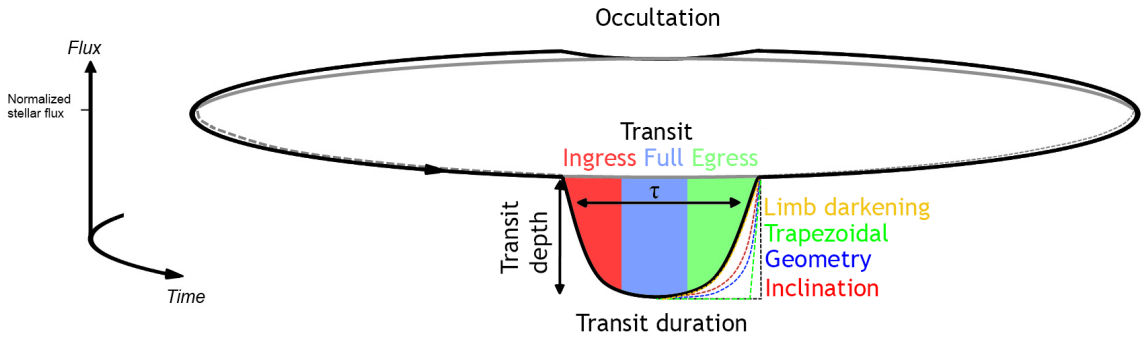

Figure 1.18: Illustration of the normalized stellar flux over time as it is being transited by a planet.

The overall shape of a transit, shown in Figure 1.18, may be considered a two-level system in 0th-order and is dominated by three effects: geometry[42], inclination angle and limb darkening of the star. During the ingress phase[43], the planet is moving in front of the star, a process that can be considered linear in flux decrease as a 1st-order approximation, assuming two square bodies that are eclipsing each other. Since the bodies are circular, the progression of brightness is smoothed. The ingress is followed by a relatively flat region where the planet is completely in front of the star.
Limb darkening has an effect on the transit light curve since a star is not a perfect uniform black body. Instead, the centre appears to have a higher effective temperature (and therefore brightness) than the outside. This effect is due to the optical depth of a star, i.e. the maximum distance from which photons inside of the star will reach the outside. Stars are multi-layered with higher temperatures in the deeper layers. A different angle between inner and outer regions means that photons from deeper layers can reach the outside from the centre. An illustration of limb darkening is provided in Figure 1.19. This effect varies with the wavelength of the observation.
What sets the transit method apart from other detection techniques is that a wealth of planetary and stellar properties can be determined from the data themselves. It also has strong synergy with spectroscopic follow-up methods.
The shape of a transit is influenced by the stellar and planetary radius and the orbital inclination. With a proper stellar characterization (see section 1.8.5), the flux ratio leads to the planet radius. Radial velocity measurements lead to very precise mass estimates since the inclination is well-constrained due to the existence of a transit and, with high-precision photometry, due to the transit shape. As shown in Figure 1.20, a more detailed study can give

[42] I.e. two circular bodies being superimposed
[43] This applies symmetrically to the egress phase.

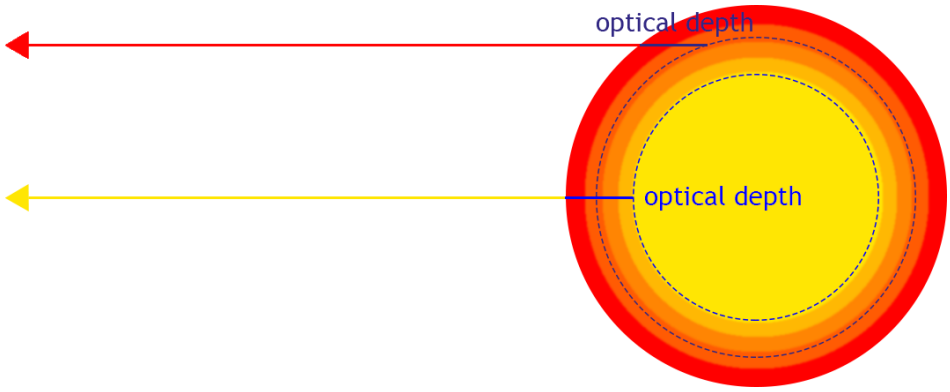

Figure 1.19: Illustration of limb darkening for a star. One can see how the constant optical path results in different visible layers, depending on the position on the surface.

insight to the planet's albedo (by reflectance), thermal radiation (by the difference between occultation and other phases), atmosphere (transit spectroscopy) and the stellar rotation through the Rossiter-McLaughlin effect. This effect was discovered back-to-back by Rossiter

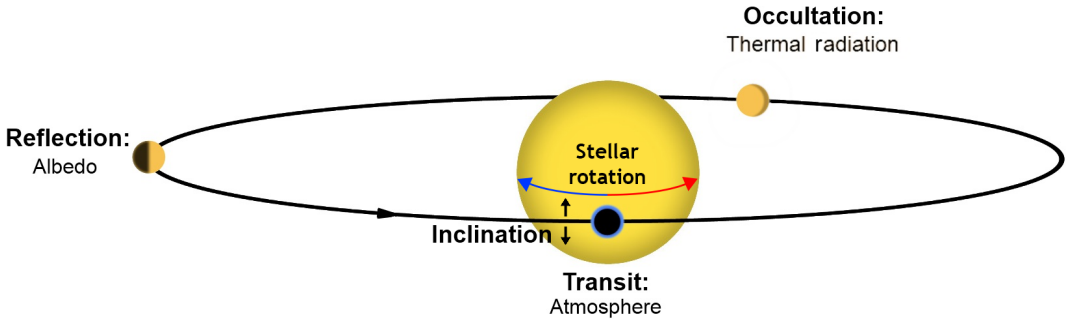

Figure 1.20: Illustration of additional properties that can be studied with the transit method or follow-up observation.

(1924) and McLaughlin (1924) when both teams noticed anomalies in the radial velocity curves of two binary systems, β Lyr and Algol, respectively[44]. The rotation of the star leads to a slight blue/redshift between the rotational sides. A transiting planet blocks out light which may be more blue- or redshifted, as shown in Figure 1.21. This effect would then be visible in the residuals of the radial velocity curve as small irregularities around the transit. The Rossiter-McLaughlin effect can be and has been measured, the first time in a planetary system for HD209458 (Queloz et al., 2000) and is mathematically described by Baluev and Shaidulin (2015). An illustration for different system configurations is shown in Figure 1.22. Overall, the transit method has demonstrated an immense potential, both in the amount and diversity of detected planets but also in its characterization success. The first discovery of a rocky planet around a main-sequence star, spectroscopy of a planet's atmosphere, determining the stellar rotation with the planet's Rossiter-McLaughlin effect, all of it was done with the transit method. With more than 1000 exoplanets and large samples, statistical analysis is now possible to a much larger degree than before. This technique is also relatively cheap. Even small-scale surveys like Super-WASP (Street et al., 2003) who use fully-robotic mounts

[44]It should however be noted that this effect was previously noticed by Schlesinger (1910) for β Lib.

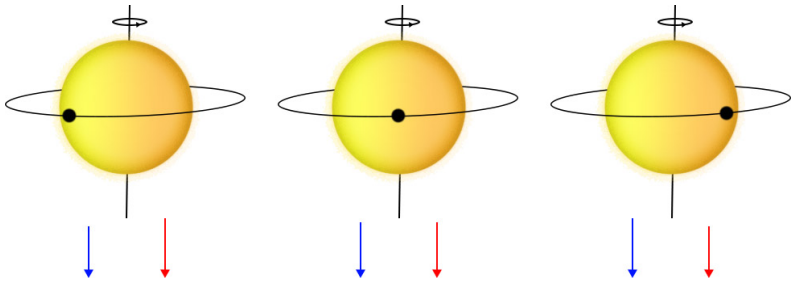

Figure 1.21: Illustration of the Rossiter-McLaughlin effect. As the planet moves across the star, it covers different areas of the star. Since the star's rotation leads to a blue/redshifting across its surface, one can detect a slight shift in overall effective temperature in the residuals of the spectroscopic fit.

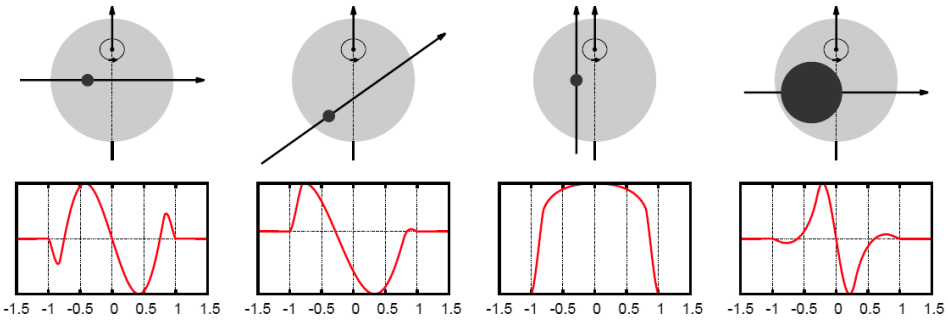

Figure 1.22: Rossiter-McLaughlin effect for different sample configurations (shown above) (taken and adapted from Baluev and Shaidulin (2015)).

with commercial CCDs and DSLR lenses can detect hundreds of planets.
However, there are two main drawbacks of this method: the probability of observing a transit (see eq. 1.16) is quickly decreasing the more distant the planet is. Adding to that, continuous coverage would be needed to detect the planet. This is different to the RV technique where even long-period planets can be detected. The transit method is therefore mostly suited for close-in planets. Surveys like Kepler (Borucki et al., 2010) that are located in space are a possible solution to this problem. An alternative way is to split up the observation into several stations that are located around the world to provide full-time coverage like HAT-South (Bakos et al., 2013) or YETI (Neuhäuser et al., 2011).
The distribution of all 2649 planets discovered with the transit method as of July 2016[45] is shown in Figure 1.23. The Hot Jupiter population is marked in green and already gives an indication that gas giants might not be as abundant unless they are closely orbiting their star as hot Jupiters or hot Neptunes. Only very few detections go beyond 1 AU - so roughly a one-year period - while as a comparison, detections up to 30 AU were achieved with the RV method (see Figure 1.14).

[45] Based on www.exoplanet.eu (Schneider et al., 2011).

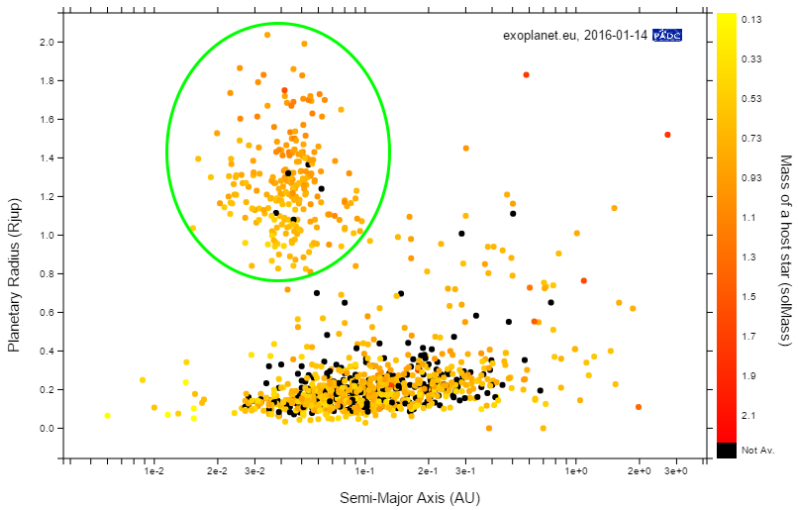

Figure 1.23: Semi-major axis over planetary mass for all 2649 exoplanets that were detected with the transit method. One can see the hot Jupiter population (marked green) in the upper left corner (extracted from www.exoplanet.eu (Schneider et al., 2011)).

1.6 Discovery status

As of July 2016, more than 2900 exoplanets have been detected and published[46], disregarding planets with a minimum mass higher than 13 M_J, with 554 planets having well-characterized orbits and properties like planetary mass and radius[47]. More than a thousand additional candidates are in the process of being followed up. The majority of detections, more than 93%, were discovered by the transit and radial velocity methods. While the RV method has dominated the discovery numbers for a long time, the transit method has shown a drastic increase over the past years with more than 1300 detections in the first half of 2016 alone, more than all other methods combined. Of the transit detections, the vast majority was detected with the Kepler Space Telescope (see section 1.6.1). The progression of discoveries per year are shown in Figure 1.24.
While the number of detections has risen rapidly over the past decade, so have the detection capabilities. As shown in Figure 1.25, four major techniques (timing, radial velocity, microlensing, transit) are capable to detect Earth-like planets by now and three more (astrometry, imaging and astrometric microlensing) will have the capability to detect at least super-Earths over the next decade. By now, hundreds of rocky planets have been discovered around main-sequence stars both directly with the RV and transit method and also indirectly through Transit Timing Variations (see also section 1.8.3). A direct Earth analogue[48] has not yet been found. With more than 4000 further planet candidates from Kepler alone[49], this may however change soon.

[46] Based on www.exoplanet.eu (Schneider et al., 2011), numbers may increase daily.
[47] Based on www.exoplanets.org (Han et al., 2014)
[48] i.e. 1 yr orbit, Earth-like radius and mass, Sun-like star.
[49] http://kepler.nasa.gov/, www.exoplanets.org

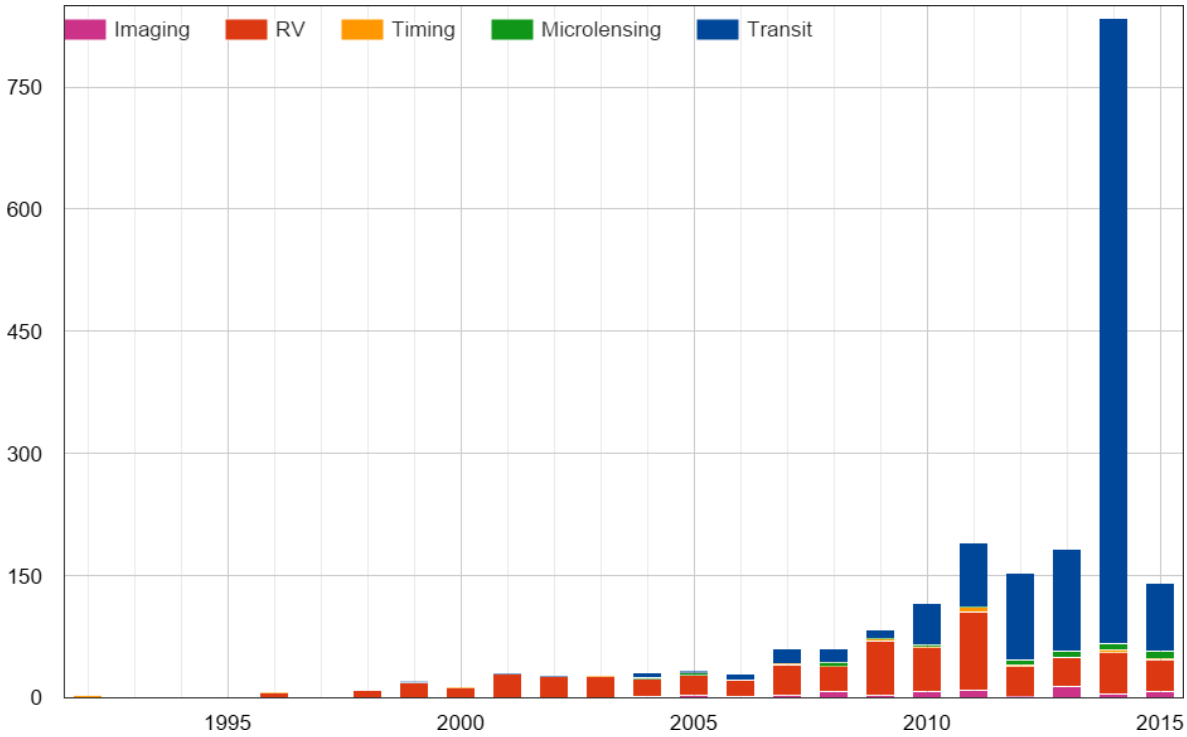

Figure 1.24: Histogram of discoveries per year with different detection methods. Note the rapid increase of detections with the transit method over the last years and the previously dominating contribution of the RV method. (data extracted from www.exoplanet.eu (Schneider et al., 2011))

1.6.1 Notable surveys

There are dozens of active surveys that search for extrasolar planets. However, several surveys deserve to be singled out due to their success. The following projects have contributed more than two thirds of all known planets.

HARPS

The High Accuracy Radial Velocity Planet Searcher (HARPS) (Mayor et al., 2003) is a high-resolution (R = 115000) echelle spectrograph, mounted on the ESO 3.6 m telescope in La Silla, Chile. It was constructed by a consortium of Swiss and French institutes (Observatoire de Geneve, Observatoire de Haute-Provence, Physikalisches Institut der Universität Bern, and the Service d'Aeronomie). Placed inside a vacuum, it simultaneously observes a target star and a ThAr calibration lamp as a reference spectrum.
During its commission phase, HARPS already reached an unprecedented accuracy of 1.7 $\frac{\mathrm{m}}{\mathrm{s}}$ which, thanks to software optimizations, got further improved down to 0.32 $\frac{\mathrm{m}}{\mathrm{s}}$ for stars with low chromospheric activity (Mayor et al., 2009). HARPS is notable for being the most successful ground-based instrument for planet detection and has further played a significant role in the follow-up of transiting planets. Since the first detection in 2004, more than 100 exoplanets have been discovered. HARPS was the first to detect a potentially habitable system (Bonfils et al., 2005), Gliese 581, containing up to six planets, although the outer two planets

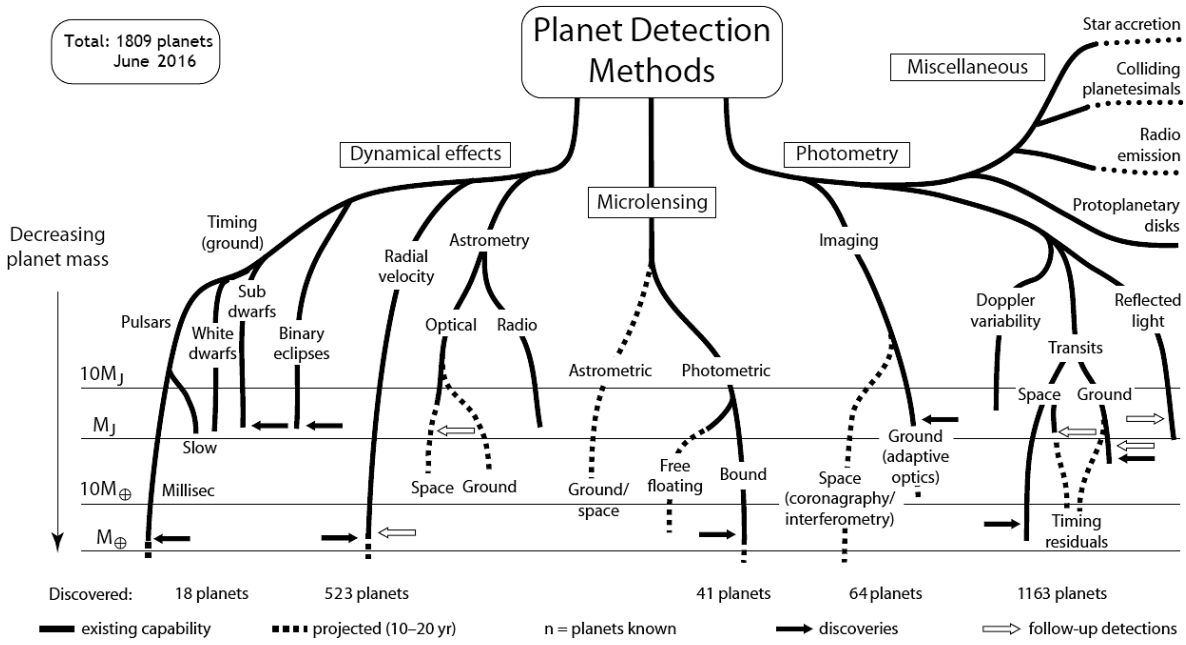

Figure 1.25: Overall success and capabilities of all planet detection methods (extracted and adapted from Perryman (2011)).

may be false detections due to stellar activity of the M-dwarf host star (Forveille et al., 2011; Hatzes, 2016). It was also the first to detect multi-planet systems and found the largest planetary system to date, HD 10180, which hosts seven planets (Lovis et al., 2011).

Figure 1.26: The ESO 3.6m telescope where HARPS is mounted, accompanied by a smaller dome that hosts its guider instrument.

Super-WASP

Super-WASP is a transit detection program organized by the IAC (Instituto de Astrofisica de Canarias). This survey noteworthy for two reasons: it is, after the Kepler project, the most successful transit survey to date and was constructed using eight commercial DSLR lenses[50] and CCD cameras[51] on two robotic mounts respectively (Pollacco et al., 2006), a system considerably cheaper than a normal science-grade telescope. Not only is the pure hardware cost lower in such a setup, the development cost is as well. The mounts are located at the Roque de los Muchachos Observatory in La Palma, Spain, and at the South African Astronomical Observatory near Sutherland in South Africa. This way, both the northern and southern hemisphere are covered.
The success of Super-WASP can be explained by its consistent exploitation of its strengths. The commercially available lenses have a relatively wide FOV of 200 mm and cannot compete with large-mirror telescopes in terms of light collection, therefore, the project focusses on the brightest stars in the sky. The fully-robotic and comparatively cheap design allows to record a high number of data points over a long time. The, compared to other surveys, relatively low photometric accuracy of 5-10 mmag (Pollacco et al., 2006) is therefore balanced by the sheer number of data points.
Besides being the most successful ground-based transit survey, Super-WASP also contributed some remarkable planets to the ever-growing list of discoveries. WASP-17b, orbiting an F6V main-sequence star, was the first[52] planet in which the measured stellar rotation (see Rossiter-McLaughlin effect in section 1.5.6) runs retrograde to the planet's motion (Anderson et al., 2010; Bayliss et al., 2010). The planet must have either formed somewhere else and then migrated inwards or have been a free-floating planet that was caught by the star's gravity. It is also one of the largest planet ever found with a radius of $1.74^{+0.26}_{-0.23}\,R_J$ despite having a very low mass of $0.486\,M_J$. The folded light curve of WASP-17b is shown in Figure 1.27.

CoRoT

CoRoT (COnvection ROtation and planetary Transits) was a space telescope operated by the CNES (French Space agency) in collaboration with the ESA (European Space Agency). Housed in a 2-stage baffle in order to reduce stray light from Earth, a 27 cm telescope observed several fields over 6 years from 2007 on (Auvergne et al., 2009). A computer failure, caused by the intense radiation outside of Earth's magnetosphere shield, ended the operation in 2013 and the telescope was moved into a lower orbit in order to burn up in the atmosphere[53].
What sets CoRoT apart from other surveys is that it was the first space-based exoplanet survey and was operated with a precision that could only be matched by the Kepler telescope, despite having a significantly smaller aperture than Kepler. The first super-Earth with a measured radius was detected by Léger et al. (2009) in the CoRoT data and for years it would be the smallest known transiting planet. For the first time, the detection of a planet's secondary eclipse was possible in the light curve data of CoRoT-1b (Snellen et al., 2009), the result of this is shown in Figure 1.28. CoRoT was only partially used for transit searches

[50] Canon EF 200 mm f1.8 L USM.
[51] 2048 x 2048 px, DW436, manufactured by Andor of Belfast.
[52] However, just shortly after HAT-P-7b, which was discovered two years before (Pál et al., 2008) was found to have a retrograde orbit as well (Winn et al., 2009).
[53] https://cnes.fr/en/web/CNES-en/10913-mission-accomplished-for-corot.php

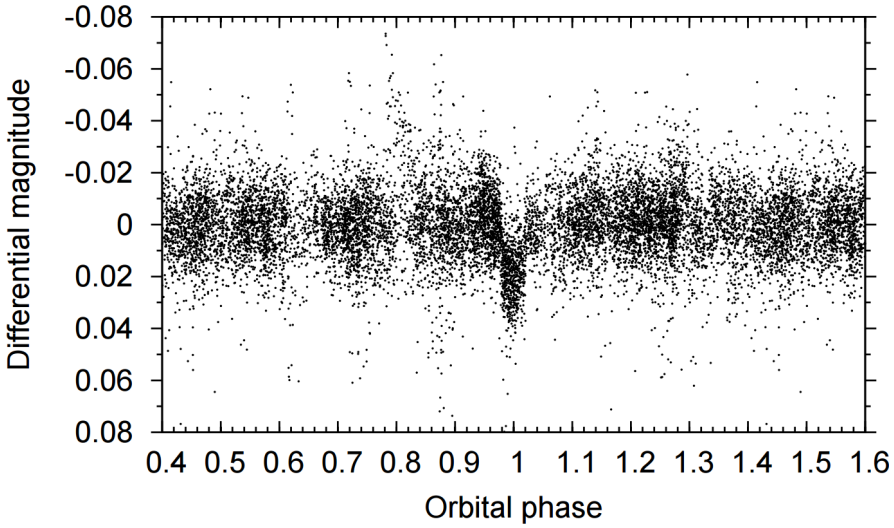

Figure 1.27: Folded light curve (p=3.735 d) of the hot Jupiter exoplanet WASP-17, with the transit occurring around phase 1.0.

with an equal focus the study of asteroseismology. Therefore, it is not nearly as successful as Kepler with 27 confirmed detections.

Kepler/K2

The Kepler space telescope was launched by NASA on March 7th, 2009 after being selected as Discovery Mission #10 by NASA in 2001[54]. The goal of the Kepler mission was the continuous observation of more than 160000 stars[55] (Jenkins et al., 2010) in a fixed region of the sky over at least 3.5 years. The telescope is based on a Schmidt design (Smiley, 1936) with an aperture of 0.95 m and a 105 sq. deg FOV. 42 CCDs with 2048 x 1024 px each lead to an overall resolution of 84 Megapixel. The stars are defocussed to 10 arcsec and 6 s exposures are co-added to either 59 s or 29.4 min for short-cadence and long-cadence data, respectively, in order to improve signal to noise and avoid saturation. Since the bandwidth of Kepler is insufficient to send back the raw data, only the relevant parts of the image, each target star and its surrounding pixels, are sent back to Earth. This amounts to about 6% of the total CCD area[56]. The telescope is not located in a Lagrange point or Earth orbit but instead trails Earth in a heliocentric orbit with a slightly longer period and semi-major axis of 372.5 days and 1.0132 AU, respectively.
After losing control over two of the four reaction wheels, the original mission of the Kepler space telescope ended and was repurposed for the "second light" survey K2 (Howell et al., 2014). Instead of continually observing the same area over years, the K2 mission now switches targets every three months, stabilized by the two remaining reaction wheels and solar pressure for the third axis (roll angle). However, the telescope still drifts slowly and can to be corrected by firing the thrusters every 6 hours[57]. Photometric precision is therefore slightly lower than

[54] http://kepler.nasa.gov/Mission/QuickGuide/history/

[55] Later on, several variable stars were disregarded, reducing the number to 156000 (Borucki et al., 2010) and then in later publications to "more than 100000 stars" (http://kepler.nasa.gov/Mission/QuickGuide/).

[56] http://keplergo.arc.nasa.gov/PyKEprimerResources.shtml

[57] However, this only happens in about 70% of all cases (Steve B Howell, private conversation).

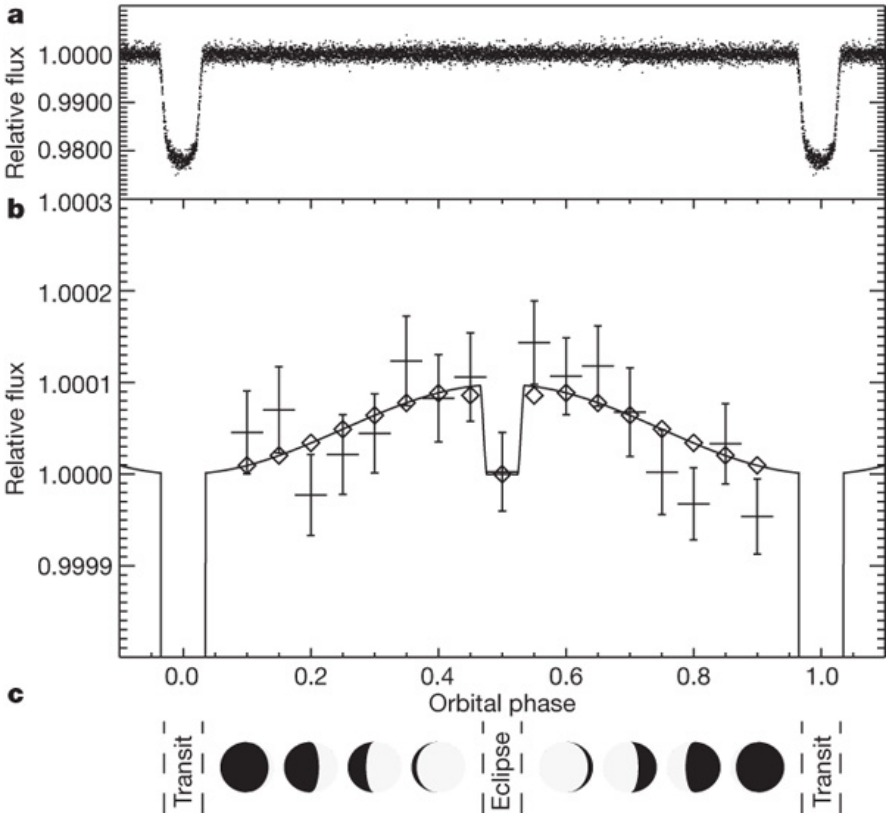

Figure 1.28: Folded light curve of CoRoT-1b, showing the slight increase in flux outside of the transit and eclipse that is due to the planet's reflected light (taken from Snellen et al. (2009)).

during the Kepler mission but can be corrected very well. The drawback is that only planets with periods smaller than 30 days can be detected since the targets are switching irrevocably. Kepler is the first - and so far only - telescope that is located in space, has a large aperture with a high-performance detector that is reaching a photometric precision of 80 ppm (Caldwell et al., 2010) and is dedicated solely to the search for planetary transits. This created a certain dominance in the field of discoveries at present with a contribution of more than half of all known exoplanets.

The impact on the field of planet detection cannot be understated. The survey generated so many planet candidates that ground-based follow-up projects are still busy years after the end of the original survey, with many more to come. Detailed studies of the occurrence rate for solar-type (Petigura et al., 2013a; Silburt et al., 2015) and cooler stars (Gaidos et al., 2013; Morton and Swift, 2014) have been performed, with robust analysis of the uncertainties (Foreman-Mackey et al., 2014).

While the amount of achievements of the Kepler survey is too high to be listed in detail, several discoveries are of special note. Kepler-9 was the first multi-planet system to be detected with the transit method (Torres et al., 2011) and, at the same time, the first transit system where TTV's were successfully measured and used to predict an additional planet. So far, only very few multi-planet systems were detected with the transit method and all of them by Kepler. It is a difficult task since it requires high-precision photometry (since some of the planets will be

rocky) and long-term continuous coverage (since some of the planets will have long periods).

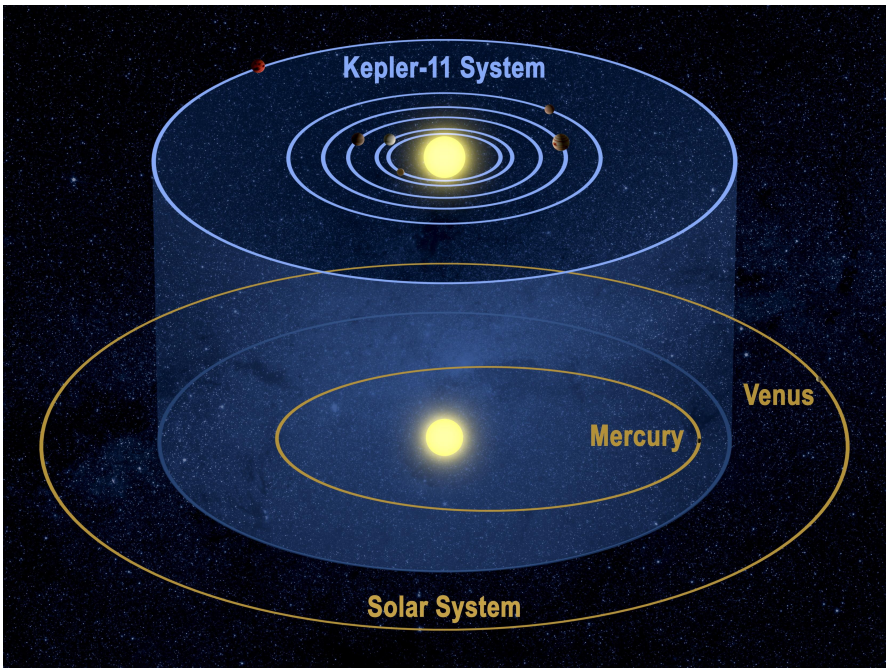

Figure 1.29: Illustration of the Kepler-11 system. Note that, although Kepler-11 is almost a solar twin, five of the planets have orbits closer than mercury and are nearly circular (source: http://www.nasa.gov/mission_pages/kepler/news/new_planetary_system.html).

Therefore, some of the signals in a multi-planet system are only very weak. Kepler-11 with its 6 planets, shown in Figure 1.29 is a curious system for several reasons. Not only is it the most numerous planetary system besides HD 10180, but also TTV's were detected which allowed the determination of the planetary masses without radial velocity. Five of the planets are located in an orbit closer than that of Mercury and the inclination varies less than 1° between all planets. How such a system can be stable or even form is still unclear.

1.6.2 Statistical properties of planets

With more than 2900 detected planets, it is now possible to perform a detailed statistical study of the stellar and planetary parameters. A selection of properties is shown in Figure 1.30. Evident from the stellar effective temperature and radius distributions is that the majority of detections are around Sun-like stars and only very few planets have been detected around giant stars or M-dwarfs. However, this should not be confounded with an increased planet-occurrence rate for solar-type stars. M and late K dwarfs are very faint, therefore the detection S/N is lower and they might get clipped out of the target list altogether. This was the case with Kepler; there, less than 3900 stars (Dressing and Charbonneau, 2013) - or less than 2.5%, of the selected targets - have an effective temperature lower than 4000 K. As an opposite, while giant stars are very bright, a detection with the transit method is more difficult due to a lower radius ratio and dwarf stars are much more common in the sky.
The distributions for planetary mass and orbital period, shown in the bottom panels of

Figure 1.30, seem to indicate two Gaussian peaks each. As discussed in section 1.3.2, giant planets undergo a rapid runaway-growth phase after their gravity allows them to collect the surrounding gas which happens at about $10\,M_\oplus$. It is therefore plausible to expect a gap between 10 and $100\,M_\oplus$. For the period distribution, shown in Figure 1.30 in the bottom right panel, the explanation may however be selection bias. Short-period planets are strongly favoured in the transit method, not only since the detection probability correlates[58] with $\Omega \propto P^{-\frac{2}{3}}$, but because the transit duration is not strongly correlated with the period and continuous data must be recorded in order to catch the required three transits. That means even Kepler is almost unable to detect planets with transits beyond 1 yr. Only one exception with $P >> 1\,yr$ exists, 1SWASP J140747.93-394542.6 (Mamajek et al., 2012), due to data taken over several years with the Super-WASP and ASAS surveys. The effect does not affect the RV method as much, however, since data have not to be taken continuously. The difference between the RV period distribution and the other detection methods is shown in the corresponding panel of Figure 1.30.

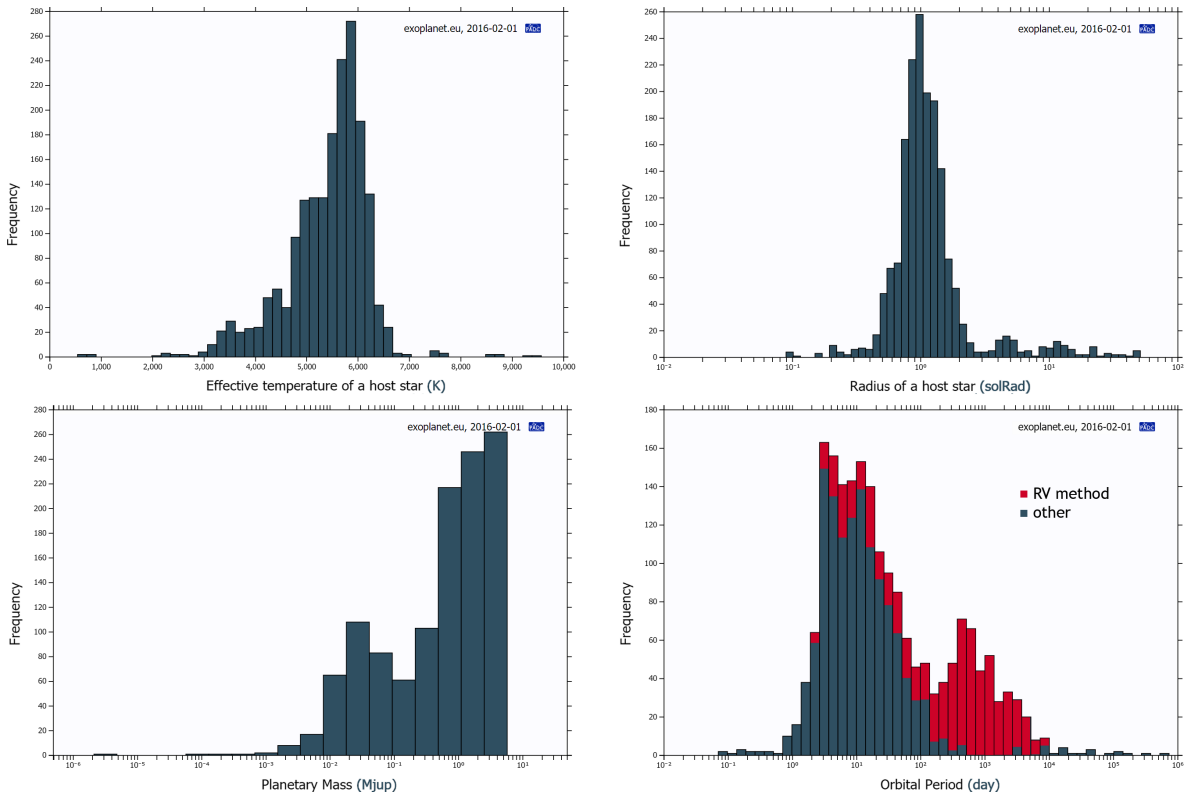

Figure 1.30: Distribution of the planet host star effective temperatures (top left quadrant), radii (top right quadrant) and planet masses (bottom left quadrant) and orbital periods (bottom right quadrant), marked red for the RV method and blue for the others (data extracted from www.exoplanet.eu (Schneider et al., 2011)).

In our Solar System, the eccentricity of planets is very low. Only Mercury's orbit is less

[58] Following equation 1.16, the probability is proportional to a^{-1} and, following Kepler's Third Law, $P^2 \propto a^3 \rightarrow \Omega \propto P^{-\frac{2}{3}}$.

circular with an orbit eccentricity of 0.2056[59]. However, especially in single-planet systems, this is not the case for exoplanets. The distribution of orbital eccentricity against the semi-major axis for all planetary systems and the general distribution of eccentricities is shown in Figure 1.31. Only for the shortest orbits of 0.02 AU and less are almost all orbits circular due to the tidal interaction between planet and star. However, the number of non-eccentric orbits may be higher than estimated right now due to bias effects in systems with low S/N (Shen and Turner, 2008).
Due to the high number of confirmed planets, it is possible to infer a theoretical orbital eccentricity distribution. Since there are biases in the distribution, a hierarchical probabilistic method should be used (Kipping, 2013). A Beta distribution[60] has been shown to be the best function to describe the eccentricity. However, Kipping (2013) finds that splitting the distribution into high-period and low-period groups results in two distinct Beta functions that provide better fits for the corresponding groups. The most likely explanation is the aforementioned circularization of low-period orbits from tidal interaction.

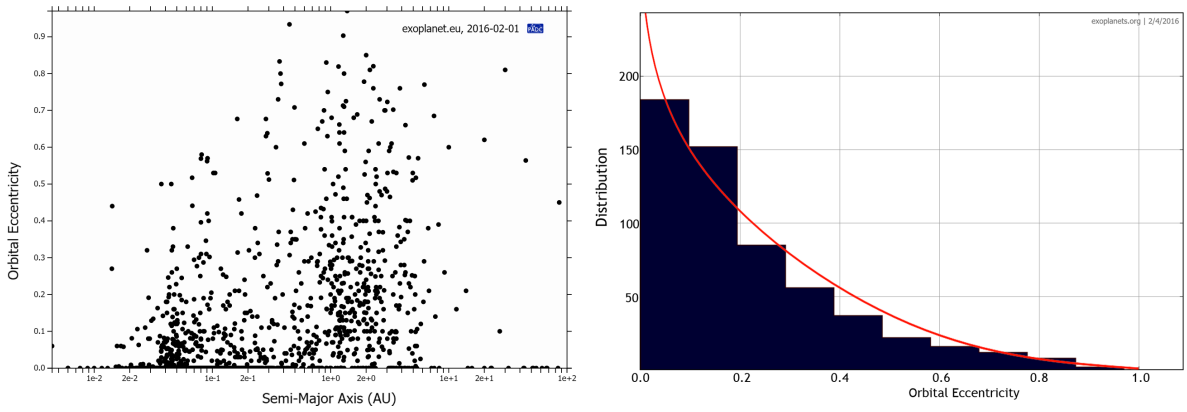

Figure 1.31: Left: distribution of orbital eccentricities against the semi-major axis. Right: distribution of orbital eccentricity with the best-fitting Beta-function from Kipping (2013) as an overlay (data for the left panel extracted from www.exoplanet.eu (Schneider et al., 2011), right panel from www.exoplanets.org (Han et al., 2014)).

M-dwarfs may be different from the other main-sequence stars concerning planet occurrence rates. Overall, while small rocky planets ($< 2.8R_{\oplus}$) are about 3.5 times more abundant than around FGK-dwarfs (Mulders et al., 2015b), Neptune-sized planets are less abundant by a factor of 2. For hot Jupiters and Jupiter-sized planets in general, the generally low occurrence rate means that the uncertainties of the small sample of Kepler are too high to make a statistically robust assessment. The goal of Pan-Planets and this PhD thesis is to tackle this open question and improve the previous occurrence rates determined from Kepler (Dressing and Charbonneau, 2013; Mulders et al., 2015b), RV surveys (Bonfils et al., 2013) and the WFCAM Transit Survey (Kovács et al., 2013; Zendejas et al., 2013).
Based on a sample of about 3900 M-dwarfs and late K dwarfs, the Kepler survey (Jenkins et al., 2010) allowed a more accurate assessment of the statistical properties of planetary systems. All gas-planets of "Mini-Neptune"-type and larger ($> 2.8R_{\oplus}$) may be more rare in orbital periods between 1-100 days (Dressing and Charbonneau, 2013; Morton and Swift,

[59] http://nssdc.gsfc.nasa.gov/planetary/factsheet/mercuryfact.html
[60] The Beta-function is defined by the variables a and b: $B(a,b) = \int_0^1 t^{a-1}(1-t)^{b-1}dt$.

2014; Dressing and Charbonneau, 2015; Mulders et al., 2015b). This is especially puzzling since the overall occurrence rate of planets appears to be higher than around FGK dwarfs. Figure 1.32 shows this discrepancy in terms of the planet occurrence rate for different stellar radii.

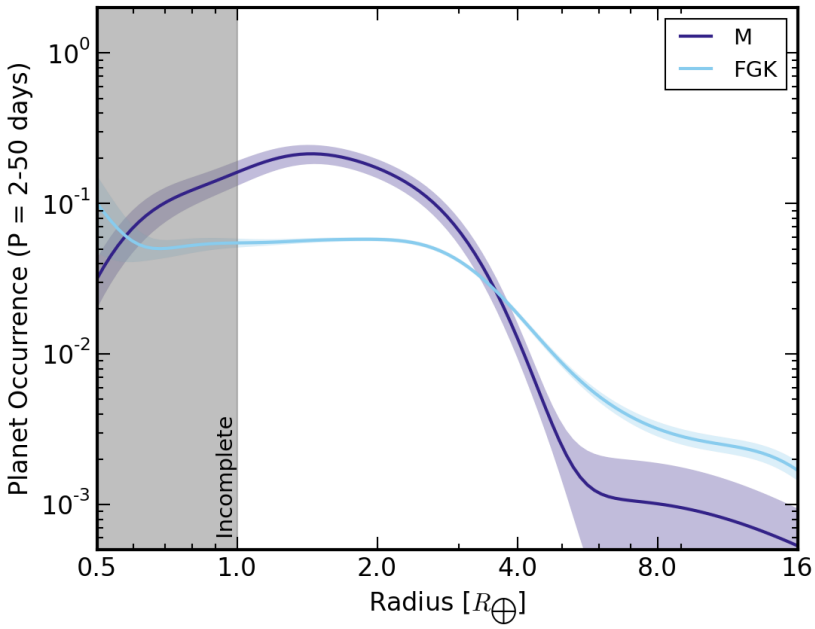

Figure 1.32: Planet occurrence rate in terms of planet radii for M-dwarfs and FGK dwarfs with periods between 2-50 days. The lines are the fitted regression curve and their 1σ confidence intervals are shown as the shaded region (taken from Mulders et al., 2015b).

1.7 Planet habitability and life

There are many arguments for the value of basic research, some economical. However, one thing sets apart the search for life. For millennia, mankind asked themselves several big questions:

"Why are we here and where do we go?"
"What is right or wrong?"
"What is life?"
"Are we alone in this universe?"

As far as we know, most of those fundamental questions will never be answered with only plausible suggestions from a biological, philosophical or religious ansatz. There is, however, one exception. The question of whether we are alone in this universe could be answered with a clear "no" if we were to detect life on other worlds. The discovery of the first planets by Mayor and Queloz (1995) not only sparked the formation of a new field of astrophysics. A new, interdisciplinary field called astrobiology came together as well which further utilizes physics, chemistry, biology and geology for the search for life. In general, astrobiology is the study of life's origin, evolution, distribution and future[61]. Previously, there had been attempts to form this field with the name exobiology which started in 1959. The concept gained significant attention after NASA detected traces of basic organic molecules in meteorites, but the broader term astrobiology is linked with the discovery of planets. By now, astrobiology has become big enough to warrant its own journals[62].

1.7.1 Definition of life

To define life may be straightforward at the first glance but it is not. There is no generic substance which is common only to the realm of organisms and does not exist in inanimate matter (Mautner, 1997). The fundamental problem is the definition of a concrete step after which a chemical system is to be considered animate, while before it is not (Tsokolov, 2009). There are several different definitions on how to properly classify life. The working definition of NASA, based on Deamer and Fleischaker (1994), assumes three characteristics:

"Life is a self-sustained chemical system capable of undergoing Darwinian evolution".

This definition is intriguing since it implies that a virus is not alive. Although it is a chemical system with its own DNA, it has no own metabolism and therefore does not fulfil the requirements of Darwinian Evolution - it further needs other hosts in order to multiply and cannot disassemble and reassemble its own DNA. This places it in the same inanimate category as prions[63]. The strength of this definition, however, is that it is not only applicable to terrestrial life, e.g. with no mention of DNA as the core of an organism or other chemical bases instead of carbon and water.
Other definitions are more specific, like the PICERAS (Program, Improvisation, Compartmentalization, Energy, Regeneration, Adaptability and Seclusion) definition from Koshland

[61] http://astrobiology.nasa.gov/about-astrobiology/, archived at https://web.archive.org/web/20081011192341/
[62] http://www.liebertpub.com/AST
[63] Proteins that can fold in several and structurally distinct ways and in their behaviour can mimic the effect of viruses.

(2002). While it is essentially similar to NASA's definition, it specifies several points. For example, instead of a "chemical system", this definition demands energy, regeneration (i.e. a metabolism) and seclusion (i.e. the ability to let enzymes only affect one certain type of molecule). However, this definition is more focused on life as we know it from Earth.

1.7.2 Planet habitability

The circumstellar habitable zone, in short habitable zone (HZ), describes the region around a star where life may develop on a suitable planet. The word derives from the Latin *"habitare"* and as such may be translated as *living* or *dwelling*. However, this implies that a planet should be called habitable if life can survive there - in this sense, Mars should also be called habitable since terrestrial microbial life such as the species deinococcus radiodurans[64] could survive on Mars. The following discussion instead assumes that habitability refers to the potential of life to form on the planet.
In a metaphor to the fairy tale of *"Goldilocks and the Three Bears"*, it is also called the Goldilocks zone for its necessary balance between several life-essential factors:

Liquid-water habitable zone (LWHZ)

The most essential factor is the necessity of, as far as we know, liquid water for life to develop. Therefore, the main differentiator is the amount of radiation from the star that is heating the planet. Kasting et al. (1993) used a one-dimensional climate model to estimate the liquid-water habitable zone (LWHZ) around solar-type stars and determined an interval of 0.95 AU-1.67 AU for a Sun-like star. The inner limit of the HZ is mostly dominated by runaway greenhouse effects while the outer is by water loss. The downside of this approach is that it constrains itself to Earth-like atmospheres[65], which again was shaped by life on Earth. Other planets might have a radically different atmospheric composition which the model does not account for. The model used by Kasting et al. (1993) also turned out to be incorrect in several aspects. Wordsworth et al. (2010) estimated that the authors might have overestimated the absorption of thermal infrared by CO_2 bands and the CO_2 and H_2O bands in general were determined incorrectly. Also, the models do not extend down to M-dwarfs which are of great interest to the science community concerning the search of life (Kopparapu et al., 2013).
The next generation of habitable zone estimates incorporates more accurate atmospheres, planet albedos (Kopparapu et al., 2013) and masses (Kopparapu et al., 2014). This becomes even more important with the rising number of super-Earths that have been detected and show a different planetary chemistry than twins of Earth. However, the aforementioned issues with the focus on Earth-like atmospheres persists. Moreover, a star's luminosity changes over its lifetime, which also has to be accounted for in the terms of the continuous habitable zone (Kasting et al., 1993).
A new, weaker HZ definition has been put forward (Petigura et al., 2013a). If a planet receives an irradiation S between 0.25 and 4 $S_\oplus$, it is potentially habitable, depending on the kind of planet. This corresponds to a semi-major axis distribution of 0.5 AU to 2 AU for the Solar System. In this definition, both Venus and Mars are included in the HZ - however, both

[64] Its amazing toughness earned it the nickname "Conan the Bacterium" (http://science.nasa.gov/science-news/science-at-nasa/1999/ast14dec99_1/).
[65] I.e. a prevalence of $N_2/O_2/CO_2$.

planets might have been habitable with different properties like a larger mass in case of Mars or a less carbon-rich composition of Venus in order to avoid its runaway greenhouse effect[66].

Radiative habitable zone

Besides liquid water, it is assumed that UV radiation has to occur both as a source of energy and as a primary catalyst to allow the synthesis of Guanine (Barks et al., 2014), one of the 4 primary chemicals of RNA. As with thermal heating, too much UV radiation is a problem because of its ability to induce the destruction of DNA and protein molecules. The fraction of UV light in a star's radiation is largely dependent on its effective temperature and, concerning main-sequence stars, its mass. Besides the LWHZ, one can therefore calculate the UV habitable zone as an additional criterion. This becomes especially relevant towards the lower mass region of the stellar population as some M-dwarfs have a considerably lower flux in the UV than compared to a G2V star like the Sun while others have even stronger UV emissions due to stellar activity and flares.

Stellar type

There are more parameters when considering a stellar system's habitability. Factors like its lifetime and the stellar variability can negatively influence or even strip away the planetary atmosphere before life has ever started. M-dwarfs, as an example, are the most abundant of all stars. At first glance they seem like the perfect type of star to sustain life with a lifetime measured in dozens of billions of years, but are most likely ill-suited. They have a strong imbalance between infrared and visible-light radiation compared to solar-type stars (Buccino et al., 2007). Their tendency to strong stellar flares also pose a threat to potential life. Their closer habitable zone, due to lower flux output, also leads to a very quick tidal lock (see section 1.3.5) and can induce desiccation due to tidal heating (Barnes et al., 2013). However, the emergence of life might still be possible since none of the issues are critically prohibitive for life. The tidal lock may not be as problematic as one might assume as heat will flow to the dark side (Joshi, 2003) and might even result in a larger habitable zone, due to the stronger infrared absorption of ice. A theoretical example for a habitable planet around an M-dwarf is a water world, e.g. a planet fully covered with water, that survived the tidal desiccation and can absorb the stellar flare radiation. Life would be quite different to that on Earth, however. Stars of F-type and hotter may however be entirely uninhabitable. Their lifetime is becoming decreasingly shorter the higher their initial stellar mass and, considering the first life formed in the order of a billion years after the birth of the Solar System, may move into the giant branch too quickly. However, the majority of all stars have lifetimes comparable to or even greater than the Sun.

Galactic habitable zone

The location of a star in its host galaxy is another factor for the habitability of its planets. The so-called galactic habitable zone (GHZ) encompasses several aspects. Being too close to the galactic centre increases the risk of nearby supernovae (Spitoni et al., 2014) while a certain amount of metallicity is needed for the formation of rocky planets (Fischer and Valenti, 2005). The stellar formation rate in a star's vicinity is therefore an essential factor, both for good

[66] see also paragraph "Other contributing factors".

and for bad. Being too far from the centre decreases the metallicity to a point where no rocky planets can form while being too close will endanger the system due to more frequent, up-close supernovae.
For the Milky Way, habitable planets will most likely be found between 7 kpc and 9 kpc with the maximum at 8 kpc (Lineweaver et al., 2004; Spitoni et al., 2014). The disc regions of a galaxy, outside of the star-forming spiral arms, are therefore a favourable environment. The Solar System is located at 8.5 kpc in such a region, placing it within the GHZ. Other models, however, argue that the majority of habitable worlds are much further away from the galactic centre at about 16 kpc which means that the Solar System is located in a very unlikely region (Vukotić et al., 2016).

Other contributing factors

There are many additional aspects that may play a role in a planet's habitability. While the volume/mass increase of a spherical body is progressing cubical with the radius, its surface increase is only quadratic. The larger a planet, the less heat it therefore emits in relation to its mass. Mars is an example of a planet that lost most of its internal energy too quickly, stopping volcanic processes and subsequently its geologic carbon-cycle. In combination with its weaker ability of atmosphere retention, this led to cooling down and an almost complete loss of atmosphere. Venus, on the other hand, emitted too much carbon dioxide, leading to a runaway greenhouse effect. It may have been habitable in the past (Barnes et al., 2016). Super-Earths may stay geologically active for a longer time than Earth-like planets. This means that the HZ has to be adjusted for the planet type and for the age of the system.
Eccentricity plays a role in a planet's climate stability. As seen in Figure 1.31 on the right, there is a wide distribution with about 80% of the known and well-characterized[67] planets having a larger eccentricity than Earth. However, this view might be biased by the contemporary dominance of giant planet discoveries, as most of the rocky planets detected with Kepler seem to have a lower eccentricity (Van Eylen and Albrecht, 2015).

1.7.3 Origin of life

Abiogenesis is the concept of life emerging from non-living matter. There is no established model but there are several different concepts to explain this process on Earth:

Nebular prebiotic chemistry: For life to emerge, several ingredients have to be present: water, organic molecules, nitrogen and a kind of energy gradient. The Miller-Urey experiment was conducted with the goal of testing whether this could have been possible 4 billion years ago (Miller, 1953). They found that, after heating up a mix of methane, ammonia, water and hydrogen, the addition of electric energy resulted in the formation of more complex organic molecules, including all 20 commonly occurring amino acids. A problem of this experiment is that the atmosphere of early Earth may have been much more abundant in CO and CO_2 (Hill and Nuth, 2003), which means that the results of this experiment may not be entirely applicable to the processes that happened. New studies now focus on the conditions of nebula in other regions of the solar system with UV radiation as an energy source instead of electricity.

[67] Data taken from www.exoplanet.org (Han et al., 2014).

Hydrothermal vent: Fissures in Earth's surface that emit geothermally heated water are called hydrothermal vents. They provide unique ecosystems for life and it is being theorized that they may have been the origin of life as well (Wachtershauser, 1990). In favour of this concept is the fact that the surfaces of vents can have catalytic properties and create simple organic molecules such as methanol (Roldan et al., 2015). This implies that the first life would have consisted of extremophiles[68] which gradually spread out and adapted to other regions.

Panspermia: Another theory is for life or complex organic molecules to have formed on other planets or other regions of space, which then got distributed by meteorites or other celestial bodies. What makes this theory plausible are meteorites found on Earth that originated from Mars, a planet which once had liquid water[69]. Microbial bacteria have shown to be able to survive even the journey on a spacecraft[70]. However, due to the absence of life outside of Earth, this theory cannot yet be proven.

1.7.4 Intelligent life

While life may be abundant in the universe, and it is possible that life exists on other planets or moons in the Solar System such as Europa (Kargel et al., 2000; Marion et al., 2003), intelligent life may be much less frequent and even if it evolved on a fraction of life-carrying planets, the very specific path of spreading out into the stars may be very unlikely. A famous argument is the Drake equation:

$$N = R_\star \cdot f_p \cdot n_h \cdot f_l \cdot f_i \cdot f_c \cdot L, \tag{1.20}$$

which attempts to determine the number N of civilizations that are able to communicate by multiplying the star formation rate (SFR) with the fractions of stars f_p that are orbited by planets, number of habitable planets per star n_h, fraction of those on which life evolves, the fraction of those which reach the technological level of radio communication and the civilization's average lifetime L. It is important to note that the lifetime of a star affects the probability of life and then intelligent life to develop. M-dwarfs may be very good host systems due to their very long lifetimes of tens of Gyr while stars more massive than F-type may be too short-lived for (intelligent) life to develop. The goal was to demonstrate how even small probabilities for the individual factors still lead to a large number of possibly communicative civilizations. The absence of such signals may be due to many reasons, however, it is entirely possible that radio-based communication is not as ubiquitous as organizations such as the Search for Extraterrestrial Intelligence (SETI) believe.

[68] Life that thrives in regions that are inimical to other life forms.
[69] doi:10.1038/ngeo2412
[70] doi:10.1038/nature.2014.15249

1.8 Transiting exoplanet follow-up

1.8.1 False-positive detection scenarios

Having detected a signal from a potential planetary transit, a multi-step process is needed to confirm and further characterize it. The drawback of the transit method is that a number of scenarios (Chabrier et al., 2009) can create a signal very similar to that of a planet. There are five common sources of false-positive identification or transit mischaracterization, illustrated in Figure 1.33, that are created by eclipsing binaries (EB's):

1. Blended[71]/Hierarchical EB system,
2. Blended/Hierarchical EB companion,
3. Eclipsing Brown dwarf[72] or low-mass star with a radius similar to Jupiter,
4. Unblended EB system (grazing eclipse),
5. Double-period EB system.

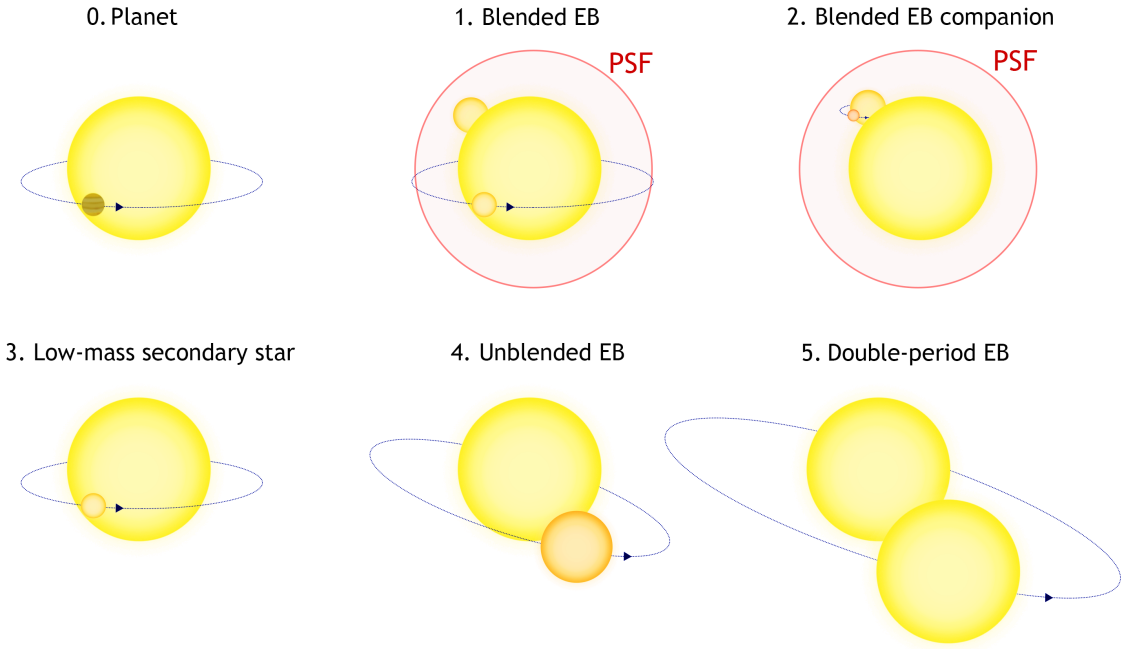

Figure 1.33: Illustration of a planetary transit (top left) and five likely false-positive scenarios: Blended EB system (top middle), hierarchical EB companion (top right), low-mass stellar companion (bottom left), EB system with shallow eclipses (bottom middle), and double-period EB system (bottom right).

Traditionally, the safest way to confirm that a planet is the transit's origin is to measure the radial velocity curve of the primary star. For this, the star has to be characterized first and

[71] I.e. unresolved due to the star's PSF.
[72] $M > 13 M_J$, see section 1.2.1.

its stellar type has to be determined, usually with low- to medium-resolution spectroscopy. Since the inclination is more constrained than with the regular RV method (i $\approx 90°$ in case of a transit), the mass can be measured quite precisely.
However, this direct approach is either sometimes not feasible, e.g. due to the star having a too faint magnitude, or strong crowding, or too small radial velocity change, or, in case of Kepler, having a high number of targets. A variety of different confirmation techniques can be utilized to rule out those alternative scenarios or constrain their likelihoods. This can then be used to validate the detection by statistically ruling out all other possible signal origins (see also section 1.8.8).

1.8.2 Light curve properties

As mentioned in section 1.5.6, the shape of a transit can provide insights into a multitude of planet and star properties and an experienced astronomer can sort out many false-positive detections already by visual inspection of the light curve. The following paragraphs are strongly oriented towards hot Neptunes and hot Jupiters though applicable to other planet populations as well. Multi-planet systems and small terrestrial planets produce very distinct signatures and are less likely to be produced by a false-positive scenario (Lissauer et al., 2011, 2014; Rowe et al., 2014).

Transit Duration

Using equation 1.18, one can determine the expected transit duration for a given stellar and planetary radius. This assumes that the planet's orbit is circular, which is the case[73] for most hot Jupiters and Neptunes. If the transit duration is significantly larger than the calculated time, the signal's origin might be a low-mass star, possibly with a tertiary companion blended inside of the PSF. This is one of the most frequent sources of false-positive detections. However, there have been cases of eccentric orbits with relatively low periods, e.g. Kepler-75b (Hébrard et al., 2013), which means that this criterion is not binding.

Transit Shape

The shape of a transit can be described analytically. Mandel and Agol (2002) published the exact equations for a planetary transit with given limb darkening (see section 1.5.6) parameters. Defining two states of a transit, ingress/egress and the bottom section where the planet fully eclipses, one can visually distinguish some eclipsing binaries. A strong flat bottom, as shown in Figure 1.34 in the left panel, means that the radius ratio between both bodies and the transiting object is likely to be a planet or brown dwarf. On the other side, a very short or even invisible bottom section[74], as seen in the right panel of Figure 1.34, is a strong indication of an eclipsing binary system, possibly with a partial eclipse.

Secondary eclipse

The star in a system is not the only object that can contribute flux. A planet, brown dwarf or binary companion also emit light to a certain degree, either by reflection (planet) or thermal emission (brown dwarf and binary companion). If the companion transits, it is very likely that

[73] Based on data taken from www.exoplanet.org (Han et al., 2014).
[74] Such an eclipse is called v-shaped (Zendejas et al., 2013).

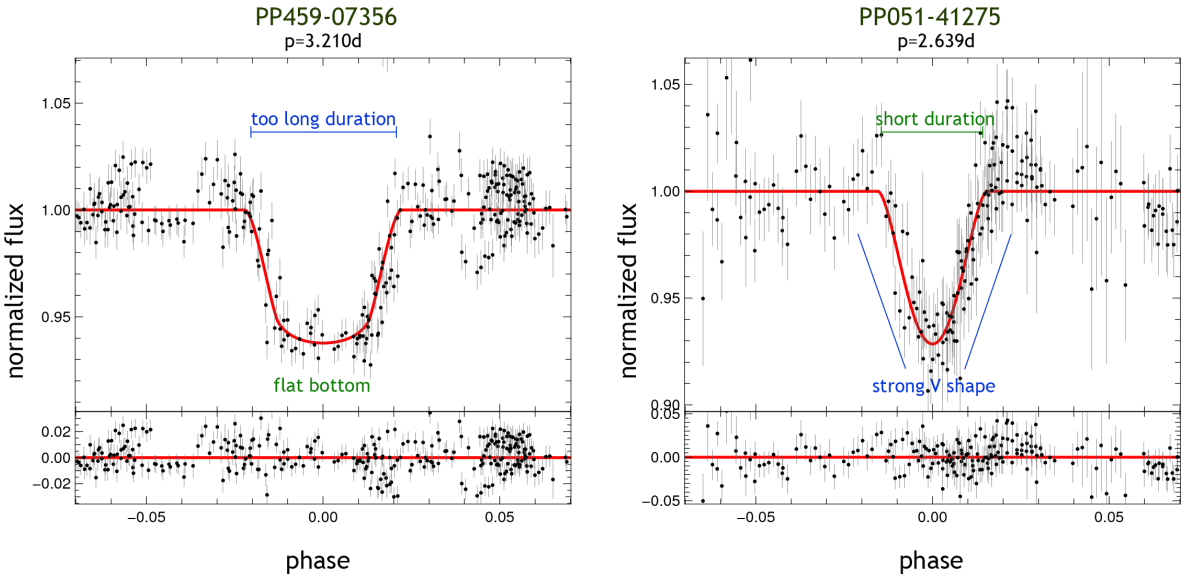

Figure 1.34: Two examples for likely false-positive planet detections from the Pan-Planets data. The red line indicates the best-fitting transit model. Candidate PP459-07356 (left panel) has a longer relative transit duration than candidate PP635-15204 (right panel) although having a higher period. PP635-15204, on the other hand, has a very v-shaped light curve with no flat bottom.

a secondary eclipse also occurs, however, the flux contribution of a planet is hardly detectable with ground-based telescope facilities, therefore a visible secondary eclipse is a likely sign of a false-positive identification. Figure 1.35 shows candidate PP205-08639 from the Pan-Planets data which displays a secondary eclipse. Although the period is very short, a hot Jupiter cannot get heated to a degree where it contributes 3% to the total flux in the i'-band (Burrows et al., 2006). The primary is a M2V dwarf according to stellar characterization with low-resolution spectroscopy[75] and SED fitting (see also section 3.2.4), hence a more plausible scenario would be a late M-dwarf of M8V type or below that has a radius with a similar order of magnitude as a hot Jupiter and shines at about 2% of the solar flux. What remains curious is a visible flux increase from the secondary eclipse towards the primary transit at phase 0.5[76], which could be interpreted as a reflection effect (Zucker et al., 2007), but should actually decrease the flux and not increase it.

Ellipsoidal variations

For a system in which the companion is a low-mass star, ellipsoidal flux variations may occur which are a tell-tale sign that the transit cannot be created by a planet. The positive amplitude of those variations is located at phases 0.25 and 0.75, therefore outside of the transit and secondary eclipse. This effect occurs due to tidal forces from the secondary (Zucker et al.,

[75] Using data from the McDonald HET lowres instrument.
[76] The Pan-Planets box fitting algorithm shifts the transit by 0.5 phase units.

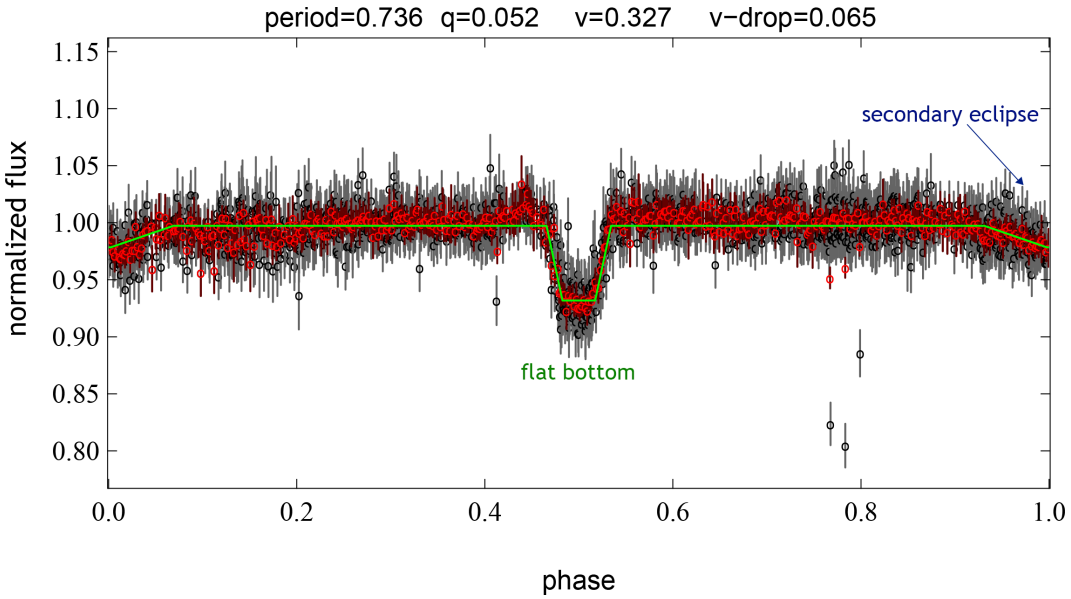

Figure 1.35: Transit detection of a hot Jupiter candidate, identified by the Pan-Planets detection pipeline. At the top, best-fitting values for period, transit duration q, trapezoidal v-shape and transit depth v-drop are given. While a flat bottom is clearly visible in the binned data points (red) and is subsequently identified by our v shape fitting (green), a secondary eclipse is also visible, hence we disregarded this candidate. Note that the transit is phase-shifted to phase 0.5.

2007) and the flux amplitude can be characterized based on following variables:

$$\frac{\Delta F}{F} = \alpha_{\text{ellip}} \left(\frac{R}{a}\right)^3 \frac{M_2}{M_1} \sin^2 i, \tag{1.21}$$

with primary and secondary masses M_1 and M_2, respectively, inclination angle i, orbital distance a and primary stellar radius R. α_{ellip} is an empirical value (Faigler et al., 2012). Detecting such variability is a tell-tale sign of a binary system since equation 1.21 scales strongly with the companion's mass. Figure 1.36 shows one such system with strong ellipsoidal variations which, besides the secondary eclipse, indicate that the companion is a low-mass star and no planet.

1.8.3 Transit timing variation

Transit timing variations, in short TTVs, occur when there is strong reciprocal interaction between the planet and another companion (see also 1.3.5), which can be the case in binary-star or multi-planet systems. If this happens in resonance (for example a 2:1 orbital period ratio), the orbit stability increases. The periodic interaction furthermore slightly slows or accelerates the planet when passing the gravitational source, leading to slightly delayed or early transits. TTVs can be a very effective tool in confirming the planetary nature of transit light curves and even detecting additional planets that do not cause visible transits (Fabrycky et al., 2012). Furthermore, this effect can be used to determine the planetary masses which becomes important for small, rocky planets that are very difficult to measure with the radial

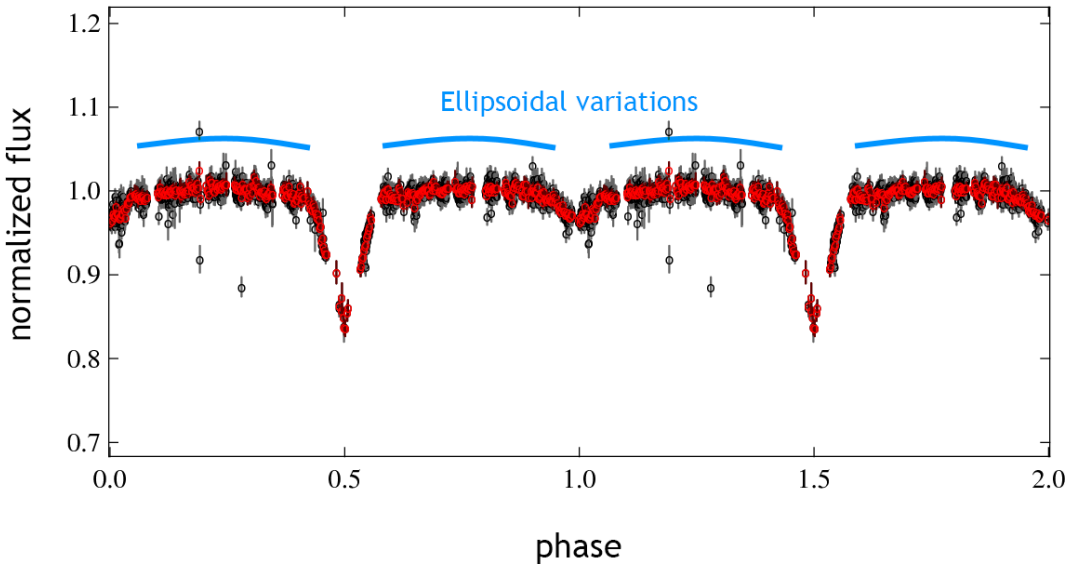

Figure 1.36: Folded (p=3.167 d) light curve of Pan-Planets target PP503-35924, showing ellipsoidal variations (marked in blue) that peak at phases 0.25 and 0.75. Data points are again binned to 500 (red). Two phases are shown for better visibility.

velocity method.
As an example for this effect, the system Kepler 11 (see also section 1.3.5) shows visible transits from 6 planets which show strong, periodical timing variations that correspond to their resonant orbits (Lissauer et al., 2011). The O-C diagram (Sterken, 2005) indicates gravitational interactions between the three innermost planets while planets d and e are linked as well.

1.8.4 Photometric follow-up

Photometric follow-up is a viable way to improve upon the transit parameters by increasing the photometric accuracy. As was the case with Pan-Planets (see sections 2 and 3), exoplanet candidates found within the data were re-observed with the 2.0 m Fraunhofer Telescope Wendelstein (FTW). There are several reasons for this process.

Period confirmation

A transit signal detected in a survey with relatively few data points which are stretched over a longer time such as Pan-Planets (see section 2.2 for more details) can have significant period uncertainties or, worse, the signal itself may be an artefact of red noise residuals. As an example, simulations based on the Pan-Planets data (see section 2.4) showed that many detections are listed with a harmonic of the actual period with a factor of two or three. Following up every planet at least once therefore ensures that the signal is real and the period was determined correctly.

Transit shape improvement

A very viable method is the use of (relatively) cheap survey telescopes for which the primary purpose is the detection of above-threshold events. Those events then get followed up with more accurate instruments. This approach is used by Pan-Planets, Super-WASP and even K2 where the nature of limited-duration photometry necessitates additional observations (Vanderburg et al., 2015). The effectiveness of this technique will be discussed in section 3.

Multi-band transit photometry

As described in Mandel and Agol (2002), the shape of a transit is dependent on the stellar limb darkening. This effect is directly related to the covered wavelength, hence the light curve shows slight difference in each filter band. In general, a transit light curve depends on three parameters, limb darkening, stellar/planetary radii and the system's inclination. This simplification disregards possible wavelength-dependent effects from the planet's atmosphere. It is very difficult to solve the degeneracy between the radius ratio and inclination (Rowe et al., 2008) if the photometric data are not very precise. Recording a multi-band transit allows to place tighter constraints on the limb darkening coefficients - hence also the stellar effective temperature - and leads to tighter constraints for the radius-ratio and inclination.
Multi-band photometry is a useful tool for distinguishing between some false-positive detection scenarios and actual planets. For example, an eclipsing binary system that is blended inside of the PSF may create a signal that looks like a planetary transit in one band but will be distinguishable in others.
Another application for this technique is a more precise radius measurement. Hot Jupiters in particular often show differing radii per photometric band, most likely due to the planet atmosphere's wavelength-dependent opacity and Rayleigh scattering (Southworth et al., 2012). Furthermore, multi-band photometry has been used to detect star spots that got covered by the planet during the transit (Southworth et al., 2016). This is, so far, the only way to characterize star spots on other stars and measure their respective radii and contrast ratio.

1.8.5 Stellar characterization

Characterization of the host star can be very important for determining the planet's properties. In general, there are two ways to identify the stellar type, photometrically and spectroscopically.

SED fitting

Every star has a spectral energy distribution (SED), a function of flux over wavelength, which is determined by the star's effective temperature and spectral line features. Folding this function with the sensitivity of each photometric band, the absolute (or apparent) magnitudes can be determined.
SED fitting can be used if the star's actual SED function is unknown. For this, one needs synthetic or empirical model SED's for the photometric bands that are being fitted. Since the star's brightness is only known in apparent magnitudes while the model SED's have absolute magnitudes, the distance has to be fitted simultaneously. An analytical solution for every model SED can be determined. The χ^2 for a given distance modulus d, apparent magnitude m, absolute magnitude M and n photometric bands x can be described by the following

expression:

$$\chi^2 = \sum_{x}^{n} \frac{(M_x - m_x + d)^2}{e_x^2}, \tag{1.22}$$

where e_x is the error of m_x. The best-fitting distance can be determined by locating the local minimum:

$$\frac{\partial \chi^2}{\partial d} = \sum_{x} \frac{2(M_x - m_x + d)}{e_x^2} \stackrel{!}{=} 0. \tag{1.23}$$

This leads to:

$$\sum_{x} \frac{d}{e_x^2} = \sum_{x} \frac{M_x - m_x}{e_x^2}, \tag{1.24}$$

$$d = \frac{\sum_{x} \frac{M_x - m_x}{e_x^2}}{\sum_{x} \frac{1}{e_x^2}}. \tag{1.25}$$

However, things become more complicated if there is significant extinction, created by dust grains in the interstellar medium (ISM) which absorb or scatter a fraction of the light that is passing through. First discovered in 1930 (Trumpler, 1930), the strength of this effect is dependent on the amount of dust and the observed wavelength. The strength of this effect varies over the spectral range and due to its property of affecting shorter-wavelength bands more strongly, it is also called reddening. It is not a smooth, continuous function but instead shows absorption lines, for example at $3.4\,\mu m$ (Adamson et al., 1990). With broad-band photometry, the extinction curve has to be multiplied with a band's sensitivity curve for the actual magnitude change. The extinction is usually given by the colour excess E(B-V) which correlates the magnitude change between the observed and intrinsic colour (B-V) of an object:

$$E_{B-V} = (B - V)_{obs} - (B - V)_{int}. \tag{1.26}$$

For other photometric bands x, the extinction effect can be converted by multiplying the colour excess with the corresponding calibrated index A_x. The method of using a three-dimensional dust map for extinction fitting will be further described in section 2.3.1.
The advantage of SED fitting is that a large number of stars can be characterized in hours without the need for costly[77] spectroscopic observations, provided there is multi-band data from surveys such as the 2 Micron All-Sky Survey (2MASS, Skrutskie et al., 2006), Sloan Digital Sky Survey (SDSS, York et al., 2000) or Pan-STARRS1 3π sky survey (PS1 3π, Magnier et al., 2013). Furthermore, it provides at least an estimate of the stellar parameters, compared to colour cuts while not being as precise as spectroscopic characterization.

[77] Costly both in observing time and money.

Low-resolution spectroscopy

Spectroscopy is the most accurate way of determining the stellar type, effective temperature and metallicity of a star. The most cost-effective way is to record low-resolution spectroscopy since its lower resolution[78] allows for a higher S/N. A 2m telescope is capable of following up 16th mag targets in less than 30 min (Ammler-von Eiff et al., 2015). Two different approaches are possible in order to classify the target:

- Based on synthetic or empirical databases, one can fit a normalized subset of the spectrum, absorption lines, against different stellar-type samples and determine the best fit by χ^2 minimization. This technique is used in chapter 3.
- By recording standard stars, usually of A0V type, the star's spectrum can be calibrated. It is then directly compared to theoretical/empirical templates (Alonso-Floriano et al., 2015), either through spectroscopic index matching or by visually comparing their general shape. The latter technique is shown in chapter 4.

Furthermore, the results from low-resolution spectroscopy can be used to improve the planet characterization. Estimates for the stellar type mean that two of the four transit shape parameters, stellar radius and limb darkening, can be constrained more stringently.

1.8.6 Radial velocity

The safest and most common way to confirm an exoplanet is by measuring the radial velocity of its host star. High- or medium-resolution spectroscopy can rule out other false-positive detection scenarios by giving an accurate mass estimate or at least give upper limits

Medium-resolution spectroscopy

Likely contamination-scenarios for a (hot Jupiter) planet detection are transiting brown dwarfs or late M-dwarfs. In addition to stellar characterization, medium-resolution spectroscopy can be used to rule out several such scenarios. Instruments like SpeX (Rayner et al., 2003) with a typical resolution of R=2000 can detect the radial velocity amplitude of brown dwarfs around M-dwarfs.

High-resolution spectroscopy

Measurement of the radial velocity and subsequently determination of the planet's mass (see section 1.5.4), is generally the most common method of confirming a transiting exoplanet since it rules out all alternative contamination scenarios.
There are two challenges for high-precision spectroscopy: with a sufficiently high resolution ($R > 20000$), S/N can become a problem for faint stars, therefore large telescopes are needed. Furthermore, having a stable wavelength reference is essential in reaching accuracies in the order of meters per second. Out of a variety of possible sources and techniques, three are either already commonly used and of particular interest for future instrumentation:

ThAr: A spectrograph with a ThAr calibration source is implemented by using two optical fibres simultaneously, one for the stellar signal, one for the ThAr lamp. What sets

[78] Usually in the order of R=1000.

this technique apart is its high number of 8400 lines over a range of about 3000 Å (Lovis and Pepe, 2007). This means that the calibration can be done over a large wavelength area to an extremely high degree and a precision of meters per second can be achieved (Perryman, 2011), although the lines are unevenly spaced (Murphy et al., 2007). Theoretically, a ThAr lamp can be even used for infrared spectroscopy although there are still issues with the calibration.
Contrary to the Iodine method, the stellar signal is not modified for a high S/N and simultaneous stellar characterization with this method. ThAr has traditionally been the favoured calibration source of many European projects such as ELODIE (Baranne et al., 1996) and its successor HARPS (see section 1.6.1).

Iodine: The utilization of molecular Iodine (I_2) vapour is a different technique to calibrating with ThAr lamps. The gas cell is placed directly in the spectroscopic light path and the (known) lines from I_2 are therefore superimposed on the star's spectrum. Through this, the spectrograph's PSF is calibrated in addition to the wavelength (Perryman, 2011) although this results in a 20%-30% loss of light and no possibility of simultaneous stellar characterization.

Laser frequency comb: Both ThAr and I_2 have disadvantages in that they are not ideal calibration sources. Theoretically, the perfect calibrator would cover the whole range from the visible to the infrared with clear, constantly spaced lines at wavelengths that are determined precisely from physics, are time-stable and do not influence the S/N of the signal. This is what laser frequency combs (Reichert et al., 1999; Jones et al., 2000; Udem et al., 2002)[79] promise to deliver. Such calibrated spectrographs could reach a precision of $0.01\,\mathrm{ms}^{-1}$ (Murphy et al., 2007). The general concept of a laser frequency comb is that these constructs can store a single pulse and automatically replenish the energy lost from emission in the lasing medium. Therefore, a highly stable pulse is produced with a broader line distribution for shorter pulse durations[80]. This technique, however, is still very new and in the process of being tested. The high-resolution echelle spectrograph FOCES (Pfeiffer et al., 1998) on Mt. Wendelstein will contain such a frequency comb for calibration.

1.8.7 Background star blend

One of the common contamination sources are background stars that are blended in the foreground star's PSF and affect the transit/eclipse signal. The light drop of the planet's transit then appears lower or an eclipsing binary system behind a transit-less star can appear as a transit-like signal. In the latter case, the eclipse appears as a planetary signal due to the combination of both fluxes which dilutes the eclipse signal. There are several ways by which one can attempt to constrain the likelihood of such an event.

Archival imaging

The digitization of old photographic plates has created the opportunity to investigate whether a star's proper motion is high enough for it to have moved at least one PSF-width on the sky. One illustration for this effect is shown in Figure 1.37 for the confirmed planet system K2-9

[79] This development led to a Nobel prize in physics: www.nobelprize.org/nobel_prizes/physics/laureates/2005
[80] Usually, femtosecond pulses are being used for astronomical frequency combs.

(Schlieder et al., 2016). The presence of a background source at the star's current location can then be excluded.

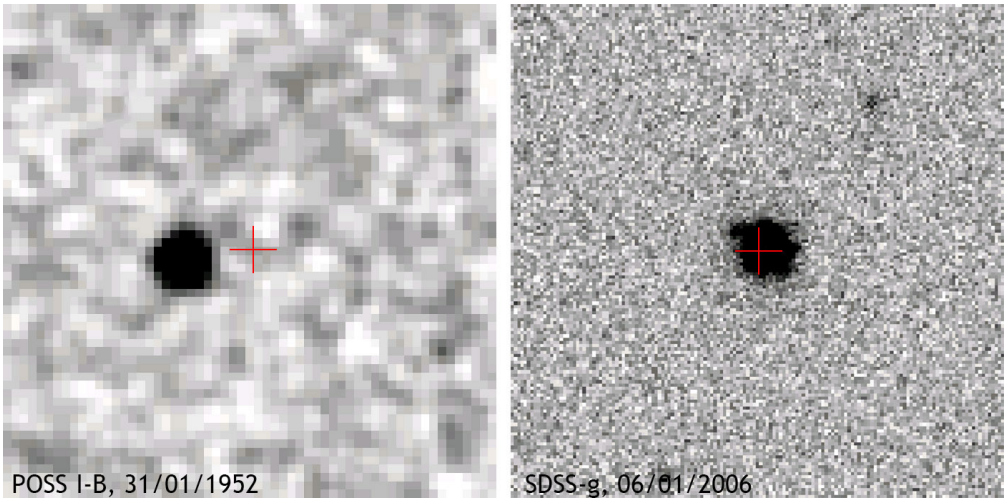

Figure 1.37: 60 x 60 arcsec archival images of planet system K2-9 with a time difference of 54 years. No background source can be seen at the planet's current location in the 1954 image, excluding this scenario from the list of possible false positives. (Created with http://irsa.ipac.caltech.edu/applications/finderchart/)

Double PSF fitting

If the PSF of an image is known, two sources can be fit with variable positions inside of the signal to investigate whether two sources are hidden in the star's PSF. For the Pan-Planets candidates (see also chapter 2) we generated reference frames with high-resolution PSF fits[81] as an additional constraint in order to identify false-positive identifications.

Adaptive Optics

Seeing, the atmospheric turbulence that smears the PSF of a star, is an effect that constrains all terrestrial observations. There are two distinct techniques which can improve the sharpness of an image. Adaptive optics (AO) was first proposed by Babcock (1953). It requires a high degree of (computer-assisted) mechanical control and after the beginning of the computer age, first successes were reported by Rousset et al. (1990).
The atmosphere induces distortions in the wavefront of a star's light which blurs the signal (Beckers, 1993). If those distortions are known, it is possible to correct them in order to regain the original signal. Usually, one uses a laser guide star, a laser-generated object that is created close to the observed star or object. A computer measures the distortions of this guiding star at a frequency of 1 kHz (Perryman, 2011), and controls actuators beneath the telescopic primary mirror to manipulate the primary's shape, cancelling out these wavefront distortions. For transiting planets, adaptive optics images can be used to create a contrast curve over the sub-arcsecond scale which can be used to rule out signal dilution from a blended background star or, depending on the results, confirm or refute the planet scenario.

[81] See also Koppenhoefer et al. (2013).

An example for adaptive optics images in the context of transit follow-up can be found in section 4. Due to technical limitations, only few telescopes are equipped with adaptive optics and there are size constraints for the primary mirror's diameter.
An alternative is the use of active optics which allows the use of thin mirrors. Factors like wind, mechanical stress or varying temperatures get corrected by actuators that are placed below the primary mirror. The adjustments are taking place over a frequency lower than 1 Hz. The New Technology Telescope (NTT[82]) in La Silla, Chile was a pioneer for this technique. With it, large-mirror telescopes like VLT and Keck can be constructed (Wilson, 1991).

Lucky imaging

Lucky imaging is very similar in concept to adaptive optics but without any need for mechanical construction. The wavefront distortions induced by seeing happen on a timescale of seconds which means that high-cadence images with a fast readout can deliver a few clean images[83]. Originally proposed by Babcock (1953) and refined by Hufnagel and Stanley (1964); Fried (1978), readout and exposure times have to be very short to be most effective (Smith et al., 2009), ideally at about 10 ms. This has long been the limiting factor for this technique since faster readout can lead to higher noise, but the newest detectors have become good enough so that this issue has been solved. Similar to adaptive optics, lucky imaging has been carried out successfully to detect nearby companions of planet systems (Faedi et al., 2013). Lucky imaging is especially interesting because of its possibly synergy with adaptive optics - both can be used at the same time to further improve the resolution.

1.8.8 Statistical validation

Programs such as the false positive probability (FPP) calculator *vespa* (Morton, 2012, 2015), which attempt to confirm transiting planets based on statistical arguments, are highly successful (Lissauer et al., 2014; Rowe et al., 2014; Morton et al., 2016) and so far contributed more than 1400 transiting-planet discoveries. Due to the large sample of discovered exoplanets and variable star systems, it is possible to validate transit signals as planetary by statistically ruling out other plausible scenarios that can create this signal.
Statistically, a transiting system can be described by i scenarios with the marginalized likelihoods L_i and priors π_i. If the probability $Pr(H_i)$ of the hypothesis H_i is to be determined, this can be described as:

$$Pr(H_i) = \frac{\pi_i L_i}{\sum_j^i \pi_j L_j}. \tag{1.27}$$

L_i represents the likelihood how closely the scenario i can be matched with the data, e.g. the shape of the transit or constraints from RV or high-resolution imaging. One can simplify equation 1.27 by merging all non-planet scenarios into the false-probability "FP" group and renaming the probability for the planet scenario into true-probability "TP":

$$Pr(H_i) = \frac{\pi_{TP} L_{TP}}{\pi_{TP} L_{TP} + \pi_{FP} L_{FP}}. \tag{1.28}$$

[82]The NTT also pioneered the fully-rotating octagonal enclosure design. The result is a comparatively small dome that is rotated in its entirety which, due to issues navigating the nightly way to the facilities, led astronomers to rename the NTT into the "No Toilet Telescope".
[83]Hence the prefix "lucky".

One has to consider all likely false-positive signals as listed in section 1.8.1. *Vespa* sorts those scenarios into six groups, consisting of three scenarios with an additional double-period case for each:

1. (a) Blended EB (BEP),
   (b) Double-period BEP,
2. (a) EB with/without blend,
   (b) Double-period EB,
3. (a) Hierarchical EB (HEP),
   (b) Double-period HEP.

Every type of scenario, be it a planet or a false-positive scenario, has a prior π_i based on the occurrence rate for the respective scenarios. For example, while about 50% of all stars are estimated to be gravitationally bound to at least one other star (Perryman, 2011), close-period eclipsing binaries have a much lower probability based on geometry and the occurrence rate of close-period binaries. Furthermore, while brown dwarfs may appear identical to hot Jupiters in terms of transit shape and depth, they seem to occur very rarely in close orbits of stars (Marcy and Butler, 2000; Udry and Santos, 2007; Kraus et al., 2008). This, however, means that the significance of the statistical assessment is directly related the accuracy of the priors. The *vespa* program performs its analysis in five steps (Morton et al., 2016):

1. Generate a posterior sample based on the fitted transit signal.
2. Create representative population simulations for each hypothesis.
3. Fit each simulated transit/eclipse.
4. Evaluate priors and likelihoods for each hypothesis and include constraints.
5. Determine the posterior probability for each hypothesis.

In the first step, the transit is fitted using the MCMC technique[84]. The scatter around the best-fitting transit curve is measured; the higher the photometric accuracy, the easier it will be to distinguish between different hypotheses. Next, a population of stellar systems is simulated for each hypothesis. For this, the TRIdimensional modeL of thE GALaxy (TRILEGAL) Galactic stellar population synthesis tool[85] (Girardi et al., 2005) is utilized and is constrained to the given stellar colours, e.g. J-K based on the 2MASS catalogue. In this step, the better the stellar characterization of the candidate star, the more accurate will be the population model. In the third step, each system gets analysed and fit with a trapezoidal model. The best-fitting trapezoid for the real transit serves as the template against which each system will be compared against. After this, *vespa* analyses the likelihoods and priors for each scenario, i.e. how many systems showed transits/eclipses that are similar to the real transit and how likely each population is, based on the priors of the stellar modelling and the resulting constraints from step 2.

[84] Therefore, the refitting of the transit is based on the same technique as our own planet parameter fitting (see section 3.2.5).

[85] http://stev.oapd.inaf.it/cgi-bin/trilegal

Parameter	Prior
Primary Mass M_A	$\propto M_A^{-2.35}, M_A > 0.1 M_\odot$
Secondary Mass M_B	$\propto (M_B/M_A)^{0.3}, 0.1 <= M_B <= M_A$
Tertiary Mass M_C	$\propto (M_C/M_A)^{0.3}, 0.1 <= M_C <= M_B$
Age [Gyr]	$1 - 15$
Metallicity [Fe/H]	$\frac{0.8}{0.15} N(0.016, 0.15) + \frac{0.2}{0.22} N(-0.15, 0.22)^a$
Extinction A_V [mag]	$0 - A_{V_{max}}$
Distance d [pc]	$\propto d^2$

Table 1.2: Priors used for stellar property fits. ^{a} - N stands for a double-Gaussian fit to the measured local metallicity distribution from TRILEGAL. The extragalactic extinction A_V is extracted from Schlegel et al. (1998).

Further constraints that are based on observational data are being weighted in this step as well. Priors used for the stellar property fits are listed in Table 1.2. Two priors for the planet population are given. The first one encompasses the geometric probability of a visible transit. While this can be described analytically, as discussed in section 1.5.6, *vespa* does the same as Pan-Planets (see also section 2.4) and randomly simulates orbital periods, inclinations, eccentricities and planetary+stellar radii. The resulting prior is therefore empirical. For the planet occurrence rate, a different approach has been taken. Equation 1.28 can be simplified by defining $L'_j := \sum_j^i \pi_i L_i$:

$$FPP = \frac{L'_{FP}}{L'_{FP} + f_p L'_{TP}}, \tag{1.29}$$

where f_p is the occurrence rate of planets in case of the true detection TP. This equation can be further simplified to:

$$FPP = \frac{1}{1 + f_p P}, \tag{1.30}$$

where P is defined as $P := \frac{L'_{TP}}{L'_{FP}}$. Now, the FPP is only dependent on the planet occurrence rate f_p and P which is determined by the results from *vespa*. For the default planet occurrence rate, *vespa* assumes a planet-hosting stellar fraction of 40% with a planet distribution in a power law of planet radii:

$$dN/dR \propto R^{-2}. \tag{1.31}$$

As a simplification, *vespa* determines the numerical value $f_{p,V}$ which is a factor that determines at which $f_p \cdot f_{p,V}$ the candidate can be considered confirmed, assuming a target FPP_V:

$$f_{p,V} = \frac{1 - FPP_V}{P \cdot FPP_V}. \tag{1.32}$$

Therefore, one can either use the generic function of f_p or replace it by empirical values, which have to be normalized to bin widths of $\pm 0.3 R_p$[86], and then consider the factor $f_{p,V}$. The occurrence rate based on equation 1.31 is at about 1.3% for the planet radius bin at $1.0\,R_J$[87], which is likely too high for the real occurrence rate of M-dwarf hot Jupiters but

[86] Using relative bin widths that are scaling with the planet radius ensures that different populations such as Jupiters and Earths can be compared.

[87] With an according bin width of $\pm 0.3\,R_J$.

close to the upper limits placed by RV surveys (Johnson et al., 2007; Bonfils et al., 2013). Generally, $f_{p,V}$ can be viewed as a criterion which evaluates how much larger or smaller the occurrence rate had to be for the candidate to become marked as a detection. For instance, a value of $f_{p,V} = 0.5$ means that the planet would be validated even for a test occurrence rate twice as low. For the threshold probability of a confirmed detection, Morton et al. (2016) uses 99%. Candidate PP140-14711, shown in Figure 1.38, is an example for a detection that would still be validated even for a significantly lower occurrence rate while candidate PP259-05801 would require a much higher occurrence rate for the planet to become validated. For our M-dwarf targets, we assume our determined occurrence rate[88] of $f_p = 0.11\%$. Furthermore, these ancillary data have to be collected for the analysis:

- RA/DEC coordinates of the target.
- Broadband photometry in g'r'i'z'y'[89]JHKW_1W_2 for SED fitting.
- Best-fitting values for T_{eff}, log(g) and, if available, [Fe/H].
- Light curve and best-fitting period and initial transit time t_0.
- Planet/star ratio $R_p/R_\star$ from the best analytical transit fit[90].
- PSF FWHM of the candidate star in the reference frame.
- Maximum secondary eclipse depth that is detected after removing the primary transit and rerunning the fit.

Using the light curve and the period, *vespa* determines the transit scatter, called the "odd-even" ratio, which limits the double-period scenarios. The higher the photometric precision of the transit is, the more constrained are the permitted differences between primary and secondary radii in the double-period case. Upper limits for the secondary companion's brightness can be imposed depending on the star's stellar type. The probability of having a blended background star can be determined if the star's PSF in the survey, stellar density and magnitude distribution in this region are known. Additional data can be used to place further constrains on the candidate fit. High-resolution photometry such as lucky imaging, adaptive optics or archival images can either fully rule out or limit the amount of light from a blended light source. High-precision photometry, even more so if transits were recorded in multiple bands, limits the range of EB systems whose signal might appear similar to a planetary transit. Since a secondary eclipse should be visible in an EB system, the lack of such a signal can also limit EB scenarios. Accurate transit measurements also limit the double-period scenarios due to tighter constraints on the difference in shape and depth between primary and secondary eclipse. Radial velocity data can also be used to limit the likelihood of an EB system. Spectroscopic characterization or SED fitting allow the determination of the primary star's limb darkening, a stellar characteristic that affects the shape of the transit. *Vespa* then combines all of the above constraints and ancillary data, simulates n[91] systems in all given

[88] See also section 3.3.3.

[89] The g'r'i'z'y' photometry from our used Pan-STARRS1 catalogue (see section 2.3.1.) is converted to the Sloan photometric system according to Tonry et al. (2012)

[90] See also section 3.2.5 for our implementation.

[91] Usually, *vespa* simulates 20000 systems with visible eclipses per scenario. However, this number can be manually adapted which we increased to 100000.

scenarios, fits each eclipse and measures the similarity of the fit to the real transit signal. Finally, the posterior probability for each hypothesis is determined by using equation 1.27.
As an example for the *vespa* analysis, we show the highly likely candidate PP140-14711 and the likely false-positive detection PP259-05801[92] in Figure 1.38. One can see that, while the likelihood for a planetary transit in case of PP259-05801 is very high, its overall result has a very high false-positive probability due to the priors. The priors for the planet population are influenced by the fitted radius - a Jupiter-sized transit is more likely than that of a planet twice of Jupiter's radius - and by the photometric accuracy of the transit fit. For our highly likely candidate PP140-14711, the high accuracy of the transit, characterized in the odd-even ratio, means that double-period scenarios can be ruled out by strongly constrained differences between the primary and secondary eclipse depth. Due to additional constraints on the secondary eclipse depth, single-period EB's can be ruled out as well. The difference between the respective likelihood values for both planet candidates is apparent with the results for PP140-14711 being lower by a factor of $\approx 10^{-1}$ while the priors have similar values. This is due to the higher photometric accuracy of PP140-14711's light curve, meaning that a smaller subset of possible transit signals can be fit to the data and can therefore be used as a rule of thumb to compare the fitting precision between candidates.
There are a few caveats to the approach of *vespa*. One issue is the use of the old IMF function from Salpeter (1955) which, while accurate for masses $M > 0.5\,M_{\odot}$, strongly overestimates the number of lower-mass stars. The general assumption is that the stellar models, population models and occurrence rates of multiple star systems and planets are known well enough to make a valid characterization possible. With recent surveys such as Kepler and SuperWASP this has improved, however, there are still open questions to the planet occurrence rate. Furthermore, *vespa* uses the Dartmouth isochrone package (Dotter et al., 2008) which is not perfectly suited for low-mass stars. Moreover, dust is fitted as a linear distance-related interpolation between zero and the extragalactic extinction A_V determined by Schlegel et al. (1998), an approach that we found to be insufficient in Pan-Planets[93].

[92] See also section 3.3.
[93] See also section 2.3.1.

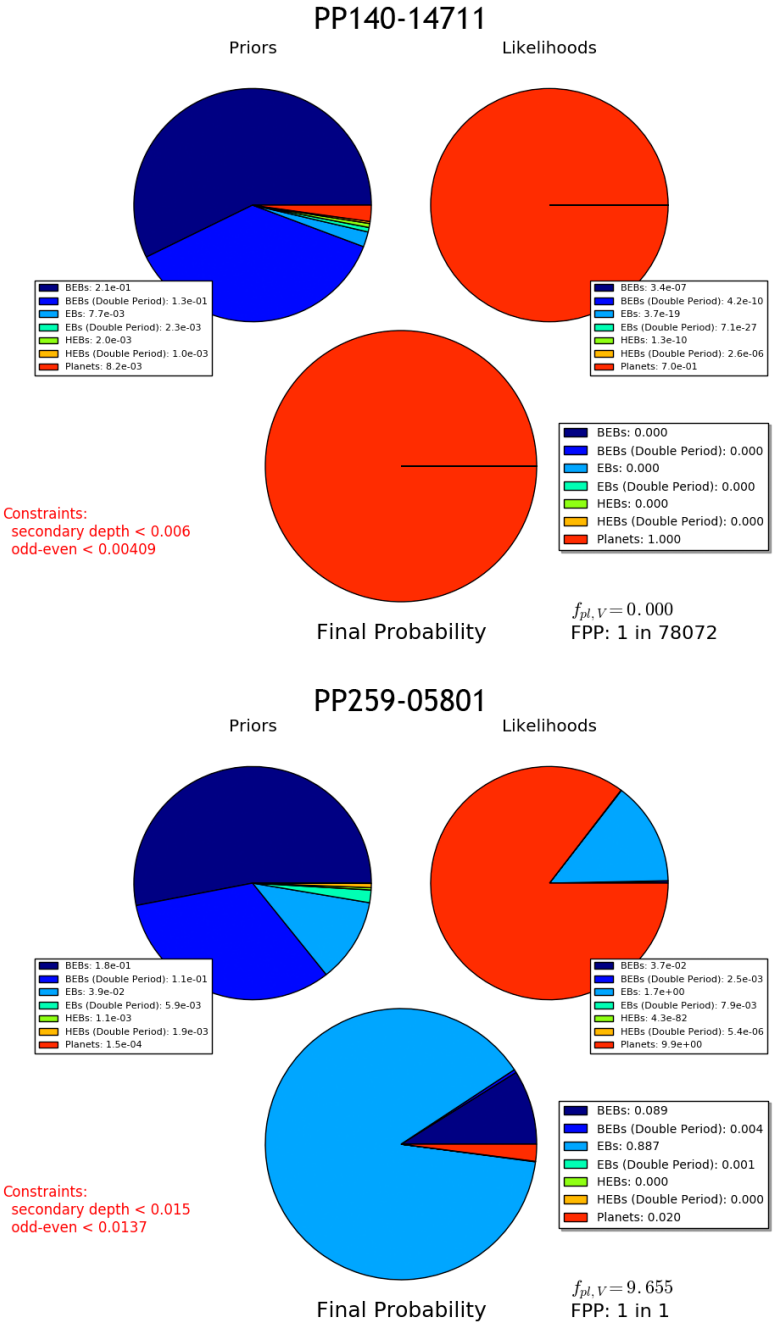

Figure 1.38: FPP summaries from *vespa* for two planet candidates. PP140-14711 (top) exhibits a very high probability for being a true detection while PP259-05810 (bottom) is a very likely false detection. Two placed constraints (red font) were the depth of the secondary eclipse and the the automatically determined photometric precision (odd-even) which is used to determine the likelihood of a double period scenario. For each scenario, a population of 100000 simulated systems was generated and analysed.

1.9 Thesis goals and structure

The main goal of this thesis is the determination of the hot-Jupiter occurrence rate around M-dwarfs. As described in sections 1.4 and 1.6.2, M-dwarfs seem to be peculiar in that their planet distributions appear to be different to that of FGK dwarfs. While transit surveys such as Kepler are very successful in discovering planets, the small M-dwarf samples in those surveys have limited the statistical assessment of the occurrence rate of M-dwarf hot Jupiters. This thesis is part of the Pan-Planets survey which surveyed a substantially larger number of M-dwarfs than other projects.
In order to perform such an analysis, one first has to identify the M-dwarf target sample. This is a critical point: the more robustly M-dwarfs are identified, the more stringent occurrence rate limits can be established. The Pan-Planets field has a high amount of interstellar extinction which reddens the individual stars. Therefore, a significant task is the proper stellar characterization of the target stars which incorporates extinction fitting. The data reduction of Pan-Planets is a challenging task that encompasses writing automatic pipelines, creating image-processing scripts for automatic masking of systematics and light curve creation and signal detection. Next, a concept for Monte Carlo simulations has to be planned and executed in order to estimate the detection efficiency based on the data. Finally, all planet candidates have to be characterized by transit shape fitting and followed up with spectroscopy and photometry.

In chapter 2, I first describe the Pan-Planets survey and data reduction, provide an overview of our M-dwarf selection method and demonstrate the accuracy of it by performing various consistency checks. Using a Monte Carlo method of transit injection, I estimate the detection efficiency of Pan-Planets for various planetary and stellar radii.
In chapter 3, I detail the follow-up of our Pan-Planets candidates in four different target categories with the Fraunhofer Telescope Wendelstein Wide Field Imager and the McDonald observatory Otto Struve telescope ES2 spectrograph. I provide the final list of vetted candidates in four target categories and determine the impact of this by providing a new upper limit for the occurrence rate for M-dwarf hot Jupiters, based on our number of candidates and the detection efficiency determined by the Monte Carlo simulations.
In chapter 4, I describe the discovery of an unusually large Neptunian planet that was found in the K2 survey. I give an overview of our follow-up layout, characterize the host star and validate the planet statistically. I discuss an anomaly which I detected in the planet's radius. Finally, I provide a summary and concluding remarks in chapter 5.

Chapter 2

Pan-Planets

It is a capital mistake to theorize before one has data. Insensibly one begins to twist facts to suit theories, instead of theories to suit facts.

Arthur Conan Doyle, Sherlock Holmes

Note: Parts of this chapter were used for the publication "Pan-Planets - Searching for Hot Jupiters around Cool Stars" (Obermeier et al., 2016).

Abstract

The Pan-Planets survey observed an area of 42 sq deg. in the galactic disk for about 165 hours. The main scientific goal of the project is the detection of transiting planets around M-dwarfs. We describe the layout of the survey and detail the data reduction and signal detection procedure. We establish an efficient procedure for determining the stellar parameters $T_{\rm eff}$ and $\log g$ of all sources using a method based on SED fitting and utilize a three-dimensional dust map and proper motion information. In this way we identify more than 60 000 M-dwarfs, which is by far the largest sample of low-mass stars observed in a transit survey to date. Using Monte Carlo simulations we calculate the detection efficiency of the Pan-Planets survey for different stellar and planetary populations.

2.1 Introduction

As of July 2015, more than 2900 exoplanets have been discovered, the majority of them with the transit method. One of the most noteworthy discoveries, first detected with the radial velocity method, is the existence of hot Jupiters and hot Neptunes which orbit closely around their host star. Such close-in gas giants were unexpected since there is no equivalent in our solar system. Those planetary systems are of significant interest, not only for their unforeseen existence but also because they are the candidates best-suited for a planetary follow-up study with transit spectroscopy. Their large size lowers the difference between planetary and stellar radius and besides the dependence on the atmospheric thickness, larger planetary radii improve the S/N of the transmission spectrum by increasing the overall surface area. The radius ratio of hot Jupiters and M-type dwarf stars is particularly favourable,

although only very few such systems have so far been detected (Johnson et al., 2012; Hartman et al., 2015; Triaud et al., 2013). It is possible that they are rarer than hot Jupiters around FGK stars since the amount of building material for planets is lower in M-dwarf systems (Laughlin et al., 2004; Ida and Lin, 2005; Johnson et al., 2010; Mordasini et al., 2012). Additionally, there is a correlation between metallicity and giant planet occurrence rates for FGK stars (Gonzalez, 1997; Santos et al., 2001; Fischer and Valenti, 2005) with indications for the same correlation for M-dwarfs (Johnson and Apps, 2009; Neves et al., 2013; Montet et al., 2014). However, there is still an ongoing discussion about the strength of the metallicity dependence for M-dwarfs (Mann et al., 2013c; Gaidos and Mann, 2014).
Radial velocity (RV) surveys (Johnson et al., 2007; Bonfils et al., 2013) set an upper limit for the occurrence rate of hot Jupiters around M-dwarfs of 1%, however, with no precise estimates due to the small sample of a few hundred target stars per survey. These low sample sizes negate high detection efficiencies.
Transit surveys such as Kepler (Mann et al., 2012; Dressing and Charbonneau, 2013; Gaidos and Mann, 2014; Morton and Swift, 2014; Dressing and Charbonneau, 2015) and the WFCAM Transit Survey (WTS) (Kovács et al., 2013; Zendejas et al., 2013) point to a fraction of less than 1% of M-dwarfs that are being accompanied by a hot Jupiter. So far, there have been few detections of such M-dwarf hot Jupiters (Johnson et al., 2012; Triaud et al., 2013; Hartman et al., 2015). However, the sample sizes were not high enough to assess the occurrence rate accurately and all detected planets orbit only early M-dwarfs.
Since radial velocity surveys provide information about the planetary mass and transit surveys about radii, it is not trivial to compare these results directly. Furthermore, many RV surveys focus on metal-rich host stars which seem to have a higher rate of hot Jupiters (Dawson and Murray-Clay, 2013).
With Pan-Planets, we aim to address this issue by providing a substantially larger sample size. This survey has been made possible by the construction of a wide-field, high-resolution telescope, namely Pan-STARRS1 (PS1).
Pan-STARRS, the Panoramic Survey Telescope and Rapid Response System, is a project which focusses on surveying and identifying moving celestial bodies, e.g. Near-Earth Objects that might collide with our planet. The Pan-STARRS1 (PS1) telescope (Kaiser et al., 2002; Hodapp et al., 2004), seen in Figure 2.1, is equipped with the 1.4 Gigapixel Camera (GPC1) which is one of the largest cameras that has ever been built. The size of the focal plane is 40 cm × 40 cm, mapped onto a 7 square field of view (Tonry and Pan-STARRS Team, 2005; Tonry and Onaka, 2009). The focal plane is constituted of 60 CCDs which are further segmented into 8×8 sub-cells with an individual resolution of ˜600×600 pixels at a scale of 0.258 arcsec per pixel. A complete overview of the properties of the GPC1 camera can be found in table 2.1. The PS1 telescope is located at the Haleakala Observatory on Maui, Hawaii. The central project of PS1 is an all-sky survey that observes the whole accessible sky area of 3π.
A science consortium of institutes in the USA, Germany, the UK and Taiwan defined 5 surveys (Hodapp et al., 2004; Carter Chambers, 2015), further split up into 12 key projects, in order to make use of the large amount of data being collected by the PS1 telescope. The surveys are:

1. The 3π Steradian Survey, covering the entire sky north of -30deg;

2. The Medium Deep Survey, 10 fields that are observed every night with higher cadence;

Figure 2.1: Pan-STARRS1, photographed right after sunset. The mountain in the distance is Mauna Kea. (Source: http://ps1sc.org/Photo_Gallery.shtml)

3. The Solar System Sweet Spot Survey with a focus on the ecliptic, searching for potentially dangerous asteroids;

4. The Stellar Transit Survey, searching for planetary transits;

5. The Deep Survey of M31, studying microlensing and variable stars.

Number 4 of these key projects is the dedicated Pan-Planets survey which has been granted 4% of the total PS1 observing time. It began its science mission in May 2010.
With about 60000 M-dwarfs in an effective FOV of 42 sq. deg., Pan-Planets is about ten times larger than previous surveys. In a sensitivity analysis of the project using Monte Carlo simulations (Koppenhoefer et al., 2009), it was estimated that Pan-Planets would be able to detect up to dozens of Jovian planets that are transiting main-sequence stars, depending on the observing time and noise characteristics of the telescope. The number of hot Jupiter detections around M-dwarfs was undetermined since there was no reliable planetary occurrence rate. The actual photometric accuracy is lower than expected (see following Section) but good enough to detect transiting hot Jupiters around K and M-dwarfs.
In Section 2.2 we describe the Pan-Planets survey and the data reduction pipeline in detail. Our stellar classification and M-dwarf selection is presented in Section 2.3. We detail our transit injection simulation pipeline that is being used for improved selection criteria and determination of the detection efficiency in Section 2.4. We detail the detection efficiency of the Pan-Planets survey and discuss the results and implications in Section 2.5. Lastly, we draw our conclusions in Section 2.6.

2.2 Survey and data reduction

2.2.1 Setup and execution

In 2009 and 2010, Pan-Planets observed three slightly overlapping fields in the direction of the Galactic plane. In the years 2011 and 2012, four fields were added to increase the total survey area to 42 square degrees in order to maximize the detection efficiency (Koppenhoefer et al., 2009). Figure 2.2 shows the position of the seven Pan-Planets fields on the sky in relation to the extragalactic dustmap of Schlegel et al. (1998).

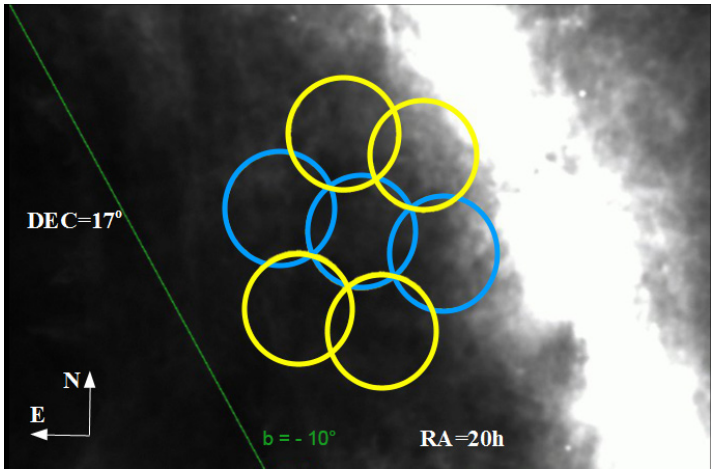

Figure 2.2: Position of the Pan-Planets fields (coordinates in J2000) in a 19° x 13° cut-out from an extragalactic dust map taken from Schlegel et al. (1998). The yellow circles correspond to the four fields with data taken only in 2011 and 2012. The blue circles correspond to the three fields with additional data taken in 2010. A pointing that close to the galactic disc means that the number of stars in the FOV is very high, however, there is strong extinction in the upper three fields.

Depending on atmospheric conditions, the exposure time was 30 s or 15 s and observations were scheduled in 1h blocks. Over the three years of the project, we acquired 165 h of observations and disregarded the further 15 h from the commissioning phase in 2009. The target magnitude range of the survey is between 13.5 and 16.0 mag in the i'-band which is expanded down to i'=18.0 mag for M-dwarfs. The i' band is ideally suited for a survey of cool stars since those are relatively bright in the infrared. Each field is split into 60 slightly overlapping sub-fields which we call skycells. The survey characteristics of Pan-Planets are summarized in Table 2.1. More information about the planning of the survey can be found in Koppenhoefer et al. (2009).
Focusing on stars smaller than the Sun has several advantages for the search for transiting planets. The most significant one is that the transit depth, which is the decrease in flux created by the planetary transit, is determined by the square of the ratio between the planetary and stellar radius. The smaller the star, the easier it is to detect the signal since the light drop increases. This makes it possible to search for hot Jupiters around very faint M-dwarfs. Moreover, the M-dwarf stellar type is the most abundant in our galaxy, meaning that there is a high number of nearby cool dwarf stars, albeit very faint (Henry et al., 2006; Winters

[1]The GPC camera has a circular layout, i.e. the corners of the detector do not get illuminated.

GPC specifications	
Telescope	1.8m Pan-STARRS1
Camera FOV	7 sq. deg.
Filters	g', r', i', z', y'
Camera Properties	8x8 CCDs [1]
CCD Properties	8x8 cells with ˜600x600 pixels
Pixel scale	0.258 arcsec/pixel
Pan-Planets characteristics	
Observation period	May 2010 - Sep. 2012
Observation time	165 hours
Survey FOV	42 sq. deg.
Survey area	$301.7° > RA > 293.7°$
	$21° > DEC > 13°$
Exposure time	15 or 30 s
	seeing-dependent
Median FWHM	1.07 arcsec
Photometric band	i'
#target stars	$\tilde{}4 \cdot 10^6$
Target brightness	13.5 mag $\leq$ i' $\leq$ 18 mag
M-dwarf targets	˜60000
White dwarf targets	˜4000
Observation time per night	1 or 3 h
Photometric precision	5-15 mmag

Table 2.1: Properties of the GPC and the Pan-Planets survey.

et al., 2015). We estimate that our sample contains up to 60000 M-dwarfs (details on our stellar classification can be found in Section 2.3). This M-dwarf sample is several times larger than in other transit surveys such as Kepler or WTS, enabling us to determine the fraction of hot Jupiters around M-dwarfs more precisely. We show the brightness distribution of our selected M-dwarf targets in Figure 2.3. Figure 2.4 shows an overview of our data reduction and signal detection pipeline, which will be described in more detail in the following sections.

2.2.2 Basic image processing

All images have been processed in Hawaii by the PS1 Image Processing Pipeline (IPP, Magnier (2006)) which applies standard image processing steps such as de-biasing, flat-fielding and astrometric calibration. Each exposure is resampled into 60 slightly overlapping sub-cells (skycells). Every skycell has a size of $\sim 6000 \times 6000$ pixels and covers an area of 30×30 arcminutes on the sky.
During the analysis of the early data releases we realized that several cells of the GPC1 CCDs, mostly located in the outer areas, exhibit a high level of systematics. To account for that, we created and applied time-dependent static masks that we provided to the IPP team for incorporation into the data reduction pipeline. Figure 2.5 shows the chip mask used for the

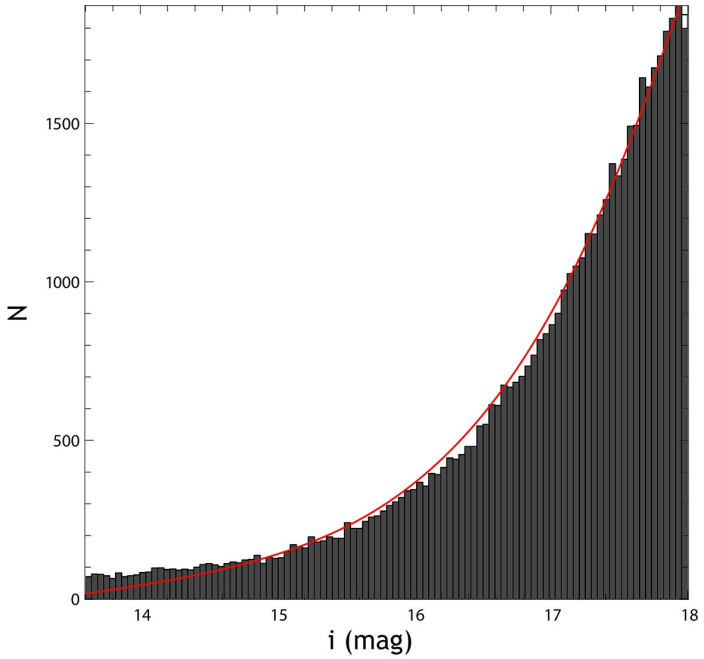

Figure 2.3: Histogram with 100 bins of the brightness distribution in our M-dwarf sample. The red line shows the distribution according to the Besançon model (Robin et al., 2003). Our fields include more bright stars than predicted by the Besançon model, but the number of stars is in good agreement for stars with magnitudes $i' \geq 14.5$ mag. A more detailed description of our stellar classification method can be found in Section 2.3.

2012 data.
The re-sampled IPP output images have been transferred to Germany and stored on disk for a further dedicated analysis within the Astro-WISE[1] environment (Begeman et al., 2013). During the ingestion of the data into Astro-WISE we correct for several systematic effects. We apply an automated algorithm that searches for and subsequently masks areas that display a systematic offset with respect to the surrounding areas (e.g. unmasked ghosts, sky background uniformities, etc.). Since satellite trails are not removed by the IPP, we apply a masking procedure based on a Hough transformation (Duda and Hart, 1972) that is available in Astro-WISE. Figure 2.6 shows an example image before and after the satellite trail masking. Blooming of very bright stars is confined to one of the 8×8 cells of each chip. We apply an algorithm that detects saturated or overexposed areas and then masks the surrounding region as demonstrated in Figure 2.7.
Since the skycells are overlapping and three of the seven field have been observed longer, the total number of frames per skycell is varying between 1700 and 8400. Figure 2.8 shows a histogram of the number of frames per skycell.
Within one skycell, there is significant masking in a majority of the frames. Our data reduction pipeline discards any frame with less than 2000 visible sources, which corresponds to an upper limit for masking of about 85%-90%, depending on the star density of the region. The histogram of remaining frames is shown in Figure 2.8 (black). One can see that many images from the overlapping regions with a high initial number of images (red) are dropped due to

[1] Astronomical Wide-field Imaging System for Europe, http://www.astro-wise.org/

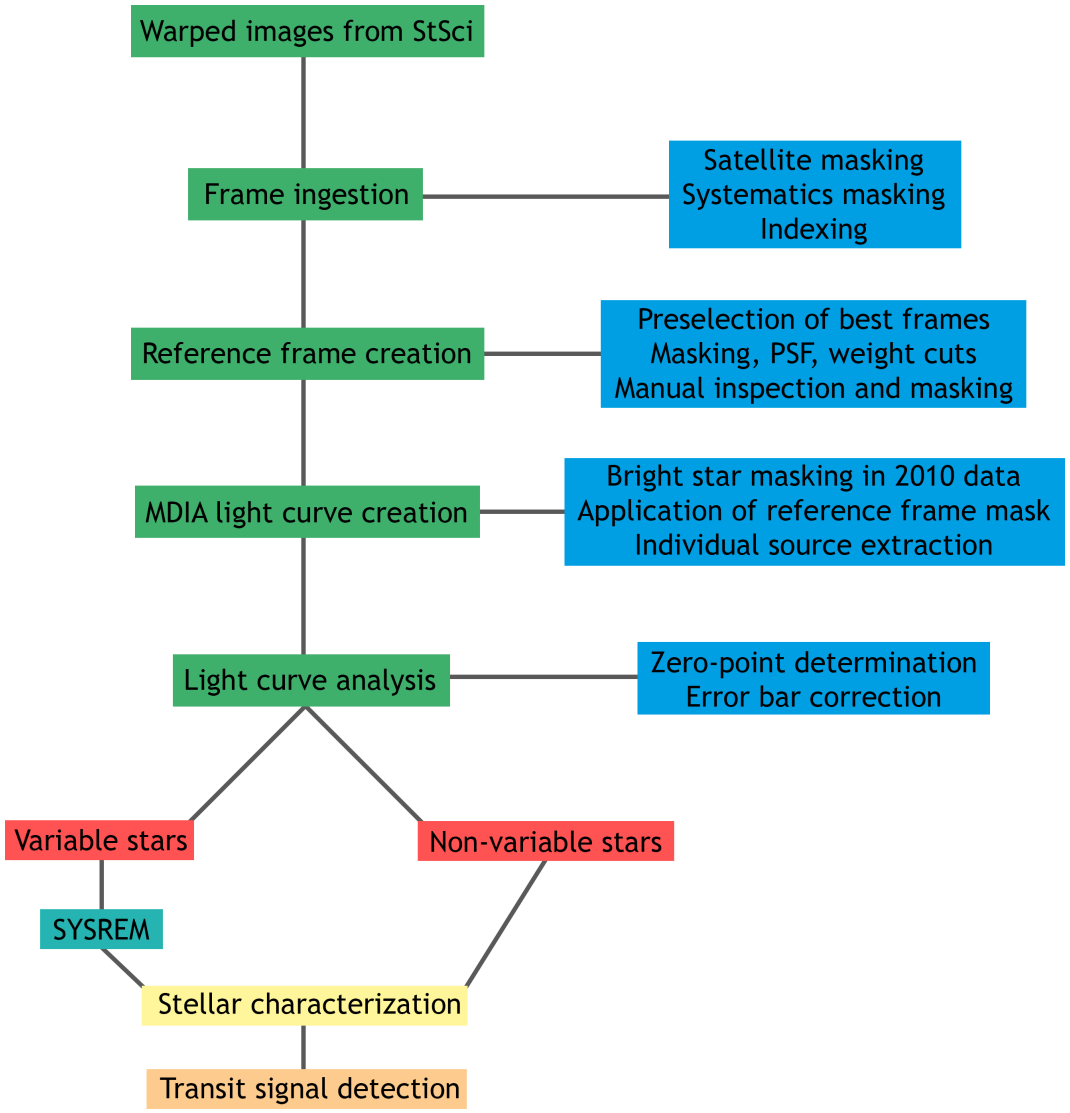

Figure 2.4: Overview of the Pan-Planets reduction and detection pipeline. The steps involved will be explained in the following sections.

high masking. The comparatively low resulting number of frames, especially in the four less visited fields, significantly influences the detection efficiency for planets with long periods or shallow transits.
There is a noticeable difference in the photometric accuracy between the 2010 data in comparison to the 2011 and 2012 data. In the first year, the camera read-out resulted in a systematic astrometric shift of bright sources (i' $\leq$ 15.5 mag) with respect to faint sources. This effect was noticed in early 2011 and fixed by adjusting the camera voltages. In order to account for the shifted bright stars, we use custom masks in our data analysis pipeline for the 2010 data.

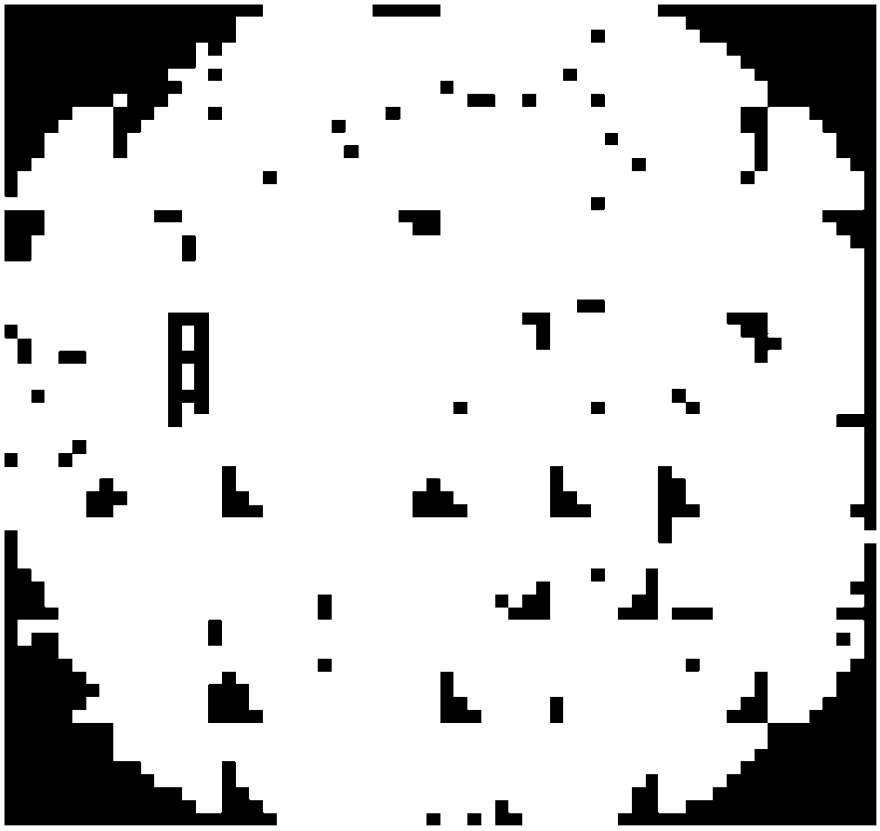

Figure 2.5: Statically masked areas in the GPC1 camera for the 2012 data. Note that the corners are not illuminated due to the circular layout of the GPC1 camera.

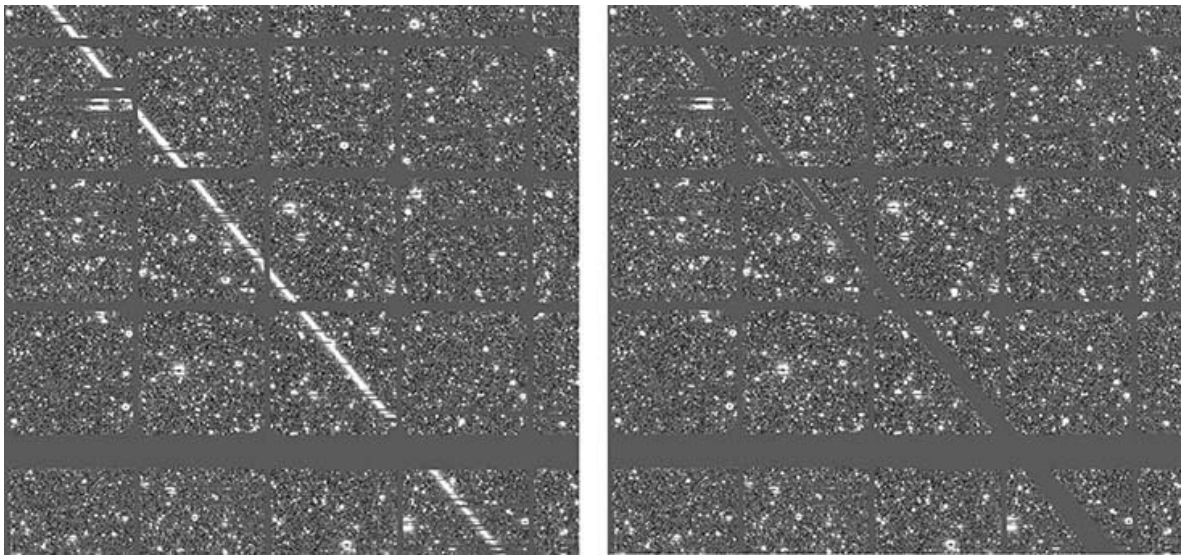

Figure 2.6: Left: Satellite trail in one of the Pan-Planets images. Right: Result after automatic masking.

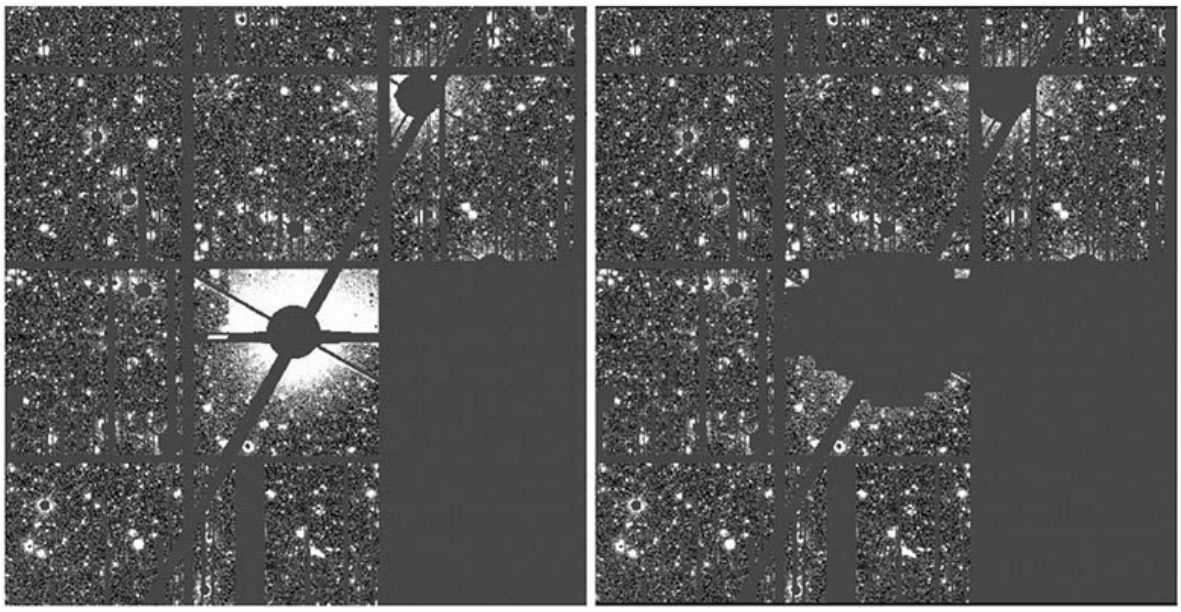

Figure 2.7: Left: Saturated area that has not been sufficiently masked. Right: Result after application of the automatic masking.

2.2.3 Light curve creation

The Pan-Planets light curves are created using the Munich Difference Imaging Analysis (MDia) pipeline (Koppenhoefer et al., 2013; Gössl and Riffeser, 2002). This Astro-WISE package makes use of the image subtraction method which was developed by Tomaney and Crotts (1996) and later by Alard and Lupton (1998). The method relies on the creation of a reference image, which is a combination of several images with the highest image quality, i.e. very good seeing and low masking. As discussed in Koppenhoefer et al. (2013), increasing the number of input images increases the S/N of the reference frame. However, each additional image broadens the PSF which means that resolution decreases. Due to the high masking in the Pan-Planets images (the average masking is ∼40% including cell gaps) we decide to use a high number of 100 input images which leads to a typical median PSF FWHM of 0.7 arcseconds in the reference frame.
The procedure to select the 100 best images is the following: after removing all frames with a masking higher than 50%, we select the 120 images with the best seeing. We determine the weight of each image on the reference frame by measuring the PSF FWHM and S/N and reject frames that possess a very low weight (less than half of the median weight) or too high weight (higher than twice the median weight), which usually results in 10 removed frames. This is necessary in order to avoid using bad images that do not contribute in S/N or images that would dominate the final reference frame and therefore add noise. Out of the remaining images we clip the frames with the broadest PSF until we have the final list for the best 100 frames. These images are subject to a visual inspection in which any leftover systematic effect is masked by hand before combining the images to create the reference frame. A contour map that shows all manual+automatic masks that were used for the 100 input frames for an

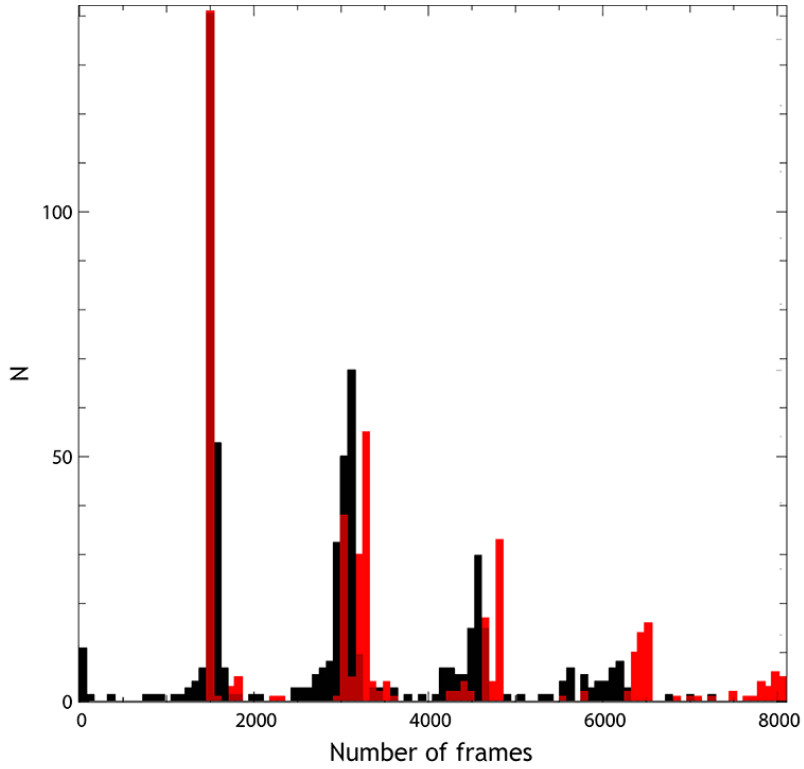

Figure 2.8: Histogram of the number of frames per skycell, of which there are 420 overall. In red we show the distribution per skycell before ingesting the images into the pipeline, in black after ingesting. One can see that the smallest overlapping region completely vanishes and only a small fraction of skycells with about 6000 frames remains.

arbitrarily selected skycell[2] is shown in Figure 2.9.

The next step is to generate the light curves for each individual source. We photometrically align each image to the reference frame and correct for background and zero-point differences. Subsequently, we convolve the reference image with a normalized kernel to match the PSF of the single image and subtract it. In the resulting difference image we perform PSF-photometry at each source position. We calculate the total fluxes by adding the flux measured in the difference images with the flux in the reference image which is measured using an iterative PSF-fitting procedure. Figure 2.10 shows a histogram of the number of datapoints for each source. One can see two broad peaks. The second peak, having more data points, is created by the additional observations for 3 fields that were taken in 2010.
Since the output light curves of MDia are at an arbitrary flux level, we calibrate them by applying a constant zero-point (ZP) correction for each skycell. For this, we use the 3π catalogue (version PV3) from Pan-STARRS1 as a reference and determine the best-fitting offset. The ZP correction for an arbitrary skycell[3] is shown in Figure 2.11.

[2]Skycell 0.24 has been picked as an arbitrarily selected skycell. To keep matters consistent, the same will also apply later on for other examples.
[3]Skycell 0.24

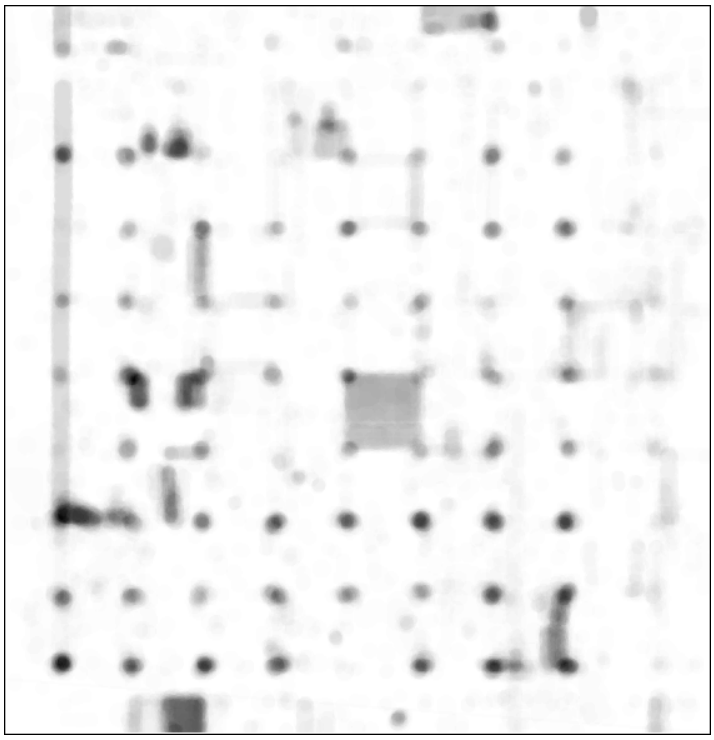

Figure 2.9: Contour map of the average manual+automatic masking applied to arbitrary skycell 0.24, skaling from 0 masks (white) to 100 masks (black). The dots correspond to the edges of the CCDs that were masked out due to flat-fielding issues.

Error bar correction

While analysing the light curves, we found that some data have a lower quality depending on the time of observing. This applies mostly to the 2009 data for which a different camera configuration and survey strategy were used. Hence, we decide to disregard the 2009 data for the further data reduction.
We perform an a-posteriori error bar correction on the light curves which is done by rescaling the error values of every light curve. On average, non-variable stars should have a ratio of 1 between the median-error value and the RMS of the light curve. We create a magnitude-dependent scaling factor for each skycell by fitting a tenth-order polynomial to the data, binned into 20 equidistant median[4] points. The distribution of the RMS/median-error ratio against the i'-band magnitude, median-binned data points and their best polynomial fit is shown in Figure 2.12 for an arbitrarily selected skycell[5].

Sysrem

To remove systematic effects that appear in many light curves, we apply the *sysrem* algorithm that was developed by Tamuz et al. (2005). The concept of *sysrem* is to analyse a large part of the data set, in our case one skycell, and identify systematic effects that affect many stars at the same time. At first it was conceptualized to remove the effects of atmospheric extinction,

[4]In order to reduce the impact of outliers.
[5]Skycell 0.24

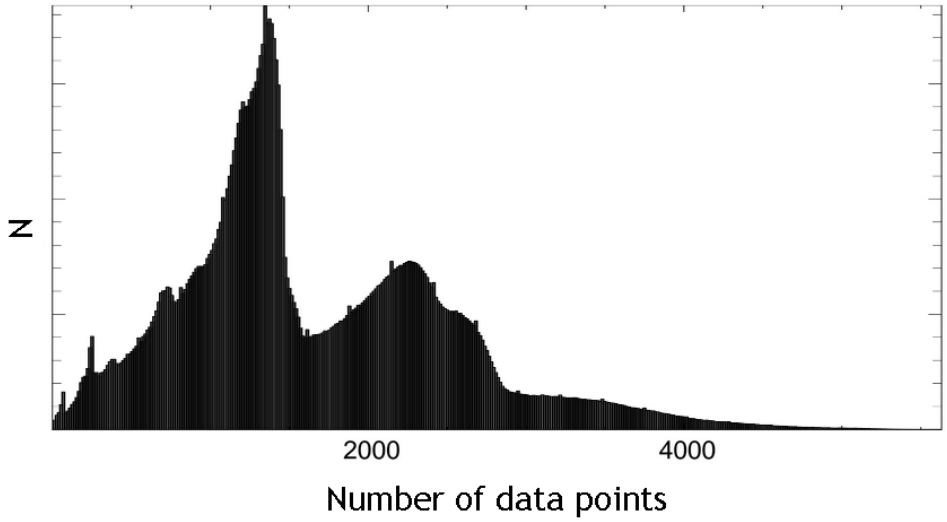

Figure 2.10: Histogram of the number of data points per source. One can see two larger peaks, being created by the additional observations for 3 fields in 2010. Overlapping regions, seeing-dependent exposure times and static masking of some detector areas broaden those peaks. The additional data from overlap further create a tail, reaching up to 5000 data points.

however, the algorithm can remove other large-scale effects as well. Let r_{ij} be the residual of the i-th star in the j-th image after subtracting its magnitude from the average with an error of σ_{ij}. Defining a_j as the airmass of the j-th image and c_i as the effective extinction coefficient of each star, one can search for the c_i that minimizes the expression:

$$S_i^2 = \sum_j \frac{(r_{ij} - c_i \cdot a_j)^2}{\sigma_{ij}^2.} \tag{2.1}$$

Assuming a known airmass, this can be solved very simply by differentiating and equating to zero, yielding:

$$c_i = \frac{\sum_j \frac{r_{ij} \cdot a_j}{\sigma_{ij}^2}}{\sum_j \frac{a_j^2}{\sigma_{ij}^2}}. \tag{2.2}$$

However, the atmospheric extinction might depend on other factors such as the weather condition as well. Therefore, one might minimize a_j instead which leads to a similar term:

$$a_j = \frac{\sum_i \frac{(r_{ij} \cdot c_i)^2}{\sigma_{ij}^2}}{\sum_i \frac{c_j^2}{\sigma_{ij}^2}} \tag{2.3}$$

Both terms are iteratively fitted, continually switching between c_i and a_j. Removing the first order effect, one can repeat this process to search for the 2nd, 3rd...nth orders. What makes *sysrem* so effective is that it does not assume any priors about the cause of the systematic effects it corrects for. Any kind of large-scale effect can be corrected, no matter what the cause. However, for *sysrem* to work properly, we have to remove stars with high intrinsic

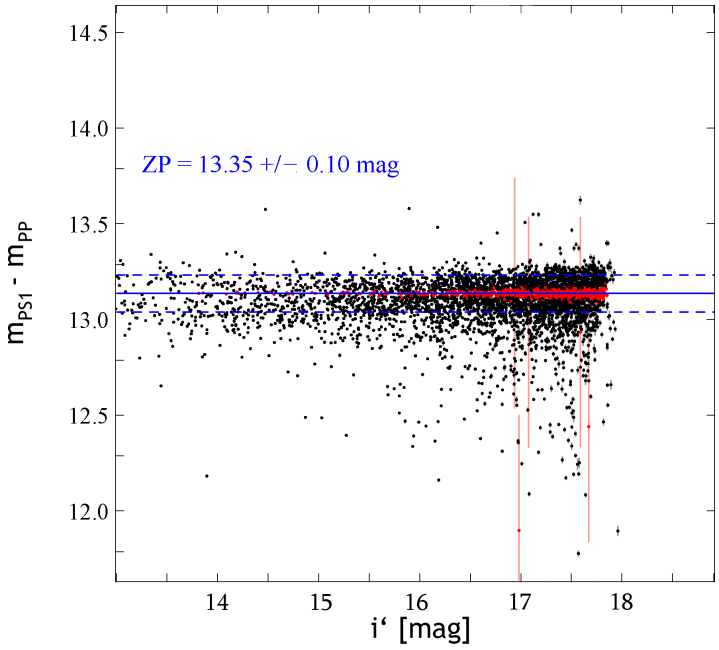

Figure 2.11: Zero-point (ZP) correction for an arbitrary skycell, cut off at the minimum target-amplitude of 18. After clipping all 3σ outliers (black), the best ZP is determined by χ^2 minimization. The ZP fit and its uncertainties are shown as a blue line and blue half-lines, respectively.

variability from the data sample beforehand. We do this by eliminating stars which have a reduced χ^2 higher than 2.5 for a constant baseline fit which subsequently also do not get corrected by *sysrem*. The distribution of the reduced χ^2 for stars in an arbitrarily selected skycell[6] is shown in Figure 2.13. On average, we include about 80% of the light curves.
Figure 2.14 shows the overall quality of the light curves and the improvement that is achieved by utilizing this algorithm, namely the RMS scatter of the Pan-Planets light curves as a function of i-band magnitude. At the bright end we achieve a precision of $\sim$5 mmag.

2.2.4 Light curve analysis

We search for periodic signals in the Pan-Planets light curves with an algorithm that is based on the box-fitting least squares (BLS) algorithm of Kovács et al. (2002). It is very effective in detecting periodical signals which can be approximated by a two level system, such as a planetary transit. It assumes a period p with a starting point t_0 and two flux levels L and H, outside and during the transit, respectively. The length of the transit in phase units is expressed by the factor q. We therefore have five parameters: p, τ, H, L and t_0.
With a dataset of n points and the fluxes x_i, i = 1,2,...,n and flux errors σ_i, we assign each

[6]Skycell 0.24

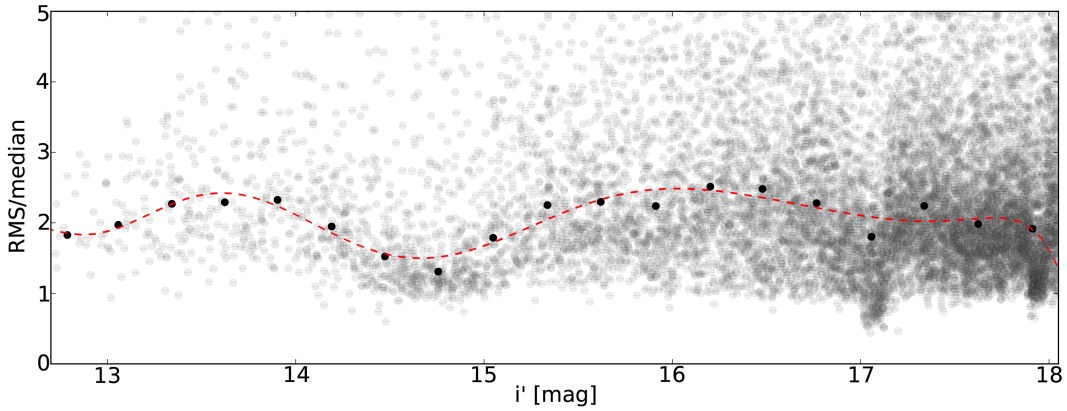

Figure 2.12: Distribution of the RMS/median-error ratio against the i'-band magnitude (grey), median-binned data points (black) and the best polynomial fit for an arbitrarily selected skycell (red half-line).

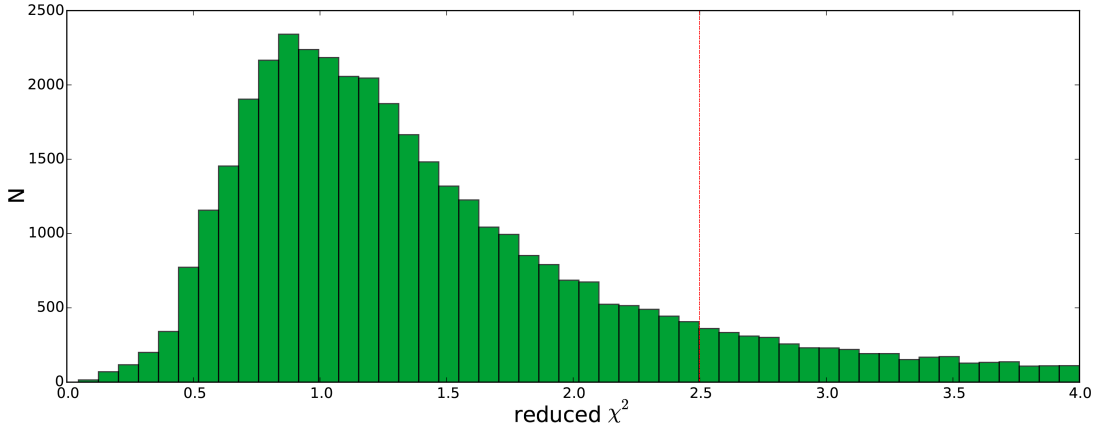

Figure 2.13: Histogram of the reduced χ^2 after a magnitude-dependent baseline fit to all light curves of an arbitrarily selected skycell (ID 0.24). The dotted red line shows the cut-off for the variable star selection.

data point a weight ω_i:

$$\omega_i = \frac{\sigma_i^{-2}}{\sum_{j=1}^{n} \sigma_j^{-2}} \tag{2.4}$$

We assume that the distribution of errors is Gaussian. One can fold the data points with a test period p, transforming the points x_i to x'_i. We get the deviation:

$$D = \sum_{i=1}^{i_1-1} \omega'_i (x'_i - H)^2 + \sum_{i=i_1}^{i_2} \omega'_i (x'_i - L)^2 + \sum_{i=i_2+1}^{n} \omega'_i (x'_i - H)^2. \tag{2.5}$$

We can simplify above equation by substituting parts with the parameters r and s:

$$s = \sum_{i=i_1}^{i_2} \omega'_i x'_i, \qquad r = \sum_{i=i_1}^{i_2} \omega'_i, \tag{2.6}$$

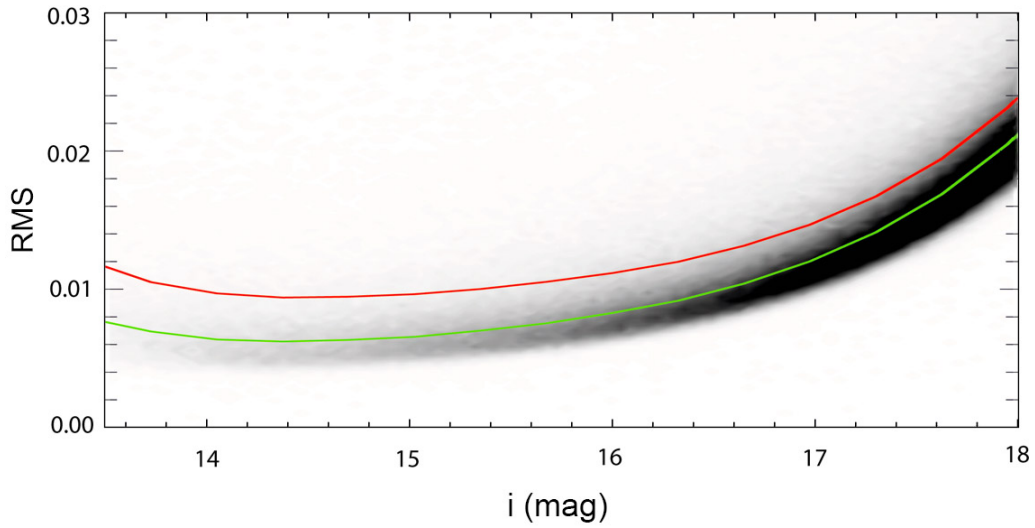

Figure 2.14: Density plot of RMS against the i-band magnitude in the central field after iterative clipping of 5σ outliers and application of the *sysrem* algorithm. The green line shows the median values in 0.2 mag bins, the red line the values before application of *sysrem*.

which we in turn use to transform L and H:

$$L = \frac{s}{r}, \qquad H = -\frac{s}{1-r}. \tag{2.7}$$

This transforms the term into:

$$D = \sum_{i=1}^{n} \omega_i' x_i^{2'} - \frac{s^2}{r(1-r)}. \tag{2.8}$$

Note that only the second term in equation 2.8 is dependent on p, L and H. We can now can characterize the quality of a fit with a given period P through the second term. We therefore we have to find the maximum for all possible pairs of (i_1, i_2). We call the maximum signal residual (SR):

$$SR = MAX \left\{ \sqrt{\frac{s^2(i_1, i_2)}{r(i_1, i_2)[1 - r(i_1, i_2)]}} \right\} \tag{2.9}$$

We extend the BLS algorithm by a trapezoid-shaped re-fitting at the detected periods, which we call transit V-shape fitting. A value of 0 corresponds to a box shape and 1 to a V. It is a better representation of the true shape of eclipse events. Further, we fit for a possible secondary transit, offset by 0.5 phase units, in order to discriminate between planets and eclipsing binaries. Eccentric orbits are not uncommon for binaries, hence the secondary might also appear at different phases. Our BLS algorithm is not optimized to detect secondary eclipses at phases other than 0.5. Eclipsing binaries of interest (see section 3.3.4) that exhibit visible eccentricity will be analysed further with an adaptation of our BLS code. More detailed information on the modifications of our BLS algorithm can be found in Zendejas et al. (2013). We test 100001 periods for each light curve that are distributed between 0.25 and 10 days and

equally spaced in 1/p. In order to speed up the fit we bin the phase folded light curve to 500 points, a number which we determined through dedicated Monte Carlo simulations (same as in Section 2.4) in which we determined the effect of binning on the detection efficiency. The transit duration is limited to 0.25 phase units. This does not constrain the planet transit duration. As an extreme case, the duration for a hot Jupiter with a 12 h period around an M5 dwarf would still be less than 0.05. For non-circular orbits, the duration can increase, however, hot Jupiters are generally on rather circular orbits[7]. The highest transit duration in our candidate sample is about 0.07. A typical plot of our signal detection output is shown in Figure 2.15.

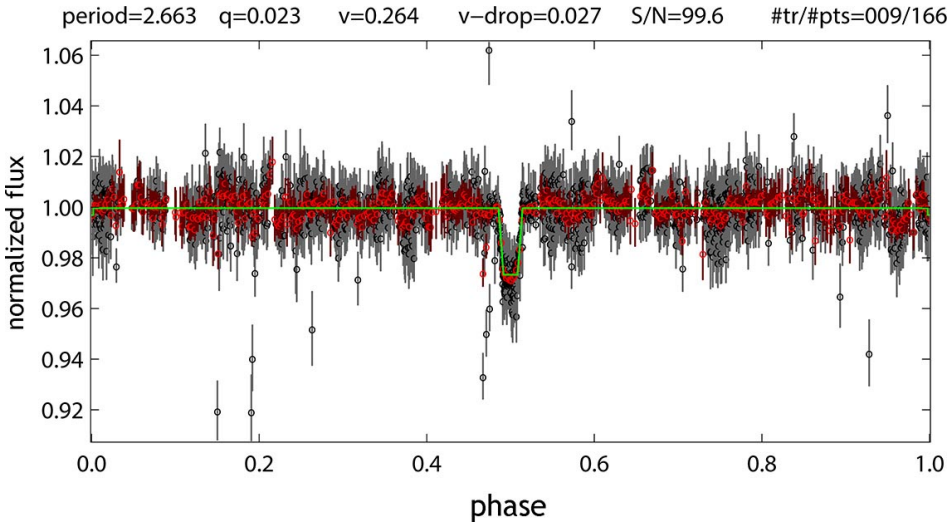

Figure 2.15: Typical plot of our signal detection algorithm for object 1.40_14711, a K dwarf being orbited by a hot Jupiter candidate. Low resolution spectroscopy confirms the stellar type determined through SED fitting (see also Section 2.3). Shown at the top are period (days), transit duration q (in units of phase), transit v shape (0 corresponds to a box, 1 to a V), transit light drop, S/N and number of transits/number of points in the transits. The binned data points are shown in red. A green line shows the best-fitting 2-level system, including the v-shape adjustment.

2.2.5 Transit recovery

Having completed the BLS run, we need to preselect the light curves with a possible signal before visual inspection due to our large sample. We retain the four best BLS detection for each light curve, i.e. those having the highest S/N. We remove results close to alias periods introduced by the window function of the observing strategy by utilizing Monte Carlo simulations (see Section 2.4). Out of the remaining detections we select the best fit, i.e. the one with the lowest χ^2 of the trapezoidal re-fit.

[7] See also section 1.6.2.

2.3 M-dwarf selection

The large number of M-dwarfs in our sample makes it infeasible to perform a spectroscopic characterization for every star. Instead, we utilize a combination of photometric and proper motion selection criteria. Strong reddening in several of our fields is problematic when using colour cuts, distant giant stars can be misclassified as M-dwarfs as well as hotter main sequence stars that appear cooler due to reddening. This kind of misclassification could lead to large uncertainties in our sample and we therefore utilize the Spectral Energy Distribution (SED) fitting method. This allows us to estimate the effective temperature of stars through fitting of synthetic SEDs to multi-band photometry and identify the best-fitting model for every star. We limit the issue of dust reddening by making use of a distance-dependent dustmap (see following Section).

2.3.1 SED fitting

A necessary assumption for SED fitting is that the model stars are physically accurate since any issue in the synthetic sample has a strong impact on the selection process. We use four synthetic stellar libraries for the fit. The first one is the Dartmouth isochrone model from Dotter et al. (2008). This database provides values for stellar mass, luminosity, surface gravity, metallicity and effective temperature. We limit the grid to solar metallicity since we encountered similar issues as Dressing and Charbonneau (2013), getting an over-abundance of high-metallicity results. Furthermore, we use the PARSEC stellar isochrones (Bressan et al., 2012) which are based on the Padova and Trieste stellar evolution code. We choose the newest version that is improved for low-mass stars (Chen et al., 2014). In order to achieve improved results at the lower mass region, we include the most recent isochrones from Baraffe et al. (2015) and the BT-Dusty models (Allard et al., 2012). Our final sample contains 25880 model stars with ages of 1-13 Gyr, masses of 0.1-40.5 $M_{\odot}$, effective temperatures of 1570-23186 K and radii of 0.13-299.61 $R_{\odot}$.
The fit becomes more precise with a higher amount of photometric information. We use the Pan-STARRS1 3π survey (version PV3) bands g', r', i', z' and the 2MASS bands J, H and K and combine those catalogues by coordinate matching. We decide not to include the PS1 y-band for our fitting process. Conversion into the PS1 photometric system is achieved by polynomial extrapolation of the z magnitude. Therefore, adding the y band would provide no useful physical information for the fit but create a bias towards the z photometry. After merging we achieve completeness for 62% of all stars while for the remaining 38% we only have PS1 photometry. Most of the missing stars are saturated in 2MASS. For stars that are listed in 2MASS, we have full photometric information in all seven bands for the majority of them (94%). We do not impose thresholds on the 2MASS quality flags. In order to stay consistent with our stellar targets, we limit the brightness range to $13.5\,\mathrm{mag} \leq \mathrm{i_{PS1}} \leq 18\,\mathrm{mag}$ for this catalogue. Our first step is to determine the best-fitting distance modulus for each isochrone and photometric band x. As shown in section 1.8.5, the distance can be determined analytically to:

$$d = \frac{\sum\limits_{x} \frac{m_x - M_x}{e_x^2}}{\sum\limits_{x} \frac{1}{e_x^2}}. \tag{2.10}$$

In case of zero extinction, this would give us the best fit for the distance. However, dust reddening is a significant factor for a large part of our fields. In order to solve this problem, we make use of the 3D dust map provided by Green et al. (2015)[8]. It gives a statistical estimate for the amount of colour excess E(B-V) for any point in our field, in distance modulus bins of 0.5 mag in the range between 4 mag and 15 mag. We therefore assign a reddening term $R(d) \cdot f_x$ for every star with a given distance modulus d, reddening coefficient f_x and photometric band x. We determine the reddening coefficients for each band through the web service NASA/IPAC Extragalactic Database (NED)[9], substituting the UKIRT J, H and K values for the 2MASS filters, using the dust estimates from Schlafly and Finkbeiner (2011).
Fitting with a step function-like dust distribution results in artefacts. A first-order linear interpolation leads to similar, albeit weaker, artefacts. We therefore smooth by fitting a 10-th order polynomial to the points. This way, the distribution is artefact-free. With the given reddening R(d) for the best-fitting distance modulus d, we iterate the fit until the converging criterion

$$d_{\text{difference}} = |d_{n+1} - d_n| \leq 10^{-4} \tag{2.11}$$

is fulfilled. This procedure is executed for each isochrone, after which we select the best fit based on the lowest χ^2 value. We interpolate missing error values in 2MASS by first fitting a magnitude-dependent polynomial to each band and then assigning the value for the given magnitude. When comparing the χ^2 values in relation to the measured distances, we find that there are usually two distinct local minima. This is explained by fitting two different stellar populations, e.g. main-sequence and giant branch. The resulting local minima sometimes show a very similar χ^2, which makes it difficult - in those cases - to distinguish between different stellar populations. In order to solve this, we include proper motion information (see following subsection) into the classification.

2.3.2 Proper motion selection

Proper motion, in short PM, quantifies the angular movement of a star over the course of time from the observer's point of view. This is strongly correlated with the distance: the closer a star is to the observer, the higher (on average) is the angular motion. Therefore we can be confident that if a star exhibits a high proper motion, the fit for the close distance is the most plausible one.
For this we utilize a combination of the USNO-B digitization of photometric plates (Monet et al., 2003), 2MASS (Skrutskie et al., 2006), the WISE All-Sky Survey (Wright et al., 2010) and the 3π Pan-STARRS1 survey[10] as described in Deacon et al. (2015). After calculating the annual proper motion, we assign each star a quality flag depending on the properties shown in table 2.2. We select every cool star with quality flag 1, even if the best fit is slightly in favour of a distant red giant, and cool stars with the best fit for a dwarf type with quality flags 2, 4 and 5.
We further use the criterion $J - K > 1$ as a flag to discriminate likely background giants from closer dwarf stars. This has proven to be very effective in the Kepler project (Mann et al., 2012).

[8] available at http://argonaut.rc.fas.harvard.edu/
[9] https://ned.ipac.caltech.edu/
[10] http://ipp.ifa.hawaii.edu/

Quality flag	PM value	Error
1	PM $\geq 6\ mas/yr$	$PM_{error}/PM \geq 0.5$
2	PM $\geq 6\ mas/yr$	$PM_{error}/PM < 0.5$
3	PM $< 6\ mas/yr$	$PM_{error}/PM \geq 0.5$
4	PM $< 6\ mas/yr$	$PM_{error}/PM < 0.5$
5	No coordinate match.	

Table 2.2: Quality flags for different proper motion PM (mas/yr). Stars having flag 3 do not pass our criteria, having no measurable proper motion.

2.3.3 Consistency check with the Besançon model

We compare our results to the Besançon model (Robin et al., 2003) which provides a synthetic stellar population catalogue for any given point of the sky. We simulate our entire FOV in 1 sq. deg. bins. We use this to estimate the distribution of spectral types in our target brightness. Choosing the criteria of an effective temperature $< 3900\,\mathrm{K}$ and surface gravity > 4, we identify 62800 M-dwarfs in the Besançon model. We select M-dwarfs in our survey with the following criteria:

- SED fitting Temperature $< 3900\,\mathrm{K}$
- Quality flag of 1 OR
  2, 4, 5 and a best fit for a nearby dwarf star

With those criteria, we select 65258 M-dwarfs in our FOV, about 12000 M-dwarf per field since there are multiple identifications in the overlapping regions. This is fairly consistent to the number of M-dwarfs in the Besançon model but our result is slightly higher. It is possible that there are false positive identifications in the selection list, reddened by dust from the galactic disc. This most likely affects identifications without proper motion data, i.e. flags 2, 4 and 5. However, the difference between our selection and the model distribution is not very large, so the amount of contamination is low.
Figure 2.16 displays our implemented M-dwarf selection and how it compares to the Besançon model. The effective temperatures are fairly consistent, assuming an uncertainty of $\pm 100\,\mathrm{K}$ for SED fitting. The distribution of distances does not seem to fit so well as the temperatures, however, we are mainly focused on fitting the effective temperature.
Figure 2.17 shows the distribution of distances for all fitted stars in comparison to the Besançon model. It seems to be very consistent in closer ranges, both distributions having their peak around 3 kpc, but there are small divergences in the occurrence of distant ($\geq 3\,\mathrm{kpc}$) stars. We are focused on nearby main-sequence stars so this is not much of a concern. In the same Figure one can see the distribution of fitted extinction E(B-V) which peaks around an E(B-V) value of 0.4.
In Figure 2.18 on the left is shown the relation between distance and reddening E(B-V) for all fitted stars while the right side of Figure 2.18 shows the average reddening in relation to the coordinates. As a comparison, we overplot the linear extinction models of 0.7 mag/kpc as used in the Besançon model (red) and 1 mag/kpc as used in (Dressing and Charbonneau, 2013) (blue). There is a noticeable difference for distances below 3 kpc to our fitting. The outliers with an E(B-V) of more than 1.0 are due to the dust-rich region close to the galactic disc, shown in Figure 2.18 on the right (top-right corner).

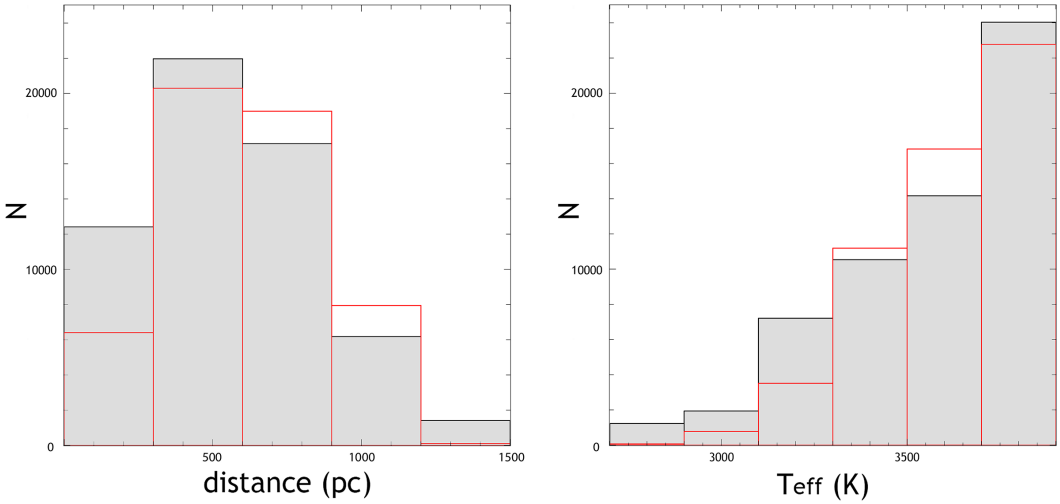

Figure 2.16: Left: distribution of distances for selected M-dwarfs from SED fitting (gray with black bar lines) and the Besançon model (red bar lines). Right: distribution of effective temperatures for selected M-dwarfs from SED fitting (gray with black bar lines) with the expected distribution from the Besançon model (red bar lines).

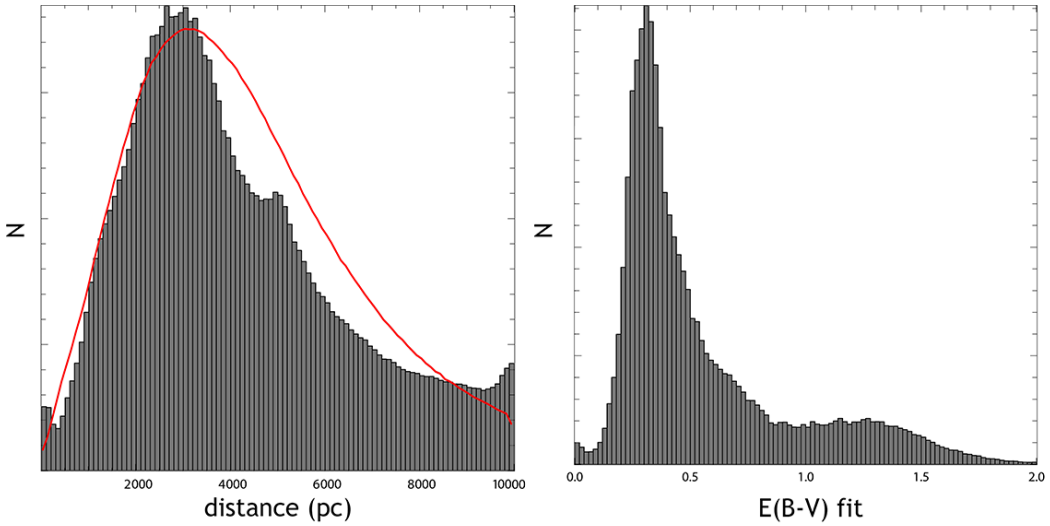

Figure 2.17: Left: distribution of distances for all fitted stellar types, with the Besançon model as a comparison (red line). Right: distribution of fitted extinction in our field.

2.3.4 Consistency check with Kepler targets

As another consistency check, we take the SED fitting results used for 31 Kepler candidate M-dwarf host stars (Dressing and Charbonneau, 2013), identify the stars in the Pan-STARRS 3π catalogue and perform SED fitting. In order to make the process more comparable, we limit our isochrones to less than solar masses, temperatures lower than 7000 K and run the comparison with their model of extinction fitting, i.e. 1 mag in the V-band per kpc.
As one can see in Figure 2.19, the results are fairly consistent but at the same time there is a systematic offset of about -25 K. A likely explanation is that the fitting results from Dressing

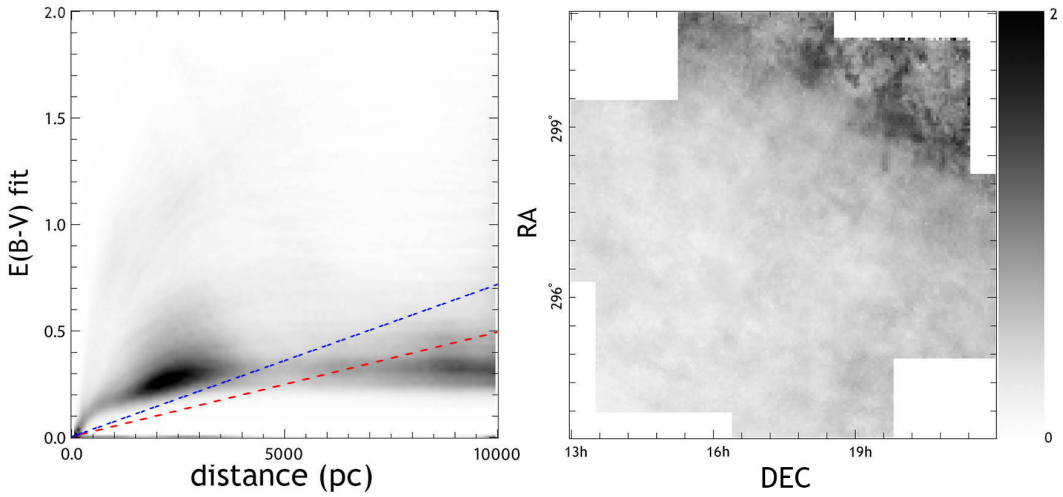

Figure 2.18: Left: fitted reddening E(B-V) against distance for all fitted stars. As a comparison, linear extinctions of 0.7 mag/kpc (red) and 1 mag/kpc in the V-band as used in the Besançon model and in Dressing and Charbonneau (2013), respectively, are overplotted as dashed lines. Right: average fitted E(B-V) in relation to the coordinates (J2000). One can see the dust-rich region in the upper right which is closer to the galactic disc.

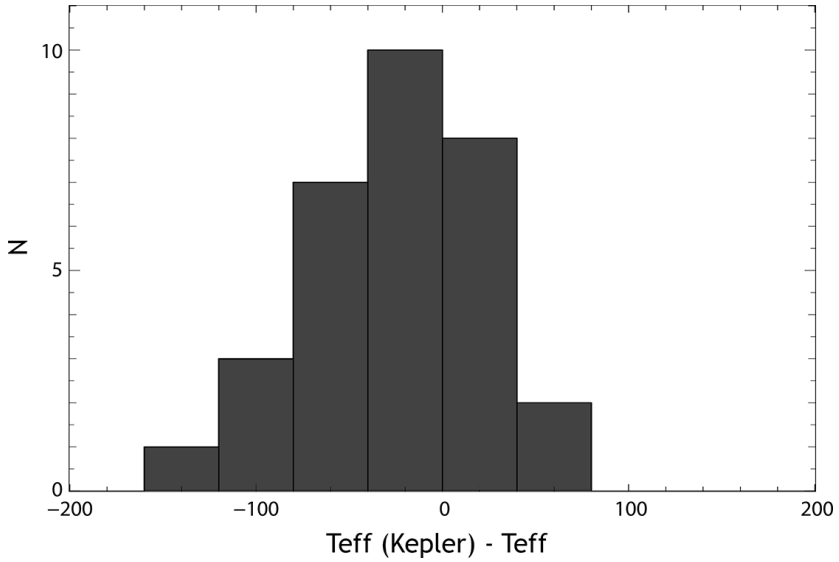

Figure 2.19: Difference of the calculated effective temperature between our SED fitting results and those of Dressing and Charbonneau (2013).

and Charbonneau (2013) are for slightly older and therefore cooler stars. Additionally, the inclusion of non-solar metallicities might also explain or contribute to the shift. However, the difference is not very large. We estimate to have an uncertainty of about $\pm 100\,K$ which is larger than the observed difference.

2.3.5 Consistency check with spectroscopically confirmed M-dwarfs

As the final consistency check, we arbitrarily select 1000 confirmed M-dwarfs out of the Sloan Digital Sky Survey Data Release 7 Spectroscopic M Dwarf Catalog (SDSS DR7) (West et al., 2011) that

- exist in the PS1 3π catalogue
- exist in the 2MASS catalogue
- have distance-dependent extinction data from Green et al. (2015)
- have data in all 7 bands
- fit our target brightness range ($13.5 \leq$ i' ≤ 18).

This way we can make sure that the comparison is as close as possible as we use our regular stellar characterization pipeline. We find that all of the listed M-dwarf candidates are being identified as M-dwarfs. Unfortunately, the effective temperatures of the SDSS DR7 catalogue are given in 200 K bins, meaning that there is an inherent error of $\pm$100 K when comparing their estimates to ours. However, as is shown in Figure 2.20, there is very good agreement in the characterized temperatures between both methods.

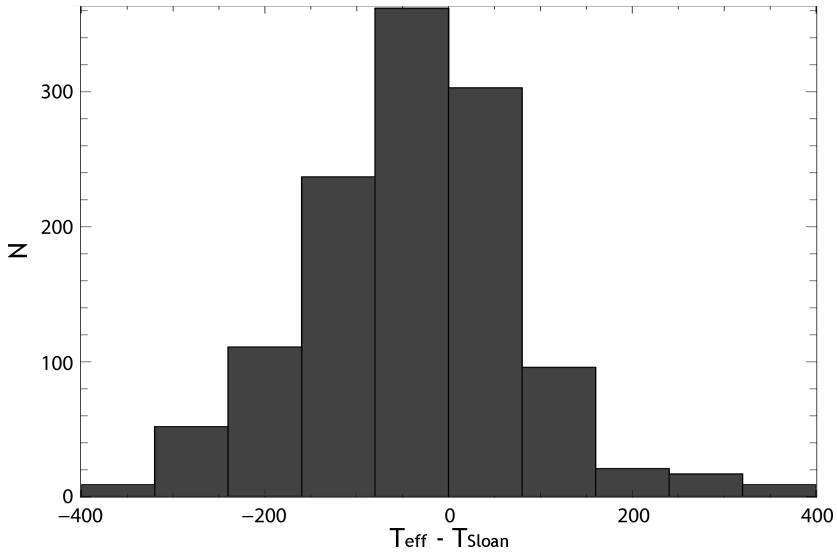

Figure 2.20: Difference in fitted temperature between SED fitting and spectral fitting of the Sloan catalogue. Note that the temperature estimates from Sloan are in 200 K bins, hence a scatter of $\pm$200 K is to be expected.

2.4 Transit injection simulations

The primary purpose of Pan-Planets is the detection of transiting hot Jupiters while setting new boundaries for the occurrence rate of close-up Jovian planets around M-dwarfs. In order to do that, we need to determine the detection efficiency of this project. We perform extensive

Monte Carlo simulations, inject planetary transit signals into the Pan-Planets light curves and attempt to recover the signal. This is similar to other recent approaches performed on Kepler data, e.g. in Petigura et al. (2013a,b), Christiansen et al. (2015) or Dressing and Charbonneau (2015). However, we utilize our full signal detection pipeline instead of inferring successful detections from calculating the number of visible transits combined with noise and signal to noise estimates. Our approach is much more suited to the peculiarities of Pan-Planets as the varying amount of data points, strong constraints for observational window functions and not well-defined systematics mean that this is the only reliable way of estimating our detection efficiency.

2.4.1 Setup

We start by selecting all previously identified M-dwarf light curves minus the identified planetary candidates and create a simulated distribution of different stellar parameters for our FOV, utilizing the Besançon model (Robin et al., 2003). Each model star is assigned a set of real light curves, based on brightness. The whole process is illustrated in Figure 2.21.

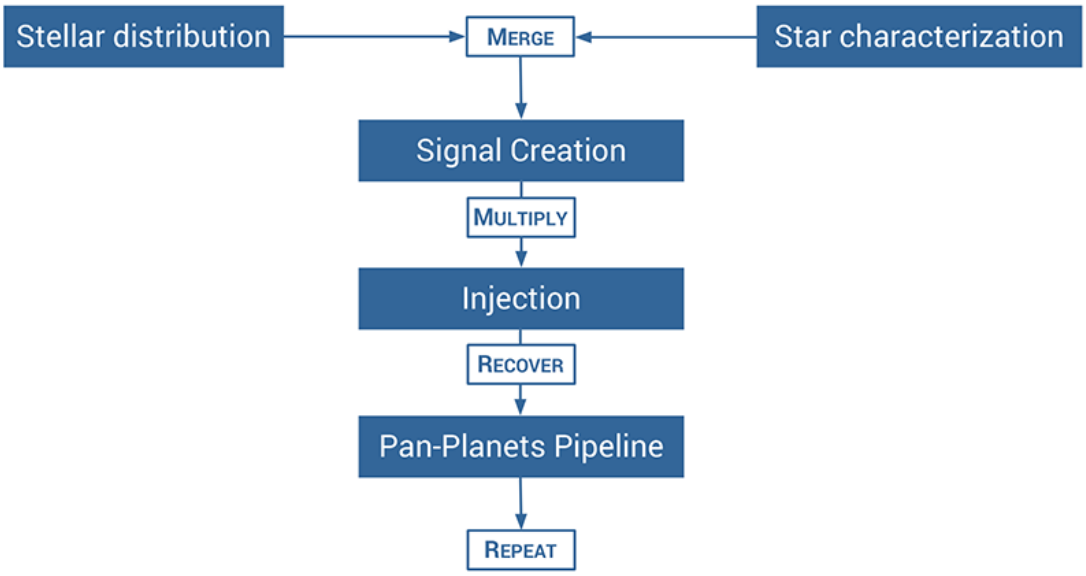

Figure 2.21: Illustration of our simulation process. We take the model stellar distribution and assign each of our characterized star to the closest-fitting model. We create a planetary signal out of the given stellar and planetary parameters, multiply it with the light curve and try to recover the injected transit with our Pan-Planets pipeline.

In the next step, we create our target planet population by setting up random distributions of period and radius in defined boundaries. In accordance with Hartman et al. (2009), Koppenhoefer et al. (2009), and Zendejas et al. (2013), we use five different populations: Jovian planets with radii 1.0-1.2 R_J and periods of 1-3 days, 3-5 days and 5-10 days plus Saturn-sized and Neptune-sized populations with periods of 1-3 days and radii of 0.6-0.8 R_J and 0.3-0.4 R_J, respectively.
We then take every star in the stellar distribution, randomly pick one of the corresponding light curves and select an arbitrary planet out of the chosen population. We assign a random

geometrical inclination of the planetary orbit to each star and calculate the criterion

$$sin(i) < \frac{R_{star} + R_{planet}}{a}, \tag{2.12}$$

where i is the inclination and a the distance to the star. For simplicity, we assume a circular orbit. If this criterion is met, we create a transit signal based on all given parameters, i.e. planetary and stellar radii, inclination, period, t_0 and corresponding limb darkening coefficients (Claret and Bloemen, 2011) for the stellar type. We multiply the simulated signal with the real light data and end up with simulated light curve that possesses all the characteristics of our survey, e.g. noise, systematics, distribution and amount of data points. Further information about the transit injection method used can be found in Koppenhoefer et al. (2009).

2.4.2 Transit recovery

As the next step we attempt to recover the simulated signals with our transit detection pipeline. We again select the 4 best periods with highest S/N for every source and remove results close to alias periods introduced by the window function of the observing strategy (see table 2.3). Most alias cuts are not directly around harmonics of 1 day but instead slightly

Excluded alias periods
0.315-0.335 days
0.498-0.500 days
0.991-1.004 days
1.586-1.594 days
1.594-1.600 days
1.965-1.975 days
2.039-2.045 days
2.359-2.360 days
3.370-3.378 days
4.022-4.030 days
4.078-4.088 days

Table 2.3: List of excluded alias periods that are common for false detections. We identified those periods as peaks in the abs(p_{sim}-p_{det})/p_{sim} histogram.

lower periods due the observation characteristic of seasonal change and large time gaps. Figure 2.22 shows the cut that we used for the alias period of 1 day. Out of the remaining folded light curves we keep the one with the best χ^2 fit. In order to examine whether we could successfully recover the signal, we compare the detected period p_{det} to the simulated period p_{sim}. This is the most reliable way of judging whether the detection was successful or not and has been utilized by other surveys as well (Kovács et al., 2013; Zendejas et al., 2013). The low number of data points in some light curves makes the false detection of an harmonic of the period not unlikely. We accept a period deviation of 0.02%, as shown in Figure 2.23, and harmonics of p_{sim} with orders of 0.5, 2 and 3 and following period deviations:

$$\frac{p_{sim}}{p_{det}} = 0.5 \pm 0.0001. \tag{2.13}$$

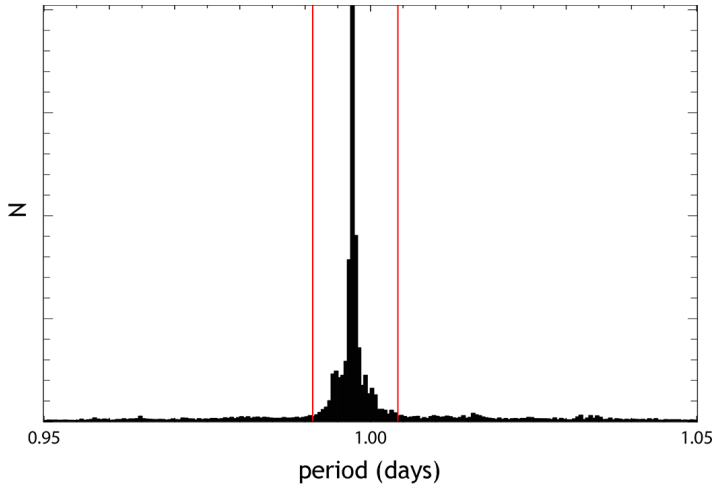

Figure 2.22: Alias period around 1 day for an arbitrary number of hot Jupiter simulation runs, comprising the whole simulated period range of 1 to 10 days. The red lines mark the excluded period range from table 2.3. Due to window functions of the survey, the peak is not directly at period 1.0 days, but slightly shifted to the left.

$$\frac{p_{sim}}{p_{det}} = 2 \pm 0.0001, \tag{2.14}$$

$$\frac{p_{sim}}{p_{det}} = 3 \pm 0.00015, \tag{2.15}$$

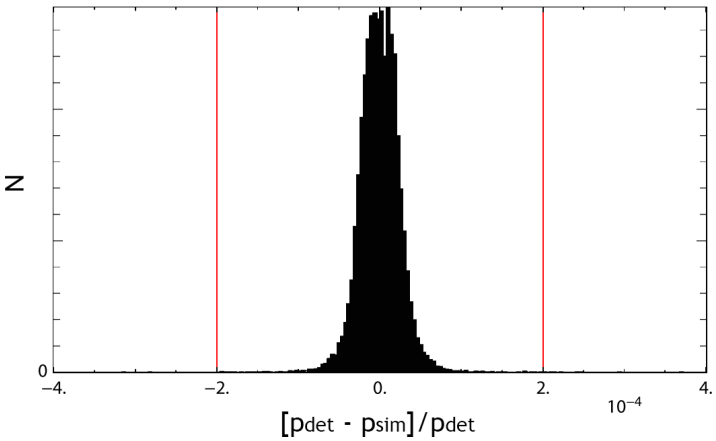

Figure 2.23: Deviation of the detected period p_{det} from the simulated period p_{sim} for an arbitrary number of hot Jupiter simulation runs, comprising of the whole field of view with periods between 1 and 3 days. For a successful detection, we require the detected period to deviate by a factor of less than 0.0002 from the simulated one (red lines).

A density plot of simulated against detected period is shown in Figure 2.24. One can see

the secondary period peaks as diagonal streaks. However, any other harmonic periods are overshadowed by random detections. We disregard those other harmonics (e.g. 0.33 or 4) in order to keep the contamination by false-positive identifications low.

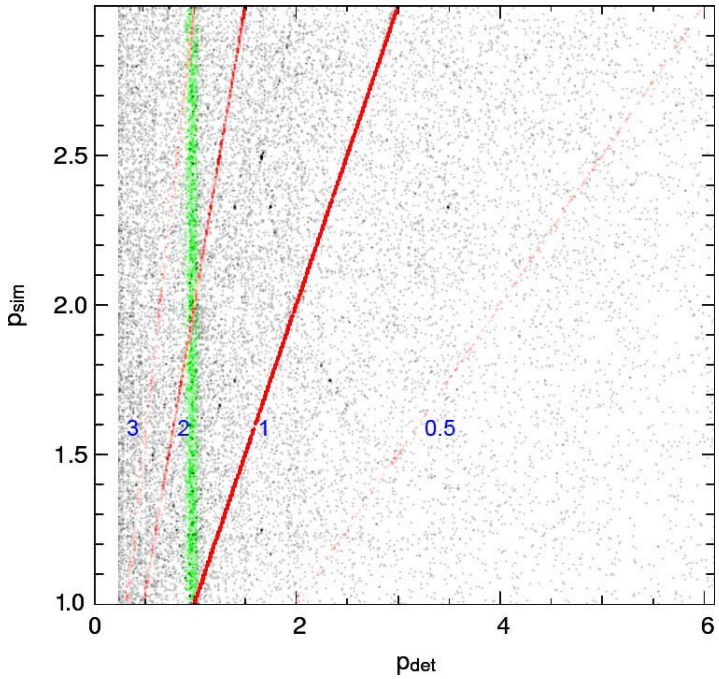

Figure 2.24: Density plot of simulated period p_{sim} against detected period p_{det} for Jovian planets with periods between 1-3 days after application of our alias removal. Marked in red are the lines for correct period identification and corresponding aliases (blue number) or half, double and triple the simulated period. Further marked in green is a period area with a high amount of false detection contaminations, removed period regions (see Table 2.3) are marked as horizontal grey lines.

Marked in the same Figure is a region around 1 day that shows an increased number of detections but is outside of our clipping limits, marked in green. While we remove the large peak around 1.00 days, shown in Figure 2.22, we cannot completely remove the area between about 0.9 to 1.1 days since that would result in too many actual transits being clipped out.
With a sample of more than 4 million light curves overall and more than 60000 M-dwarfs, it is necessary to eliminate a large amount of light curves before visual inspection. Many surveys use a S/N criterion for preselection, however, this can be improved upon.
We take a set of simulated light curves, correct periods already selected, and set up the unmodified set of light curves as the training sample. Before starting the simulation, we remove our planetary candidates from the list of simulation targets. We take the reasonable assumption that even if there is a remaining undiscovered planetary signal in the sample, the effect will be negligible since the set consists of more than 60000 light curves.
We optimize the selection criteria that we then use on the real data. Using the same approach as Zendejas et al. (2013), we set up a grid of over 100000 possible combinations of parameters, including S/N, transit depth, transit V shape and transit duration. We settle on the criteria that are shown in table 2.4. Besides S/N, additional criteria have shown to be very effective in reducing the number of false detections: the number of points in the transit - to rule out

random noise detections - and criteria for transit duration and depth - to filter out obvious eclipsing binaries.
As a last step we account for the visual selection bias. A signal that has been detected with the correct period and passed all of the selection criteria could still be disregarded in our visual inspection in case of only a partially visible transit. Figure 2.25 shows such a detection that was disregarded in the last step. We implement a visual bias filter that eliminates folded

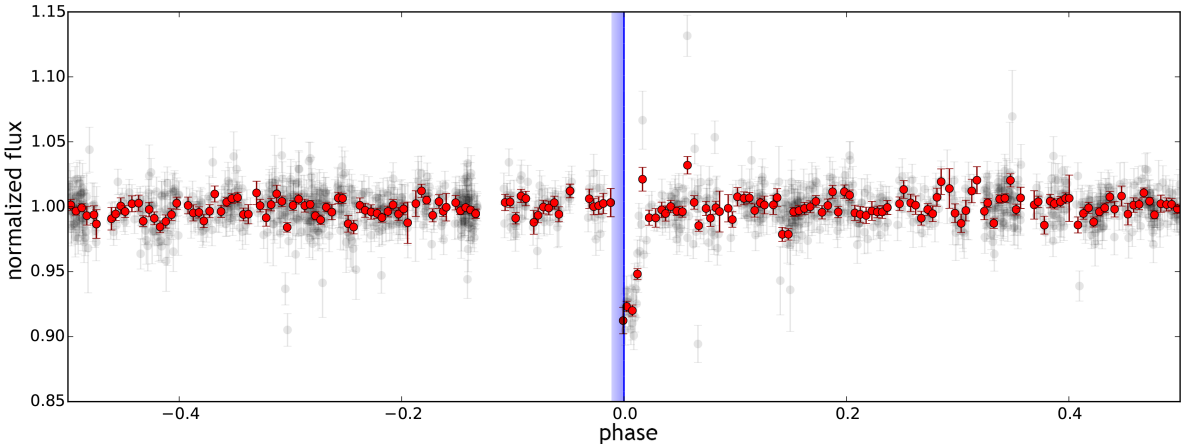

Figure 2.25: Folded light curve of a simulated VHJ that was disregarded by the visual bias filter. The data (light grey) are binned into 200 points (red). Since the ingress phase of the transit (marked blue) is missing, it would be difficult to establish whether the actual eclipse could be deeper or if the period is accurate enough for follow-up.

transit light curves that show gaps during the eclipse, something which would lead us to dismiss the candidate in the real sample. In order to optimize this algorithm, we preselect an arbitrary set of 200 planet-injected light curves with periods of 1-10 days. We mark those that we would accept and those we would rule out and then recreate those results with our automatic filter. This visual bias filter removes about 8% of the remaining light curves.
We optimize this process for a number of 60 remaining light curves per field while recovering as many simulated objects as possible. The results are shown in table 2.4. This number is the best compromise based on our simulations since decreasing it will impact our detection efficiency while increasing it will lead to additional detections.

2.5 Discussion

2.5.1 Detection Efficiency

For each planet population, we repeat 100 simulation runs per M-dwarf and 40 runs per FGK star. This adds up to 50 million individual runs per planet population for M-dwarfs and 245 million runs for the FGK star population. We end up with a recovery ratio for the individual planetary populations shown in Table 2.5. One can see that the detection efficiency is increasing strongly for lower periods and larger radii. A histogram of the detection efficiency against the period for M-dwarfs can be seen in Figure 2.26 on the top panel.
One has to keep in mind that the recovery efficiencies shown in table 2.5 include possible cases of barely observable transits - even the slightest overlaps between planet and star are being

Criterion	Remaining	Removed	Change
Input	65258	-	-
Alias clipping	57054	8204	-12.6%
S/N $\geq$ 12	5490	51564	-90.4%
Transit points $\geq$ 15	5072	418	-7.61%
Transit duration $\leq$ 0.1	599	4473	-88.2%
Transit depth $\leq$ 0.15	553	46	-7.76%
Transit V shape $\leq$ 0.7	535	18	-3.10%
Secondary S/N $\leq$ 10	419	116	-21.8%

Table 2.4: List of selection criteria and their impact on the M-dwarf light curve signal detection. S/N and transit duration served as criteria with the highest impact, the former for eliminating false detections from random noise patterns, the latter for separation from binaries.

M-dwarf	Simulated	Recovered	Efficiency
VHJ	772870	45.6%	40.6%
HJ	471484	17.5%	14.5%
WJ	198983	7.3%	5.45%
VHS	772044	19.8%	18.5%
VHN	767916	10.3%	9.68%
K, G, F dwarf			
VHJ	2476929	9.32%	8.72%

Table 2.5: Detection efficiencies for different planet populations. For M-dwarfs, we use all 65258 targets minus the planet candidates, for KGF dwarfs we use 460910 targets, excluding the planet candidates. The percentage of recovered planets is calculated by normalizing the number of correct detections by the number of possible detections (see Eq. 2.12). The efficiency is determined after selection criteria, alias clipping and visual bias filter have been applied to the results from the BLS analysis. For smaller stellar radii, larger planetary radii and shorter periods, the efficiency is higher.

simulated where the transit would take place within only a few seconds. There further are simulated light curves that are not observable due to data gaps or badly timed transits that constantly fall outside of our observing windows. Even with perfectly accurate photometry it would therefore be impossible to reach 100% detection efficiency. The detection efficiency in relation to the stellar radius is shown in the bottom panel of Figure 2.26. It is clear that the stellar radius has a significant impact on the detection rate as the efficiency strongly decreases after 0.5 $R_{\odot}$. Since the efficiency reaches a plateau before that, we assume that this is the maximum achievable detection efficiency with Pan-Planets. The other transit signals may be lost in observation gaps or in strong stellar variability which masks the signal and cannot be properly distinguished due to an insufficient number of data points. For K, F and G dwarfs combined, we expect to detect $3.0^{+3.3}_{-1.6}$ transiting VHJs, assuming an occurrence rate of $0.1408 \cdot (1^{+1.1}_{-0.54})$% based on the OGLE-III transit search (Gould et al., 2006).

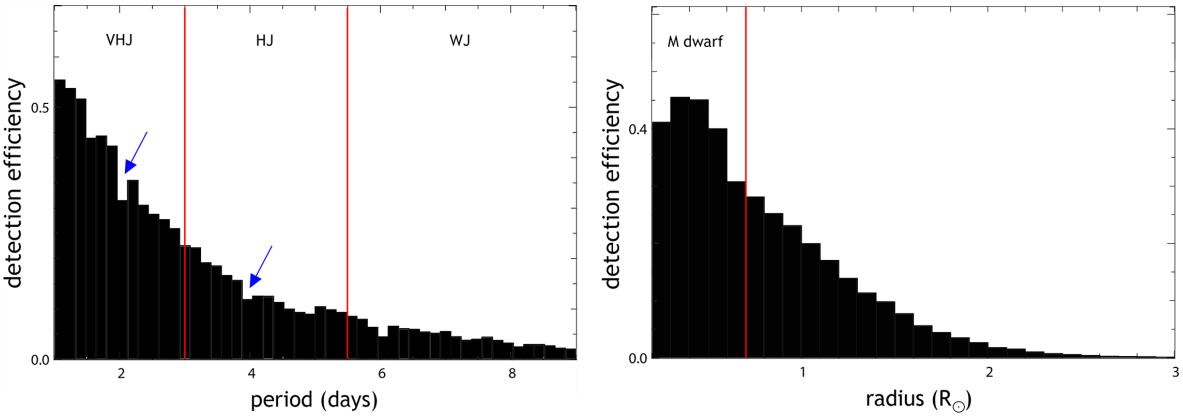

Figure 2.26: Left: Detected period against detection efficiency for all hot Jupiter populations around M-dwarfs (divided by red lines). One can see two gaps at 1.6 and 4.0 days, resulting from our alias detection removal (blue arrows). Right: Histogram of stellar radius against detection efficiency. We combined the results from the M-dwarf VHJ simulation and the VHJ simulations for hotter dwarf stars (divided by red line).

2.6 Conclusion

In the years 2010-2012, the Pan-Planets survey observed seven overlapping fields in the Galactic disk for about 165 hours. The main scientific goal of the project is to find transiting planets around M dwarfs, however, with more than 4 million sources brighter than i'=18 in the 42 sq. deg. survey area the data are a valuable source for a diversity of scientific research.
We established an efficient procedure to determine the stellar parameters $T_{\rm eff}$ and $\log g$ of all sources using a method based on SED fitting, utilizing a three-dimensional dust map and proper motion information. In this way we were able to identify more than 65 000 M-dwarfs which is by far the biggest sample of low-mass stars observed in a transit survey up to now.
Using a optimized difference imaging data processing pipeline we reached a photometric precision of 5 mmag at the bright end at around $i_{P1} = 15$ mag. This makes Pan-Planets sensitive to short period hot Jupiters and hot Neptunes around M-dwarfs and short period hot Jupiters around hotter stellar types.
To search for planetary transits we used a modified BLS algorithm. We applied several selection criteria which have been optimized using Monte Carlo simulations in order to reduce the number of visually inspected light curve from several million down to a about 60 per field. We detected several planet candidates around M-dwarfs and hotter stars which are currently being followed up. In addition, we found many interesting low-mass eclipsing binaries and eclipsing white dwarf systems which we will study in detail in the current observing season.

Chapter 3

Follow-up and candidates

Astronomy compels the soul to look upwards and leads us from this world to another.

Plato (undated)

Note: Parts of this chapter were used for the publication "Pan-Planets - Searching for Hot Jupiters around Cool Stars" (Obermeier et al., 2016).

Abstract

In this chapter, we detail the follow-up that was performed for the identified planet candidates in several categories. We describe the observation layout and data reduction for the Wendelstein Wide Field Imager and the Otto Struve telescope ES2 spectrograph with which we performed transit follow-up and spectroscopic characterization, respectively. Based on the results from our Monte Carlo simulations, we expect to find $3.0^{+3.3}_{-1.6}$ hot Jupiters around F, G, and K-dwarfs with periods lower than 10 days based on the planet occurrence rates derived in previous surveys. For M-dwarfs, the percentage of stars with a hot Jupiter is under debate. Theoretical models expect a lower occurrence rate than for larger main sequence stars. However, radial velocity surveys find upper limits of about 1% due to their small sample, while the Kepler survey finds a occurrence rate that we estimate to be at least $0.17(^{+0.67}_{-0.04})\%$, making it even higher than the determined fraction from OGLE-III for F, G and K stellar types, $0.14(^{+0.15}_{-0.076})\%$. With the large sample size of Pan-Planets, we are able to determine an occurrence rate of $0.11(^{+0.37}_{-0.02})\%$ in case one of our candidates turns out to be a real detection. If, however, none of our candidates turn out to be true planets, we are able to put an upper limit of 0.34% with a 95% confidence on the hot Jupiter occurrence rate of M-dwarfs. This limit is a significant improvement over previous estimates where the lowest limit published so far is 1.1% found in the WFCAM Transit Survey. Therefore we cannot yet confirm the theoretical prediction of a lower occurrence rate for cool stars.

3.1 Introduction

Having completed the data reduction and light curve analysis, we identified the candidates in four target categories. Although the primary objective is the detection of hot Jupiters around M-dwarfs, the large sample size allows for additional secondary objectives:

M-dwarf hot Jupiters: The presumed rarity of those planets, the small samples from previous surveys and deep transit signals make them the main target of Pan-Planets (see also Chapter 2). Based on Monte Carlo simulations (see Section 2.4), our survey is sensitive enough to detect the majority of hot Jupiters. The drawback of this category is the - on average - faint magnitude of the targets, which complicates the follow-up. We draw our conclusions about the occurrence rate of M-dwarf hot Jupiters at the end of this chapter.

Bright K/G/F-dwarf hot Jupiters: Monte Carlo simulations show that the sensitivity of Pan-Planets is good enough to detect hot Jupiters around main-sequence stars up to stellar type F. While a large number of hot Jupiters have already been discovered, only a few orbit late K-dwarfs. Furthermore, a radius anomaly accompanies about half of those close-up gas giants which is not yet fully understood (Spiegel and Burrows, 2013; Lopez and Fortney, 2016). Increasing the sample, especially for cool stars, may be advantageous for the solution of this issue.

M-dwarf eclipsing binaries: While M-dwarfs are the most abundant stars and the fraction of binary M-dwarfs is rather high at $0.11^{+0.02}_{-0.04}$ (Shan et al., 2015), only very few (~ 20, Kraus et al., 2011; Nefs et al., 2013) systems are characterized well. Measuring the fundamental parameters of eclipsing binaries (period, eclipse shape, radial velocities) enables the determination of both star's radii and masses. While studying the effective temperatures and radii of short-period binary systems, an anomaly for both was detected, having overestimated temperatures by 10% and underestimated the radii between 5%-10% (Kraus et al., 2011) compared to theoretical models like the Dartmouth isochrones (Dotter et al., 2008). This indicates that these models cannot yet fully reproduce the physics of late M-dwarfs. We have collected a larger number of presumed M-dwarf binary systems and are in the process of following them up spectroscopically. Having access to a larger sample may provide valuable information to calibrate the mass-radius and mass-temperature relations.

Variable systems: Due to the large number of light curves ($\approx 4 \cdot 10^9$), it is likely that extremely rare or uncommon variable systems may be detected. We have created a list of interest, including ID's of all sources with entries in SIMBAD[1] and stars which we identified as white dwarfs, using colour-cuts from Girven et al. (2011) that we converted to the PS1 photometric system.

[1] http://simbad.u-strasbg.fr/simbad/

3.2 Target selection

3.2.1 Pan-Planets data

For a more detailed review of the Pan-Planets data, see Section 2.2.2. In brief, we processed our data with the difference imaging method and collected up to 5000 points per star. We cleaned up the data with the *sysrem* algorithm and an algorithm which removes outliers, bad nights and data points from overlapping regions if they are divergent in their zeropoint. We further trained this algorithm by using the simulated transits from our Monte Carlo simulations (see Section 2.4) to maximize the efficiency.
We used our trapezoidal box fitting algorithm to identify the best planet candidates in our data and utilized the simulated data for the optimization of the selection criteria in order to retain about 60 light curves per field for visual inspection. Having completed that, we selected 22 candidates overall in both categories for further study.
These targets are the basis for the Wendelstein photometric follow-up, providing period and transit shape estimates, and the basis for spectroscopic follow-up with the McDonald observatory by providing a list of targets.

3.2.2 Wendelstein photometric follow-up

Overview

The Wendelstein observatory is located in the Bavarian Alps at 1838 m above sea level. It is equipped with the 2 m Fraunhofer Telescope Wendelstein (FTW, Hopp et al., 2014), the largest science-grade optical telescope in Germany. Due to constraints from the location, it was built in an Alt-Azimuth mount and fitted into a compact 8.5 m dome. The FTW is shown in Figure 3.1.
The first instrument that got installed for scientific use is the Wendelstein Wide Field Imager (WWFI, Kosyra et al., 2014), a 64 MP camera, mapped onto a FOV of 0.5 $\deg^2$ and split into a grid of 2 x 2 CCDs which are further divided into 2 x 2 cells with a resolution of 4 MP each. The pixel scale of 0.2 arcsec/px is similar to the one of Pan-STARRS1's GPC (0.258 arcsec/px). The WWFI is robotically operated and a number of different filters can be inserted, most importantly *u'g'r'i'z'y'*.
The Wendelstein observatory allows the flexible follow-up of our targets. Having quick access to observing time makes the FTW an excellent telescope for the study of transit events.

Preparation and observations

We followed up our targets over the course of 2015 from April until the end of September. During that time, the Pan-Planets fields were visible long enough to allow the observation of a full transit and the photometric baseline. Using our program *catchtransit*, we predicted the transit timings of the targets and added up to 1 h before and after the transit, depending on airmass and time of the night. Having a long baseline before and after the transit allows for accurate normalization of the light curve. We created a priority list, based on the information from SED fitting and the preliminary results from our planet parameter fitting (see section 3.2.4).
Our goal was to first follow up every high-priority planet candidate, i.e. candidates with a clean light curve and a good model for the transit, to confirm that the signal is a true

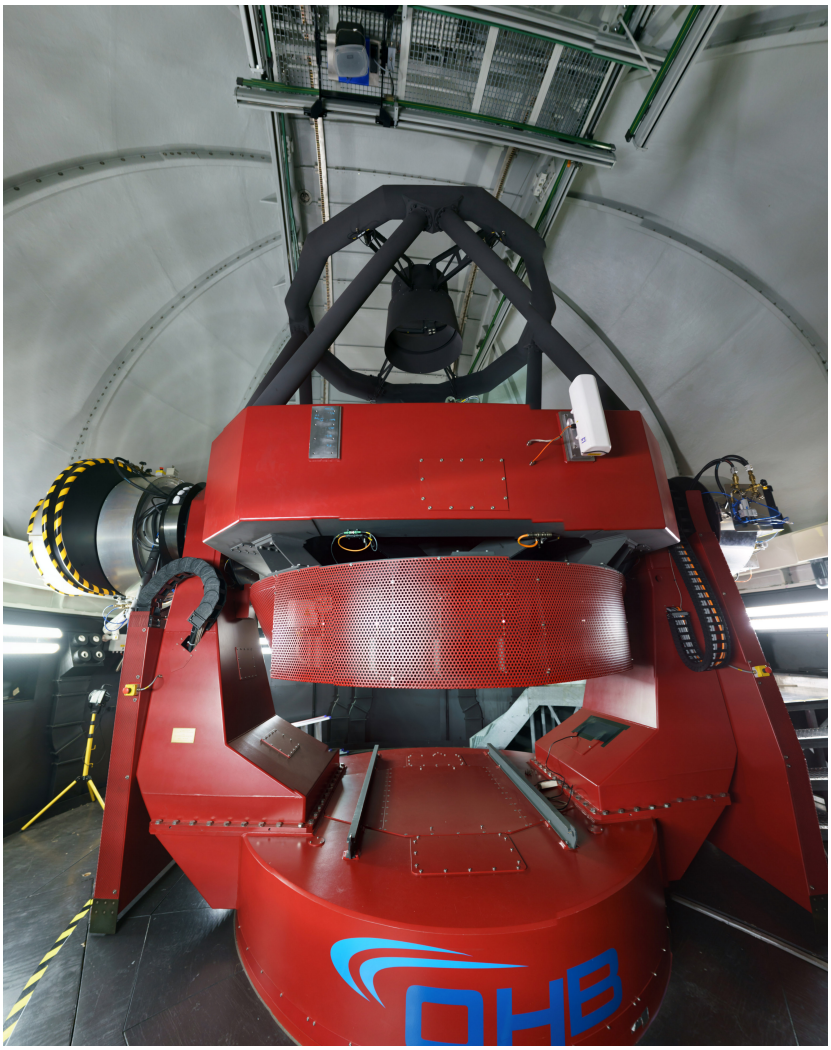

Figure 3.1: The FTW during the setup phase in the twilight.

detection and that the period was determined correctly. For this, even bad nights with large seeing and cloud coverage could be sufficient. We chose the i'-band which is very similar to the Pan-Planets band. This way, the same limb darkening coefficients can be used for fitting and the data can be merged easily. Furthermore, observing during moonlight is less of an issue than in the visible bands. We placed the target in the upper left cell of the q4 (bottom right) quadrant, which has the best photometric performance.
After each target in the high-priority list had been observed at least once, we changed the observing tactic. We re-observed the high-priority targets if the weather conditions were good enough to allow to improve the planet-parameter fitting, based on the new transit data. Bad nights were filled up with targets from the low-priority list.
We calculated the exposure times such that the target stars produce a maximum of about 20000 counts in order to avoid nonlinearity effects (Kosyra et al., 2014). This translates to an exposure time of 20 sec for the brightest targets while in case of fainter targets, we balanced this with the issue of not saturating too many stars in the FOV. Hence, we limited the maximum exposure time to 90 seconds for our fainter targets.

Data reduction

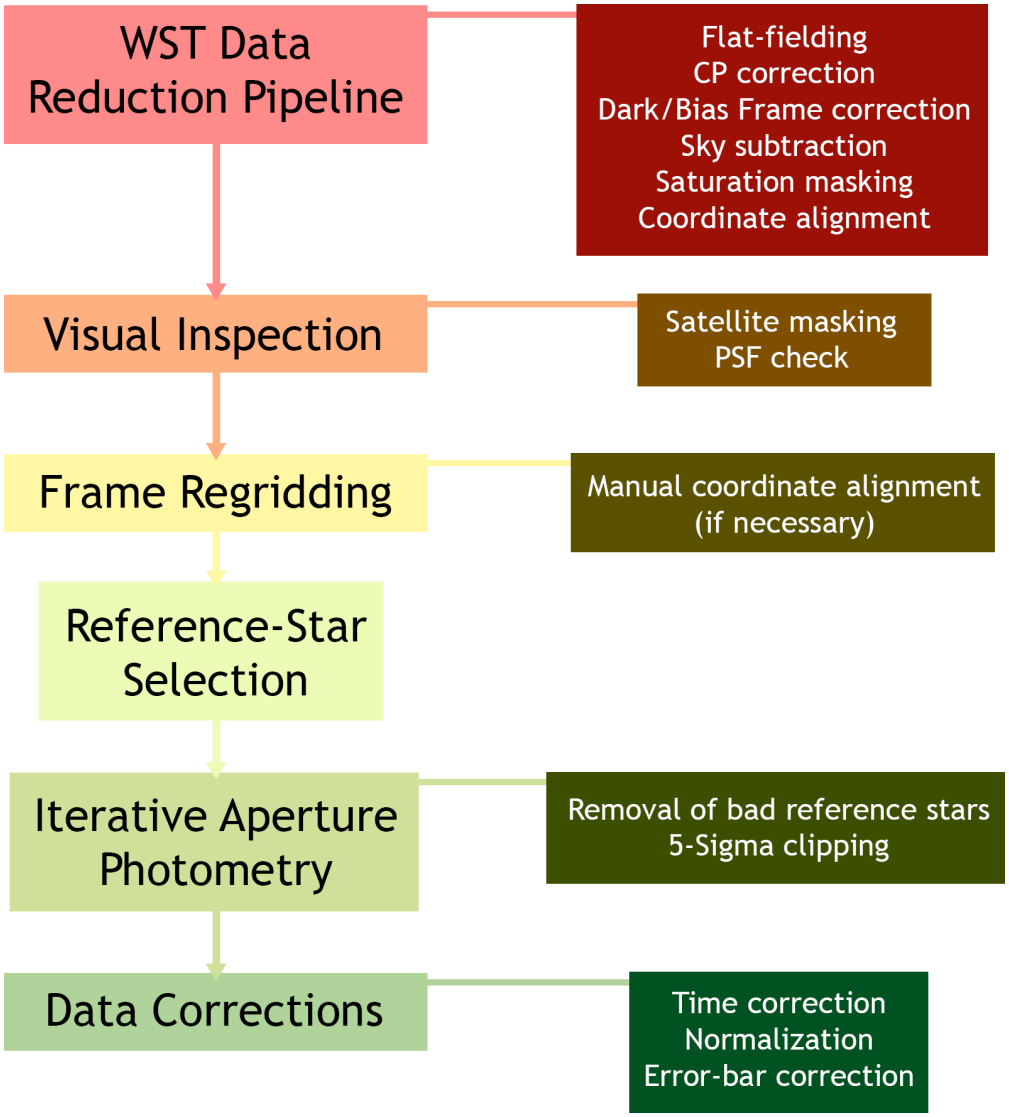

Figure 3.2: Schematics of the complete Wendelstein transit follow-up pipeline.

After completing the observations, we processed the downloaded files with the custom Wendelstein data reduction pipeline. It performs automatic flat fielding, saturation masking, sky subtraction, charge persistence correction, dark/bias processing and coordinate alignment. We visually inspected every frame and masked out satellite traces if necessary. In this step, we further removed frames that exhibited a critical issue like a too large PSF or non-functioning tracking. Depending on whether the automatic coordinate alignment was successful or not, we regridded the frames automatically or manually. We selected about 60 reference stars which were defined by being bright, isolated and radially distributed around the target star. This was necessary to ensure that the effect of variability in sky brightness, for example through passing-by cirrus clouds, was minimized. We performed aperture photometry and optimized the accuracy for each individual night and candidate. For this, we

measured the RMS of the out-of-transit baseline and iterated this process until the optimal parameters were found. Reference stars with high variability got eliminated and we further clipped high-RMS reference stars until we ended up with a number of about 15.
As the final step, we applied a time-correction based on the target's stellar coordinates and Earth's position in the solar system, normalized the transit by fitting a second-order polynomial through the baseline before and after the transit and finally corrected the error bars based on the scatter of the baseline. The whole process is illustrated in Figure 3.2. We normalized the Pan-Planets light curve and the Wendelstein light curve against each other, after which we combined the data. One such transit that was recorded with the WWFI is

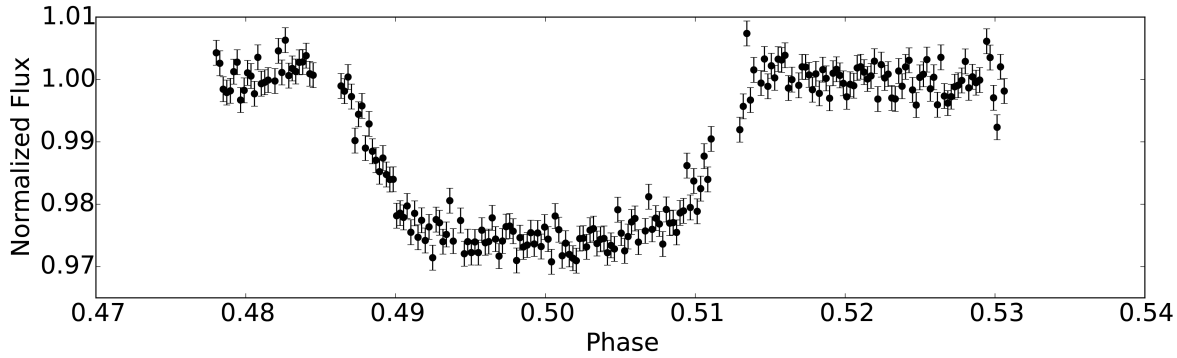

Figure 3.3: Transit of planetary candidate PP140-14711, recorded with the wide field imager on the 2 m FTW. We observed in the i'-band with exposure times of 30 s. The phase is already corrected for the measured period offset of 3.3 s.

shown in Figure 3.3. We measured a deviation of 38 minutes from the predicted transit time which equates to a period error of about 3.3 s.
Altogether, we observed 38 transits, 26 of which covered at least half of the transit. The other 12 had to be aborted due to technical problems or cloud cover. In this summary, we disregarded observing runs that contain less than 5 frames. The number of cancelled observations is relatively high but this is not surprising since the observations were often carried out as a backup during bad weather. Overall, 22 planet candidates were observed. 4 targets did not show a transit, either due to a too large period uncertainty or due to a false detection. A complete list of candidates and observations is given in Table 3.1.

3.2.3 McDonald spectroscopic follow-up

Overview

The McDonald observatory is located on Mount Locke in the Davis Mountains of West Texas at an altitude of 2070 m and is operated by the University of Texas in Austin. It has a long history of scientific discoveries, stretching back to 1939 when the - then - second-largest optical telescope[2], the Otto Struve telescope, was constructed. While nowadays the observatory is better known for its 2.7 m Harlan J Smith telescope[3] and the 9.2 m Hobby-Eberly Telescope (HET) (Ramsey et al., 1998), the Otto Struve telescope is still in active use and has been retrofitted with modern CCD cameras and a new spectrograph (Ries and Riddle, 2014). For

[2]https://mcdonaldobservatory.org/research/telescopes/Struve
[3]https://mcdonaldobservatory.org/research/telescopes/HJSmith

the purpose of planet-candidate follow-up, low-resolution spectroscopy can be used to measure the stellar parameters by absorption line fitting accurately enough to determine the stellar type.

Observations and data reduction

We observed our targets with the ES2 spectrograph. Its resolution is low- to medium-resolution (R=600-2500)[4] and can be equipped with 2 CCD detectors, CC1 and TI1, which are optimized for the red and the blue part of the spectrum, respectively. Since our candidates are quite faint, we chose the lower-resolution gratings with about 600 grooves/mm each, leading to a resolution of 1300. We split the observation in at least three blocks to minimize contamination from cosmic rays. For the fainter candidates, we selected observing times of 1800 s while for brighter targets we chose 900 s.
We split the observations into two groups, depending on the stellar types. For M and late K[5] dwarfs, we chose the CC1 detector and observed a spectral range of 580 nm - 720 nm while FG-dwarfs were observed with TI1 in a spectral range of 420 nm - 560 nm. We calibrated the spectra's wavelengths with Neon and Argon lamps for the red and blue spectra, respectively. Dark, bias and flat images were taken during the afternoon and after observations.
The observations took place between UT July 14-24 2015. Most targets could be isolated and followed up properly while a few (see Table 3.1) were not possible to follow up due to too faint magnitudes or crowding. Overall, we recorded spectra for 13 planet-candidate targets.
Our method of processing the data is shown in Figure 3.4. We reduced the spectra with a custom pipeline, based on a python wrapper which utilizes other processing tools. As a first step, bias and dark frames get subtracted and flat-fielding is applied. We prepared the data by rotating the frames and removing cosmic ray signals. Depending on the selected detector, we calibrated the frames with the Neon- or Argon-lamp spectra in order to assign each pixel a corresponding wavelength. We extracted this information and merged the multiple spectra we recorded for each star. After normalizing the continuum of the spectra and clipping outliers, we averaged the data in each wavelength bin. Since the data for each candidate were taken consecutively in a single night each, we do not need to adjust the spectra for radial velocity shifts between each other. Figure 3.5 shows the five individual spectra and the combined spectrum for planet candidate PP140-14711. We perform absorption line fitting on the final spectra. A normalized spectrum is needed for this and we create 20 bin points, spaced evenly over the wavelength of the spectrum. We determine the median flux of each bin and iteratively clip outliers. Then, we fit cubic splines through these points and use the result to normalize the complete spectrum by dividing each data point with the value of the spline function. Depending on the detector, we pursue a different strategy:

- For the FGK-star targets with the TI1 detector, we fit the H_β and Mgb[6] lines in the wavelength ranges of 480 nm - 500 nm and 500 nm -540 nm, respectively. We disregard the H_γ line due to low S/N.
- For M-dwarfs and the CC1 detector, we fit NaD, TiO, H_α and CaH_2 lines. For this, we extract wavelength segments of 5860 Å - 5940 Å, 6060 Å - 6170 Å, 6510 Å - 6590 Å and 6810 Å - 6890 Å, respectively (Mann et al., 2012). Furthermore, we include the

[4] http://www.as.utexas.edu/mcdonald/facilities/2.1m/es2.html
[5] E.g. candidate PP140-14711.
[6] Corresponding to the b_1, b_2, and b_4 lines in the Fraunhofer designation.

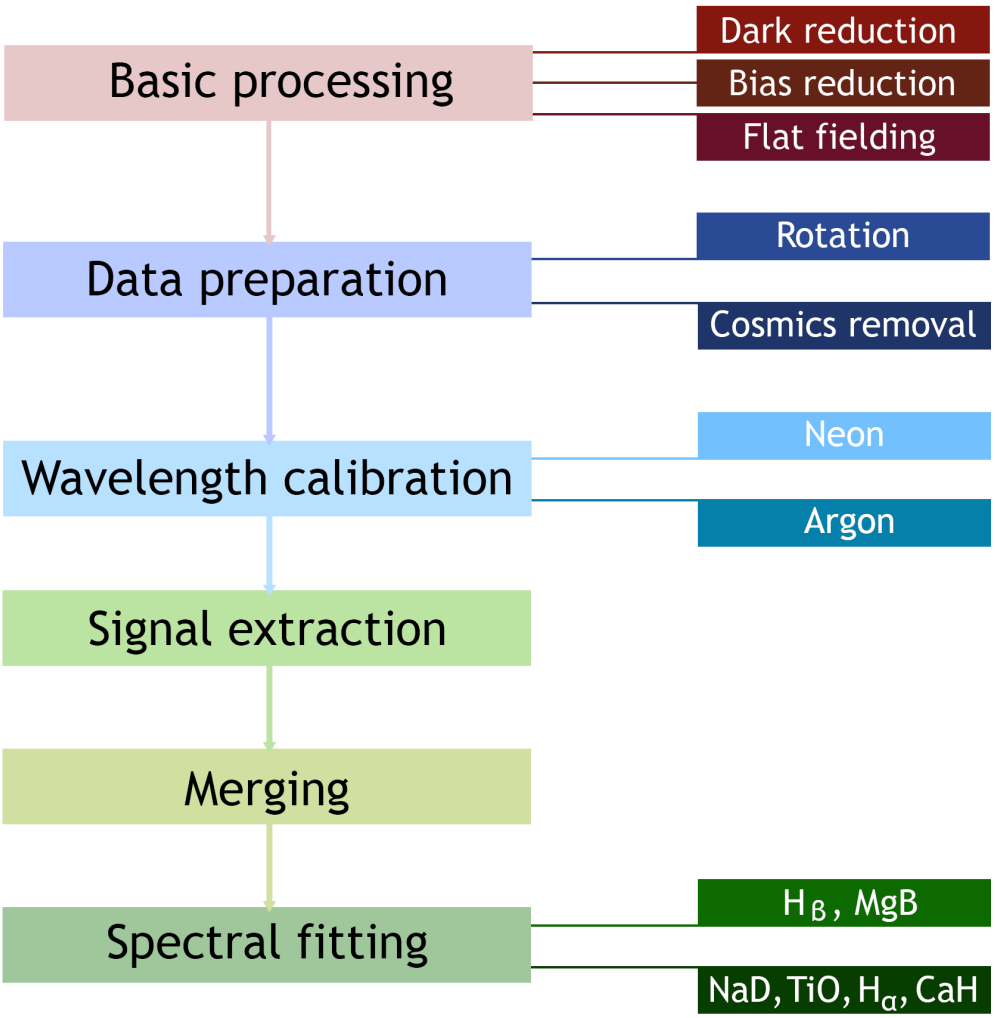

Figure 3.4: Illustration of the low-resolution spectroscopy data reduction pipeline for the Otto Struve ES2 instrument.

gravity-sensitive region of 6470-6530 Å which is dominated by the Ba II, Fe I, Mn I, and Ti I lines (Torres-Dodgen and Weaver, 1993).

We determine the best fit by χ^2 minimization of the deviation between the extracted spectra and synthetic absorption line models. We use the SYNSPEC IDL interface[7] (Hubeny and Lanz, 1995) to create a set of models with different effective temperatures and surface gravities. Our final grid contains models with effective temperatures $T_{\rm eff}$ ranging from 3000 K - 8250 K and surface gravities log(g) ranging from 1.5 - 5.0 in steps of 250 K and 0.5, respectively. We limit the models to solar metallicity due to the low resolution and S/N of the spectra.
Since the synthetic spectra have a significantly higher resolution, we convolve them with the

[7] http://nova.astro.umd.edu/Synspec49/synspec.html

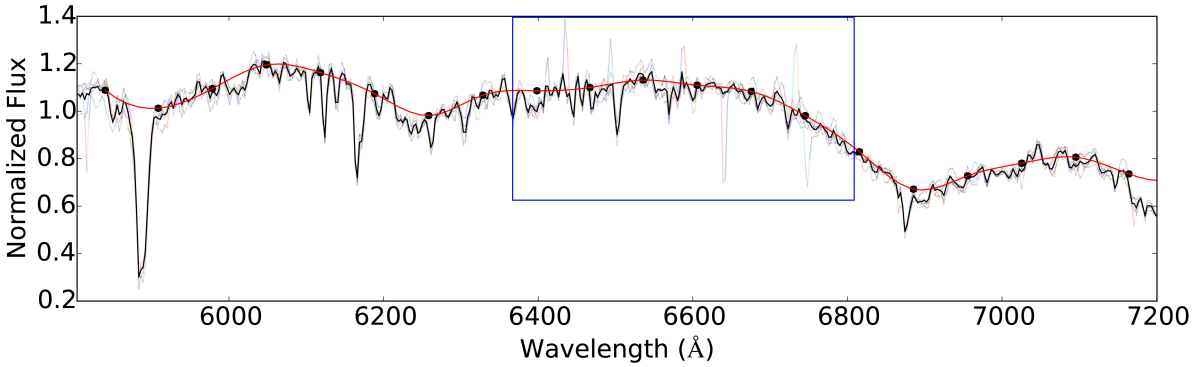

Figure 3.5: Combined spectral lines (black) of planet candidate PP140-14711 and the five individual spectra (light coloured lines). The red line shows the cubic spline fit for the continuum normalization. The cutout in Figure 3.6 is indicated by the blue box.

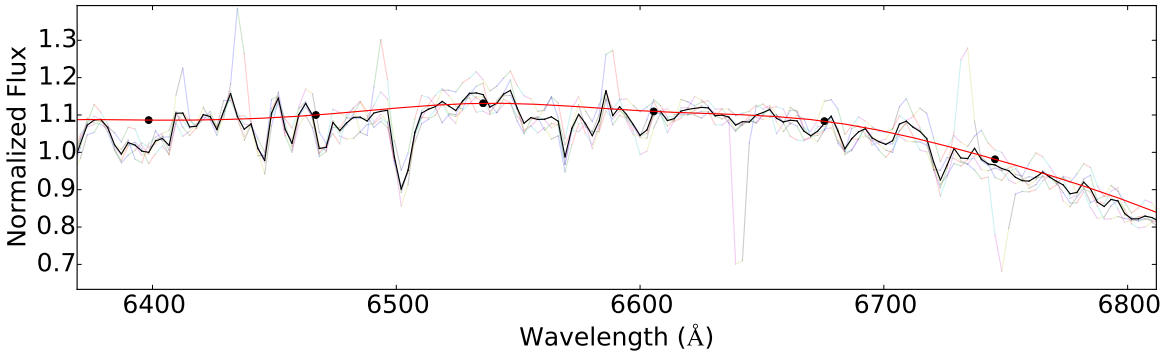

Figure 3.6: Cutout from Figure 3.5, showing the merge of the five individual spectra (light coloured lines) and the H_α-region (656.28 nm) in more detail. The absorption feature at 650 nm is likely a superimposition of six narrow O II lines (based on the absorption line list from http://www.pa.uky.edu/ peter/atomic/).

determined Full Width Half Maximum (FWHM) of the ES2 spectra, 0.6 nm. We allow minor[8] multiplicative shifts in the relative flux to correct for a possible imperfect normalization and simultaneously fit the spectral shift due to the systemic radial velocity. This also serves as a consistency check: the line shifts should be homogeneous across the individual spectral lines, otherwise we flag the fitted line as invalid. An example for an individually shifted and fitted line can be seen in Figure 3.7. After all lines are fitted, we average the best fits for effective temperature and log(g) for each fitted segment and reject outliers if the spectral shift indicates an error in the fitting process.

[8]E.g. between 0.95 and 1.05.

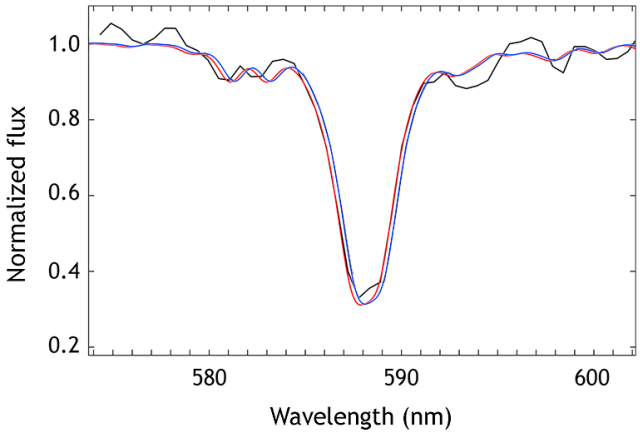

Figure 3.7: Best spectral fit (red) of the Na I line of the spectrum taken with the Otto Struve telescope ES2 spectrograph (black) for planetary candidate PP140-14711. The synthetic spectrum was convolved to the instrument's FWHM and the original line (blue) was shifted by 110kms^{-}1 and its flux was adjusted to the measured spectrum.

3.2.4 SED fitting

In addition to spectroscopic characterization, we determine the candidate systems' stellar type with SED fitting. As described in Section 2.3.1, we simultaneously and iteratively fit the distance and distance-dependent extinction until both converge.

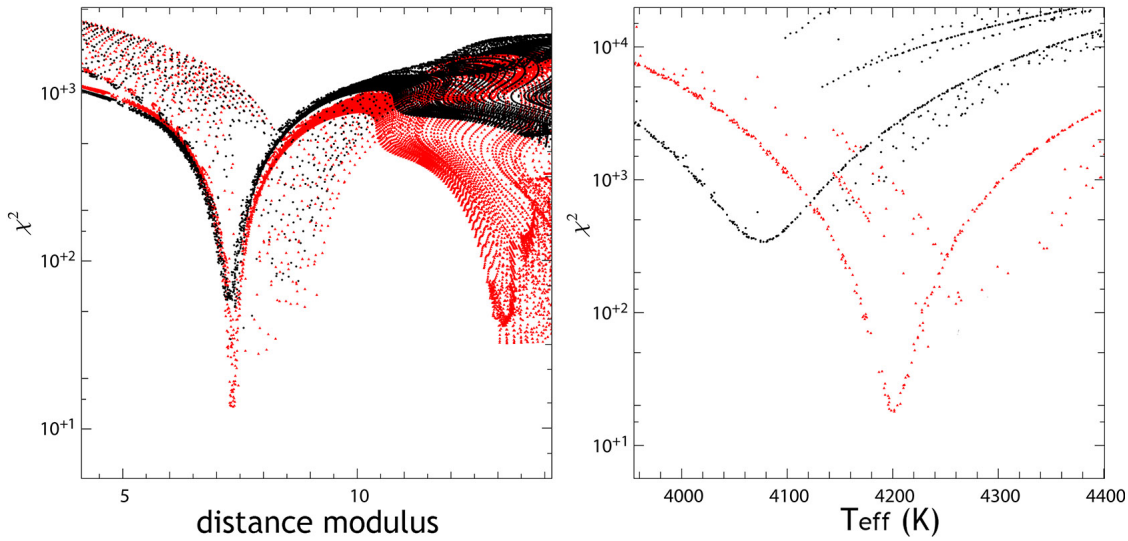

Figure 3.8: Left: χ^2 vs. distance modulus for hot Jupiter candidate system PP140-14711 with our implemented version of extinction fitting (red), compared with a fit without extinction fitting (black). Right: χ^2 vs. effective temperature for the same system with (red) and without (black) extinction fitting.

As an example, the results for the planet candidate PP140-14711 are shown in Figure 3.8. The best fit for the distance is d = 293 pc and T_{eff} = 4208 K for effective temperature. It is clear that there is no alternative fit, e.g. a distant K or G giant reddened by extinction, that

would have an equally low χ^2. One can furthermore see that our extinction fitting shifts the best-fitting temperature by about 125 K and that SED fitting considerably improves the χ^2 of the fit.
In order to compare the results from spectroscopy to SED fitting and also include the χ^2 distribution, we create a contour map of the lowest χ^2 fit in each region for surface gravity log(g) and effective temperature T_{eff} and show the best results from both stellar characterizations (see Figures 3.10 and 3.17 as examples in sections 3.3.1 and 3.3.2, respectively). Finally, we use the relations from Pecaut and Mamajek (2013) and translate the fitted effective temperatures into stellar types.

3.2.5 Planet parameter fitting

Having characterized the star, we fit the planetary and orbital properties. The parameters that we fit are the period p, initial transit time t_0, planet radius R_P, stellar radius $R_\star$ and the orbital inclination i. Based on the results from stellar characterization, we choose the according quadratic limb darkening parameters[9] which we retrieve from Claret and Bloemen (2011)[10]. In order to speed up the process, we use a Markov Chain Monte Carlo (MCMC) algorithm and furthermore improve the fitting speed by utilizing multiple CPU threads. We begin by setting the period and initial transit time from our signal detection result and create a fine grid over which we sample a range of test values for orbit inclination, planet radius and stellar radius. Having determined the starting location with the lowest χ^2, we perform a random walk, slightly changing each of the five parameters and selecting the new parameter value if the fit improves. The process ends if the χ^2 improvement is below a threshold of 10^{-7}. While we impose priors for the stellar radius based on SED fitting and spectroscopy, we extend the grid to cover roughly $0.8\,R_\odot$. If the resulting best-fitting stellar radius is significantly different from our characterization results, it is a possible indication for an eclipsing binary system.
After the fit has converged, we construct a transit model that incorporates all parameters. Examples can be seen in sections 3.3.1 and 3.3.2 in Figures 3.10 and 3.17, respectively. With the accurate transits from the WWFI and more precise stellar characterization, we apply the *vespa* algorithm. We supply it with the combined photometry from Pan-Planets and Wendelstein, give priors based on SED fitting and spectroscopy and provide a maximum for the secondary eclipse depth based on the light curve variation. Finally, we disregard candidates with a FPP of 100%.

[9] See section 1.5.6.
[10] http://vizier.cfa.harvard.edu/viz-bin/VizieR?-source=J/A+A/529/A75

ID	RA (J2000)	DEC (J2000)	Obs	S	Period	LC	i' [mag]	ES2 Exp	Det	T_{SED} [K]	T_{spec} [K]	E(B-V)
PP041-20669	296.0352986	17.0723044	1	1	yes	yes	17.05	—	CC1	3693	—	0.39
PP042-11118⋆	295.8969406	16.9735190	2	1	yes	no	15.17	1800	TI1	6065	6250	0.68
PP051-41275	295.3104312	17.6113728	1	1	yes	yes	17.60	—	CC1	3767	—	0.83
PP054-19415	294.4451647	17.4336549	0	0	—	—	16.84	3600	CC1	5258	5125	0.92
PP114-13080	296.7291433	16.0994114	1	1	yes	yes	17.69	—	CC1	3942	—	0.30
PP127-21645⋆	297.7908841	16.9126047	5	2	yes	yes	15.43	1800	TI1	4592	4667	0.39
PP140-14711⋆	299.0506019	17.5700095	4	3	yes	yes	14.48	3600	CC1	4251	4150	0.094
PP155-16969	296.5583518	17.9014368	3	2	yes	yes	16.11	2400	TI1	5587	5125	0.38
PP215-08245	298.8738926	16.6147993	1	1	no	—	17.95	—	CC1	3586	—	0.20
PP259-05801	300.3562987	18.8088101	2	1	yes	yes	16.18	3600	CC1	3825	3625	0.14
PP317-29811	299.2634096	19.3263252	1	0	—	—	15.53	2100	TI1	5122	—	0.38
PP322-07250	297.3461732	18.9933642	1	1	yes	yes	14.71	1800	TI1	6913	6750	0.42
PP403-05317⋆	299.5485058	13.6496368	5	4	yes	yes	16.74	3600	CC1	4032	4000	0.13
PP409-03981	300.3379534	13.9557166	1	1	yes	yes	15.40	2400	TI1	6354	6500	0.24
PP431-20818	297.9460556	14.8721187	1	1	yes	yes	14.40	2700	TI1	6445	6500	0.20
PP449-01504⋆	300.5155850	15.7110982	1	1	no	—	17.13	—	CC1	3753	—	0.14
PP459-07356⋆	299.8437871	16.2168547	1	1	yes	yes	17.35	—	CC1	6248	—	0.26
PP532-08590⋆	297.3577146	19.1381856	2	1	yes	yes	17.69	—	CC1	3264	—	0.17
PP609-24279	298.1324449	13.6848765	1	1	no	—	17.26	—	CC1	3838	—	0.53
PP628-05369	296.7382008	14.1224994	0	—	—	—	14.83	2700	CC1	3469	—	0.25
PP635-15204⋆	297.0579775	14.6060948	2	1	yes	yes	17.43	4800	CC1	3181	low S/N	0.087
PP635-18831	297.1737584	14.6465819	1	0	—	—	17.82	—	CC1	3197	—	0.15

Table 3.1: Planet candidates that were followed up with the WWFI and Otto Struve telescope ES2 spectrograph, with the number of observations, number of successful observations, successful/unsuccessful period recovery and a flag (LC) indicating whether the light curve was used in the final analysis, i'-band magnitude, ES2 exposure time, used detector, fitted temperature results from SED fitting and spectroscopy and finally the fitted extinction E(B-V). Initial high-priority targets are marked with "⋆". Most candidates fainter than 17th magnitude could not be followed up successfully with spectroscopy and were either aborted after the first exposure or if the target could not be identified in the guiding camera. Exposure times are only listed for successful observations.

3.3 Results

3.3.1 M-dwarf planets

After completing our characterization process, we retained 2 planetary M-dwarf candidates and 2 additional low-priority candidates. Their properties are shown in Tables 3.2 and 3.3. As an additional check, we retrieved archival images for every candidate to verify whether the proper motion is large enough to see the star's movement over time[11].

- PP403-05317, shown in Figure 3.10, is a planet candidate with one of the lowest periods of any known exoplanet with P = 0.416 d and orbits an M0 dwarf. So far, there are only 3 confirmed hot Jupiter systems around M-dwarfs (Johnson et al., 2012; Triaud et al., 2013; Hartman et al., 2015) and it would be the shortest-period hot Jupiter ever found. The spectrum shows weak H_α-line emission which is a clear sign of an M-dwarf and indicative of stellar activity.

- PP635-15204, shown in Figure 3.11, is a hot Jupiter candidate and orbits a relatively faint M4V dwarf. Due to the faint magnitude (i' = 17.43 mag) of the star, its motion in archival images could not be determined but its proper motion has a flag of 1. The light curve shows variability of 1%-2% and the ES2 spectrum shows strong H_α-line emission, however, the S/N of the spectrum is too low to yield a reliable characterization with only one fitted line. The results from *vespa* determine a high likelihood for a true detection, however, it is not yet constrained tightly enough to lead to a definitive conclusion. If confirmed, this is the smallest star ever to host a giant planet.

- PP532-08590, shown in Figure 3.12, is a hot Jupiter candidate in orbit around a very faint (i' = 17.69) M4V dwarf. Crowding in combination with the magnitude lead to the failure of the spectroscopic follow-up with ES2. Archival imaging cannot be used for measuring the star's movement due to the same reasons, but its proper motion was flagged with 1. The star exhibits variability of about ±2% which we attribute to spots on the star's rotating surface. Based on *vespa*, the target is very likely a false detection of an eclipsing binary system due to the transit shape.

- PP259-05801, shown in Figure 3.13, is a hot Jupiter candidate around an M3V dwarf. The spectrum shows strong H_α emission, again indicative of an active M-dwarf, and the star's movement can be detected in archival images, shown in Figure 3.9. Based on the final transit-model fitting, a possible secondary eclipse depth measured to be up to 1.5% and *vespa*, this candidate has a high likelihood for being a false-positive detection which is why we rate it at the lowest priority for follow-up.

[11] See also section 1.8.7.

ID	Spectrum	T_{SED} [K]	T_{spec} [K]	PM	AI	R_{star} [$R_\odot$]
PP403-05317	yes	3899	4000	1	yes	0.58
PP635-15204	yes	3181	≈3500	1	no	0.30
PP259-05801	yes	3680	3500	1	yes	0.46
PP532-08590	no	3197	—	1	—	0.15

Table 3.2: Stellar properties for all M-dwarf planet candidates, showing their ID, i'-band magnitude, whether a spectrum was recorded with ES2, effective temperatures T_{SED} and T_{spec}, proper motion flag PM, visible motion in the archival images AI and the stellar radius R_{star}.

ID	period [d]	T_0	R_{planet} [R_J]	FPP
PP403-05317	0.416018313	2455668.156685187	1.09	0.052
PP635-15204	2.629281785	2455667.716736036	1.68	0.167
PP259-05801	2.471898730	2455366.799764323	2.59	0.980
PP532-08590	2.512569127	2455668.027553192	1.63	0.907

Table 3.3: Planetary properties for all M-dwarf planet candidates, showing their ID, coordinates right ascension RA and declination DEC, period, initial transit time T_0 and the planetary radius R_{planet}.

Figure 3.9: Archival images of planet candidate PP259-05801, taken in 1951 (left) and 1994 (right). One can see that the star moved about two pixels, which corresponds to 2 arcsec, over the course of 43 years. However, the prediction based on proper motion is a movement of about 0.41 arcsec - either the coordinate mapping of the DSS1 and DSS2 frames was inaccurate or the proper motion was underestimated.

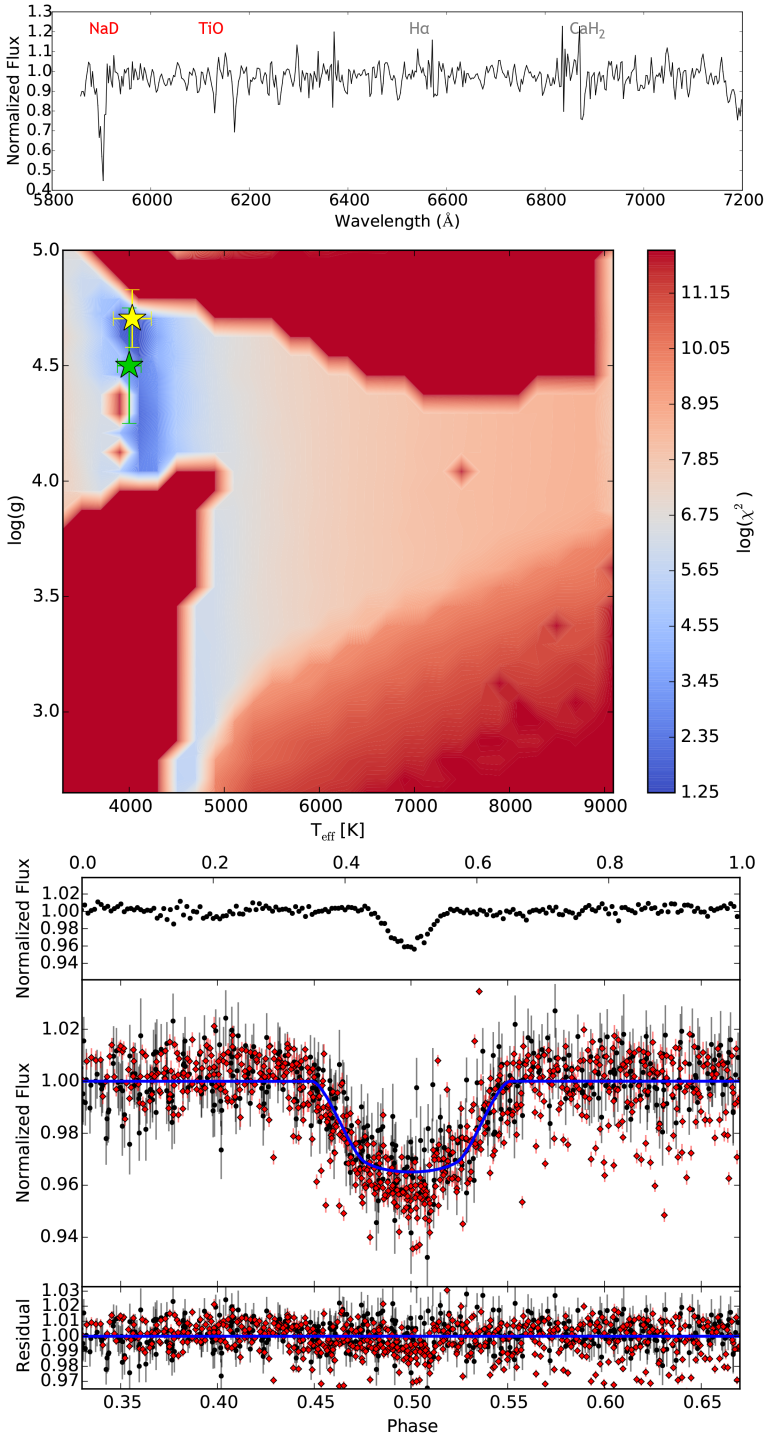

Figure 3.10: Spectrum (top) with line indicators (red if used), stellar parameter fits (middle) with the result from SED fitting (yellow) and spectroscopy (green), folded light curve (bottom) with the best-fitting model (blue line) and data from Pan-Planets (black circles) and FTW (red diamonds) of candidate PP403-05317.

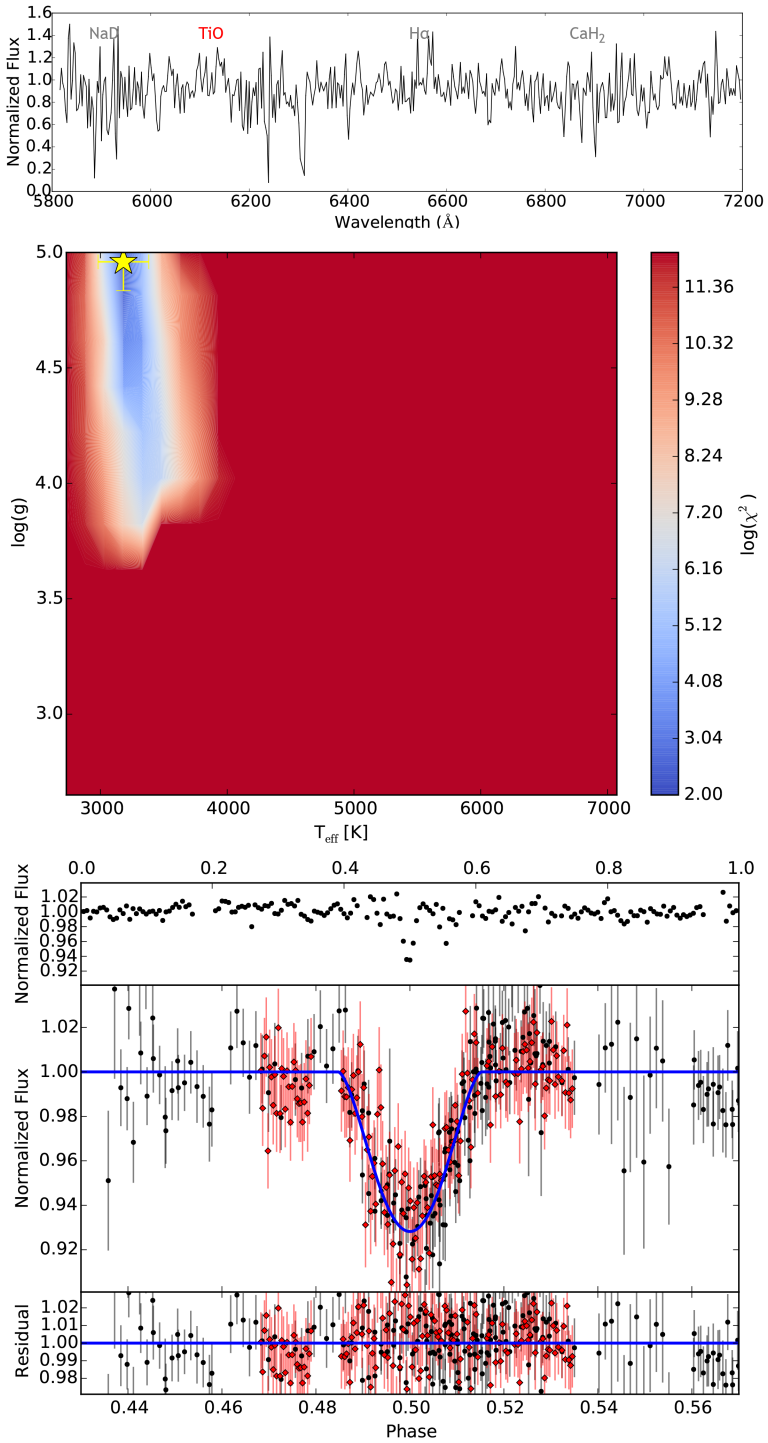

Figure 3.11: Spectrum (top) with line indicators (red if used), stellar parameter fits (middle) with the result from SED fitting (yellow), folded light curve (bottom) with the best-fitting model (blue line) and data from Pan-Planets (black circles) and FTW (red diamonds) of candidate PP635-15204. We did not include the result from spectroscopy in the middle panel due to its bad fit with only one used spectral line. The H_α line is seen in emission, a clear indication of an M-dwarf.

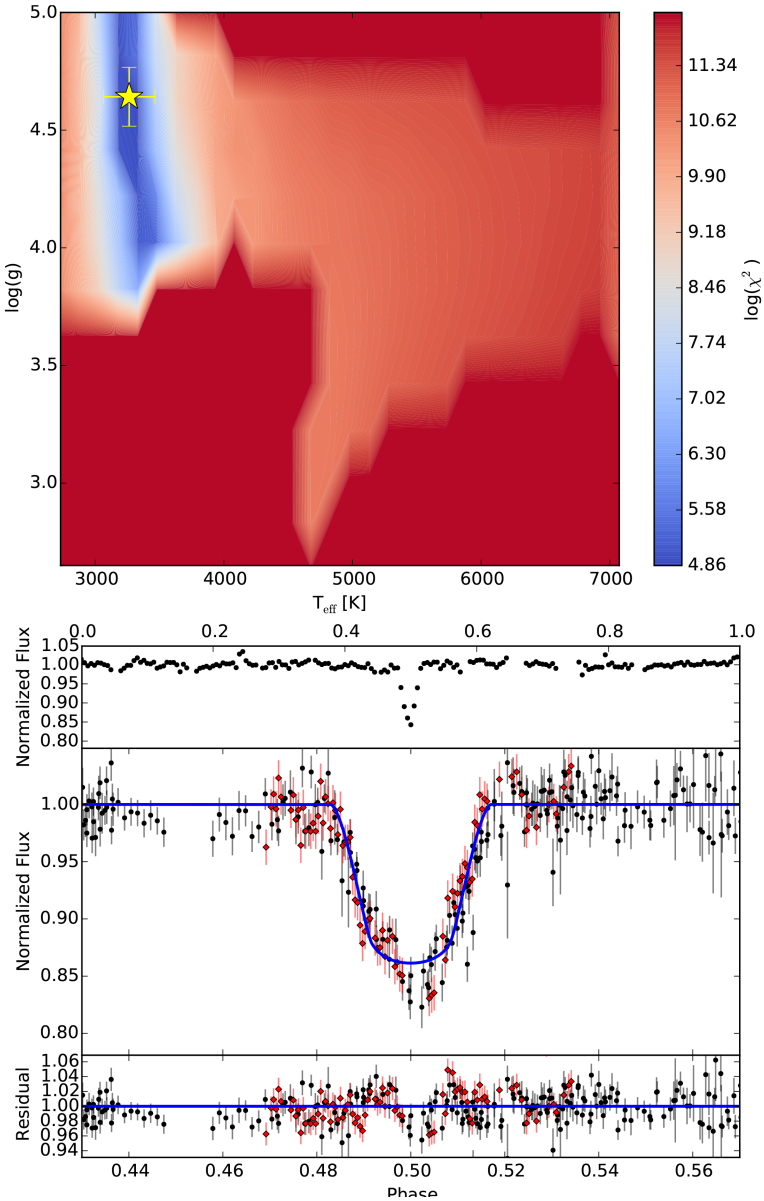

Figure 3.12: Stellar parameter fit (top) with the result from SED fitting (yellow), folded light curve (bottom) with the best-fitting model (blue line) and data from Pan-Planets (black circles) and FTW (red diamonds) of candidate PP532-08590.

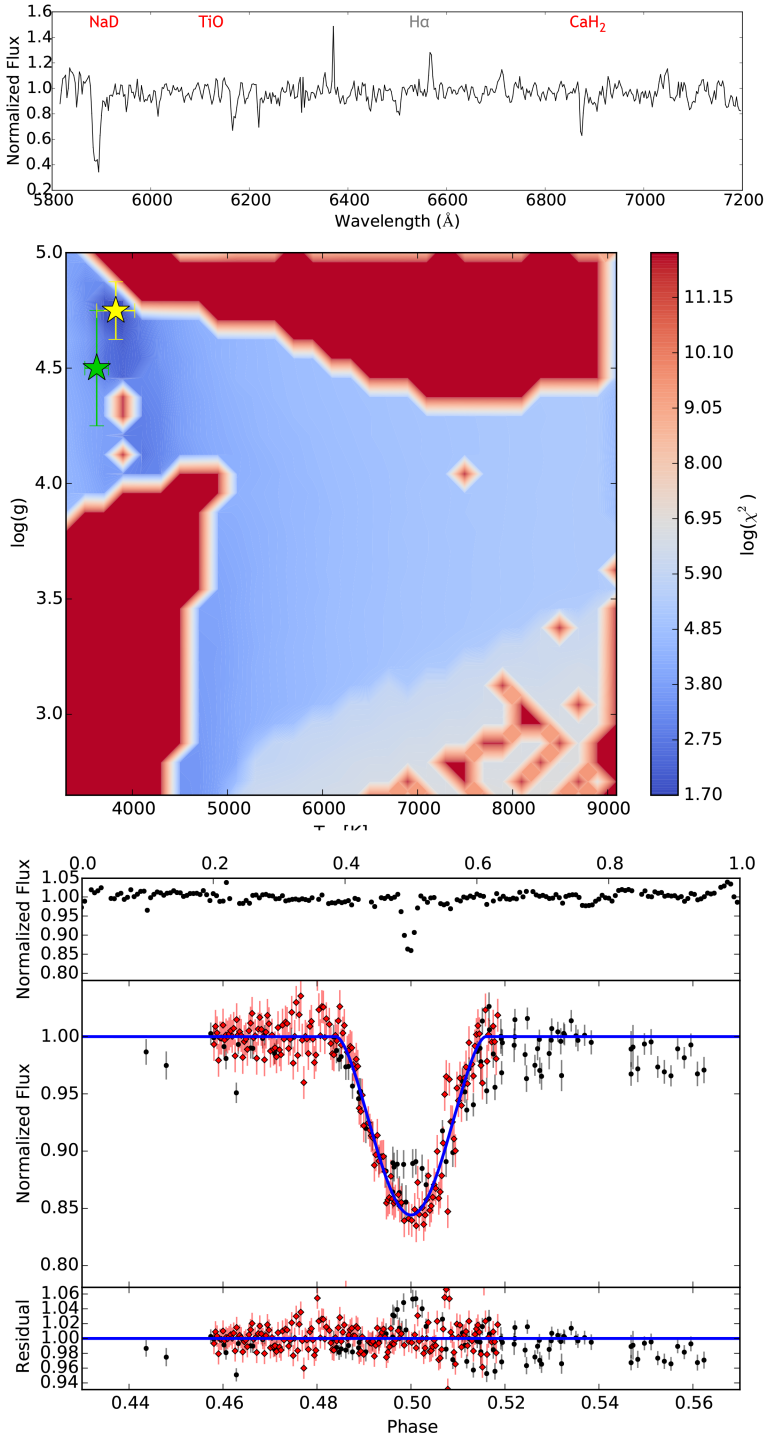

Figure 3.13: Spectrum (top) with line indicators (red if used), stellar parameter fits (middle) with the result from SED fitting (yellow) and spectroscopy (green), folded light curve (bottom) with the best-fitting model (blue line) and data from Pan-Planets (black circles) and FTW (red diamonds) of candidate PP259-05801. The H_α line is seen in emission, a clear indications of an M-dwarf.

3.3.2 Bright FGK-dwarf planets

After completing our vetting process, we retained 4 FGK-dwarf planet candidates, 2 of them being high-priority candidates. Their properties are shown in Tables 3.4 and 3.5. As an additional check, we retrieved archival images for each candidate to verify whether the proper motion is strong enough to visually detect the star's movement over time[12].

- PP140-14711, shown in Figure 3.17, orbits a K6V dwarf with an effective temperature of about 4200 K. Only few late K-dwarf hot Jupiters such as HAT-P-54b (Bakos et al., 2015) are known. We already obtained four preliminary RV measurements, recorded using the Keck HIRES instrument (Vogt et al., 1994), between UT October 01-31 2015. Our observations followed the procedures of the California Planet Search (CPS, Howard et al., 2010). We used the "C2" decker, providing a spectral resolution of R = 55000, and subtracted the sky from the stellar spectrum. The initial observation was done without an Iodine cell for stellar characterization. A cut-out of the H_α-region is shown in Figure 3.14. After the first reconnaissance spectrum for characterization, an Iodine

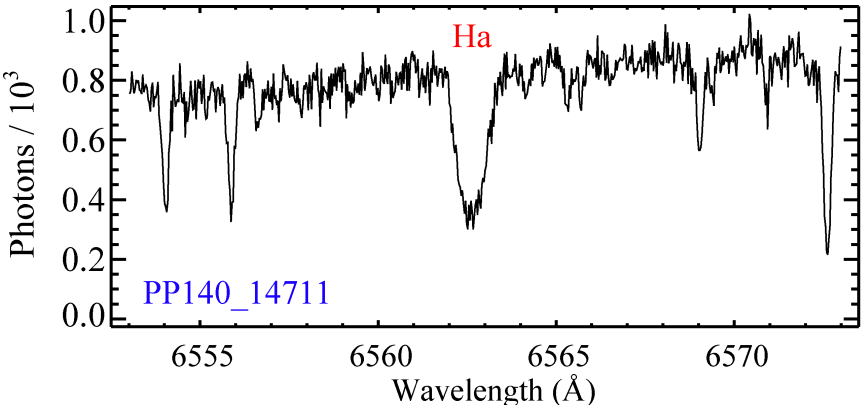

Figure 3.14: High-resolution spectrum recorded with HIRES at the Keck 8 m telescope. The H_α line is relatively weak, indicative of a late K or early M-dwarf.

cell was injected during the observations for wavelength calibration. The resulting radial velocity curve is shown in Figure 3.15. With an amplitude of about 110 ms^{-1}, the best preliminary fit of the planet's mass is 0.57 M_J. However, additional observations are necessary for an accurate mass determination.

- PP127-21645, shown in Figure 3.18, is a hot-Jupiter candidate in orbit around a K4V dwarf. With a period of 1.75 days, it has one of the shortest periods in our candidate list. While the spectrum is noisy, its K4V dwarf type is also confirmed by SED fitting. The star exhibits detectable movement in the archival images (see Figure 3.16) and has a slightly variable baseline, visible in the unfolded data, which might indicate starspots and/or stellar activity.

- PP042-11118, shown in Figure 3.19, is a planet candidate in orbit around an F8V dwarf. The correct stellar type cannot be determined precisely by SED fitting which yields a more distant giant star that is reddened by extinction. However, we can rule out this

[12] See also section 1.8.7.

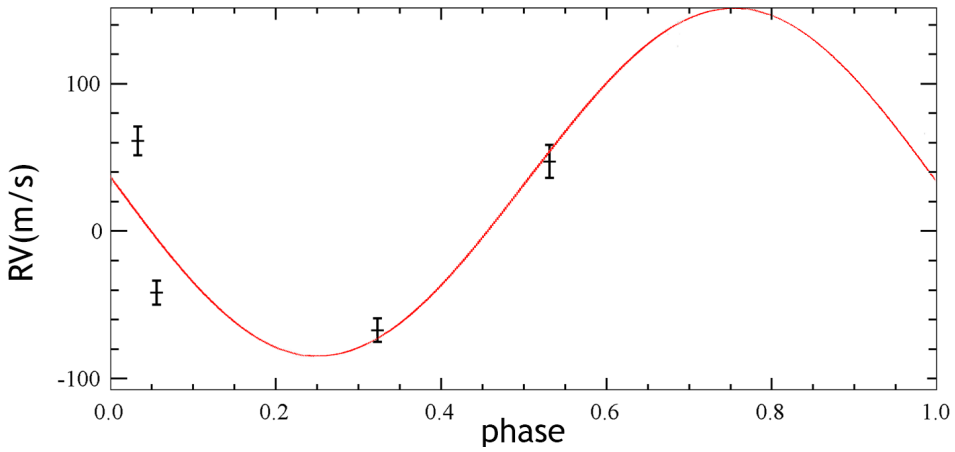

Figure 3.15: Best fit for the radial velocity points of planet candidate PP140-14711.

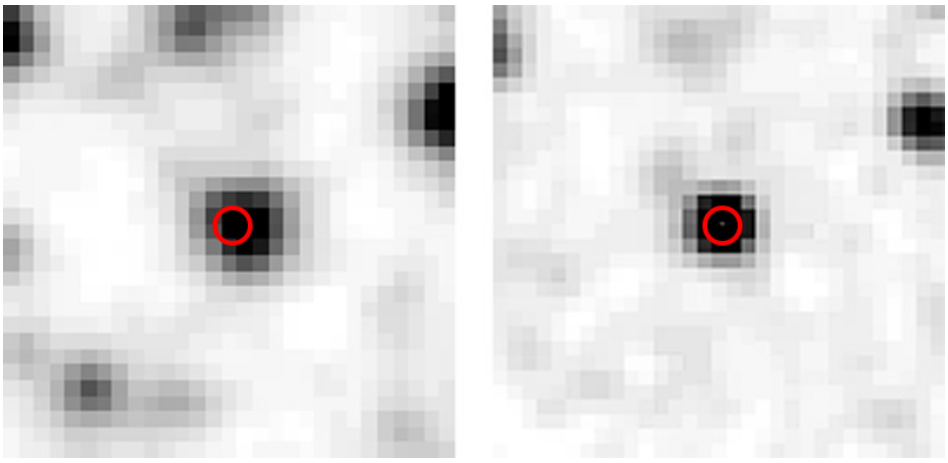

Figure 3.16: Archival images of planet candidate PP127-21645, taken in 1954 (left) and 1990 (right). One can see that the star moved about one pixel, which corresponds to 1 arcsec, over the course of 46 years. Based on proper motion, the expected motion is about 0.64 arcsec.

scenario due to additional low-resolution spectroscopy data from the McDonald HET LRS instrument, taken 4 years ago, which indicated a main-sequence star at about 6000 K. Additionally, the star has a proper motion flag of 1, which is why we repeated the SED fitting and restricted the process to main-sequence stars. The result is very consistent with spectroscopy at an estimate of 6064 K.

- PP155-16969, shown in Figure 3.20, is a planet candidate around a G7V dwarf. The best model for this planet has a large radius of 1.92 R_J which is either indicative of a false-positive detection or of planetary inflation (Batygin et al., 2011). SED fitting is very inconsistent with the results from spectroscopy with a difference between the determined log(g). Together with the results from *vespa* which indicate a likely false-positive detection, it is possible that this candidate may consist of two individual stars which in turn leads to an erroneous result for SED fitting.

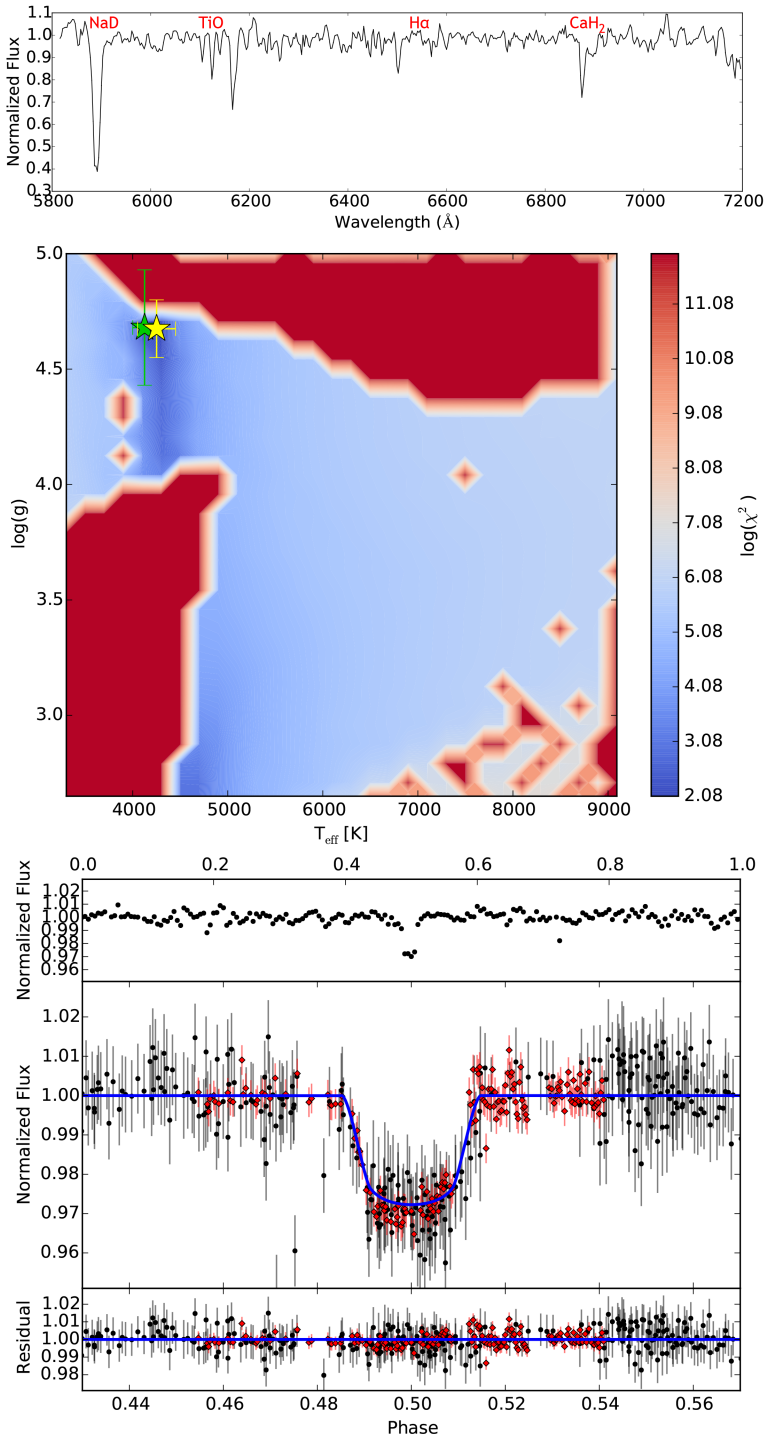

Figure 3.17: Spectrum (top) with line indicators (red if used), stellar parameter fits (middle) with the result from SED fitting (yellow) and spectroscopy (green), folded light curve (bottom) with the best-fitting model (blue line) and data from Pan-Planets (black circles) and FTW (red diamonds) of candidate PP140-14711.

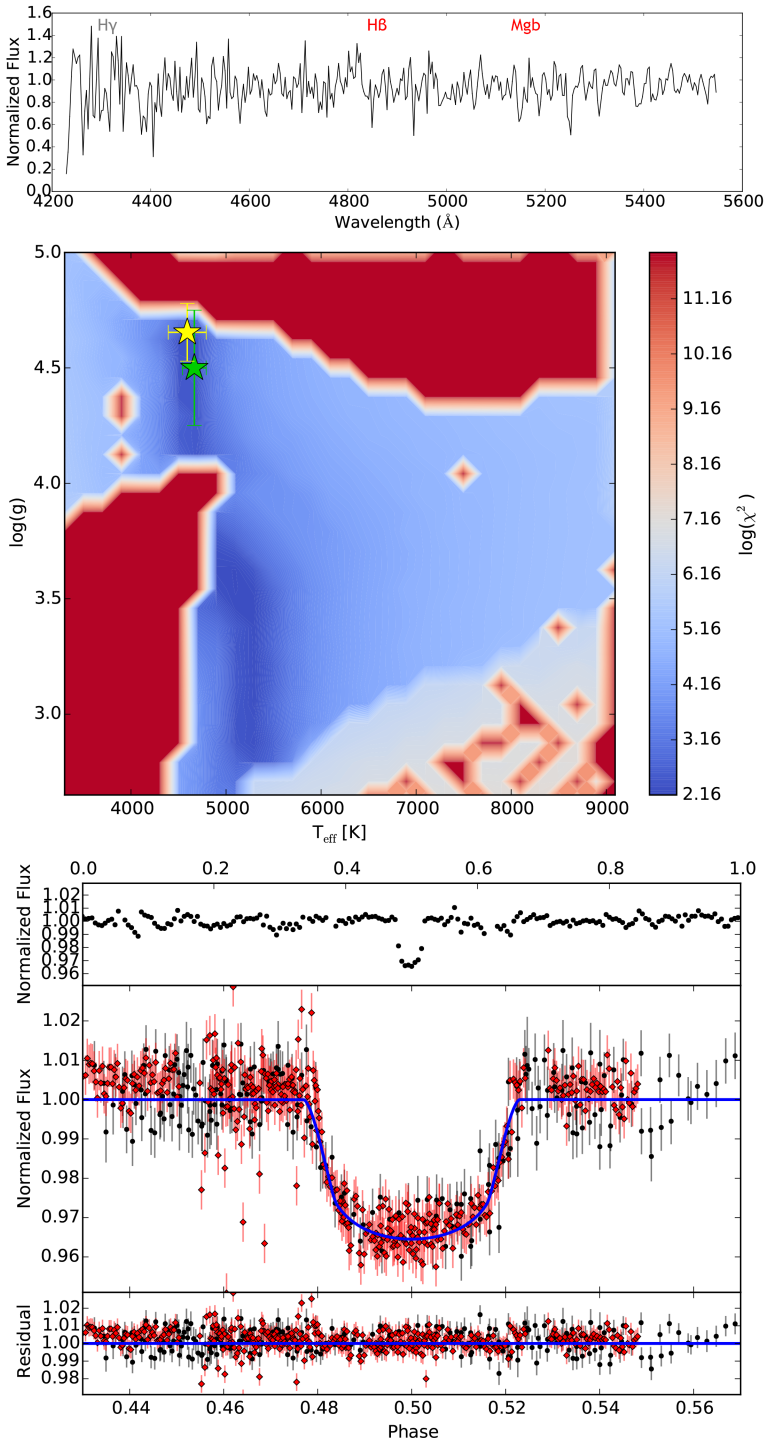

Figure 3.18: Spectrum (top) with line indicators (red if used), stellar parameter fits (middle) with the result from SED fitting (yellow) and spectroscopy (green), folded light curve (bottom) with the best-fitting model (blue line) and data from Pan-Planets (black circles) and FTW (red diamonds) of candidate PP127-21645.

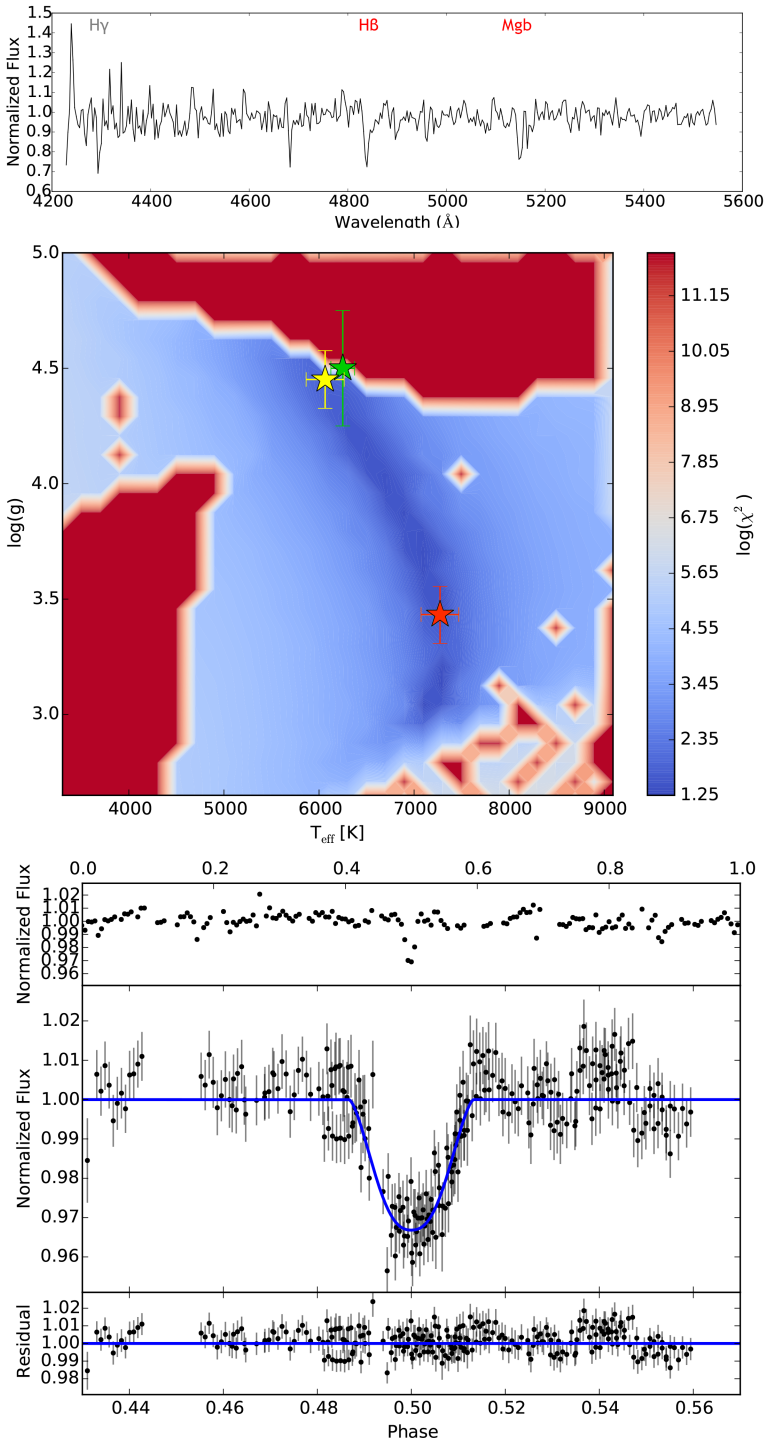

Figure 3.19: Spectrum (top) with line indicators (red if used), stellar parameter fits (middle) with the results from SED fitting for main-sequence (yellow) and giant stars (red) and spectroscopy (green), folded light curve (bottom) with the best-fitting model (blue line) and data from Pan-Planets (black circles) of candidate PP042-11118.

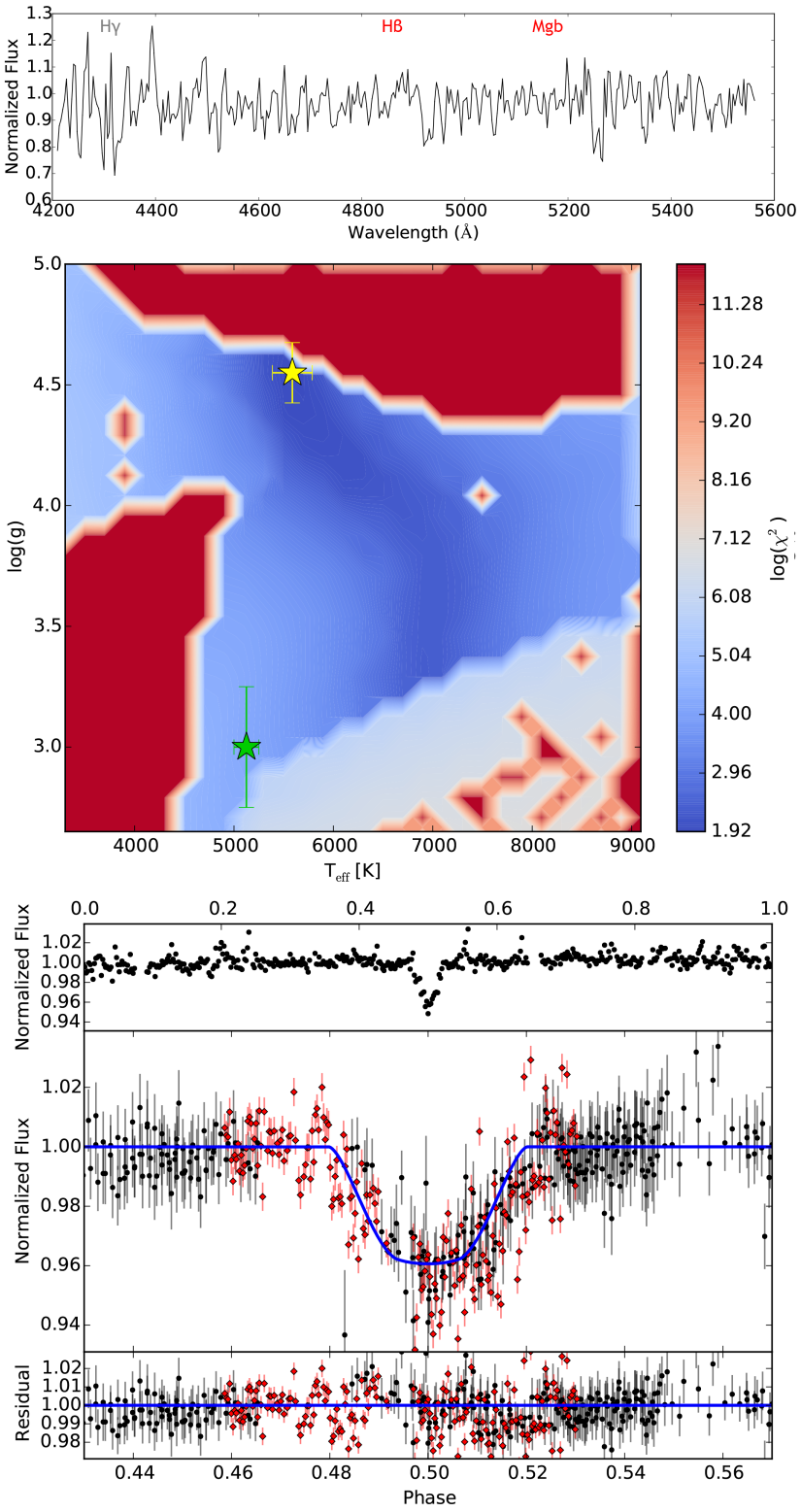

Figure 3.20: Spectrum (top) with line indicators (red if used), stellar parameter fits (middle) with the result from SED fitting (yellow) and spectroscopy (green), folded light curve (bottom) with the best-fitting model (blue line) and data from Pan-Planets (black circles) and FTW (red diamonds) of candidate PP155-16969.

ID	i' [mag]	T_{SED} [K]	T_{spec} [K]	PM	AI	R_{star} [$R_\odot$]
PP127-21645	15.43	4591	4667	1	1	0.66
PP140-14711	14.48	4251	4125	1	0	0.61
PP042-11118	15.17	6064*	6250	1	0	1.03*
PP155-16969	16.11	5587	5125	5	0	0.86

Table 3.4: Stellar properties for all FGK-dwarf planet candidates, showing their ID, i'-band magnitude, whether a spectrum was recorded with ES2, effective temperatures T_{SED} and T_{spec}, proper motion flag PM, visible motion in the archival optics AO and the stellar radius R_{star}. Candidate PP042-11118, marked with a "$\star$", has an inconsistent SED fitting result with a strong preference for late-type stars with a surface gravity of $\log(g)<3.5$.

ID	period [d]	T_0	R_{planet} [R_J]	FPP
PP140-14711	2.663423209	2455367.738464192	1.17	0.000
PP127-21645	1.752223864	2455679.254400454	1.26	0.053
PP042-11118	4.046999150	2455678.504519418	1.88	0.10
PP155-16969	2.341023650	2455678.516332626	1.92	0.984

Table 3.5: Planetary properties for all FGK-dwarf planet candidates, showing their ID, coordinates right ascension RA and declination DEC, period, initial transit time T_0 and the planetary radius R_{planet}.

3.3.3 Simulation results

We use the results from our Monte Carlo simulations (see section 2.4) to set new limits to the planet occurrence rate around low-mass stars. Our large sample means that, assuming a null result in which none of the M-dwarf candidates turn out to be actual planets, we can set new upper limits for the planetary occurrence rates of hot Jupiters around those stars. The number of detections is characterized with a Poisson distribution, therefore, assuming a number of k planets in our sample, the probability of having N_{det} planets is:

$$P_k = \frac{N_{det}^k}{k!} e^{-N_{det}}. \tag{3.1}$$

In our simulations, the geometric probability for a visible transit is empirically being accounted for.Between 9.8% (1 d ≤ p ≤ 3 d) to 2.5% (5 d ≤ p ≤ 10 d) of the simulated Hot-Jupiter transits pass our visibility criterion (see Eq. 2.12). The detection efficiency is therefore a combination of the geometric probability $P_{transit}$ and the detection efficiency P_{det}. We now assume the null result, e.g. $k = 0$. In order to compare our results to Kovács et al. (2013) and Zendejas et al. (2013), we also use a confidence interval of 95%. Solving

$$P(N_{det} < N_{max}) = \int_0^{N_{max}} e^{-N} dN = 0.95, \tag{3.2}$$

we get N_{max}=3. We can calculate the upper limit by replacing the number of observed planets N_{det} with the product of the number of stars with the detection efficiency and fraction f so that $N_{det} = N_{stars} \cdot P_{det} \cdot P_{transit} \cdot f$:

$$f_{95\%} \leq \frac{3}{N_{stars} \cdot P_{det} \cdot P_{transit}}. \tag{3.3}$$

Taking into account the individual detection efficiencies in every field, the geometric probability for each period bin and assuming that the distribution of planetary radii is even, we end up with an upper limit of 0.34%. This is a significantly lower result than those found in previous surveys where small sample sizes counteracted higher detection efficiencies. Splitting up the results for M0-M2 and M2-M4 sub groups as done in Kovács et al. (2013) and Zendejas et al. (2013), we derive upper limits of 0.49% and 1.1%, respectively. However, we possess two plausible M-dwarf hot Jupiter candidates. One target, PP635-15204, is a M4V M-dwarf while the other M-dwarf candidate, PP403-05317, is at the very border between M-dwarfs and late K-dwarfs. The FPP for PP635-15204 is still rather high with a remaining probability of 17%, hence we assume one correctly identified hot Jupiter. We calculate the occurrence rate to be $0.11^{+0.37}_{-0.02}$% with a 95% confidence limit. For the upper uncertainty, we integrate equation 3.2 in the range of 1 to N_{max} and determine the fraction limit. For the lower uncertainty, we consider the scatter of our simulations and calculate the difference between the average and minimum detected planets per simulation run. It may look counter-intuitive that a successful detection lowers the supposed fraction but one has to keep in mind that the null result describes the upper limit, while a successful detection allows for an estimate of the fraction. Additionally, the uncertainties of the fraction estimate are higher than the null result's limit. As another comparison, we determine the best-case results from the Kepler survey. We assume a number of 3897 stars in the temperature range between 3000 K and

4000 K in the distribution of Dressing and Charbonneau (2013) and simulate a system with the same hot Jupiter population as ours for the given stellar radius. If the criterion

$$sin(i) < \frac{R_{star} - R_{planet}}{a}, \tag{3.4}$$

e.g. a full transit of the planet, is met, we assume a successful detection due to the photometric accuracy and the long baseline of Kepler. Note that this criterion is different to eq. 2.12: here we assume a full eclipse of the planet. The resulting fraction with one confirmed planet (Johnson et al., 2012) is $0.17(^{+0.67}_{-0.04})\%$, an occurrence rate that is on par with our own results although 50% higher and with larger uncertainties due to the small sample of cool Kepler stars. The inclusion of stars up to 4000 K means that this fraction cannot be compared

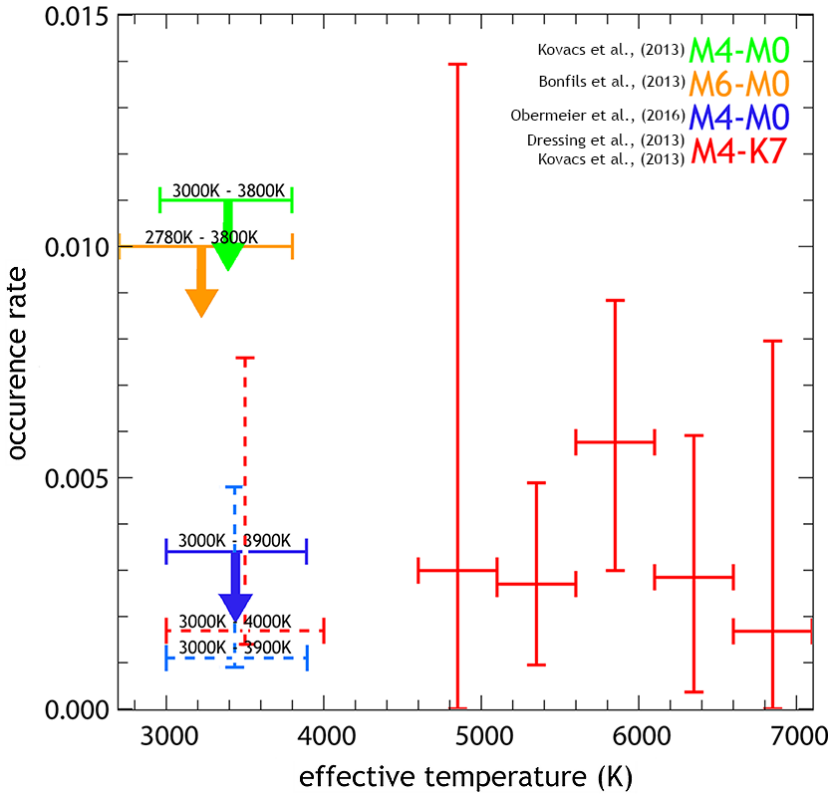

Figure 3.21: Adaptation of Figure 13 in Kovács et al. (2013), showing the hot Jupiter fractions determined by different surveys. We added our new results, marked in dark blue (upper limit) and light blue dotted line (fraction in case of a successful detection). Orange shows the limits derived from radial velocity surveys (Bonfils et al., 2013), red from the Kepler survey (extracted by Kovács et al. (2013)), red in dotted lines from our own simulations for Kepler and green from the WFCAM transit survey (Zendejas et al., 2013).

directly to our results. Furthermore, there are three additional hot Jupiter candidates in the Kepler database[13], KOIs 3749.01, 1654.01 and 1176.01. All of their radii are very close to that of Jupiter and show no signs of inflation, e.g. radii much larger than 1 R_J that is frequent for hot Jupiters. It is possible that they are in fact Brown Dwarfs or low-mass stellar

[13] http://exoplanetarchive.ipac.caltech.edu/

companions, so further follow-up will be necessary to determine their true nature. This means that Kepler's occurrence rate limits might end up being higher than assumed here, depending on whether or not all of the remaining Kepler candidates are planets.
We illustrate the impact of this new occurrence limit in Figure 3.21. Our result pushes the upper limit down to the level of other main-sequence stars. The hot-Jupiter occurrence rates for FGK-dwarfs are estimated to be at about $0.45^{+0.54}_{-0.25}\%$ based on the analysis of (Gould et al., 2006) or 0.3%-0.6%, depending on stellar type, based on the analysis of Kepler data (Howard et al., 2012; Kovács et al., 2013). However, theoretical models (Ida and Lin, 2005; Johnson et al., 2010; Mordasini et al., 2012) point to an even lower fraction for M-dwarfs.

Comparison to the expected number of detections

When comparing our measured detection efficiency to the predictions of Koppenhoefer et al. (2009), one has first to consider the difference in the number of data points per star. Pan-Planets was scheduled for 4% of the total observing time, which we actually received. However, Koppenhoefer et al. (2009) assumed that this would add up to 280 h, while in the end we received 165 h because of different reasons (delayed fully operational readiness, weather, maintenance). This significantly decreased the detection efficiency. The change in observing time was shown to have a non-linear impact, e.g. doubling the amount of observing time increased the number of detected planets by a factor of three (see tables 8 and 9 in Koppenhoefer et al. (2009)) for periods longer than 3 days. Furthermore, while we assumed a precision up to 4 mmag red noise residual, the majority of light curves now has a precision between 5-10 mmag. There is no directly comparable simulation, so we would have to adjust the previous red noise models. The unforeseen issues for bright stars in 2010 could also not have been taken into account, meaning that there are less than 1500 data points for any bright source (i' $\leq$ 15.5 mag).
We scale down table 8 in Koppenhoefer et al. (2009), which assumes 120 hours of data taken in one year, for the aforementioned effects - a red noise residual level of 5 mmag and fewer data points than previously assumed which leads to the final number $n_d = 3.0^{+3.3}_{-1.6}$. We find our expected number of detected hot Jupiters to be consistent with the scaled estimate of n_d =7.4±2.9 detections. Overall, based on the results from *vespa*, we have 5 high-probability planet candidates. Three of them are around FGK-dwarfs while one more, PP403-05317, is not yet clearly identified as either M or K. Therefore, our estimated number of $3.0^{+3.3}_{-1.6}$ shows excellent agreement with the results.

3.3.4 M eclipsing binaries

We identified 205 systems that were classified as binary M-dwarfs. The complete list is detailed in Table A.2 in the appendix chapter. In the following, we provide samples for different categories of these systems. In every figure, the period is folded and repeated for an additional phase for better visual clarity.

- Target PP512-01847, shown in Figure 3.22, is an example for a contact eclipsing binary system[14] with a very short period of 0.23 d.

[14] I.e. a system where both stars are so close that their surfaces touch at the inner Lagrange point L1.

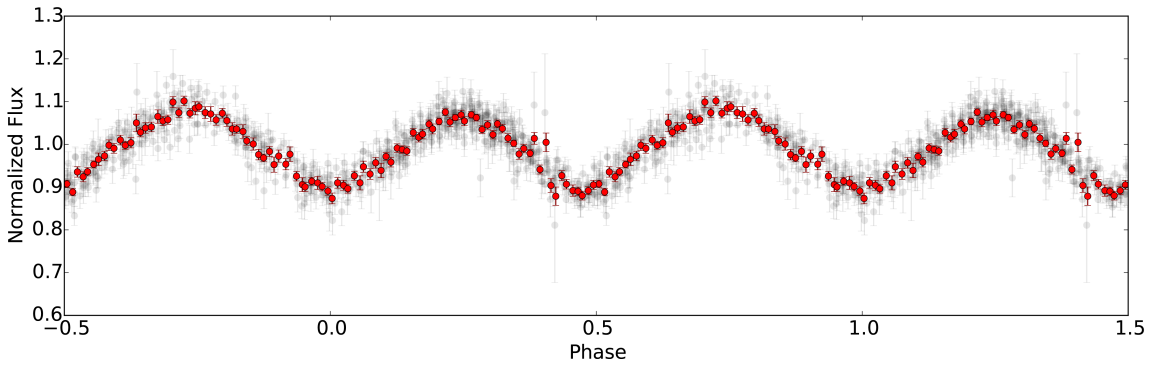

Figure 3.22: Folded light curve (p=0.23 d) of the contact M-dwarf binary system PP512-01847. The data points (light grey) are binned into 100 points per phase (red).

- Target PP632-22966, shown in Figure 3.23, is a semi-detached eclipsing binary system that consists of two M-dwarfs nearly identical in size which orbit each other at a very short period of 0.23 d.

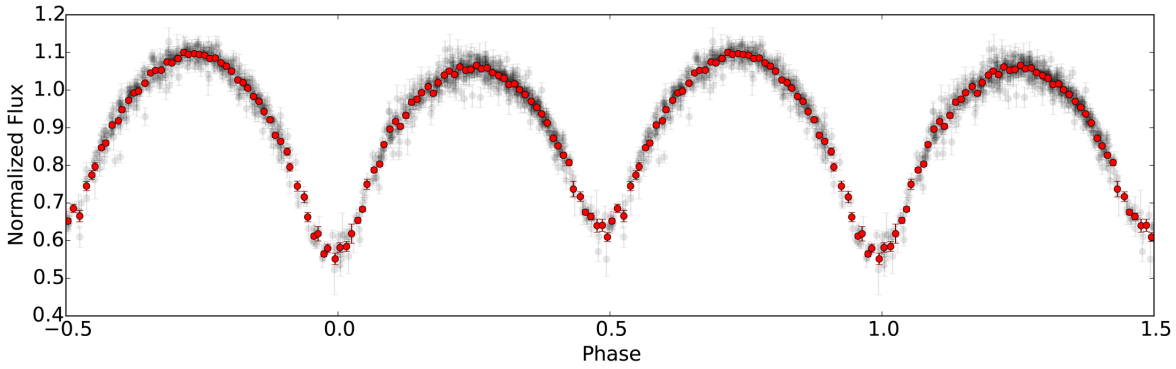

Figure 3.23: Folded light curve (p=0.23 d) of the eclipsing M-dwarf binary system PP632-22966. The data points (light grey) are binned into 100 points per phase (red).

- Target PP111-24974 is an eclipsing-binary system that appears to be in the transition between semi-detached and detached. Curiously, while the region between phases 0 and 0.5 appears flat and like that of a detached system, the region between phases 0.5 and 1 indicates a semi-detached state. The system exhibits to have strong variability of about ±8% which we estimate to be due to the stellar rotation. Based on the SR-diagram (see also section 2.2.4 and equation 2.9), the variability may be periodic with a SR-peak at 0.78 days and correspond to the rotation period of one of the two stars.
- Target PP602-20459 is an example for a completely detached M-dwarf binary system. The depths of the primary and secondary eclipses indicate that the primary star is about 50% larger than the secondary.

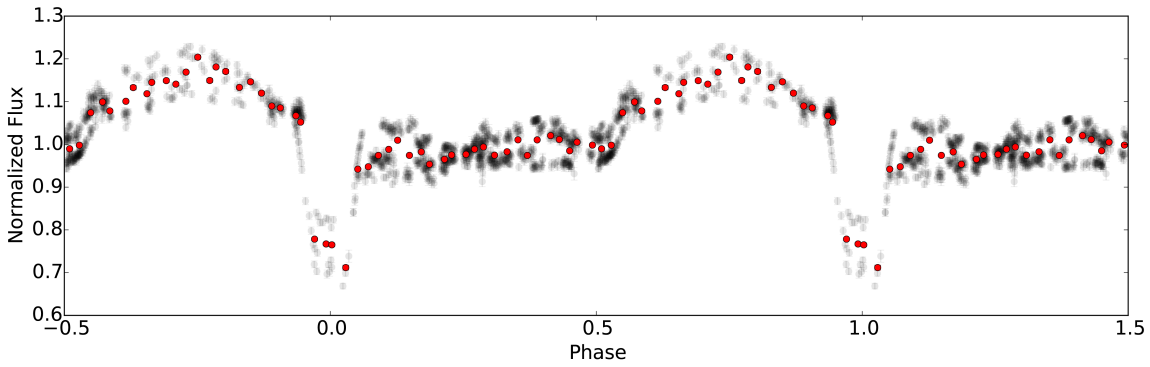

Figure 3.24: Folded light curve (p=7.19 d) of the eclipsing M-dwarf binary system PP111-24974. The data points (light grey) are binned into 50 points per phase (red).

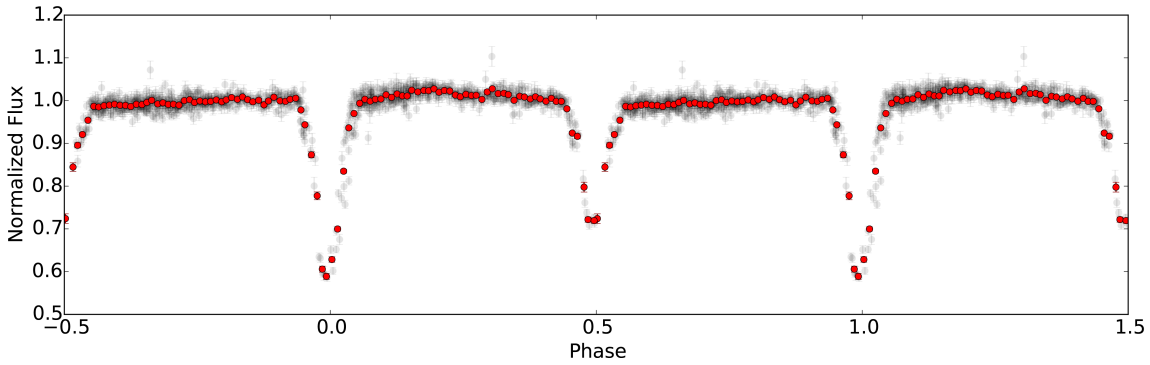

Figure 3.25: Folded light curve (p=0.59 d) of the eclipsing M-dwarf binary system PP602-20459. The data points (light grey) are binned into 50 points per phase (red).

- Target PP036-18215, shown in Figure 3.26, is an Algol-type EB which appears to be a system where only the primary contributes to the light curve.

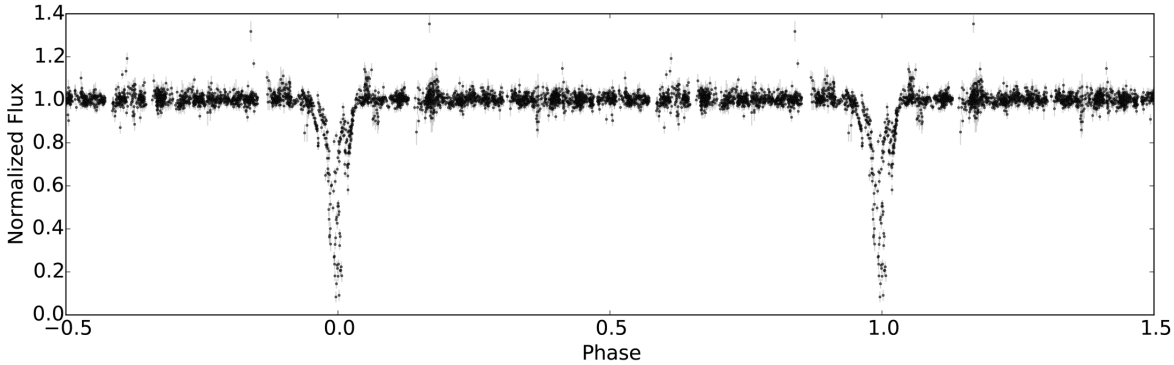

Figure 3.26: Folded light curve (p=3.6 d) of the eclipsing M-dwarf binary system PP036-18215.

3.3.5 Variable systems

PP050-06948

The analysis of the white-dwarf sample (see section 3.1) revealed a very curious system. Target PP050-06948, shown in Figure 3.27, is a variable system with a period of p=2.63 d. There are several aspects that make this system remarkable:

- Periodical stability over 4 years.
- Broad (≈0.1 phase) primary eclipse and no visible secondary eclipse in the normalized, phase-folded light curve (see Figure 3.28).
- Roughly sinusoidal variability with a peak at phase 0.5.
- Based on colour cuts (Girven et al., 2011), the primary appears to be a white dwarf. However, this is incompatible with the broad, rounded shape of the eclipse.

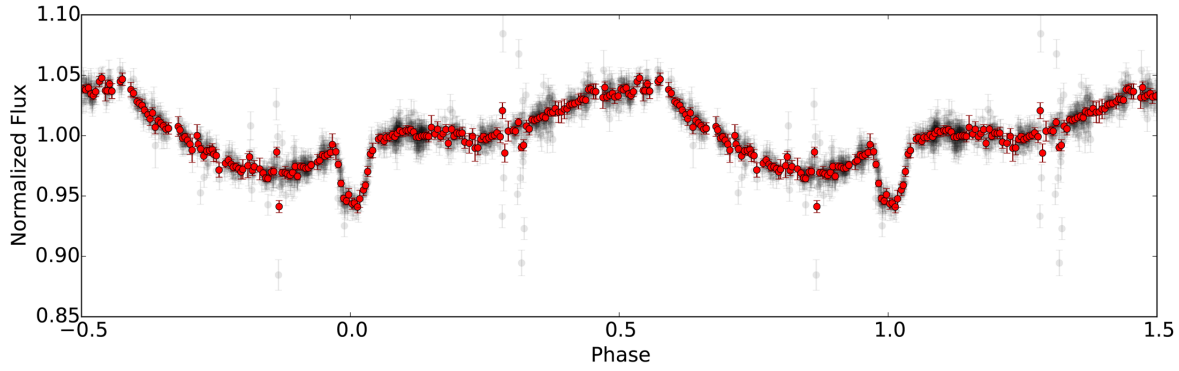

Figure 3.27: Folded light curve (p=2.63 d) of variable star PP050-06948.

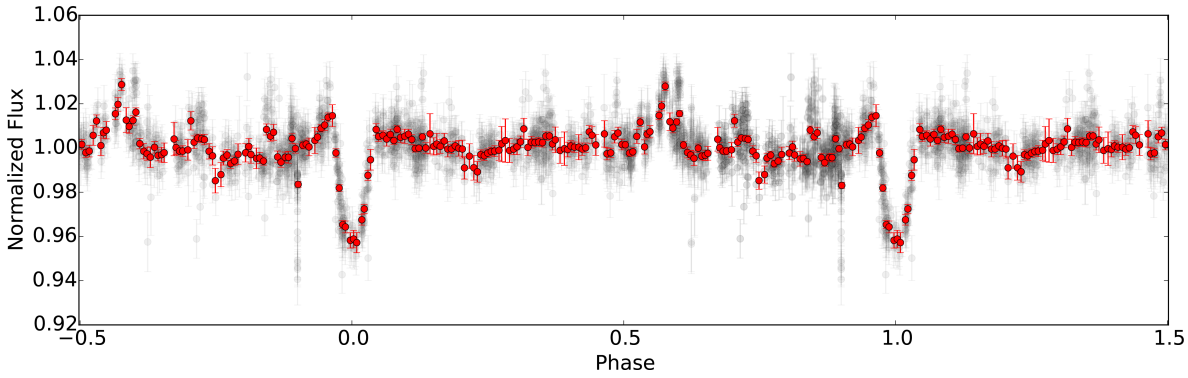

Figure 3.28: Folded light curve (same as Figure 3.27) but normalized by fitting the out-of-eclipse baseline.

Due to the mysterious nature of this candidate, we recorded low-resolution spectra with ES2 in both detectors TI1 and CC1. The normalized spectra are shown in Figures 3.29 and 3.30. After visually comparing the spectra to those of different stellar types, there is a strong

indication that the primary is a blue straggler due to the presence of a deep CaH_2 line at 6900Å, which is not seen in the otherwise very similar white dwarf spectrum. Additional information about PP050-06948 is given in Table 3.6.
Blue stragglers are rare stars that are hotter and larger than other stars at the main-sequence turn-off point (Mapelli et al., 2006). They most likely form either by collision (Glebbeek et al., 2008), which is more likely in clusters, or by mass transfer through Roche-lobe overflow (Ivanova, 2015) in a Primordial-Binary (PB) system. It is, therefore, likely that this system is a recently formed blue straggler that is still gaining mass from its lower-mass companion. Multiband photometry and RV measurements will allow a better analysis of this system in the future.

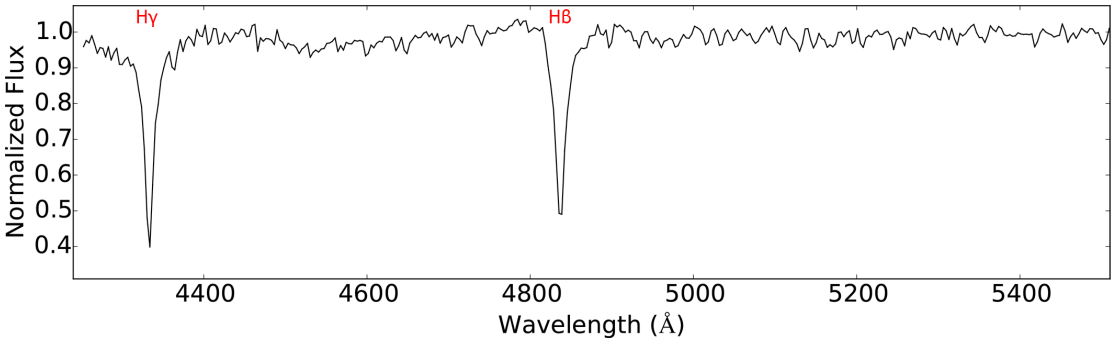

Figure 3.29: TI1 spectrum of PP050-06948. Spectral lines are indicated in red.

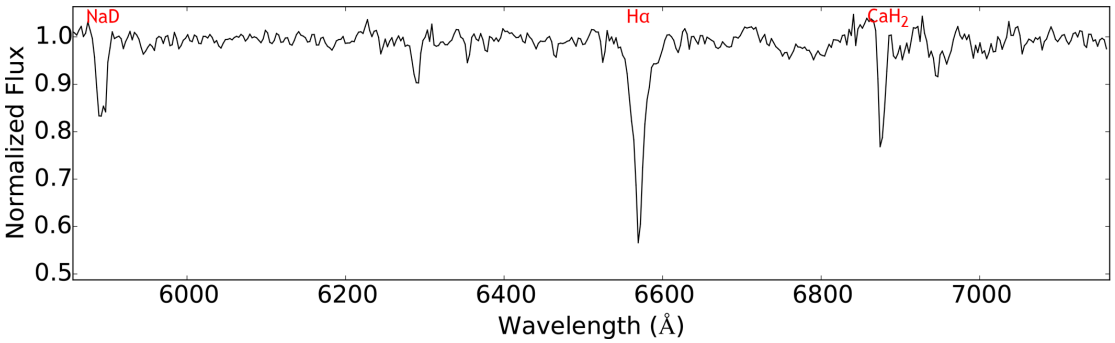

Figure 3.30: CC1 spectrum of PP050-06948. Spectral lines are indicated in red.

ID	RA (J2000)	DEC (J2000)	period (d)	T_0	PM
PP050-06948	295.6122397	17.2936616	2.63225337	2455823.0284827	7

g' [mag]	r' [mag]	i' [mag]	z' [mag]	J [mag]	H [mag]	K [mag]
13.52±0.007	13.50±0.006	13.54±0.008	13.59±0.007	12.83±0.02	12.77±0.02	12.67±0.03

Table 3.6: Properties of PP050-06948.

UU Sagittae

A search through the SIMBAD database revealed the presence of the planetary nebula Abell 63 (Abell, 1966) in our field of view with the eclipsing binary UU Sagittae at its centre. Originally identified by Hoffleit (1932), Bond et al. (1978) first characterized this system, a post common-envelope EB, as the central star of this nebula and determined its period. Further studies (Walton et al., 1993; Bell et al., 1994; Afşar and Ibanoğlu, 2008) measured the light curve, eclipse depth and radial velocity of this system in more detail. Having identified UU Sagittae as our target PP043-25874, we noticed a previously undetected variability in the primary eclipse depth. The system shows year-by-year variation with the most striking difference being between the data of 2009+2010 and 2011+2012, shown in Figure 3.31. We are in the process of studying this system further.

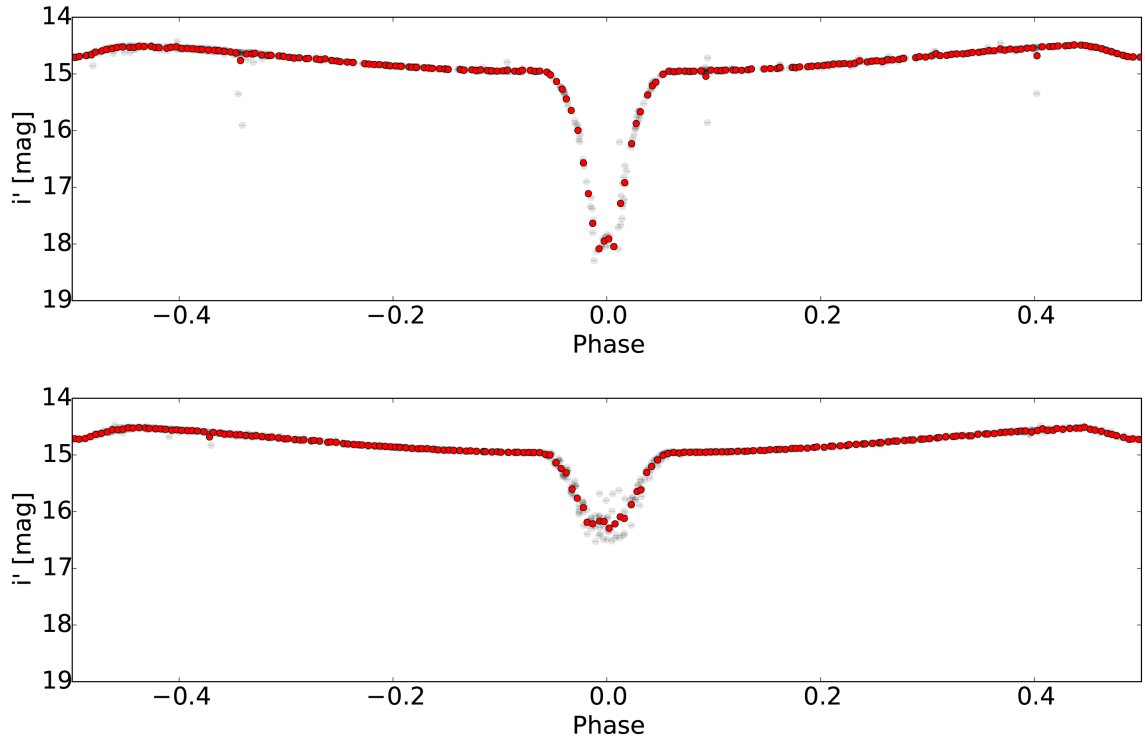

Figure 3.31: Folded light curve (p=0.465 d) of UU Sagittae, showing the 2009-2010 (top) and 2011-2012 (bottom) data. The flux has been converted into magnitudes for better visibility of the variable primary eclipse depth.

3.4 Summary

The Wide-Field Imager in the 2.0 m Fraunhofer Teleskop Wendelstein proved to be a highly effective instrument for improving the photometric precision during the planet candidate's transits. In the near future, multi-band photometry with the new 3-channel camera 3KK (Lang-Bardl et al., 2010) will allow the characterization of multiple bands in just a few observing runs.

We used the 2.08 m Otto Struve ES2 instrument for the spectroscopic follow-up of our targets. While the S/N was too low for most candidates fainter than i'=16 mag, we could successfully confirm the stellar type for the other candidates with the exceptions of PP042-11118 and PP155-16969 which were wrongly characterized. This also served as a test for the precision of broadband-photometry classification and SED fitting fared very well, especially considering the variable dust reddening.

We detected a variety of different targets of interest in the Pan-Planets data, from planet candidates and large-number M-dwarf EBs to rare variable stars. The planet candidates are the primary targets for follow-up, especially the M-dwarf and late K-dwarf samples. Overall, we have five high-priority planet candidates that we aim to follow up with high-precision spectroscopy as soon as possible to determine their mass and rule out a false-positive identification. The preliminary RV data that was collected for PP140-14711 already indicates that this planet may soon become the first confirmed planet, *Pan-Planets 1b*.

Using Monte Carlo simulations we determined the detection efficiency of the Pan-Planets survey for several stellar and planetary populations. We expect to find $3.0^{+3.3}_{-1.6}$ hot Jupiters around F, G and K-dwarfs with periods lower than 10 days based on the planet occurrence rates derived in previous surveys. For M-dwarfs, the fraction of stars with a hot Jupiter is under debate. With the large sample size of Pan-Planets, we were able to determine a planet fraction of $0.11(^{+0.37}_{-0.02})\%$ in case one of our candidates turns out to be a real detection. For this result, we considered the average detection rate of the simulations and compared the scatter at a 95% confidence.

If however none of our candidates is real, we were able to put a 95% confidence upper limit of 0.34% on the hot Jupiter occurrence rate of M-dwarfs. This limit is higher than the calculated fraction in case of a successful detection, however, the uncertainties of the fraction are in turn higher than this upper limit. This result is a significant improvement over previous estimates where the lowest limit published so far is 1.1%, found in the WTS survey (Zendejas et al., 2013), or, using our approach to estimate the generous best case for Kepler, $0.17(^{+0.67}_{-0.04})\%$. Despite the significant improvement, our upper limit is still comparable to the occurrence rate of hot Jupiters around F, G and K-dwarfs, even more so in case of a successful detection. The estimates from Gould et al. (2006) based on the OGLE-III transit search seem to be in good agreement with our new limits. Therefore we could not yet confirm the theoretical prediction of a lower rate for cool stars. Other surveys with even larger M-dwarf samples and/or better detection efficiency will be needed to answer this question.

Besides the planet candidates, we identified a large number of eclipsing M-dwarf binary systems. We are in the process of collecting medium-resolution spectra with SpeX (Rayner et al., 2003) and aim to provide a full catalogue with all EB's and fitted parameters to the scientific community in the near future.

Having access to 4 million light curves means that any type of statistically rare systems may be found. We detected the peculiar variable system PP050-06948 which may provide additional insights into the formation of blue stragglers. For the planetary nebula Abell 63, the collection of photometry over the course of 4 years led to the realization that the primary eclipse depth of the central star varies over time - something that had been unnoticed in the past decades.

Chapter 4

A low-mass planet found in the Praesepe open cluster with K2

He is not worthy of the honey-comb, That shuns the hives because the bees have stings.

William Shakespeare, The Tragedy of Locrine (1595) III, II. 39. Shakespeare Apocrypha

*Note: Parts of this chapter were used for the publication "*K2 *Discovers a Busy Bee: An Unusual Transiting Neptune Found in the Beehive Cluster" (Obermeier et al. 2016b, submitted to A & A).*

Abstract

Open clusters have been the focus of several exoplanet surveys but only a few planets have so far been discovered. The *Kepler* spacecraft revealed an abundance of small planets around small, cool stars. The high star density of clusters makes their members prime targets for high-precision exoplanet transit searches. *Kepler*'s new mission, *K2*, is targeting several open clusters and star forming regions around the ecliptic and enables the search for transiting planets around their low-mass constituents. Here, we report the discovery of the first transiting planet in the intermediate-age (800 Myr) Beehive cluster (Praesepe). EPIC 211916756 is a faint (Kp = 15.5) M3.0 $\pm$ 0.5 dwarf from *K2*'s Campaign 5 with an effective temperature of $T_{\rm eff} = 3471 \pm 124$ K, approximately solar metallicity and a radius of $R_\star = 0.402 \pm 0.050\,R_\odot$. Around this star we detected a planet with a radius of $R_{\rm p} = 3.47^{+0.78}_{-0.53}\,R_\oplus$ and an orbital period of p = 10.132 days. We combined photometry, medium/high-resolution spectroscopy, adaptive optics/speckle imaging and archival survey images to validate the planet by ruling out any false positive detection scenarios and further characterize the system. The planet's radius is very unusual as M-dwarf field stars rarely have Neptune-sized transiting planets (Mulders et al., 2015a). The comparatively large radius of EPIC 211916756b is consistent with the other recently discovered cluster planets K2-25b (Hyades) and K2-33b (Upper Scorpius) which indicates systematic differences in the evolutionary states or formation of cluster stars in contrast to field stars. These discoveries from *K2* provide a snapshot of planet formation and evolution in cluster environments and thus make excellent objects to test differences between field-star and cluster planet populations.

4.1 Introduction

Exoplanet science is still a young field but what stands out is the strong diversity in the properties of both discovered planets and their host stars. Already a short time after the first transiting planet was detected by Charbonneau et al. (2000); Henry et al. (2000), surveys were initiated with a focus on open clusters for a variety of reasons. The higher density of stars gives surveys access to more stars for a given field of view. Age, distance and metallicity of the member stars are well determined, yielding more precise estimates for the planetary and stellar parameters. Furthermore, most observed field stars[1] are relatively old (≥ 1 Gyr) while many currently targeted clusters present a younger sample (10-800 Myr). In addition, planet formation in stellar clusters may well be very different due to stronger and more frequent gravitational interactions between the stars. Planets in younger clusters may also be undergoing thermal evolution, radial contraction, or receive high irradiation from their active host stars. Therefore, open clusters are an excellent laboratory to test planet formation and evolution models. Initial transit surveys that focussed on 47 Tuc (Gilliland et al., 2000; Weldrake et al., 2005), NGC 2301 (Howell et al., 2005) and NGC 7789 (Bramich and Horne, 2006), respectively, found no evidence for transiting planets. Since then, fourteen planets have been discovered in open clusters, namely in NGC 6811 (Meibom et al., 2013), NGC 2423 (Lovis and Mayor, 2007), M67 (Brucalassi et al., 2014, 2016), the Beehive (Praesepe) (Quinn et al., 2012), the Hyades (Quinn et al., 2014; Mann et al., 2016a; David et al., 2016) and Upper Scorpius (David et al., 2016; Mann et al., 2016b). All planets in M67, the planet in NGC 2423, one planet in the Hyades and the Praesepe planets were detected with the radial velocity (RV) method. All planets in NGC 6811, one planet in the Hyades and the planet in Upper Scorpius were discovered with the transit method. Additionally, a $\sim$2 Myr old hot Jupiter located in the Taurus-Auriga star forming region was detected via the RV method (Donati et al., 2016). All detections were of planets that likely harbor significant gaseous envelopes.

All transiting planets were detected with the *Kepler* space telescope. After the failure of two of its four reaction wheels, the original mission of the *Kepler* space telescope ended and was redirected for the "second light" survey *K2* (Howell et al., 2014). Instead of continuously observing the same area over years, the *K2* mission now switches fields every three months, stabilized by the two remaining reaction wheels and solar photon pressure for the third axis (roll angle). However, the telescope still drifts slowly and has to be corrected by firing the thrusters every 6 hours. Photometric precision is therefore slightly lower than during the *Kepler* mission but, as will be described in the following section, can be corrected very well.

The Beehive cluster (M44), also called Praesepe, is an open cluster targeted by *K2* in Campaign 5. It is nearby ($d = 183 \pm 8$ pc, van Leeuwen, 2009; Majaess et al., 2011) and of intermediate age. Past estimates placed the age of Praesepe at around 600 Myr (Fossati et al., 2008) but new estimates that take into account the effects of rotation in its high-mass members suggest an age as old 800 Myr (Brandt and Huang, 2015a). Furthermore, the kinematics (Madsen et al., 2002), metallicity (Dobbie et al., 2006) and age (Brandt and Huang, 2015a) of Praesepe are very similar to the Hyades cluster. The age of Hyades was also redetermined to 800 Myr (David and Hillenbrand, 2015; Brandt and Huang, 2015b) and it is now assumed that both clusters may share the same origin.

[1] While most stars form in embedded clusters, those usually dissipate in a timescale of 10 Myr (Lada and Lada, 2003) and we hence call them field stars.

Since transit signals become stronger the smaller the host star's radii, M-dwarfs are promising targets for the detection of small planets in open clusters. Dressing and Charbonneau (2015) estimate an abundance of rocky and small sub-Neptunian planets around those stars with periods shorter than 200 days at an average of 2.5 ± 0.2 planets per star with radii between $1 - 4\,R_{\oplus}$. Here, we present the discovery and validation of a transiting Neptune-sized planet in orbit around the Praesepe-member, low-mass star EPIC 211916756 which was detected in *K2* Campaign 5. In Section 4.2 we describe the layout of our photometric and spectroscopic follow-up and detail the subsequent results in Section 4.3. We validate the candidate as a planet in Section 4.4, discuss the impact of our findings in the context of exoplanets in clusters and the field in Section 4.5, and provide concluding remarks in Section 4.6.

4.2 Observations

4.2.1 K2 target selection and photometry

We identified the star EPIC 211916756 as a potential M-dwarf target and high probability member of the Praesepe cluster in our *K2* Campaign 5 (GO5006 - PI Schlieder) proposal. Other groups also proposed this star as a potential *K2* target (GO5011 - PI Beichman, GO5048 - PI Guzik, GO5095 - PI Agueros, GO5097 - PI Johnson).
EPIC 211916756 was observed during *K2* Campaign 5 with nearly continuous photometry from 2015 Apr 27 to 2015 Jul 10. We extracted the photometry from the pixel data which we downloaded from the MAST[2]. Our photometric extraction pipeline is described in more detail in Petigura et al. (2015) and Crossfield et al. (2015). During *K2* operations, the telescope is torqued by solar radiation pressure which causes it to slowly roll around the boresight. This motion causes stars to drift across the CCD by about 1 pixel every 6 hours. As stars are sampled by different pixels, intra-pixel sensitivity and flat-fielding variations cause the apparent brightness of the star to change. Thruster fires to correct for this drift affect the pointing and therefore pixel position greatly, giving the overall photometry a saw-tooth shape. We solve for the roll angle between each frame and an arbitrary reference frame and model the time- and roll-dependent brightness variations by using a Gaussian process. Further, we adjust the size of our square extraction aperture to minimize the residual noise in the corrected light curve. This balances two competing effects: larger apertures yield smaller systematic errors while smaller apertures include less background noise. The square extraction aperture ($r = 1$ pixel $\approx 4''$) for EPIC 211916756 is shown in Figure 4.5 on the left panel. The resulting, de-trended light curve exhibited slow, periodic, $\sim$1% modulations with a period of about 24 days which we attribute to spots on the star's rotating surface. The timescale of this variation is long compared to other M-dwarfs in Praesepe and places EPIC 211916756 among the slowest rotators in the cluster (see also section 4.3.5). This variation is fitted and removed to produce the final light curve which is shown in the top panel of Figure 4.1.
We searched through the optimized light curve with the TERRA algorithm which is described in more detail by Petigura et al. (2013b). In short, it searches for periodic photometric dimmings, in first order box-shaped, and fits them with a model from Mandel and Agol (2002). Using TERRA, we detected a transit signal in the light curve of EPIC 211916756 with a period of $P = 10.132$ d and a signal-to-noise ratio (S/N) of 23.97. The phase-folded light curve is shown in the bottom panel of Figure 4.1, centred around the transit event.

[2]The Mikulski Archive for Space Telescopes.

We subtracted the detected transits and iterated the TERRA algorithm to search for other transits at different periods but did not detect any secondary signals. It is not possible to identify periods longer than 25 days since the algorithm requires at least three visible transits for a detection and the overall observing time was 75 days. Visual inspection also did not reveal any additional transit features.

4.2.2 Photometric follow-up

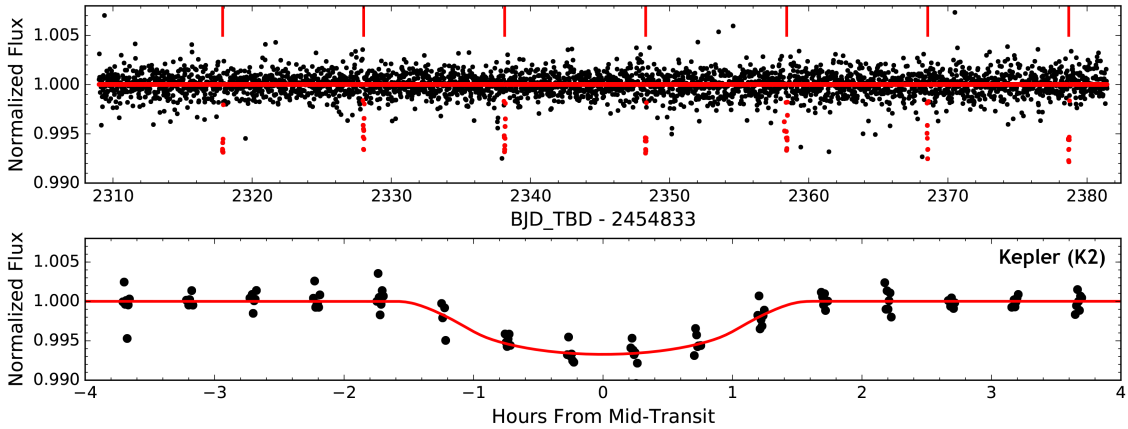

Figure 4.1: Top: Calibrated and normalized photometry for EPIC 211916756, recorded in the Kepler-band with K2. The upper red lines indicate the detected transits with the corresponding points also marked in red. Bottom: Period-folded light curve with the best-fitting transit model overlaid as a red line.

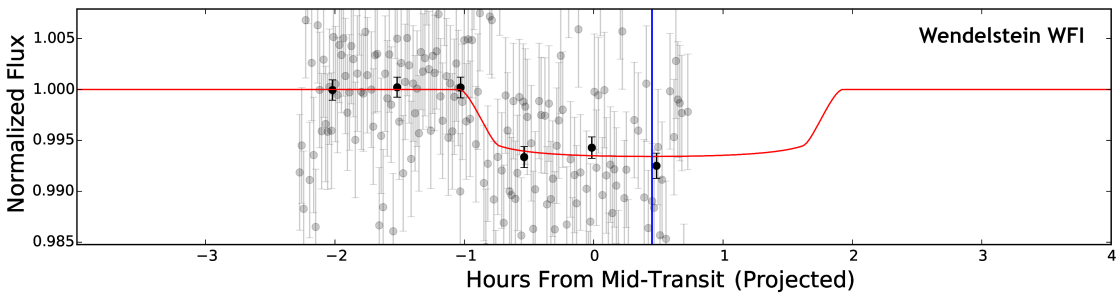

Figure 4.2: Normalized photometry in the i'-band for EPIC 211916756, recorded with the Wendelstein WFI. We overlaid the best-fitting transit model based on the *K2* data (see Figure 4.1), adapted with the corresponding quadratic limb darkening parameters for the i'-band. The binned points (black) agree very well with the model (red line) and share the same eclipse depth as the K2 light curve. The transit was shifted by about 27 min (new centre indicated by the blue line) which indicates an error in the initial period estimate within the fitting uncertainties. The original points (light grey) are shown in the background.

We observed EPIC 211916756 with the 2.0 m Fraunhofer Telescope Wendelstein (FTW) (Hopp et al., 2014), using the Wide Field Imager (WFI) (Kosyra et al., 2014), on Mt. Wendelstein in the Bavarian Alps. An independent transit detection from a ground-based facility

serves not only to confirm the period and estimate its uncertainty, but also as evidence for the planetary nature of the transit from a common eclipse depth at different wavelengths. Multi-band transit photometry can be used to characterize the planet's atmosphere or rule out false positive detections (Mislis et al., 2010; Southworth et al., 2012; Mancini et al., 2013; Ciceri et al., 2016). The limb darkening coefficients differ across photometric bands and can be used to differentiate between planetary signals and those of shallow-eclipse EBs. EPIC 211916756 was therefore followed up in the i'-band on UT April 16 2016 during suboptimal weather with seeing between 1″ and 3″ and cirrus activity. This led to aborting the observations after about three hours, or around mid-transit. However, due to the relative isolation of the target and reference stars on the CCD, the data were still salvageable and we could identify the transit after binning the data in 30 min intervals. The light curve, seen in Figure 4.2, shows the expected transit depth of 0.7% and agrees very well with the overlaid best-fitting transit model from the *K2* data, adjusted for the respective i'-band limb darkening coefficients. This light curve is already time-corrected and indicates a slight shift in phase. This implies that our initial period estimate may have been off by a few seconds per cycle, an effect seen in follow-up of previous *K2* planet discoveries (see Beichman et al., 2016), but it's still inside of the period uncertainty (see also § 4.5) of ≈ 60 sec. Following up transiting planets over larger baselines and therefore improving period accuracy is a valuable step in preserving the ephemeris for future studies.

4.2.3 IRTF/SpeX

We observed our target with the near-infrared cross-dispersed spectrograph (SpeX, Rayner et al., 2003) on the 3.0 m NASA Infrared Telescope Facility on Mauna Kea. EPIC 211916756 was observed on UT December 09 2015 under excellent conditions with a clear sky and an average seeing of 0.5″. We used the instrument's short cross dispersed mode (SXD) with the 0.3 x 15″ slit which provides a wavelength range of 0.68-2.5 μm and a resolution of R $\approx$ 2000. The target was placed at two locations along the slit and was observed in an ABBA pattern with 16×185s integrations for a total integration time of 2960 s. For telluric correction and wavelength calibration, we observed an A0 standard star plus arc and flat lamp exposures right after the target. We reduced the data with the SpeXTool package (Vacca et al., 2003; Cushing et al., 2004) which performs flat fielding, sky subtraction, bad pixel removal, spectral extraction/combination, telluric correction, wavelength+flux calibration and order merging. We achieved a median signal-to-noise ratio (SNR) of 70 per resolution element in the J- (1.25 μm), 80 in the H- (1.6 μm) and 60 in the K-band (2.2 μm). We compare the JHK-band spectra to late-type standards from the IRTF Spectral Library, seen in Figure 4.3. The best visual match for EPIC 211916756 lies between M2 and M3 standards across all infrared bands.

4.2.4 Keck/HIRES

We obtained a high-resolution optical spectrum of EPIC 211916756 using the HIRES echelle spectrometer on the 10m Keck I telescope (Vogt et al., 1994) on UT December 23 2015. Our observation followed the procedures of the California Planet Search (CPS, Howard et al., 2010). We used the "C2" decker, providing a spectral resolution of R = 55000, and subtracted the sky from the stellar spectrum. We utilized the HIRES exposure meter to automatically terminate the exposure when SNR = 32 per pixel was achieved. The HIRES spectrum was

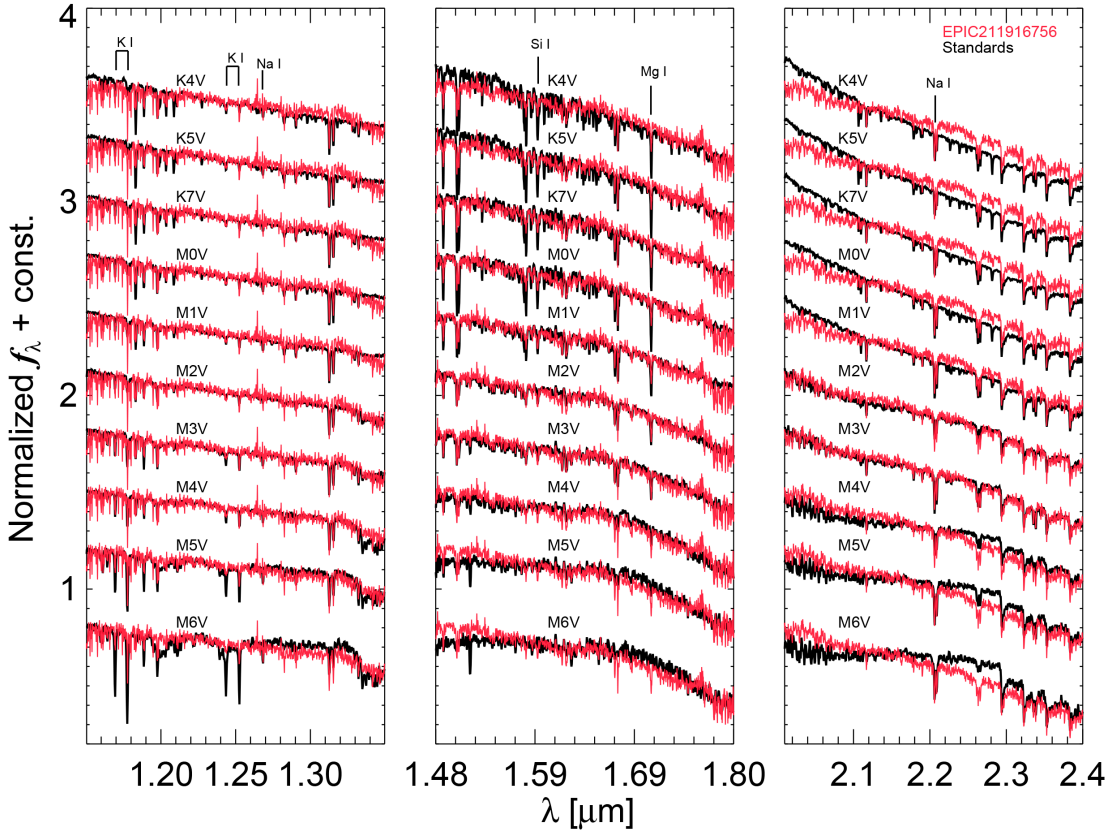

Figure 4.3: JHK-band IRTF/SpeX spectra of EPIC 211916756, compared to K4V-M6V standard spectra from the IRTF spectral library. Each spectrum is normalized to the continuum. The closest visual match for our target are types M2V and M3V in all three bands. This is consistent with our SED fitting results and spectral typing using spectroscopic indices.

reduced using standard CPS procedures and cover ∼3600 – 8000 Å. Two additional spectra were obtained on UT December 24 and 29 using a redder setting of HIRES at R=48,000; these data are described in Pepper et al. (2016, in prep.).

4.2.5 Keck/NIRC2

We obtained high resolution NIR images of EPIC 211916756 with NIRC2 on the 10m Keck II telescope, using the target as a natural guide star to drive the adaptive optics (AO) system. We observed the target on UT January 16 2016 in the K-band, following a multi-point dither pattern with integration times short enough to avoid saturation. We used the dithered images to subtract the sky background and remove the dark current, then aligned, flat-fielded and stacked the individual images. The star appears single and has no close companions within several arcseconds. To estimate the sensitivity of the NIRC2 observations, we injected fake sources with SNR = 5 into the combined image at separations that are integral multiples of the star's FWHM. We show our final image and the 5σ sensitivity curve in the left panel of Figure 4.4.

4.2.6 Gemini-N/DSSI

We also obtained speckle imaging of EPIC 211916756 on UT January 16 2016 in two narrow band filters centred at 880 nm and 692 nm using the DSSI camera (Horch et al., 2009) which is mounted on the 8m Gemini North telescope. We followed a standard observing procedure where the star was centred in the field, guiding was established, and images were taken using 60 ms exposures. The data were reduced and combined into a final reconstructed image using the techniques described in Horch et al. (2011) and Howell et al. (2012). These procedures perform automatic model fits (single, double, triple) and provide estimates of the magnitude difference and separation for multiple systems. EPIC 211916756 was found to be a single star. We measured the background sensitivity of the reconstructed DSSI image by using a series of concentric rings (annuli) centred on the target. The innermost annulus is at the telescope diffraction limit where our sensitivity is zero. The sensitivities in the subsequent annuli are interpolated using a cubic spline to produce a smooth sensitivity curve. The 880 nm reconstructed DSSI image and sensitivity curve are shown in the right panel of Figure 4.4.

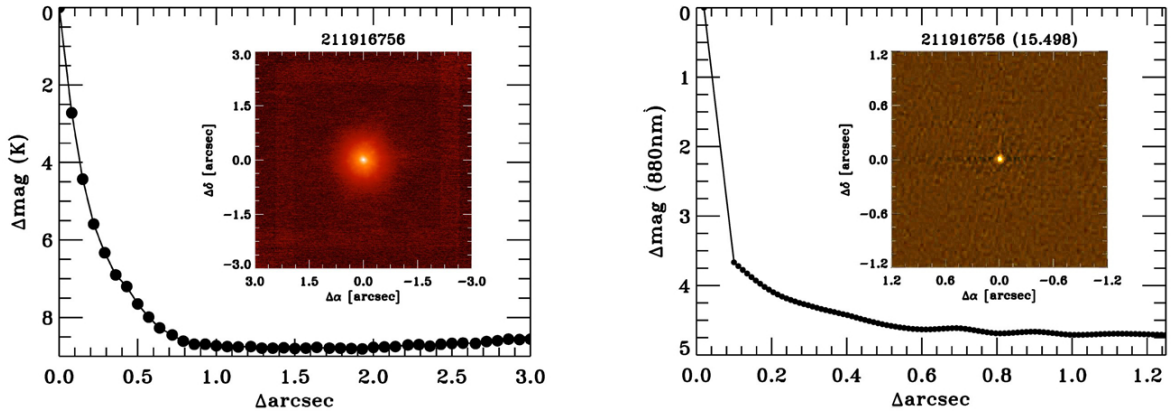

Figure 4.4: High-resolution imaging of EPIC 211916756. Left: NIRC2 K-band image and contrast curve. Right: DSSI 880 nm reconstructed image and contrast curve. The star appears single in both images and the sensitivity curves rule out the majority of close companions or background stars that would contribute significant flux to the transit light curve.

4.2.7 Archival imaging

Data taken from photographic plates, now digitally scanned and available online, cover several decades of astrometry. Our target was first observed in 1954 by the Digital Sky Survey (DSS) in the red and blue channels with an additional epoch from 1989 and 1990, respectively. We show the red DSS plates from 1954 and 1989 in Figure 4.5. The images are centred on the epoch 2015 coordinates of the target in the EPIC database (08:37:27.059, +18:58:36.07) and the K2 aperture is overlaid as a green square. The target's proper motion of 1.4 arcsec over the course of 35 years results in a visible shift in position, seen in comparison of the middle and left panels in Figure 4.5. Based on the archival data, there is no indication for a background star at the 2015 epoch position. If there is a star still hidden in the background it must be quite faint in which case it would not significantly dilute the transit signal.

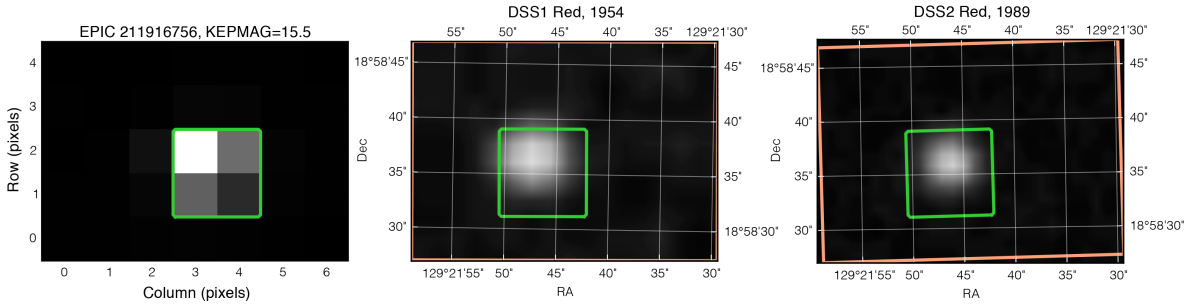

Figure 4.5: *K2* photometry with the pixels used for the light curve creation (left). DSS (red) plates observed in 1954 (middle) and 1989 (right). The circle shows the dimensions and location of the aperture that was used for the candidate's photometry. Over these past 35 years, EPIC 211916756 moved about 1.4 arcsec, which is noticeable in comparison of both archival images.

4.3 Host star characterization

Validation of the transiting planet candidate and constraints for its physical parameters require detailed characterization of the host star's properties. We used several approaches to estimate the fundamental parameters of EPIC 211916756, including medium-resolution spectroscopy, multi-band photometry and kinematics. We place further constraints on close bound companions and background stars from our high-resolution spectroscopy and imaging. The results of these data are used to perform a false positive probability analysis of the planet candidate and estimate its properties. The final stellar properties are shown in Table 4.1.

4.3.1 Medium-resolution spectroscopy

We apply the index based methods of Mann et al. (2013a,b, 2015) and equivalent width (EW) based methods of Newton et al. (2014, 2015) to our SpeX spectrum in order to estimate the metallicity, temperature, radius, and luminosity of EPIC 211916756. These approaches are calibrated empirically by using wide M-dwarf binary companions and nearby bright M-dwarf standards with interferometrically measured radii. Our SpeX spectrum, shown in Figure 4.3, suffers from poor telluric correction in the J and H-bands. These residuals result from the long exposure time of the target which led to a large time baseline (nearly 1 hour) and non-ideal airmass difference (>0.1) between the target and A0 calibrator. To avoid the systematic effects introduced when using the index based methods of Mann et al. (2013b) in regions of poor telluric correction (Mann et al., 2013a; Newton et al., 2015), we use only their K-band relations. Prior to any analyses, the spectrum was shifted by its radial velocity estimated via cross-correlation with an M-dwarf standard.
To estimate the star's metallicity, we use IDL software provided by A. Mann and E. Newton[3]. Using the Mann et al. (2013a) K-band index relations, we estimate a metallicity $[\mathrm{Fe/H}] = 0.09 \pm 0.09$ dex. The K-band EW based methods of Newton et al. (2014) provide $[\mathrm{Fe/H}] = 0.12 \pm 0.14$ dex. The uncertainties were estimated through using Monte-Carlo sampling by introducing small variations in the data and measuring their impact on the fitting result. These estimates are consistent with each other and also with the metallicity of Prae-

[3]https://github.com/awmann/metal, https:// github.com/ernewton/nirew

Parameter	EPIC 211916756	Reference
Epoch	J2000	1
RA	08:37:27.059	1
DEC	+18:58:36.07	1
μ_α	-36.7 ± 3.0 mas yr^{-1}	2
μ_δ	-15.1 ± 3.0 mas yr^{-1}	2
RV	35.2 ± 0.2 km s^{-1}	3
K_p	15.498 mag	1
g'	17.779 ± 0.00240 mag	4
r'	16.596 ± 0.00110 mag	4
i'	15.369 ± 0.00079 mag	4
z'	14.789 ± 0.00096 mag	4
y'	14.529 ± 0.00220 mag	4
J	13.312 ± 0.01700 mag	5
H	12.738 ± 0.02300 mag	5
K	12.474 ± 0.01900 mag	5
Spectral Type	M3.0 $\pm$ 0.5	6
$T_{\rm eff}$	3471 ± 124 K	6, 8
$T_{\rm eff}$	3400 ± 100 K	7
d	171 ± 15 pc	7
d	172 ± 14 pc	3
[Fe/H]	0.11 ± 0.17	6, 8
Radius	0.402 ± 0.050 R$_\odot$	6, 8
Radius	0.381 ± 0.070 R$_\odot$	7
Luminosity	0.021 ± 0.008 L$_\odot$	6, 8
Mass	0.361 ± 0.069 M$_\odot$	6
Density	7.81 ± 1.90g cm^{-3}	6

Table 4.1: Stellar parameters for EPIC 211916756. References are: 1 - EPIC Catalogue; 2 - Kraus and Hillenbrand (2007); 3 - this work; 4 - Pan-STARRS1 3π catalogue (version PV3); 5 - 2MASS catalogue; 6 - this work, using (Mann et al., 2016a); 7 - this work, using SED fitting from Obermeier et al. (2016); 8 - this work, using Newton et al. (2015)

sepe, [Fe/H] $= 0.12 \pm 0.04$ dex (Boesgaard et al., 2013).
We estimate the effective temperature using the K-band index relations of Mann et al. (2013b) and the H-band EW-based relations of Newton et al. (2015) using IDL software provided by A. Mann and E. Newton[4]. The K-band relations provide $T_{\rm eff} = 3460 \pm 73$ K where the adopted uncertainty is the scatter in the polynomial fit. The H-band relations yield $T_{\rm eff} = 3481 \pm 100$ K. The uncertainty was again estimated by using Monte Carlo sampling of the measurement error in the spectrum. These consistent effective temperatures are used to estimate the radius and luminosity of the star using the aforementioned empirical calibrations. Following the Mann et al. (2013b) relations, we estimate the stellar radius $R_* = 0.393 \pm 0.036$ R$_\odot$ and luminosity $L_* = 0.017 \pm 0.006$ L$_\odot$. The Newton et al. (2015) relations provide a radius $R_* = 0.411 \pm 0.034$ R$_\odot$ and luminosity $L_* = 0.024 \pm 0.006$ L$_\odot$. These fundamental parameters, estimated by using different methods, are consistent at the $< 1\sigma$

[4]https://github.com/awmann/Teff_rad_mass_lum, https://github.com/ernewton/nirew

level. We adopt the means of these estimates for further analyses and calculate conservative uncertainties by adding the individual errors in quadrature. The best fit for the star's distance is 169 ± 12, consistent with membership in the Praesepe cluster. All final values are provided in Table 4.1. The methods of Mann et al. (2013b) also provide estimates of the star's mass and density, $M_* = 0.361 \pm 0.069$ $M_\odot$ and $\rho_* = 7.81 \pm 1.90$ g cm^{-3}, respectively. We further used the H20_K2 index (Rojas-Ayala et al., 2012) to estimate the spectral type of the star. We determine EPIC 211916756's type to be M3.0 $\pm$ 0.5, consistent with visual comparisons to standard stars and our spectroscopic temperature estimates.

4.3.2 SED fitting

We utilize the SED fitting code from Obermeier et al. (2016) as an additional layer of our stellar type characterization. In contrast to spectroscopy, this approach relies on broad-band photometry. We extract the Pan-STARRS1 3π data for this star and cross-match its coordinates with the 2MASS catalogue. For the synthetic stellar SED catalog, we use the newest version of the PARSEC isochrones package (Bressan et al., 2012) which includes improvements for low-mass stars that were calibrated for Praesepe (Chen et al., 2014). The age of the cluster is known (Brandt and Huang, 2015b), therefore we restrict the synthetic model population to 800 Myr and Praesepe's metallicity of ([Fe/H] = 0.12 dex). Since the isochrone models are for nonrotating stars, we furthermore include a second set of isochrones at 650 Myr. Furthermore, we create a 10th order polynomial to interpolate between the distance-dependent extinction values given in the 3D dust map from Green et al. (2015)[5] and iteratively fit distance and extinction until both converge. We find that the final photometric fits for temperature and radius, $T_{\rm eff} = 3386 \pm 100$ K and $R_* = 0.43 \pm 0.070 R_\odot$, agree very well with the spectroscopic results and the extinction is negligible with $E(B-V) = 0.0016$. The better fit was for the 650 Myr model with a marginally better χ^2 of 7.83 against 7.97. We also estimate a distance of 171 $\pm$15 pc which is consistent with a Praesepe cluster membership and the derived distance of 172 $\pm$14 pc based on kinematic distance and K-band magnitude.

4.3.3 High-resolution spectroscopy

We use the methodology and algorithm of Kolbl et al. (2015) to search for blended background stars or close spectroscopic binary companions in the HIRES spectrum. The secondary line analysis compares the observed spectrum to a suite of about 600 well characterized, slowly rotating HIRES spectra of FGKM stars from the California Planet Search and attempts to identify residuals consistent with a fainter secondary star. For faint, late-type stars like EPIC 211916756, this method is sensitive to spectroscopic companions projected within one half the HIRES slit width (0.4″), with approximate V-band fluxes as small as 3% of the primary flux and ΔRV $>$ 10km s^{-1}. This sensitivity range complements our high-contrast imaging. The algorithm further measures the barycentrically-corrected primary RV using telluric lines. The analysis revealed no secondary lines within the above sensitivity limits. Using the colour-temperature conversions of Pecaut and Mamajek (2013), we estimate that the Kolbl et al. (2015) analysis of our HIRES spectrum rules out a large range of close companions on circular orbits down to $\sim$M5.5 types on $\sim$75 day or shorter orbits. Additionally, we measure RV $= 35.2 \pm 0.2$ km s^{-1} which consistent with other Praesepe members. The combined RV constraints from our multi-epoch HIRES observations are described further in section 4.4.1.

[5]http:// argonaut.rc.fas.harvard.edu/

We further cross-correlated our HIRES spectrum with a slowly rotating, rotationally broadened M-dwarf standard to place constraints on the projected rotational velocity $v\sin i$. This analysis revealed that the star has a low rotational velocity with the best-match broadened spectrum having $v\sin i < 3$ km s^{-1}. This low $v \sin i$ and the long rotation period ($\sim$24 days) estimated from de-trended *K2* photometry are consistent with the slowest rotating Praesepe M-dwarfs presented in Douglas et al. (2014). Both indications of slow rotation are also consistent with the low level of magnetic activity inferred from the Hα line. The slow rotation of this intermediate age M-dwarf is remarkable when considering its close in planet (see §**??**) and may indicate differences in angular momentum evolution due to initial conditions, the primordial disk, planet formation, or planet migration. In contrast, the very similar Hyades M-dwarf planetary system K2-25 is among the fastest rotating M-dwarfs in that cluster with a period of $\sim$1.9 days (Douglas et al., 2014; Mann et al., 2016a; David et al., 2016).

4.3.4 High-resolution imaging

Using the Gemini/DSSI speckle results, we can constrain the contamination from nearby sources. The DSSI data in the 880 nm band provide the best constraints to bound and background companions at very close separations. At a separation of 0.1″, our sensitivity to companions is Δmag(880 nm) $\approx$ 3.5 mag.
Our Keck/NIRC2 AO imaging provides deeper constraints on close background and bound companions at larger separations. At separations of 0.5″ and 0.2″, we estimate to be sensitive to companions with ΔK $\approx$ 8 mag and ΔK $\approx$ 5 mag, respectively. This effectively rules out all background sources within these separations that could contribute significant flux to the light curve. We use the relations of Pecaut and Mamajek (2013) to estimate that our combined Keck and Gemini imaging rule out all bound companions at the same distance down to the hydrogen burning limit at separations of 0.1″ ($\sim$17 AU) and well into the brown dwarf regime at $\gtrsim$ 0.5″ ($\sim$86 AU). We use both our Keck/NIRC2 and Gemini/DSSI contrast curves as constraints in the false positive probability analysis.

4.3.5 Cluster membership, kinematics, and age

EPIC 211916756 was first identified as a candidate member of Praesepe by Williams et al. (1994) and was subsequently included in the proposed member lists of several works including Hambly et al. (1995) and Adams et al. (2002). Kraus and Hillenbrand (2007) combined photometry, astrometry, and the kinematics of well defined cluster members in a maximum likelihood analysis to estimate that EPIC 211916756 has a >99% probability of cluster membership. To further investigate its Praesepe membership, we use the star's partial kinematics and the methods described in Lépine and Simon (2009) to estimate a kinematic distance (d_{kin}) and predicted radial velocity (RV_p). In the analysis we adopt the UVW Galactic velocities of Praesepe from van Leeuwen (2009) and estimate errors using Monte Carlo sampling. We find $d_{kin} = 172 \pm 14$ pc, consistent with our SED-based estimates of the star's distance and the average cluster distance, and $RV_p = 34.1 \pm 0.9$ kms^{-1}, consistent with our measured RV from Keck/HIRES spectroscopy. The consistency of these predictions and measurements, along with the spectroscopic indications of activity in our HIRES data, confirms the membership of EPIC 211916756 in the low-mass population of Praesepe which places a conservative constraint on its age of 600-800 Myr. We also use the kinematic distance and K-band magnitude of the star to determine its luminosity using the conversions of Pecaut and Mamajek (2013)

to $L_* = 0.021 \pm 0.003\ L_\odot$. At the age of Praesepe, an M3 dwarf is expected to be on the main sequence and has stopped radial contraction. We can therefore combine our measured effective temperature and luminosity through the Stefan-Boltzman law to estimate the star's radius, $R_* = 0.40 \pm 0.01\ R_\odot$. These alternate estimates of the star's fundamental parameters are consistent with those from our SpeX spectroscopy and SED fitting.

4.4 Planet validation

4.4.1 False positive probability

Our collected data in form of photometry, spectroscopy, and high-resolution imaging can be used to place a number of constraints on the data in order to limit or even completely rule out all of the plausible false-positive scenarios (see section 1.8.8). In the *K2* data itself, we detected no secondary eclipse that would be indicative of an EB. Based on archival photometry, high-resolution imaging and high-resolution spectra, a background source is strongly constrained to less than 3% of flux dilution and can be ruled out completely for a separation of more than 0.2 arcsec. This makes any kind of background blend or triple system very improbable. In case a background blend did exist, it would not impact the planet parameters significantly due to the low flux contribution.
For a more quantitative assessment, we utilize the false positive probability (FPP) calculator *vespa* (Morton, 2012, 2015) which is open source and freely available online[6]. This program compares the light curve to transit shapes created by false-positive sources and combines this with priors about stellar population, multiplicity frequencies and the planet occurrence rate for the corresponding fitted parameters (see also section 1.8.8). We supply the algorithm with all of our determined constraints:

- Stellar parameters (radius, effective temperature, limb-darkening coefficient)
- Multi-band photometry from Pan-STARRS1, 2MASS, and WISE
- Contrast curves from adaptive optics and speckle imaging
- Light curve and period from *K2*

Furthermore, we also extract the photometric light curve from Vanderburg and Johnson (2014), remove the periodic modulations, recover the signal with the Pan-Planets signal detection pipeline (Obermeier et al., 2016) and then perform the same analysis. This way, we end up with an independent confirmation based on a different data reduction and signal detection routine. Based on all of the above constraints, the results from *vespa* rule out all false positive scenarios to a FPP of less than 0.02% for both analyses. The more strongly constrained result, using the reduced light curves from Vanderburg and Johnson (2014) and fitting the signal based on the methodology of Obermeier et al. (2016), is shown in Figure 4.6. While *vespa* does not fit blended planetary systems, there are strong constraints on this scenario based on high-resolution imaging and the upper limit of 3% in flux dilution for background sources which makes this scenario highly unlikely. As an additional layer of security, we furthermore obtained three RV points based on high-resolution spectroscopy in order to constrain any EB or double-period EB scenario independently of *vespa*.

[6] https://github.com/timothydmorton/vespa

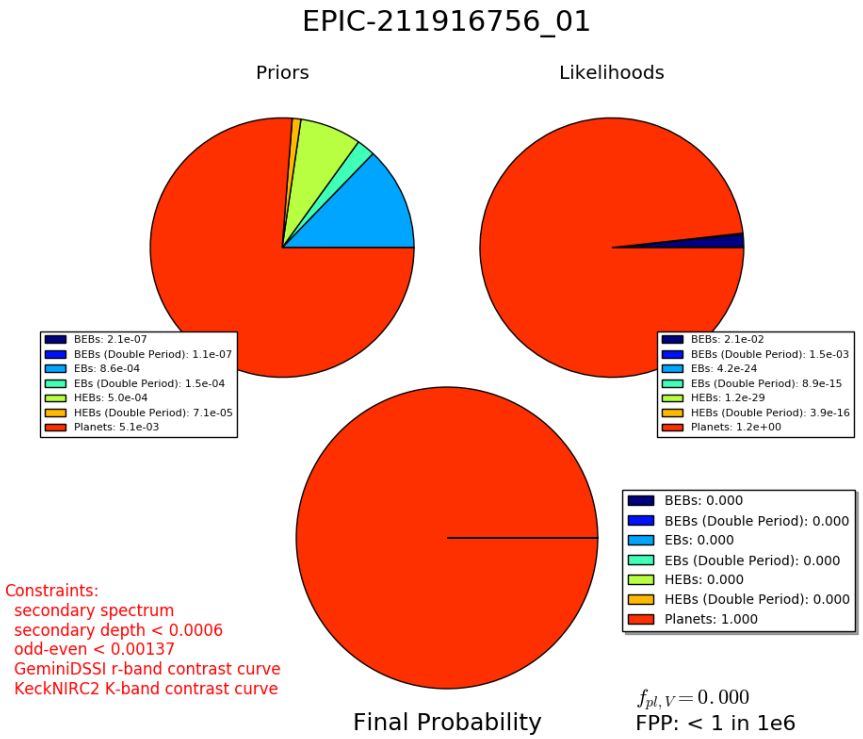

Figure 4.6: FPP result from *vespa* for EPIC 211916756. Constraints are shown in red in the bottom left. The odd-even factor is a limit for the difference between primary and secondary eclipse in case of the double-period scenario and is determined by the photometric precision of the transit.

Unblended EB system

The unblended EB scenario consists of very shallow eclipses of both stars which may emulate a planet's transit light curve. There are many constraints to this scenario in the case of EPIC 211916756: the signal of a secondary eclipse is absent in the light curve data and the obtained Keck spectrum excludes the presence of a second star down to $10\,\mathrm{kms}^{-1}$ and 3% flux. Based on both our own observation with HIRES and the two additional data points from Pepper et al. (2016, in prep.), we cover a time baseline of 6 days. We construct an upper limit for the RV function, assuming a circular orbit, with the highest amplitude that can still be fit to the data at 5σ. The resulting function, shown in Figure 4.7, has an amplitude of $\mathrm{RV}_{\mathrm{max}} = 941\mathrm{ms}^{-1}$ which equates to a companion mass of $5.25\mathrm{M}_{\mathrm{J}}$, a giant planet.

Double-period EB system

The double-period case is different to other scenarios in that it assumes an EB system in which both partners have the same size and eclipse each other; the period is therefore twice as long. This changes fundamental parameters such as the relative eclipse duration and impacts the secondary eclipse criterion - strong constraints on the secondary eclipse make this scenario even more likely. It was the only scenario for which *vespa* estimated a noteworthy probability of about 0.5%. However, additional factors help in ruling out this scenario completely.

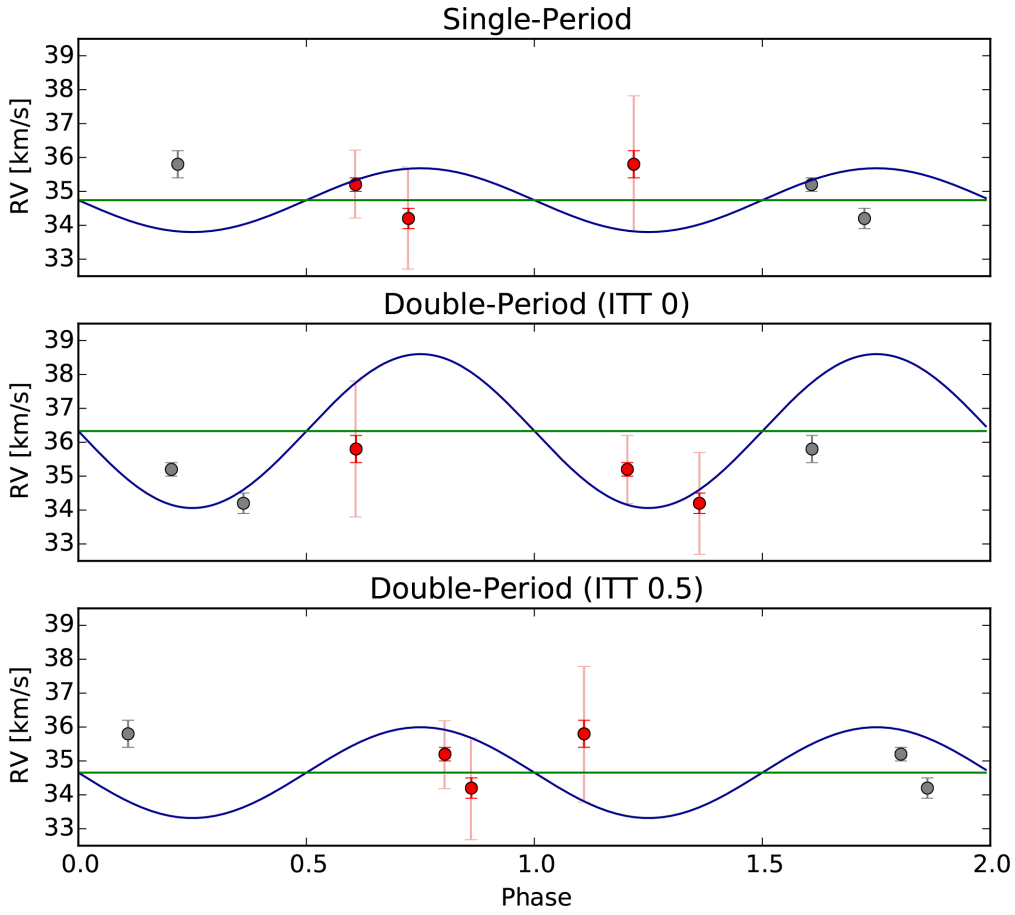

Figure 4.7: Radial velocity points (red) for EPIC 211916756 in the single-period (top) and double-period scenario (middle+bottom), phased to the corresponding period and ITT scenario. ITT stands for the initial time phase of the first recorded eclipse, i.e. whether the primary or secondary star eclipsed first. The RV curve (blue) shows the maximum amplitude consistent with the data at 5σ. Two phases are shown for better clarity with repeated points greyed out and the error bars of the points are given 1σ (red) and 5σ (light red). The green line shows the baseline fit.

Both partners must have similar radii in this case. As with the single-period EB scenario, we combine our HIRES RV measurement with the two measurements presented in Pepper et al. (2016, in prep.) to cover a total time baseline of 6 days. These RV measurements cover a substantial portion of the transiting planet candidate's phase and allow us to construct an RV curve for the maximum amplitude at the 5σ level, which is shown in Figure 4.7. Two cases have to be considered, depending on whether the initial transit time (ITT) was at phase 0 or 0.5 (ITT 0 and ITT 0.5, respectively), i.e. whether the first eclipse was in front of the primary or secondary star. We place an RV limit of $\mathrm{RV_{max}}$=2270 $\mathrm{ms^{-1}}$ for ITT 0 and $\mathrm{RV_{max}}$ =1343 $\mathrm{ms^{-1}}$ for ITT 0.5. Taking the stellar mass determined by medium-resolution spectroscopy and assuming a circular orbit, this translates to 15.46 $\mathrm{M_J}$, a low-mass brown dwarf, or 9.14 $\mathrm{M_J}$, a giant planet. Any stellar companion would produce a much stronger RV signal and an eclipse of the primary in front of a brown dwarf cannot create an identically

deep eclipse signal. Furthermore, brown dwarf companions have already been ruled out by *vespa* due to the rarity of close-orbit brown dwarf companions (Marcy and Butler, 2000; Udry and Santos, 2007; Kraus et al., 2008).
Furthermore, EPIC 211916756 has a probability of more than 99% for being a member of the Praesepe cluster which means that the baseline of the fitted RV curve for the case of ITT 0, RV = 36.3 km s^{-1}, should be consistent with the cluster RV$_{\rm p}$ = 34.1 ± 0.9 kms^{-1}. ITT 0 is only consistent at 3σ which further decreases the likelihood of this scenario. In contrast, the RV baseline for a single-period transiting planet scenario is very consistent with a best fit of 34.8 kms^{-1}. Therefore, in combination with all of the other constraints (e.g. AO imaging, archival optics, stellar characterization), we can rule out this scenario independently from *vespa*.

4.5 Planet parameters

We analyse the light curve of EPIC 211916756 with an approach similar to the one described in more detail by Crossfield et al. (2015)[7]. In brief: Relying on the *emcee* package (Foreman-Mackey et al., 2013), we first use the open-source BATMAN light curve code (Kreidberg, 2015) to fit a transit model based on Mandel and Agol (2002). This approach is very similar to the Pan-Planets MCMC fitting model (see section 3.2.5). Utilizing the free and open-source LDTk/pyLDTk package from Parviainen and Aigrain (2015)[8], we propagate our measured T$_{\rm eff}$, surface gravity, metallicity and their respective uncertainties into limb-darkening coefficients for use as priors in our fit. The overall fitted parameters in our analysis are the candidate's orbital period P, initial transit time T_0, inclination i, eccentricity e, longitude ω, scaled semi-major axis $a/R_\star$ and the fractional candidate radius $R_p/R_\star$. The starting parameters for the fit are taken from our TERRA output. In the fit, we do not assume any kind of TTV's in the light curve. The best-fitting properties and their uncertainties are shown in Table 4.2.

Parameter	Units	EPIC 211916756
T$_0$	BJD$_{\rm TDB}$ - 2454833	$2338.1477^{+0.0018}_{-0.0019}$
P	d	$10.13389^{+0.00068}_{-0.00077}$
i	deg	$88.77^{+0.86}_{-1.59}$
$R_P/R_\star$	%	$7.86^{+1.69}_{-0.93}$
R$_\star$/a	—	$0.0400^{+0.0187}_{-0.0068}$
T_{14}	hr	$2.84^{+0.36}_{-0.26}$
T_{23}	hr	$2.18^{+0.26}_{-0.72}$
a	AU	$0.0653^{+0.0039}_{-0.0045}$
R_P	R_E	$3.47^{+0.78}_{-0.53}$
$R_\star$	$R_\odot$	$0.402^{+0.050}_{-0.050}$
$M_\star$	$M_\odot$	$0.361^{+0.069}_{-0.069}$

Table 4.2: Best-fitting properties of EPIC 211916756 and its planet based on the BATMAN code.

[7]Further information about the most up- to-date method will be found in Crossfield et al. (2016), in prep.
[8]https://github.com/hpparvi/ldtk

We estimate the planet's mass by using the mass-radius relation[9] provided by Wolfgang and Lopez (2015) and Wolfgang et al. (2016), $M/M_\oplus = 2.7(R/R_\oplus)^{1.3}$. This results in a mass $M_P = 13.71 \pm 3.62\ M_\oplus$[10]. However, using the relation provided by Weiss and Marcy (2014), $M/M_\oplus = 2.69(R/R_\oplus)^{0.93}$, we get $M_P = 8.77^{+1.88}_{-0.53}\ M_\oplus$. A third mass-radius relation, published by Chen and Kipping (2016)[11], yields $M_P = 8.26^{+1.77}_{-0.50}\ M_\oplus$[12] based on the relation $M/M_\oplus = (R/R_\oplus)^{1.70}$. The mass-radius models therefore lead to different estimates of the planet's mass. While the results from Wolfgang and Lopez (2015) are higher than the other two, the difference is still small enough for the masses to be marginally consistent with each other. The absence of TTV's in the system means that the planet's mass cannot be determined through other means as of now. Based on the Wolfgang and Lopez (2015) result with a mass of $M_P = 13.71 \pm 3.62\ M_\oplus$ and a stellar mass of $0.361^{+0.069}_{-0.069} M_\odot$, we estimate the RV amplitude of this planet to be $6.8 \pm 1.8\,m\,s^{-1}$,

4.6 Discussion

So far, only very few planets have been detected in clusters, even less with the transit method. EPIC 211916756b is only the third known planet in an open cluster that orbits around an M-dwarf. It most likely belongs to the class of Neptune-size planets with a similar chemical composition and H/He atmospheres (Marcy et al., 2014; Weiss and Marcy, 2014; Rogers, 2015).
However, it is remarkable that the occurrence rate of planets with the radius and period of both K2-25 (Mann et al., 2016a; David et al., 2016) and EPIC 211916756b is very low around field stars (Dressing and Charbonneau, 2015; Mulders et al., 2015b). Furthermore, the recently discovered planet K2-33b in the open cluster Upper Scorpius (David et al., 2016; Mann et al., 2016b) exhibits an unusually large radius as well.
While there are four discovered systems with planet radii similar to EPIC 211916756b and K2-25b, they are even larger and orbit higher-mass stars. Furthermore, the received stellar flux appears to be significantly higher. The distribution of planetary radii and received radiation against the host star mass is shown in Figure 4.8. We placed following restrictions: All planets in this Figure have to be confirmed and we extract the most recent planetary and stellar parameters from the NASA exoplanet archive (Akeson et al., 2013). Furthermore, the host star radii have to be below $0.5\,R_\odot$ and the planet irradiance was calculated when missing.
The probability of detecting three such planets in a cluster without any detections in the larger field star sample, plus another detection in a scarcely populated region of larger-radius planets, is too low to be random chance. We present two possible implications from this:

- The formation of short-period planets is different in clusters due to gravitational interactions during migration. An indication for this may be the higher occurrence rate of hot Jupiters in M67 measured by Brucalassi et al. (2016). However, Meibom et al. (2013) found an occurrence rate similar to that of field stars for NGC 6811. As of now, there is insufficient information to confirm this theory.

[9] And their code: https://github.com/dawolfgang/MRrelation
[10] The code cannot handle asymmetrical errors, hence we selected the larger of both uncertainties.
[11] https://github.com/chenjj2/forecaster
[12] The code cannot handle asymmetrical errors, hence we used the larger of both uncertainties.

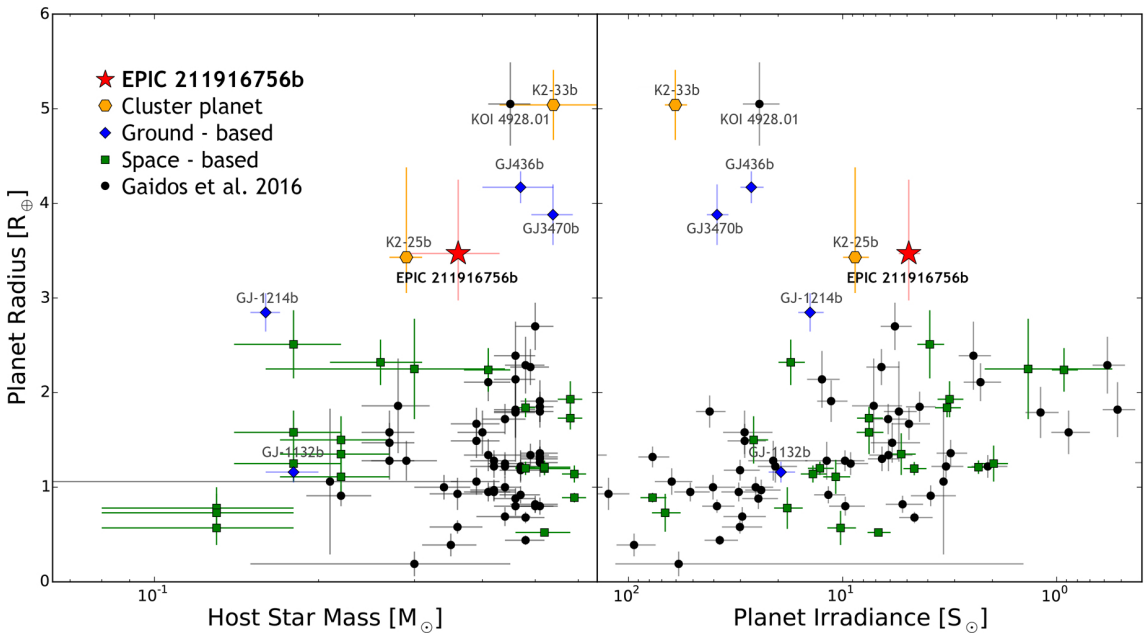

Figure 4.8: Planet radius as a function of the host star mass (left) and received radiation (right), comparing our discovery EPIC 211916756 (red star) to planet detections in open clusters (orange hexagons), ground-based surveys (blue diamonds), space-based (Kepler+K2) surveys (green squares), and revised values for several Kepler planets from Gaidos et al. (2016) (black circles). Similar to Mann et al. (2016a), only stellar radii below 0.5 $R_\odot$ and periods below 100 d were included. Two exceptions to those criteria are RV-planet GJ 3470b and K2-33b which got added due to their similarity despite a larger host star radius. All RV detections and inflated planets are labelled.

- M-dwarfs remain active for several hundred Myr after their formation to a varying degree (Shkolnik and Barman, 2014). Strong UV emission in the relatively young Hyades and Praesepe cluster M-dwarfs might lead to the inflation seen in Figure 4.8. Young planets may also be larger due to initial heat from formation (Mann et al., 2016a).

- It is possible that this is due to a selection bias since young stars are more active. Their variability may mask many of the small-planet transit signals, leading to a perceived imbalance. However, EPIC 211916756 is only weakly active so while a selection bias may exist, it is unlikely to be the sole reason.

Measuring the stellar UV activity and the planet's mass will allow to determine whether the reason behind the large radii is inflation due to strong UV irradiation and/or initial heat. If that were the case, they could be seen as outliers of the general planet mass-radius relation and might be similar to GJ 436b, a Neptune-sized planet first detected by RV measurements (Butler et al., 2004) that is showing visible transits (Gillon et al., 2007) and appears to evaporate (Ehrenreich et al., 2015). However, as can be seen in Figure 4.8 on the right, GJ 436b receives several times of EPIC 211916756b's radiation so it is questionable whether this may apply here. Both cluster detections also orbit noticeably smaller stars than the larger Neptunian planets.

Besides this anomaly, EPIC 211916756b is also intriguing for a number of other reasons, especially for having a well-determined distance, (young) age and metallicity. Only very few planets are known around relatively young stars and new detections will contribute towards establishing a more accurate timeline of a planet's development.
Assuming a circular orbit - considering the transit duration shows no indication of ellipticity a valid simplification - and using the mass-radius relation from Wolfgang and Lopez (2015), we calculate the radial velocity amplitude to $6.8 \pm 1.8\,\mathrm{m\,s^{-1}}$. While an accuracy of $\mathrm{m\,s^{-1}}$ is entirely feasible today with instruments like HIRES or HARPS, the target is too faint to realistically achieve this with today's telescopes in reasonable observing times. However, future dedicated infrared spectrographs such as CARMENES, IRD, HPF and SPIRou (Quirrenbach et al. (2014), Artigau et al. (2014), Kotani et al. (2014) and Mahadevan et al. (2012), respectively) will allow the determination of the planet's mass. This in turn will also provide additional data for the calibration of the mass-radius relation of Neptune-sized gas planets. Next-generation large telescopes such as the E-ELT or the TMT may enable a detailed study of the planet's atmosphere.
As an alternative to spectroscopy, multi-band photometry enables a more detailed study of the planet, even for stars that are too faint for atmosphere spectroscopy. Since the transit depth may change in different photometric bands due to Rayleigh scattering or varying opacities, the atmosphere can be modelled (Southworth et al., 2012; Mancini et al., 2013; Ciceri et al., 2016). While this is possible to do with single-band photometric instruments, simultaneous multi-band capture with GROND (Greiner et al., 2008) or the upcoming 3 channel imager 3KK at Mt. Wendelstein (Lang-Bardl et al., 2010) would be much more advantageous.

4.7 Summary

We report on the discovery of a Neptune-sized planet in the Beehive cluster (Praesepe) that orbits a cool dwarf star. Discussing and subsequently ruling out each possible false-positive detection scenario, we validate the planetary nature of this candidate. Using detailed follow-up, including ground-based transit recording, spectroscopy and high-resolution imaging, we characterize both the host star and its planet. We noticed a radius anomaly for this planet and the previously detected K2-25b, both planets around M-dwarfs in clusters. Both of them possess radii that are in a region seemingly unpopulated by planets orbiting comparable field stars. Detailed study and future observations will reveal whether this is due to different planet formation or evolution in open clusters.

Chapter 5

Summary and outlook

End? No, the journey doesn't end here.

J.R.R. Tolkien, The Return of the King (novel)

The rising number of exoplanet detections means that statistical analyses can be carried out in order to characterize the occurrence rate of different planets around different stars. As already discussed in sections 1.6.2 and 1.9, M-dwarfs diverge in their planet occurrence from other stars: They are presumed to host less Jovian and Neptunian planets and even less hot Jupiters. The goal of this thesis was to constrain the occurrence rates and improve on the previous upper limits of around 1%.

Planet formation in cluster stars may also happen differently than in field stars. Over the past decade, a paradigm change has occurred concerning the presumed planet abundance in open clusters. While at first, after several unsuccessful surveys, the assumption grew that planet formation in a cluster may in some way be different and possibly strongly reduced compared to field stars (Haisch et al., 2001; Bonnell et al., 2001; Debes and Jackson, 2010), it is now becoming clear that planets are just as frequent (van Saders and Gaudi, 2011; Meibom et al., 2013) and not negatively influenced by the typical orbit interactions (Adams et al., 2006; Spurzem et al., 2009). New RV planet discoveries even indicate that the occurrence rate of hot Jupiters may be *higher* than around field stars (Brucalassi et al., 2016).

In the first chapter, we introduced the concept of exoplanets and how they can be classified. We described planet formation and discussed different detection techniques. Furthermore, we summarized formalisms that are relevant to the following chapters such as transit follow-up and false-positive detections.
The second chapters describes the Pan-Planets project, a photometric survey dedicated to the detection of hot Jupiters which transit M-dwarfs. We detailed our data reduction, target selection, and Monte Carlo transit-injection simulations. Utilizing SED fitting, we matched every star with synthetic SED templates and accounted for extinction reddening by utilizing a three-dimensional dust map. A total of 65000 M-dwarfs were identified in the field of view, enough to make a statistical assessment of the planet occurrence rate. We performed extensive Monte Carlo simulations to assess the detection efficiency of Pan-Planets and optimize the preselection of the targets for visual verification.
In the third chapter, we described our four target categories. After identifying the most

promising candidates, we followed up the exoplanet candidates photometrically with the Fraunhofer Telescope Wendelstein Wide Field Imager in order to confirm the period estimate and improve the fit of the transit shape. Furthermore, we recorded spectra with the McDonald Otto Struve ES2 spectrograph and used them to characterize the candidate host stars. We combined all of our collected data, created transit models and processed all available information into the false-positive probability program *vespa*. With this, we could already statistically confirm one planet and identify four high-probability candidates. We assessed the Pan-Planets data and constrained the occurrence rate to a more precise degree of $0.11(^{+0.37}_{-0.02})\%$ in case of a confirmed detection or otherwise an upper limit of 0.34%. Previous surveys had higher upper limits of about 1%, therefore we were able to set a much more stringent estimate. The hot-Jupiter occurrence rates for FGK-dwarfs were estimated to be at about 0.45% based on the analysis of (Gould et al., 2006) with similar results from the Kepler survey, where the occurrence rates were estimated to be between 0.3%-0.6%, depending on stellar type (Howard et al., 2012; Kovács et al., 2013). Our results therefore indicate a difference between the occurrence rates of hot Jupiters for FGK-dwarfs against M-dwarfs. If none of our M-dwarf planet candidates get validated, the null result is still lower than the occurrence rate estimates for FGK-dwarfs. However, it is quite intriguing that we were able to detect two high-priority hot Jupiter candidates around late K-dwarfs. If there is a difference between M-dwarfs and FGK-dwarfs, the cut-off must be quite abrupt. We conclude this chapter with a discussion of our other target categories, M-dwarf eclipsing binaries and variable systems. The fourth and final chapter is about a discovery we made in the Praesepe (Beehive) cluster, using data from the K2 survey. We collected medium- and high-resolution spectroscopy, adaptive optics and speckle imaging data and followed up the planet with the Wendelstein Wide Field Imager. Using all of the available data, we characterized the host star and determined the false-positive probability of this planet with *vespa*. Furthermore, we discussed a radius anomaly for this planet which seems to be common in cluster planets.

Over the past years, the progress in the search for extrasolar planets has accelerated rapidly. While a decade ago just more than 200 exoplanets were known, this number has now increased by a factor of 14. The public interest is growing as well and citizen-science projects like Planet Hunters[1] actively put this enthusiasm to use with several confirmed discoveries based on input from the amateur community. Kepler's contribution to this explosion of discoveries deserves special recognition. However, this also introduces a change in how future surveys will be conducted. Small-scale projects will most likely only continue in specialized niches, as is the case for Pan-Planets. Due to the prospects of easier follow-up, bright stars are already the main focus of several ground-based robotic surveys such as Super-WASP (Pollacco et al., 2006) and HAT-South (Bakos et al., 2013). In the future, space-based surveys like TESS (Ricker et al., 2015), CHEOPS (Broeg et al., 2013) and PLATO (Rauer et al., 2014) and additional ground-based surveys such as Evryscope (Law et al., 2014) and NGTS (Wheatley et al., 2013) will further observe the whole sky, leading to a complete coverage of all bright stars where each project is contributing own data. Direct imaging, carried out with next-generation telescopes like E-ELT and JWST (Gardner et al., 2006), will allow the characterization of exoplanet atmospheres down to Earth-sized planets.

[1] https://www.planethunters.org/

Appendix A

Appendix

$M_\odot$	$1.99\ 10^{30}$ kg
M_J	$1.90\ 10^{27}$ kg
$M_\oplus$	$5.97\ 10^{24}$ kg
$R_\odot$	$6.96\ 10^{8}$ m
R_J	$7.14\ 10^{7}$ m
$R_\oplus$	$6.37\ 10^{6}$ m
$L_\odot$	$3.84\ 10^{26}$ W
AU	$1.50\ 10^{11}$ m
pc	$3.09\ 10^{16}$ m

Table A.1: Astrophysical constants used throughout this work.

A.1 Acronyms

AU Astronomical Unit, $149.60 \cdot 10^6$ km

CCD Charged coupled device

DEC Declination

GPC1 Gigapixel Camera of Pan-STARRS1

IAU International Astronomical Union

FWHM Full-width half maximum

Pan-Planets The Pan-STARRS1 Planet Survey

PSF Point spread function

RA Right ascension

S/N Signal-to-noise ratio

SED Spectral energy distribution

A.2 Additional tables

ID	RA (J2000)	DEC (J2000)	T_{eff} [K]	i' [mag]	period [d]	T_0
PP453-05705	298.9599143	15.7739332	3774	16.00	0.15013530	2455667.16476
PP455-24938	298.0664537	15.9683828	3565	17.12	0.18316444	2455365.90989
PP512-01847	295.9004414	17.9871674	3654	18.11	0.22896000	2455667.21949
PP013-23689	294.5160503	15.6409142	3637	16.71	0.22985951	2455365.97728
PP632-22966	298.2334517	14.7167112	3872	18.38	0.23479736	2455365.97728
PP451-23096	299.4370360	16.0324448	3531	17.95	0.23784512	2455679.16596
PP235-09044	300.3062391	17.7714028	3959	17.20	0.25271510	2455365.93231
PP032-32860	296.5242449	16.8055010	3729	17.63	0.25609014	2455366.02178
PP026-35677	295.9776872	16.4847896	3637	17.93	0.25953297	2455365.96910
PP134-18802	298.3078559	17.2500753	3886	17.75	0.25986344	2455365.93785
PP602-08743	297.4369333	13.1390926	3197	17.55	0.26215240	2455667.27094
PP039-13870	294.0865776	16.6440436	3723	18.48	0.26690747	2455365.99686
PP621-21999	296.6490360	13.9378706	3969	17.96	0.27231323	2455667.08679
PP655-17542	295.6743649	15.2997697	3197	18.29	0.27696803	2455667.24677
PP045-13457	294.9156436	16.9928576	3723	17.10	0.27879680	2455365.98264
PP121-15029	296.9548960	16.4699333	3965	17.67	0.28143315	2455366.13850
PP553-29819	295.4870995	20.0778010	3691	18.24	0.28338245	2455667.07749
PP542-26245	296.5552671	19.6822659	3838	18.02	0.28405392	2455667.10500
PP526-37105	296.6672225	19.0742641	3815	16.73	0.28410099	2455667.16102
PP634-09005	297.5498800	14.5287315	3197	17.25	0.29465857	2455667.26646
PP031-20706	293.9888061	16.3681676	3687	16.66	0.29553229	2455366.01849
PP336-06081	298.0990153	19.7268496	3987	17.87	0.30990374	2455667.06613
PP417-11286	300.4058632	14.4338776	3981	18.10	0.31733858	2455667.16340
PP659-19398	297.0761008	15.7711994	3903	17.11	0.32671286	2455667.06379
PP435-15531	299.8058238	15.2059517	3520	17.98	0.32814499	2455667.27660
PP419-14539	299.6830502	14.4800577	3539	16.56	0.33179050	2455667.21828
PP039-08767	293.9177223	16.5939374	3767	17.83	0.33355941	2455365.92367
PP535-13977	296.1410112	19.2243465	3843	17.41	0.33403387	2455667.12316
PP311-37625	298.3787278	18.9159435	3355	18.36	0.33428791	2455678.19817
PP520-01062	295.8015536	18.3454726	3616	17.71	0.35691447	2455667.09534
PP655-03341	295.6657536	15.1742538	3953	16.25	0.36262979	2455678.33621
PP009-36308	296.1729660	15.7498153	3637	17.93	0.36293688	2455366.20881
PP531-04582	294.7192667	18.7576437	3767	18.47	0.36304449	2455678.09925
PP305-12758	297.6544004	18.3398868	3197	16.41	0.36338309	2455365.92437
PP531-08675	294.7396165	18.8027488	3797	17.60	0.36793789	2455706.30750
PP612-08614	296.9118943	13.4244599	3649	18.14	0.37184051	2455668.19026
PP047-09188	294.0025560	16.9560366	3268	18.00	4.64281805	2455370.20723
PP509-35626	296.7463098	18.3201484	3863	15.62	5.35611262	2455670.46629
PP450-21114	299.8201789	16.0142279	3779	16.28	5.78506659	2455673.17876
PP550-24953	296.6639622	20.0431242	3929	16.71	5.85663787	2455710.62497
PP046-09699	294.4504932	16.9617022	3539	18.34	6.08730588	2455366.82202

PP656-34586	298.3209298	15.9270354	3197	16.29	0.39659850	2455667.22275
PP531-29478	294.7484120	19.0303384	3774	17.68	0.40765162	2455679.41394
PP517-36067	296.9334456	18.7448865	3745	17.53	0.40783588	2455667.20721
PP351-25051	298.3607573	20.6243178	3764	17.19	0.41221956	2455680.35939
PP547-09783	294.5724212	19.5429423	3723	17.33	0.41230879	2455667.40274
PP545-37428	295.3992843	19.7848298	3745	18.06	0.41502386	2455667.38612
PP539-15663	294.6119433	19.2462623	3501	17.32	0.42085180	2455667.37003
PP454-19725	298.3209324	15.9270352	3197	16.29	0.44205733	2455365.89615
PP559-12707	296.0684255	20.2967171	3723	17.67	0.45952362	2455667.42104
PP037-23775	294.6816305	16.7309455	3682	18.05	0.46286117	2455366.29742
PP253-09942	299.6243877	18.4750136	3838	17.46	0.48046509	2455366.34996
PP531-05850	294.7070762	18.7683205	3723	17.87	0.48051896	2455667.48861
PP632-05296	298.4859261	14.4857648	3971	18.09	0.48239848	2455667.50030
PP553-03210	295.3833106	19.8240458	3535	18.25	0.48919889	2455678.48102
PP603-12823	297.1086563	13.1598789	3838	17.84	0.49260072	2455667.28894
PP529-34926	295.4817686	19.0492823	3806	16.83	0.50444330	2455667.21737
PP546-15544	295.0719541	19.5890274	3761	17.53	0.50714439	2455667.39336
PP558-27659	296.3319002	20.4398064	3394	17.36	0.51543956	2455667.19681
PP509-14274	296.9258760	18.1072822	3442	16.68	0.53112150	2455667.17382
PP101-09886	298.5216393	15.7145510	3287	17.21	0.53852954	2455366.16392
PP027-38470	295.3539311	16.5051435	3604	15.98	0.55072650	2455366.14746
PP545-14297	295.4585348	19.5725512	3391	18.07	0.57741999	2455667.21757
PP538-37316	294.8163441	19.4426745	3576	17.56	0.60326668	2455667.13299
PP061-22248	294.6105595	17.8470792	3767	16.23	0.60524749	2455366.43797
PP259-09279	300.5257095	18.8580177	3539	17.54	0.64251867	2455366.36165
PP047-33168	294.0750582	17.2224841	3774	15.34	0.64469336	2455365.94764
PP550-15703	296.5966723	19.9606832	3619	17.93	0.65329232	2455678.26322
PP531-06746	294.6611412	18.7792861	3767	17.65	0.66094945	2455667.25628
PP214-23952	299.2313001	16.8570036	3761	14.54	0.67844906	2455365.97714
PP550-30944	296.3061271	20.0992807	3690	17.37	0.68698619	2455667.30429
PP123-08561	296.2746763	16.3755200	3883	16.11	0.68828256	2455366.28599
PP560-34098	295.9604505	20.4737513	3554	17.71	0.69433193	2455667.08989
PP552-29551	295.8692041	20.0875998	3716	17.80	0.73739968	2455667.24233
PP626-27125	297.6733266	14.3937724	3909	17.60	0.74635992	2455668.36624
PP035-19558	295.3896499	16.6914540	3714	16.72	0.76083764	2455366.56984
PP524-23811	297.1131934	18.9179943	3885	18.10	0.78618859	2455667.56220
PP014-15883	294.3082544	15.5947508	3779	17.72	0.78943741	2455365.92679
PP020-45559	295.0487390	16.1913558	3426	18.23	0.80525563	2455366.12628
PP539-13826	294.6979982	19.2278504	3576	18.08	0.80909954	2455667.15313
PP535-19941	295.9912869	19.2802579	3845	17.64	0.81053716	2455667.66879
PP550-21973	296.3789643	20.0184139	3723	17.82	0.81113987	2455667.21390
PP349-37370	299.2981690	20.7921304	3723	17.65	0.81447595	2455667.47331
PP536-08656	295.7450502	19.1755718	3554	15.09	0.82315818	2455667.58399
PP551-40984	296.0951561	20.1876727	3206	15.99	0.83506725	2455667.70866
PP022-22711	294.4687163	15.9948478	3793	16.08	0.84324142	2455366.11849
PP030-32964	294.2856223	16.4480067	3649	17.05	0.86406774	2455366.38410
PP558-01493	296.6182653	20.1759116	3706	17.58	0.86559776	2455706.70319
PP061-22248	294.6105595	17.8470792	3767	16.23	0.86893537	2455366.15411

PP559-29131	295.9877050	20.4534999	3741	16.32	0.87007039	2455667.55311
PP560-12272	295.8140983	20.2880276	3408	17.63	0.87619809	2455667.28788
PP536-25878	295.5956425	19.3473180	3958	15.77	0.88482968	2455667.43935
PP543-03725	295.9687094	19.4791202	3767	17.37	0.89465272	2455667.19780
PP544-32579	295.8939967	19.7309440	3449	17.10	0.89600527	2455667.71342
PP654-03489	296.0932031	15.1939970	3926	17.97	0.90122566	2455668.19783
PP540-39903	297.1232966	19.8354868	3774	18.27	0.90326757	2455678.85647
PP051-24396	295.3074236	17.4674834	3358	18.25	0.90815656	2455366.38669
PP530-41122	294.9071815	19.0824058	3591	18.03	0.92023834	2455678.03311
PP559-28395	296.0138436	20.4477406	3390	17.87	0.92515496	2455667.73897
PP035-25033	295.3761646	16.7389069	3197	17.65	0.93143837	2455368.87541
PP303-08526	298.2949620	18.3339197	3913	17.40	0.93294323	2455368.91445
PP309-24565	299.3255156	18.8607015	3973	16.49	0.93829302	2455366.45689
PP508-16575	297.1568911	18.1335020	3818	16.81	1.05496360	2455678.62160
PP554-04915	295.1178953	19.8633756	3535	17.88	1.05936499	2455668.01386
PP559-31018	295.9604527	20.4737511	3554	17.71	1.06354127	2455667.20689
PP023-28334	294.0723029	16.1358474	3408	17.18	1.07745633	2455366.24000
PP660-04742	296.9071199	15.5699184	3460	15.97	1.08831691	2455667.04593
PP035-01394	295.3539309	16.5051471	3604	15.98	1.10139234	2455366.15475
PP539-24189	294.7202140	19.3378991	3774	16.47	1.10300333	2455667.55091
PP548-34603	297.3767920	20.1536414	3806	17.98	1.12075745	2455678.75569
PP158-16121	298.2599109	18.4115456	3539	17.06	1.13928212	2455368.68849
PP114-18461	296.7332339	16.1573907	3848	17.51	1.15054938	2455366.90997
PP622-08221	296.1652580	13.7866475	3594	15.30	1.15471517	2455668.55634
PP538-17287	294.8529158	19.2302003	3591	17.33	1.23543641	2455667.87972
PP544-21409	295.9717532	19.6331965	3520	17.04	1.26419601	2455667.20605
PP146-02742	296.8806686	17.4424989	3197	17.71	1.26989079	2455366.71786
PP528-11294	295.7987132	18.8266534	3767	17.48	1.28905087	2455667.84873
PP020-45559	295.0487390	16.1913558	3426	18.23	1.34820571	2455366.17730
PP212-22551	299.8326799	16.8431410	3197	17.30	1.38829115	2455366.72558
PP552-22671	295.8328858	20.0235215	3368	17.59	1.39788248	2455668.19616
PP022-36660	294.4348002	16.1230451	3774	18.13	1.45709177	2455368.43785
PP520-28428	295.9094486	18.5956852	3818	17.62	1.45870135	2455667.19305
PP648-32334	298.4901027	15.5694145	3480	17.28	1.51991028	2455667.18290
PP522-44340	294.8262133	18.7609336	3825	15.68	1.54588211	2455706.12376
PP055-26657	294.1166651	17.5499295	3197	17.44	1.58621353	2455368.98242
PP118-26125	298.0868028	16.6179278	3885	18.12	1.62476815	2455366.12165
PP560-17764	295.8619002	20.3348763	3449	17.68	1.62976377	2455667.81757
PP548-31070	297.1206613	20.1225357	3936	16.79	1.63114118	2455668.49397
PP546-15650	295.0439809	19.5924226	3913	18.00	1.64400252	2455679.01961
PP053-02913	294.5610360	17.2493369	3579	17.36	1.65495510	2455366.45856
PP558-09090	296.3699458	20.2628314	3513	17.41	1.66679247	2455668.36368
PP535-30274	296.2027431	19.3800243	3987	16.05	1.68791103	2455668.31665
PP549-18293	296.9947653	19.9847157	3815	16.49	1.70149464	2455667.99709
PP325-07451	299.3389758	19.3952172	3236	17.48	1.70767110	2455667.04116
PP123-13162	296.5070099	16.4200905	3973	17.10	1.70852387	2455366.60458
PP645-28083	296.2873526	15.0673988	3509	17.70	1.71424387	2455667.27142
PP537-33215	295.2213093	19.3749231	3761	18.30	1.75435914	2455668.65766

PP004-36667	295.2364952	15.4099955	3197	17.23	1.75767753	2455365.94052
PP643-27122	297.3521097	15.0832000	3936	17.54	1.77437593	2455680.46580
PP654-03489	296.0932031	15.1939970	3926	17.97	1.80246247	2455668.19539
PP047-33168	294.0750582	17.2224841	3774	15.34	1.82342190	2455365.82798
PP223-10066	298.8614763	16.9999559	3488	16.82	1.82435001	2455366.17571
PP022-40885	294.3892081	16.1826628	3745	16.40	1.83484555	2455367.07570
PP559-28395	296.0138436	20.4477406	3390	17.87	1.85031677	2455667.74277
PP058-41337	295.6892973	17.9807657	3549	17.59	1.85647782	2455367.97709
PP557-03147	296.9853890	20.1853075	3950	15.59	1.86180462	2455668.40440
PP621-35268	296.2877402	14.0683587	3987	16.14	1.88403394	2455668.44477
PP054-21335	294.1458455	17.4556483	3774	17.90	1.91076978	2455368.52379
PP053-16337	294.8355909	17.3855417	3349	16.46	1.91276062	2455366.90492
PP614-11917	296.0030152	13.4696163	3354	17.77	1.92824504	2455667.13631
PP343-40084	298.5807717	20.4319858	3965	14.77	1.96145956	2455668.60677
PP531-28359	294.7089044	19.0183185	3449	17.92	1.96294300	2455668.48425
PP545-36815	295.5399452	19.7764519	3863	16.84	1.96355749	2455678.81374
PP055-16703	293.9501200	17.4070444	3197	18.34	1.96550593	2455368.35218
PP125-11814	298.7682773	16.8481163	3596	17.06	1.98877196	2455366.00585
PP101-19187	298.7519977	15.8350778	4029	14.87	1.99029701	2455396.08512
PP035-33356	295.5613810	16.8156257	3549	17.64	1.99430483	2455366.00256
PP538-24343	295.1391653	19.3020035	3774	16.45	1.99504487	2455706.07731
PP457-16545	300.2127089	16.4290212	3767	14.94	1.99779842	2455367.72577
PP054-13662	294.2857957	17.3778699	3616	17.42	2.04502143	2455367.13537
PP410-20697	300.0949443	14.2226738	3996	17.26	2.12198889	2455667.49673
PP016-21308	296.4767873	16.0350049	3555	16.71	2.12840937	2455367.71337
PP040-19917	296.3678584	17.0441973	3197	17.87	2.15306707	2455366.56055
PP539-37067	294.6320365	19.4864703	3501	17.76	2.16122757	2455667.13788
PP550-30944	296.3061271	20.0992807	3690	17.37	2.20685132	2455667.75295
PP123-08561	296.2746763	16.3755200	3883	16.11	2.21516463	2455366.84700
PP044-11866	295.0507532	16.9732032	3282	17.25	2.22058885	2455369.10052
PP161-01335	297.1568969	18.1335026	3818	16.81	2.23901841	2455366.81146
PP027-38470	295.3539311	16.5051435	3604	15.98	2.45176244	2455366.42821
PP514-09603	295.1356048	18.0825754	3890	17.44	2.68818339	2455668.27867
PP414-05300	298.3613684	13.9610593	3628	17.31	2.78218179	2455667.84964
PP549-23180	296.6639232	20.0430655	3929	16.71	2.92830546	2455707.69418
PP503-35924	296.0834023	17.9692487	3987	16.05	3.15699985	2455669.63493
PP508-13394	297.2299781	18.1003005	3885	17.06	3.22739040	2455668.24535
PP552-29749	295.8195000	20.0902507	3825	16.60	3.28285090	2455667.98290
PP643-23418	297.2713627	15.0451755	3958	15.68	3.32123770	2455679.63396
PP322-08743	297.1471777	19.0064579	3714	15.19	3.35484106	2455669.70336
PP347-38077	297.0745509	20.3796551	3929	15.90	3.36308542	2455678.56667
PP538-37427	294.9187445	19.4434937	3232	17.60	3.47278896	2455669.63930
PP339-03824	296.7771669	19.6795238	3493	16.92	3.49747831	2455667.99469
PP507-00273	294.8509715	17.6063852	3576	17.68	3.55781991	2455678.34268
PP036-18215	295.1917069	16.6831056	3403	16.45	3.58485042	2455369.75731
PP027-25493	295.6051851	16.3807128	3525	18.31	3.82777003	2455367.80955
PP054-19415	294.4451647	17.4336549	3539	16.84	3.97766145	2455367.24506
PP121-22680	297.1979136	16.5422292	3996	16.88	4.08539407	2455368.08346

PP047-09188	294.0025560	16.9560366	3268	18.00	4.64281805	2455370.20723
PP509-35626	296.7463098	18.3201484	3863	15.62	5.35611262	2455670.46629
PP450-21114	299.8201789	16.0142279	3779	16.28	5.78506659	2455673.17876
PP550-24953	296.6639622	20.0431242	3929	16.71	5.85663787	2455710.62497
PP046-09699	294.4504932	16.9617022	3539	18.34	6.08730588	2455366.82202
PP528-19665	295.8697577	18.9033140	3723	16.59	6.35991292	2455672.98523
PP034-31701	295.7310010	16.8035010	3716	16.63	6.55258920	2455370.94248
PP637-12376	296.4094286	14.5531266	3902	14.77	7.18084970	2455672.09764
PP261-18060	299.6480932	18.9533029	3287	17.79	7.53978854	2455366.52780
PP114-18461	296.7332339	16.1573907	3848	17.51	7.55947688	2455367.54463
PP359-31377	298.3749233	21.0584488	3774	17.68	7.64082031	2455679.73980
PP261-25870	299.5631757	19.0656978	3841	17.18	8.07875633	2455368.10979
PP510-12577	296.6441277	18.1037012	3539	17.28	8.20736974	2455668.16167
PP039-11370	294.0470870	16.6185673	3539	16.67	8.29419264	2455375.58063
PP661-13792	296.3583080	15.6589977	3711	18.09	9.57876688	2455671.41802
PP304-33229	298.2166709	18.5299688	3987	17.10	9.61056613	2455457.67420

Table A.2: List of identified M-dwarf eclipsing binaries and periodically variable systems. Individual identification, RA/DEC coordinates, SED fitting temperatures, i'-band magnitude, period and initial eclipse time T_0 are listed.

Bibliography

Abell, G. O. (1966). Properties of Some Old Planetary Nebulae. *The Astrophysical Journal*, 144:259.

Adams, F. C., Proszkow, E. M., Fatuzzo, M., and Myers, P. C. (2006). Early Evolution of Stellar Groups and Clusters: Environmental Effects on Forming Planetary Systems. *The Astrophysical Journal*, 641:504–525.

Adams, J. D., Stauffer, J. R., Skrutskie, M. F., Monet, D. G., Portegies Zwart, S. F., Janes, K. A., and Beichman, C. A. (2002). Structure of the Praesepe Star Cluster. *The Astronomical Journal*, 124:1570–1584.

Adamson, A. J., Whittet, D. C. B., and Duley, W. W. (1990). The 3.4-micron interstellar absorption feature in CYG OB2 no. 12. *Monthly Notices of the Royal Astronomical Society*, 243:400–404.

Afşar, M. and Ibanoğlu, C. (2008). Two-colour photometry of the binary planetary nebula nuclei UU Sagitte and V477 Lyrae: oversized secondaries in post-common-envelope binaries. *Monthly Notices of the Royal Astronomical Society*, 391:802–814.

Akeson, R. L., Chen, X., Ciardi, D., Crane, M., Good, J., Harbut, M., Jackson, E., Kane, S. R., Laity, A. C., Leifer, S., Lynn, M., McElroy, D. L., Papin, M., Plavchan, P., Ramírez, S. V., Rey, R., von Braun, K., Wittman, M., Abajian, M., Ali, B., Beichman, C., Beekley, A., Berriman, G. B., Berukoff, S., Bryden, G., Chan, B., Groom, S., Lau, C., Payne, A. N., Regelson, M., Saucedo, M., Schmitz, M., Stauffer, J., Wyatt, P., and Zhang, A. (2013). The NASA Exoplanet Archive: Data and Tools for Exoplanet Research. *Publications of the Astronomical Society of Pacific*, 125:989–999.

Alard, C. and Lupton, R. H. (1998). A Method for Optimal Image Subtraction. *Astrophysical Journal*, 503:325–331.

Alibert, Y., Carron, F., Fortier, A., Pfyffer, S., Benz, W., Mordasini, C., and Swoboda, D. (2013). Theoretical models of planetary system formation: mass vs. semi-major axis. *Astronomy and Astrophysics*, 558:A109.

Alibert, Y., Mordasini, C., Benz, W., and Winisdoerffer, C. (2005). Models of giant planet formation with migration and disc evolution. *Astronomy and Astrophysics*, 434:343–353.

Allard, F., Homeier, D., and Freytag, B. (2012). Models of very-low-mass stars, brown dwarfs and exoplanets. *Philosophical Transactions of the Royal Society of London Series A*, 370:2765–2777.

ALMA Partnership, Brogan, C. L., Pérez, L. M., Hunter, T. R., Dent, W. R. F., Hales, A. S., Hills, R. E., Corder, S., Fomalont, E. B., Vlahakis, C., Asaki, Y., Barkats, D., Hirota, A., Hodge, J. A., Impellizzeri, C. M. V., Kneissl, R., Liuzzo, E., Lucas, R., Marcelino, N., Matsushita, S., Nakanishi, K., Phillips, N., Richards, A. M. S., Toledo, I., Aladro, R., Broguiere, D., Cortes, J. R., Cortes, P. C., Espada, D., Galarza, F., Garcia-Appadoo, D., Guzman-Ramirez, L., Humphreys, E. M., Jung, T., Kameno, S., Laing, R. A., Leon, S., Marconi, G., Mignano, A., Nikolic, B., Nyman, L.-A., Radiszcz, M., Remijan, A., Rodón, J. A., Sawada, T., Takahashi, S., Tilanus, R. P. J., Vila Vilaro, B., Watson, L. C., Wiklind, T., Akiyama, E., Chapillon, E., de Gregorio-Monsalvo, I., Di Francesco, J., Gueth, F., Kawamura, A., Lee, C.-F., Nguyen Luong, Q., Mangum, J., Pietu, V., Sanhueza, P., Saigo, K., Takakuwa, S., Ubach, C., van Kempen, T., Wootten, A., Castro-Carrizo, A., Francke, H., Gallardo, J., Garcia, J., Gonzalez, S., Hill, T., Kaminski, T., Kurono, Y., Liu, H.-Y., Lopez, C., Morales, F., Plarre, K., Schieven, G., Testi, L., Videla, L., Villard, E., Andreani, P., Hibbard, J. E., and Tatematsu, K. (2015). The 2014 ALMA Long Baseline Campaign: First Results from High Angular Resolution Observations toward the HL Tau Region. *The Astrophysical Journal Letters*, 808:L3.

Alonso-Floriano, F. J., Morales, J. C., Caballero, J. A., Montes, D., Klutsch, A., Mundt, R., Cortés-Contreras, M., Ribas, I., Reiners, A., Amado, P. J., Quirrenbach, A., and Jeffers, S. V. (2015). CARMENES input catalogue of M dwarfs. I. Low-resolution spectroscopy with CAFOS. *Astronomy and Astrophysics*, 577:A128.

Ammler-von Eiff, M., Sebastian, D., Guenther, E. W., Stecklum, B., and Cabrera, J. (2015). The power of low-resolution spectroscopy: On the spectral classification of planet candidates in the ground-based CoRoT follow-up. *Astronomische Nachrichten*, 336:134–144.

Anderson, D. R., Hellier, C., Gillon, M., Triaud, A. H. M. J., Smalley, B., Hebb, L., Collier Cameron, A., Maxted, P. F. L., Queloz, D., West, R. G., Bentley, S. J., Enoch, B., Horne, K., Lister, T. A., Mayor, M., Parley, N. R., Pepe, F., Pollacco, D., Ségransan, D., Udry, S., and Wilson, D. M. (2010). WASP-17b: An Ultra-Low Density Planet in a Probable Retrograde Orbit. *The Astrophysical Journal*, 709:159–167.

Armitage, P. J. and Rice, W. K. M. (2005). Planetary migration. *"A Decade Of Extrasolar Planets Around Normal Stars", STScI May Symposium 2005*.

Artigau, É., Kouach, D., Donati, J.-F., Doyon, R., Delfosse, X., Baratchart, S., Lacombe, M., Moutou, C., Rabou, P., Parès, L. P., Micheau, Y., Thibault, S., Reshetov, V. A., Dubois, B., Hernandez, O., Vallée, P., Wang, S.-Y., Dolon, F., Pepe, F. A., Bouchy, F., Striebig, N., Hénault, F., Loop, D., Saddlemyer, L., Barrick, G., Vermeulen, T., Dupieux, M., Hébrard, G., Boisse, I., Martioli, E., Alencar, S. H. P., do Nascimento, J.-D., and Figueira, P. (2014). SPIRou: the near-infrared spectropolarimeter/high-precision velocimeter for the Canada-France-Hawaii telescope. In *Ground-based and Airborne Instrumentation for Astronomy V*, volume 9147 of *Proceedings of the SPIE*, page 914715.

Auvergne, M., Bodin, P., Boisnard, L., Buey, J.-T., Chaintreuil, S., Epstein, G., Jouret, M., Lam-Trong, T., Levacher, P., Magnan, A., Perez, R., Plasson, P., Plesseria, J., Peter, G., Steller, M., Tiphène, D., Baglin, A., Agogué, P., Appourchaux, T., Barbet, D., Beaufort, T., Bellenger, R., Berlin, R., Bernardi, P., Blouin, D., Boumier, P., Bonneau, F., Briet, R., Butler, B., Cautain, R., Chiavassa, F., Costes, V., Cuvilho, J., Cunha-Parro, V., de

Oliveira Fialho, F., Decaudin, M., Defise, J.-M., Djalal, S., Docclo, A., Drummond, R., Dupuis, O., Exil, G., Fauré, C., Gaboriaud, A., Gamet, P., Gavalda, P., Grolleau, E., Gueguen, L., Guivarc'h, V., Guterman, P., Hasiba, J., Huntzinger, G., Hustaix, H., Imbert, C., Jeanville, G., Johlander, B., Jorda, L., Journoud, P., Karioty, F., Kerjean, L., Lafond, L., Lapeyrere, V., Landiech, P., Larqué, T., Laudet, P., Le Merrer, J., Leporati, L., Leruyet, B., Levieuge, B., Llebaria, A., Martin, L., Mazy, E., Mesnager, J.-M., Michel, J.-P., Moalic, J.-P., Monjoin, W., Naudet, D., Neukirchner, S., Nguyen-Kim, K., Ollivier, M., Orcesi, J.-L., Ottacher, H., Oulali, A., Parisot, J., Perruchot, S., Piacentino, A., Pinheiro da Silva, L., Platzer, J., Pontet, B., Pradines, A., Quentin, C., Rohbeck, U., Rolland, G., Rollenhagen, F., Romagnan, R., Russ, N., Samadi, R., Schmidt, R., Schwartz, N., Sebbag, I., Smit, H., Sunter, W., Tello, M., Toulouse, P., Ulmer, B., Vandermarcq, O., Vergnault, E., Wallner, R., Waultier, G., and Zanatta, P. (2009). The CoRoT satellite in flight: description and performance. *Astronomy and Astrophysics*, 506:411–424.

Babcock, H. W. (1953). The Possibility of Compensating Astronomical Seeing. *Publications of the Astronomical Society of the Pacific*, 65:229.

Bakos, G. Á., Csubry, Z., Penev, K., Bayliss, D., Jordán, A., Afonso, C., Hartman, J. D., Henning, T., Kovács, G., Noyes, R. W., Béky, B., Suc, V., Csák, B., Rabus, M., Lázár, J., Papp, I., Sári, P., Conroy, P., Zhou, G., Sackett, P. D., Schmidt, B., Mancini, L., Sasselov, D. D., and Ueltzhoeffer, K. (2013). HATSouth: A Global Network of Fully Automated Identical Wide-Field Telescopes. *Publications of the Astronomical Society of the Pacific*, 125:154–182.

Bakos, G. Á., Hartman, J. D., Bhatti, W., Bieryla, A., de Val-Borro, M., Latham, D. W., Buchhave, L. A., Csubry, Z., Penev, K., Kovács, G., Béky, B., Falco, E., Kovács, T., Howard, A. W., Johnson, J. A., Isaacson, H., Marcy, G. W., Torres, G., Noyes, R. W., Berlind, P., Calkins, M. L., Esquerdo, G. A., Lázár, J., Papp, I., and Sári, P. (2015). HAT-P-54b: A Hot Jupiter Transiting a 0.6 $M_{\odot}$ Star in Field 0 of the K2 Mission. *The Astronomical Journal*, 149:149.

Baluev, R. V. and Shaidulin, V. S. (2015). Analytic models of the Rossiter-McLaughlin effect for arbitrary eclipser/star size ratios and arbitrary multiline stellar spectra. *Monthly Notices of the Royal Astronomical Society*, 454:4379–4399.

Baraffe, I., Homeier, D., Allard, F., and Chabrier, G. (2015). New evolutionary models for pre-main sequence and main sequence low-mass stars down to the hydrogen-burning limit. *Astronomy and Astrophysics*, 577:A42.

Baranne, A., Queloz, D., Mayor, M., Adrianzyk, G., Knispel, G., Kohler, D., Lacroix, D., Meunier, J.-P., Rimbaud, G., and Vin, A. (1996). ELODIE: A spectrograph for accurate radial velocity measurements. *Astronomy and Astrophysics Supplement*, 119:373–390.

Barks, H. L., Buckley, R., Grieves, G. A., Di Mauro, E., Hud, N. V., and M., O. T. (2014). Guanine, Adenine, and Hypoxanthine Production in UV-Irradiated Formamide Solutions: Relaxation of the Requirements for Prebiotic Purine Nucleobase Formation. *ChemBioChem*, 787:L29.

Barnes, J. W., Quarles, B., Lissauer, J. J., Chambers, J., and Hedman, M. M. (2016). Obliquity Variability of a Potentially Habitable Early Venus. *ArXiv e-prints*.

Barnes, R., Mullins, K., Goldblatt, C., Meadows, V. S., Kasting, J. F., and Heller, R. (2013). Tidal Venuses: Triggering a Climate Catastrophe via Tidal Heating. *Astrobiology*, 13:225–250.

Batygin, K., Stevenson, D. J., and Bodenheimer, P. H. (2011). Evolution of Ohmically Heated Hot Jupiters. *The Astrophysical Journal*, 738:1.

Bayliss, D. D. R., Winn, J. N., Mardling, R. A., and Sackett, P. D. (2010). Confirmation of a Retrograde Orbit for Exoplanet WASP-17b. *The Astrophysical Journal Letters*, 722:L224–L227.

Beccari, G. and Carraro, G. (2015). *Introduction to the Theory of Stellar Evolution*, page 1.

Beckers, J. M. (1993). Adaptive optics for astronomy - Principles, performance, and applications. *Annual review of astronomy and astrophysics*, 31:13–62.

Begeman, K., Belikov, A. N., Boxhoorn, D. R., and Valentijn, E. A. (2013). The Astro-WISE datacentric information system. *Experimental Astronomy*, 35:1–23.

Beichman, C., Livingston, J., Werner, M., Gorjian, V., Krick, J., Deck, K., Knutson, H., Wong, I., Petigura, E. A., Christiansen, J., Ciardi, D., Greene, T. P., Schlieder, J. E., Line, M., Crossfield, I., Howard, A., and Sinukoff, E. (2016). Spitzer Observations of Exoplanets Discovered with The Kepler K2 Mission. *ArXiv e-prints*.

Bell, S. A., Pollacco, D. L., and Hilditch, R. W. (1994). Direct Optical Observations of the Secondary Component of Uu-Sagittae. *Monthly Notices of the Royal Astronomical Society*, 270:449.

Boesgaard, A. M., Roper, B. W., and Lum, M. G. (2013). The Chemical Composition of Praesepe (M44). *The Astrophysical Journal*, 775:58.

Boley, A. C. (2009). The Two Modes of Gas Giant Planet Formation. *The Astrophysical Journal Letters*, 695:L53–L57.

Bond, H. E., Liller, W., and Mannery, E. J. (1978). UU Sagittae - Eclipsing nucleus of the planetary nebula Abell 63. *The Astrophysical Journal*, 223:252.

Bonfils, X., Delfosse, X., Udry, S., Forveille, T., Mayor, M., Perrier, C., Bouchy, F., Gillon, M., Lovis, C., Pepe, F., Queloz, D., Santos, N. C., Ségransan, D., and Bertaux, J.-L. (2013). The HARPS search for southern extra-solar planets. XXXI. The M-dwarf sample. *Astronomy and Astrophysics*, 549:A109.

Bonfils, X., Forveille, T., Delfosse, X., Udry, S., Mayor, M., Perrier, C., Bouchy, F., Pepe, F., Queloz, D., and Bertaux, J.-L. (2005). The HARPS search for southern extra-solar planets. VI. A Neptune-mass planet around the nearby M dwarf Gl 581. *Astronomy and Astrophysics*, 443:L15–L18.

Bonfils, X., Mayor, M., Delfosse, X., Forveille, T., Gillon, M., Perrier, C., Udry, S., Bouchy, F., Lovis, C., Pepe, F., Queloz, D., Santos, N. C., and Bertaux, J.-L. (2007). The HARPS search for southern extra-solar planets. X. A m sin i = 11 M planet around the nearby spotted M dwarf. *Astronomy and Astrophysics*, 474:293–299.

Bonnell, I. A., Smith, K. W., Davies, M. B., and Horne, K. (2001). Planetary dynamics in stellar clusters. *Monthly Notices of the Royal Astronomical Society*, 322:859–865.

Borucki, W. J., Koch, D., Basri, G., Batalha, N., Brown, T., Caldwell, D., Caldwell, J., Christensen-Dalsgaard, J., Cochran, W. D., DeVore, E., Dunham, E. W., Dupree, A. K., Gautier, T. N., Geary, J. C., Gilliland, R., Gould, A., Howell, S. B., Jenkins, J. M., Kondo, Y., Latham, D. W., Marcy, G. W., Meibom, S., Kjeldsen, H., Lissauer, J. J., Monet, D. G., Morrison, D., Sasselov, D., Tarter, J., Boss, A., Brownlee, D., Owen, T., Buzasi, D., Charbonneau, D., Doyle, L., Fortney, J., Ford, E. B., Holman, M. J., Seager, S., Steffen, J. H., Welsh, W. F., Rowe, J., Anderson, H., Buchhave, L., Ciardi, D., Walkowicz, L., Sherry, W., Horch, E., Isaacson, H., Everett, M. E., Fischer, D., Torres, G., Johnson, J. A., Endl, M., MacQueen, P., Bryson, S. T., Dotson, J., Haas, M., Kolodziejczak, J., Van Cleve, J., Chandrasekaran, H., Twicken, J. D., Quintana, E. V., Clarke, B. D., Allen, C., Li, J., Wu, H., Tenenbaum, P., Verner, E., Bruhweiler, F., Barnes, J., and Prsa, A. (2010). Kepler Planet-Detection Mission: Introduction and First Results. *Science*, 327:977.

Bramich, D. M. and Horne, K. (2006). Upper limits on the hot Jupiter fraction in the field of NGC 7789. *Monthly Notices of the Royal Astronomical Society*, 367:1677–1685.

Brandt, T. D. and Huang, C. X. (2015a). Bayesian Ages for Early-type Stars from Isochrones Including Rotation, and a Possible Old Age for the Hyades. *The Astrophysical Journal*, 807:58.

Brandt, T. D. and Huang, C. X. (2015b). The Age and Age Spread of the Praesepe and Hyades Clusters: a Consistent, ˜800 Myr Picture from Rotating Stellar Models. *The Astrophysical Journal*, 807:24.

Bressan, A., Marigo, P., Girardi, L., Salasnich, B., Dal Cero, C., Rubele, S., and Nanni, A. (2012). PARSEC: stellar tracks and isochrones with the PAdova and TRieste Stellar Evolution Code. *Monthly Notices of the Royal Astronomical Society*, 427:127–145.

Broeg, C., Fortier, A., Ehrenreich, D., Alibert, Y., Baumjohann, W., Benz, W., Deleuil, M., Gillon, M., Ivanov, A., Liseau, R., Meyer, M., Oloffson, G., Pagano, I., Piotto, G., Pollacco, D., Queloz, D., Ragazzoni, R., Renotte, E., Steller, M., and Thomas, N. (2013). CHEOPS: A transit photometry mission for ESA's small mission programme. In *European Physical Journal Web of Conferences*, volume 47 of *European Physical Journal Web of Conferences*, page 03005.

Brucalassi, A., Pasquini, L., Saglia, R., Ruiz, M. T., Bonifacio, P., Bedin, L. R., Biazzo, K., Melo, C., Lovis, C., and Randich, S. (2014). Three planetary companions around M 67 stars. *Astronomy and Astrophyics*, 561:L9.

Brucalassi, A., Pasquini, L., Saglia, R., Ruiz, M. T., Bonifacio, P., Leão, I., Canto Martins, B. L., de Medeiros, J. R., Bedin, L. R., Biazzo, K., Melo, C., Lovis, C., and Randich, S. (2016). Search for giant planets in M67. III. Excess of hot Jupiters in dense open clusters. *Astronomy and Astrophysics*, 592:L1.

Buccino, A., Lemarchand, G., and Mauas, P. (2007). UV habitable zones around M stars. *Icarus*, 192:582–587.

Burrows, A., Sudarsky, D., and Hubeny, I. (2006). Theory for the Secondary Eclipse Fluxes, Spectra, Atmospheres, and Light Curves of Transiting Extrasolar Giant Planets. *The Astrophysical Journal*, 650:1140–1149.

Butler, R. P., Vogt, S. S., Marcy, G. W., Fischer, D. A., Wright, J. T., Henry, G. W., Laughlin, G., and Lissauer, J. J. (2004). A Neptune-Mass Planet Orbiting the Nearby M Dwarf GJ 436. *The Astrophysical Journal*, 617:580–588.

Caldwell, D. A., Kolodziejczak, J. J., Van Cleve, J. E., Jenkins, J. M., Gazis, P. R., Argabright, V. S., Bachtell, E. E., Dunham, E. W., Geary, J. C., Gilliland, R. L., Chandrasekaran, H., Li, J., Tenenbaum, P., Wu, H., Borucki, W. J., Bryson, S. T., Dotson, J. L., Haas, M. R., and Koch, D. G. (2010). Instrument Performance in Kepler's First Months. *The Astrophysical Journal Letters*, 713:L92–L96.

Campbell, B., Walker, G. A. H., and Yang, S. (1988). A search for substellar companions to solar-type stars. *Astrophysical Journal*, 331:902–921.

Carter Chambers, K. (2015). The Pan-STARRS Surveys. *IAU General Assembly*, 22:2257776.

Chabrier, G., Baraffe, I., Leconte, J., Gallardo, J., and Barman, T. (2009). The mass-radius relationship from solar-type stars to terrestrial planets: a review. In Stempels, E., editor, *15th Cambridge Workshop on Cool Stars, Stellar Systems, and the Sun*, volume 1094 of *American Institute of Physics Conference Series*, pages 102–111.

Chambers, J. E. (2016). Pebble Accretion and the Diversity of Planetary Systems. *ArXiv e-prints*.

Charbonneau, D., Brown, T. M., Burrows, A., and Laughlin, G. (2007). When Extrasolar Planets Transit Their Parent Stars. *Protostars and Planets V*, pages 701–716.

Charbonneau, D., Brown, T. M., Latham, D. W., and Mayor, M. (2000). Detection of Planetary Transits Across a Sun-like Star. *The Astrophysical Journal*, 529:L45–L48.

Chauvin, G., Lagrange, A.-M., Dumas, C., Zuckerman, B., Mouillet, D., Song, I., Beuzit, J.-L., and Lowrance, P. (2004). A giant planet candidate near a young brown dwarf. Direct VLT/NACO observations using IR wavefront sensing. *Astronomy and Astrophysics*, 425:L29–L32.

Chen, J. and Kipping, D. M. (2016). Probabilistic Forecasting of the Masses and Radii of Other Worlds. *ArXiv e-prints*.

Chen, Y., Girardi, L., Bressan, A., Marigo, P., Barbieri, M., and Kong, X. (2014). Improving PARSEC models for very low mass stars. *Monthly Notices of the Royal Astronomical Society*, 444:2525–2543.

Christiansen, J. L., Clarke, B. D., Burke, C. J., Seader, S., Jenkins, J. M., Twicken, J. D., Catanzarite, J. D., Smith, J. C., Batalha, N. M., Haas, M. R., Thompson, S. E., Campbell, J. R., Sabale, A., and Kamal Uddin, A. (2015). Measuring Transit Signal Recovery in the Kepler Pipeline II: Detection Efficiency as Calculated in One Year of Data. *The Astrophysical Journal*, 810:95.

Ciceri, S., Mancini, L., Southworth, J., Lendl, M., Tregloan-Reed, J., Brahm, R., Chen, G., D'Ago, G., Dominik, M., Figuera Jaimes, R., Galianni, P., Harpsøe, K., Hinse, T. C., Jørgensen, U. G., Juncher, D., Korhonen, H., Liebig, C., Rabus, M., Bonomo, A. S., Bott, K., Henning, T., Jordán, A., Sozzetti, A., Alsubai, K. A., Andersen, J. M., Bajek, D., Bozza, V., Bramich, D. M., Browne, P., Calchi Novati, S., Damerdji, Y., Diehl, C., Elyiv, A., Giannini, E., Gu, S.-H., Hundertmark, M., Kains, N., Penny, M., Popovas, A., Rahvar, S., Scarpetta, G., Schmidt, R. W., Skottfelt, J., Snodgrass, C., Surdej, J., Vilela, C., Wang, X.-B., and Wertz, O. (2016). Physical properties of the planetary systems WASP-45 and WASP-46 from simultaneous multiband photometry. *Monthly Notices of the Royal Astronomical Society*, 456:990–1002.

Claret, A. and Bloemen, S. (2011). Gravity and limb-darkening coefficients for the Kepler, CoRoT, Spitzer, uvby, UBVRIJHK, and Sloan photometric systems. *Astronomy and Astrophysics*, 529:A75.

Cloutier, R. and Lin, M.-K. (2013). Orbital migration of giant planets induced by gravitationally unstable gaps: the effect of planet mass. *Monthly Notices of the Royal Astronomical Society*, 434:621–632.

Cossou, C., Raymond, S. N., Hersant, F., and Pierens, A. (2014). Hot super-Earths and giant planet cores from different migration histories. *Astronomy and Astrophysics*, 569:A56.

Crossfield, I. J. M., Petigura, E., Schlieder, J. E., Howard, A. W., Fulton, B. J., Aller, K. M., Ciardi, D. R., Lépine, S., Barclay, T., de Pater, I., de Kleer, K., Quintana, E. V., Christiansen, J. L., Schlafly, E., Kaltenegger, L., Crepp, J. R., Henning, T., Obermeier, C., Deacon, N., Weiss, L. M., Isaacson, H. T., Hansen, B. M. S., Liu, M. C., Greene, T., Howell, S. B., Barman, T., and Mordasini, C. (2015). A Nearby M Star with Three Transiting Super-Earths Discovered by K2. *The Astrophysical Journal*, 804:10.

Cushing, M. C., Vacca, W. D., and Rayner, J. T. (2004). Spextool: A Spectral Extraction Package for SpeX, a 0.8-5.5 Micron Cross-Dispersed Spectrograph. *Publications of the Astronomical Society of Pacific*, 116:362–376.

David, T. J., Conroy, K. E., Hillenbrand, L. A., Stassun, K. G., Stauffer, J., Rebull, L. M., Cody, A. M., Isaacson, H., Howard, A. W., and Aigrain, S. (2016). New Pleiades Eclipsing Binaries and a Hyades Transiting System Identified by K2. *The Astronomical Journal*, 151:112.

David, T. J. and Hillenbrand, L. A. (2015). The Ages of Early-type Stars: Strömgren Photometric Methods Calibrated, Validated, Tested, and Applied to Hosts and Prospective Hosts of Directly Imaged Exoplanets. *The Astrophysical Journal*, 804:146.

Dawson, R. I. and Murray-Clay, R. A. (2013). Giant Planets Orbiting Metal-rich Stars Show Signatures of Planet-Planet Interactions. *The Astrophysical Journal Letters*, 767:L24.

Deacon, N. R., Kraus, A. L., Mann, A. W., Magnier, E. A., Chambers, K. C., Wainscoat, R. J., Tonry, J. L., Kaiser, N., Waters, C., Flewelling, H., Hodapp, K. W., and Burgett, W. S. (2015). A Pan-STARRS1 study of the relationship between wide binarity and planet occurrence in the Kepler field. *ArXiv e-prints*.

Deamer, D. and Fleischaker, G. (1994). *Origins of life: the central concepts*. Jones and Bartlett Publishers.

Debes, J. H. and Jackson, B. (2010). Too Little, Too Late: How the Tidal Evolution of Hot Jupiters Affects Transit Surveys of Clusters. *The Astrophysical Journal*, 723:1703–1710.

Dipierro, G., Price, D., Laibe, G., Hirsh, K., Cerioli, A., and Lodato, G. (2015). On planet formation in HL Tau. *Monthly Notices of the Royal Astronomical Society*, 453:L73–L77.

Dobbie, P. D., Napiwotzki, R., Burleigh, M. R., Barstow, M. A., Boyce, D. D., Casewell, S. L., Jameson, R. F., Hubeny, I., and Fontaine, G. (2006). New Praesepe white dwarfs and the initial mass-final mass relation. *Monthly Notices of the Royal Astronomical Society*, 369:383–389.

Dodson-Robinson, S. E., Bodenheimer, P., Laughlin, G., Willacy, K., Turner, N. J., and Beichman, C. A. (2008). Saturn Forms by Core Accretion in 3.4 Myr. *Astrophysical Journal, Letters*, 688:L99–L102.

Donati, J. F., Moutou, C., Malo, L., Baruteau, C., Yu, L., Hébrard, E., Hussain, G., Alencar, S., Ménard, F., Bouvier, J., Petit, P., Takami, M., Doyon, R., and Cameron, A. C. (2016). A hot Jupiter orbiting a 2-million-year-old solar-mass T Tauri star. *Nature*, 534:662–666.

Dotter, A., Chaboyer, B., Jevremović, D., Kostov, V., Baron, E., and Ferguson, J. W. (2008). The Dartmouth Stellar Evolution Database. *The Astrophysical Journals*, 178:89–101.

Douglas, S. T., Agüeros, M. A., Covey, K. R., Bowsher, E. C., Bochanski, J. J., Cargile, P. A., Kraus, A., Law, N. M., Lemonias, J. J., Arce, H. G., Fierroz, D. F., and Kundert, A. (2014). The Factory and the Beehive. II. Activity and Rotation in Praesepe and the Hyades. *The Astrophysical Journal*, 795:161.

Dressing, C. D. and Charbonneau, D. (2013). The Occurrence Rate of Small Planets around Small Stars. *Astrophysical Journal*, 767:95.

Dressing, C. D. and Charbonneau, D. (2015). The Occurrence of Potentially Habitable Planets Orbiting M Dwarfs Estimated from the Full Kepler Dataset and an Empirical Measurement of the Detection Sensitivity. *The Astrophysical Journal*, 807:45.

Duda, R. O. and Hart, P. E. (1972). Use of the hough transformation to detect lines and curves in pictures. *Commun. ACM*, 15(1):11–15.

Ehrenreich, D., Bourrier, V., Wheatley, P. J., Lecavelier des Etangs, A., Hébrard, G., Udry, S., Bonfils, X., Delfosse, X., Désert, J.-M., Sing, D. K., and Vidal-Madjar, A. (2015). A giant comet-like cloud of hydrogen escaping the warm Neptune-mass exoplanet GJ 436b. *Nature*, 522:459–461.

Eyer, L., Holl, B., Pourbaix, D., Mowlavi, N., Siopis, C., Barblan, F., Evans, D. W., and North, P. (2013). The Gaia Mission. *Central European Astrophysical Bulletin*, 37:115–126.

Eyer, L., Rimoldini, L., Holl, B., North, P., Zucker, S., Evans, D. W., Pourbaix, D., Hodgkin, S. T., Thuillot, W., Mowlavi, N., and Carry, B. (2015). The Gaia Mission, Binary Stars and Exoplanets. In Rucinski, S. M., Torres, G., and Zejda, M., editors, *Living Together: Planets,*

Host Stars and Binaries, volume 496 of *Astronomical Society of the Pacific Conference Series*, page 121.

Fabrycky, D. C., Ford, E. B., Steffen, J. H., Rowe, J. F., Carter, J. A., Moorhead, A. V., Batalha, N. M., Borucki, W. J., Bryson, S., Buchhave, L. A., Christiansen, J. L., Ciardi, D. R., Cochran, W. D., Endl, M., Fanelli, M. N., Fischer, D., Fressin, F., Geary, J., Haas, M. R., Hall, J. R., Holman, M. J., Jenkins, J. M., Koch, D. G., Latham, D. W., Li, J., Lissauer, J. J., Lucas, P., Marcy, G. W., Mazeh, T., McCauliff, S., Quinn, S., Ragozzine, D., Sasselov, D., and Shporer, A. (2012). Transit Timing Observations from Kepler. IV. Confirmation of Four Multiple-planet Systems by Simple Physical Models. *The Astrophysical Journal*, 750:114.

Faedi, F., Staley, T., Gómez Maqueo Chew, Y., Pollacco, D., Dhital, S., Barros, S. C. C., Skillen, I., Hebb, L., Mackay, C., and Watson, C. A. (2013). Lucky imaging of transiting planet host stars with LuckyCam. *Monthly Notices of the Royal Astronomical Society*, 433:2097–2106.

Faigler, S., Mazeh, T., Quinn, S. N., Latham, D. W., and Tal-Or, L. (2012). Seven New Binaries Discovered in the Kepler Light Curves through the BEER Method Confirmed by Radial-velocity Observations. *The Astrophysical Journal*, 746:185.

Fischer, D. A. and Valenti, J. (2005). The Planet-Metallicity Correlation. *The Astrophysical Journal*, 622:1102–1117.

Foreman-Mackey, D., Hogg, D. W., Lang, D., and Goodman, J. (2013). emcee: The MCMC Hammer. *Publications of the Astronomical Society of Pacific*, 125:306–312.

Foreman-Mackey, D., Hogg, D. W., and Morton, T. D. (2014). Exoplanet Population Inference and the Abundance of Earth Analogs from Noisy, Incomplete Catalogs. *The Astrophysical Journal*, 795:64.

Forgan, D. and Rice, K. (2013). Towards a population synthesis model of objects formed by self-gravitating disc fragmentation and tidal downsizing. *Monthly Notices of the Royal Astronomical Society*, 432:3168–3185.

Forveille, T., Bonfils, X., Delfosse, X., Alonso, R., Udry, S., Bouchy, F., Gillon, M., Lovis, C., Neves, V., Mayor, M., Pepe, F., Queloz, D., Santos, N. C., Segransan, D., Almenara, J. M., Deeg, H., and Rabus, M. (2011). The HARPS search for southern extra-solar planets XXXII. Only 4 planets in the Gl 581 system. *ArXiv e-prints, submitted to Astronomy and Astrophysics*.

Fossati, L., Bagnulo, S., Landstreet, J., Wade, G., Kochukhov, O., Monier, R., Weiss, W., and Gebran, M. (2008). The effect of rotation on the abundances of the chemical elements of the A-type stars in the Praesepe cluster. *Astronomy and Astrophysics*, 483:891–902.

Fried, D. L. (1978). Probability of getting a lucky short-exposure image through turbulence. *Journal of the Optical Society of America (1917-1983)*, 68:1651–1658.

Gaidos, E., Fischer, D. A., Mann, A. W., and Howard, A. W. (2013). An Understanding of the Shoulder of Giants: Jovian Planets around Late K Dwarf Stars and the Trend with Stellar Mass. *The Astrophysical Journal*, 771:18.

Gaidos, E. and Mann, A. W. (2014). M Dwarf Metallicities and Giant Planet Occurrence: Ironing Out Uncertainties and Systematics. *Astrophysical Journal*, 791:54.

Gaidos, E., Mann, A. W., Kraus, A. L., and Ireland, M. (2016). They are small worlds after all: revised properties of Kepler M dwarf stars and their planets. *Monthly Notices of the Royal Astronomical Society*, 457:2877–2899.

Galicher, R., Marois, C., Zuckerman, B., and Macintosh, B. (2013). Fomalhaut b: Independent Analysis of the Hubble Space Telescope Public Archive Data. *The Astrophysical Journal*, 769:42.

Gammie, C. F. (2001). Nonlinear Outcome of Gravitational Instability in Cooling, Gaseous Disks. *Astrophysical Journal*, 553:174–183.

Gardner, J. P., Mather, J. C., Clampin, M., Doyon, R., Greenhouse, M. A., Hammel, H. B., Hutchings, J. B., Jakobsen, P., Lilly, S. J., Long, K. S., Lunine, J. I., McCaughrean, M. J., Mountain, M., Nella, J., Rieke, G. H., Rieke, M. J., Rix, H.-W., Smith, E. P., Sonneborn, G., Stiavelli, M., Stockman, H. S., Windhorst, R. A., and Wright, G. S. (2006). The James Webb Space Telescope. *Space Science Reviews*, 123:485–606.

Gaudi, B. S. (2010). Exoplanetary Microlensing. *ArXiv e-prints; Refereed chapter in EXOPLANETS, edited by S. Seager.*

Gilliland, R. L., Brown, T. M., Guhathakurta, P., Sarajedini, A., Milone, E. F., Albrow, M. D., Baliber, N. R., Bruntt, H., Burrows, A., Charbonneau, D., Choi, P., Cochran, W. D., Edmonds, P. D., Frandsen, S., Howell, J. H., Lin, D. N. C., Marcy, G. W., Mayor, M., Naef, D., Sigurdsson, S., Stagg, C. R., Vandenberg, D. A., Vogt, S. S., and Williams, M. D. (2000). A Lack of Planets in 47 Tucanae from a Hubble Space Telescope Search. *The Astrophysical Journal*, 545:L47–L51.

Gillon, M., Pont, F., Demory, B.-O., Mallmann, F., Mayor, M., Mazeh, T., Queloz, D., Shporer, A., Udry, S., and Vuissoz, C. (2007). Detection of transits of the nearby hot Neptune GJ 436 b. *Astronomy and Astrophysics*, 472:L13–L16.

Girardi, L., Groenewegen, M. A. T., Hatziminaoglou, E., and da Costa, L. (2005). Star counts in the Galaxy. Simulating from very deep to very shallow photometric surveys with the TRILEGAL code. *Astronomy and Astrophysics*, 436:895–915.

Girven, J., Gänsicke, B. T., Steeghs, D., and Koester, D. (2011). DA white dwarfs in Sloan Digital Sky Survey Data Release 7 and a search for infrared excess emission. *Monthly Notices of the Royal Astronomical Society*, 417:1210–1235.

Glebbeek, E., Pols, O. R., and Hurley, J. R. (2008). Evolution of stellar collision products in open clusters. I. Blue stragglers in N-body models of M 67. *Astronomy and Astrophysics*, 488:1007–1015.

Goldreich, P. and Tremaine, S. (1980). Disk-satellite interactions. *Astrophysical Journal*, 241:425–441.

Gonzalez, G. (1997). The stellar metallicity-giant planet connection. *Monthly Notices of the Royal Astronomical Society*, 285:403–412.

Gonzalez, J.-F., Laibe, G., Maddison, S. T., Pinte, C., and Ménard, F. (2015). ALMA images of discs: are all gaps carved by planets? *Monthly Notices of the Royal Astronomical Society*, 454:L36–L40.

Gössl, C. A. and Riffeser, A. (2002). Image reduction pipeline for the detection of variable sources in highly crowded fields. *Astronomy and Astrophysics*, 381:1095–1109.

Gould, A., Dorsher, S., Gaudi, B. S., and Udalski, A. (2006). Frequency of Hot Jupiters and Very Hot Jupiters from the OGLE-III Transit Surveys toward the Galactic Bulge and Carina. *Acta Astronomica*, 56:1–50.

Green, G. M., Schlafly, E. F., Finkbeiner, D. P., Rix, H.-W., Martin, N., Burgett, W., Draper, P. W., Flewelling, H., Hodapp, K., Kaiser, N., Kudritzki, R. P., Magnier, E., Metcalfe, N., Price, P., Tonry, J., and Wainscoat, R. (2015). A Three-dimensional Map of Milky Way Dust. *The Astrophysical Journal*, 810:25.

Greiner, J., Bornemann, W., Clemens, C., Deuter, M., Hasinger, G., Honsberg, M., Huber, H., Huber, S., Krauss, M., Krühler, T., Küpcü Yoldaş, A., Mayer-Hasselwander, H., Mican, B., Primak, N., Schrey, F., Steiner, I., Szokoly, G., Thöne, C. C., Yoldaş, A., Klose, S., Laux, U., and Winkler, J. (2008). GROND a 7-Channel Imager. *Publications of the Astronomical Society of Pacific*, 120:405–424.

Haisch, Jr., K. E., Lada, E. A., and Lada, C. J. (2001). Disk Frequencies and Lifetimes in Young Clusters. *The Astrophysical Journal*, 553:L153–L156.

Hambly, N. C., Steele, I. A., Hawkins, M. R. S., and Jameson, R. F. (1995). Very low mass stars in the galactic cluster Praesepe. *Astronomy and Astrophysicss*, 109.

Han, E., Wang, S. X., Wright, J. T., Feng, Y. K., Zhao, M., Fakhouri, O., Brown, J. I., and Hancock, C. (2014). Exoplanet Orbit Database. II. Updates to Exoplanets.org. *Publications of the Astronomical Society of the Pacific*, 126:827–837.

Hansen, B. M. S. and Murray, N. (2012). Migration Then Assembly: Formation of Neptune-mass Planets inside 1 AU. *The Astrophysical Journal*, 751:158.

Hansen, B. M. S. and Murray, N. (2013). Testing in Situ Assembly with the Kepler Planet Candidate Sample. *The Astrophysical Journal*, 775:53.

Hartman, J. D., Bayliss, D., Brahm, R., Bakos, G. Á., Mancini, L., Jordán, A., Penev, K., Rabus, M., Zhou, G., Butler, R. P., Espinoza, N., de Val-Borro, M., Bhatti, W., Csubry, Z., Ciceri, S., Henning, T., Schmidt, B., Arriagada, P., Shectman, S., Crane, J., Thompson, I., Suc, V., Csák, B., Tan, T. G., Noyes, R. W., Lázár, J., Papp, I., and Sári, P. (2015). HATS-6b: A Warm Saturn Transiting an Early M Dwarf Star, and a Set of Empirical Relations for Characterizing K and M Dwarf Planet Hosts. *The Astronomical Journal*, 149:166.

Hartman, J. D., Gaudi, B. S., Holman, M. J., McLeod, B. A., Stanek, K. Z., Barranco, J. A., Pinsonneault, M. H., Meibom, S., and Kalirai, J. S. (2009). Deep MMT Transit Survey of the Open Cluster M37 IV: Limit on the Fraction of Stars with Planets as Small as $0.3R_J$. *Astrophysical Journal*, 695:336–356.

Hatzes, A. P. (2016). Periodic H alpha variations in GL 581: Further evidence for an activity origin to GL 581d. *Astronomy and Astrophysics*, 585:A144.

Hatzes, A. P., Cochran, W. D., Endl, M., McArthur, B., Paulson, D. B., Walker, G. A. H., Campbell, B., and Yang, S. (2003). A Planetary Companion to γ Cephei A. *Astrophysical Journal*, 599:1383–1394.

Heath, M. J. and Doyle, L. R. (2004). From Near-Synchronously Rotating Planets to Tidal Lock: A New Class of Habitable Planets Examined for Forest Habitability. In Norris, R. and Stootman, F., editors, *Bioastronomy 2002: Life Among the Stars*, volume 213 of *IAU Symposium*, page 225.

Heber, U. (2009). Hot Subdwarf Stars. *Annual Review of Astronomy and Astrophysics*, 47:211–251.

Hébrard, G., Almenara, J.-M., Santerne, A., Deleuil, M., Damiani, C., Bonomo, A. S., Bouchy, F., Bruno, G., Díaz, R. F., Montagnier, G., and Moutou, C. (2013). KOI-200 b and KOI-889 b: Two transiting exoplanets detected and characterized with Kepler, SOPHIE, and HARPS-N. *Astronomy and Astrophysics*, 554:A114.

Henry, G. W., Marcy, G. W., Butler, R. P., and Vogt, S. S. (2000). A Transiting "51 Peg-like" Planet. *The Astrophysical Journal*, 529:L41–L44.

Henry, T. J., Jao, W.-C., Subasavage, J. P., Beaulieu, T. D., Ianna, P. A., Costa, E., and Méndez, R. A. (2006). The Solar Neighborhood. XVII. Parallax Results from the CTIOPI 0.9 m Program: 20 New Members of the RECONS 10 Parsec Sample. *The Astronomical Journal*, 132:2360–2371.

Henry, T. J., Kirkpatrick, J. D., and Simons, D. A. (1994). The solar neighborhood, 1: Standard spectral types (K5-M8) for northern dwarfs within eight parsecs. *The Astronomical Journal*, 108:1437–1444.

Hilditch, R. W. (2001). *An Introduction to Close Binary Stars*.

Hill, H. G. M. and Nuth, J. A. (2003). The Catalytic Potential of Cosmic Dust: Implications for Prebiotic Chemistry in the Solar Nebula and Other Protoplanetary Systems. *Astrobiology*, 3:291–304.

Hodapp, K. W., Kaiser, N., Aussel, H., Burgett, W., Chambers, K. C., Chun, M., Dombeck, T., Douglas, A., Hafner, D., Heasley, J., Hoblitt, J., Hude, C., Isani, S., Jedicke, R., Jewitt, D., Laux, U., Luppino, G. A., Lupton, R., Maberry, M., Magnier, E., Mannery, E., Monet, D., Morgan, J., Onaka, P., Price, P., Ryan, A., Siegmund, W., Szapudi, I., Tonry, J., Wainscoat, R., and Waterson, M. (2004). Design of the Pan-STARRS telescopes. *Astronomische Nachrichten*, 325:636–642.

Hoffleit, D. (1932). New Variable Stars in Aquila. *Harvard College Observatory Bulletin*, 887:9–13.

Holman, M. J. and Murray, N. W. (2005). The Use of Transit Timing to Detect Terrestrial-Mass Extrasolar Planets. *Science*, 307:1288–1291.

Hopp, U., Bender, R., Grupp, F., Goessl, C., Lang-Bardl, F., Mitsch, W., Riffeser, A., and Ageorges, N. (2014). Commissioning and science verification of the 2m-Fraunhofer Wendelstein Telescope. In *Ground-based and Airborne Telescopes V*, volume 9145 of *Proceedings of the SPIE*, page 91452D.

Horch, E. P., Gomez, S. C., Sherry, W. H., Howell, S. B., Ciardi, D. R., Anderson, L. M., and van Altena, W. F. (2011). Observations of Binary Stars with the Differential Speckle Survey Instrument. II. Hipparcos Stars Observed in 2010 January and June. *The Astronomical Journal*, 141:45.

Horch, E. P., Veillette, D. R., Baena Gallé, R., Shah, S. C., O'Rielly, G. V., and van Altena, W. F. (2009). Observations of Binary Stars with the Differential Speckle Survey Instrument. I. Instrument Description and First Results. *The Astronomical Journal*, 137:5057–5067.

Horner, J., Hinse, T. C., Wittenmyer, R. A., Marshall, J. P., and Tinney, C. G. (2012). A dynamical analysis of the proposed circumbinary HW Virginis planetary system. *Monthly Notices of the Royal Astronomical Society*, 427:2812–2823.

Howard, A. W., Johnson, J. A., Marcy, G. W., Fischer, D. A., Wright, J. T., Bernat, D., Henry, G. W., Peek, K. M. G., Isaacson, H., Apps, K., Endl, M., Cochran, W. D., Valenti, J. A., Anderson, J., and Piskunov, N. E. (2010). The California Planet Survey. I. Four New Giant Exoplanets. *The Astrophysical Journal*, 721:1467–1481.

Howard, A. W., Marcy, G. W., Bryson, S. T., Jenkins, J. M., Rowe, J. F., Batalha, N. M., Borucki, W. J., Koch, D. G., Dunham, E. W., Gautier, III, T. N., Van Cleve, J., Cochran, W. D., Latham, D. W., Lissauer, J. J., Torres, G., Brown, T. M., Gilliland, R. L., Buchhave, L. A., Caldwell, D. A., Christensen-Dalsgaard, J., Ciardi, D., Fressin, F., Haas, M. R., Howell, S. B., Kjeldsen, H., Seager, S., Rogers, L., Sasselov, D. D., Steffen, J. H., Basri, G. S., Charbonneau, D., Christiansen, J., Clarke, B., Dupree, A., Fabrycky, D. C., Fischer, D. A., Ford, E. B., Fortney, J. J., Tarter, J., Girouard, F. R., Holman, M. J., Johnson, J. A., Klaus, T. C., Machalek, P., Moorhead, A. V., Morehead, R. C., Ragozzine, D., Tenenbaum, P., Twicken, J. D., Quinn, S. N., Isaacson, H., Shporer, A., Lucas, P. W., Walkowicz, L. M., Welsh, W. F., Boss, A., Devore, E., Gould, A., Smith, J. C., Morris, R. L., Prsa, A., Morton, T. D., Still, M., Thompson, S. E., Mullally, F., Endl, M., and MacQueen, P. J. (2012). Planet Occurrence within 0.25 AU of Solar-type Stars from Kepler. *Astrophysical Journals*, 201:15.

Howell, S. B., Horch, E. P., Everett, M. E., and Ciardi, D. R. (2012). Speckle Camera Imaging of the Planet Pluto. *Publications of the Astronomical Society of Pacifics*, 124:1124–1131.

Howell, S. B., Sobeck, C., Haas, M., Still, M., Barclay, T., Mullally, F., Troeltzsch, J., Aigrain, S., Bryson, S. T., Caldwell, D., Chaplin, W. J., Cochran, W. D., Huber, D., Marcy, G. W., Miglio, A., Najita, J. R., Smith, M., Twicken, J. D., and Fortney, J. J. (2014). The K2 Mission: Characterization and Early Results. *Publications of the Astronomical Society of the Pacific*, 126:398–408.

Howell, S. B., VanOutryve, C., Tonry, J. L., Everett, M. E., and Schneider, R. (2005). A Search for Variable Stars and Planetary Occultations in NGC 2301. II. Variability. *The Publications of the Astronomical Society of the Pacific*, 117:1187–1203.

Hubeny, I. and Lanz, T. (1995). Non-LTE line-blanketed model atmospheres of hot stars. 1: Hybrid complete linearization/accelerated lambda iteration method. *The Astrophysical Journal*, 439:875–904.

Hubickyj, O., Bodenheimer, P., and Lissauer, J. J. (2004). Evolution of Gas Giant Planets Using the Core Accretion Model. In Garcia-Segura, G., Tenorio-Tagle, G., Franco, J., and Yorke, H. W., editors, *Revista Mexicana de Astronomia y Astrofisica Conference Series*, volume 22 of *Revista Mexicana de Astronomia y Astrofisica Conference Series*, pages 83–86.

Hufnagel, R. E. and Stanley, N. R. (1964). Modulation Transfer Function Associated with Image Transmission through Turbulent Media. *Journal of the Optical Society of America (1917-1983)*, 54:52.

Ida, S. and Lin, D. N. C. (2005). Dependence of Exoplanets on Host Stars' Metallicity and Mass. *Progress of Theoretical Physics Supplement*, 158:68–85.

Ivanova, N. (2015). *Binary Evolution: Roche Lobe Overflow and Blue Stragglers*, page 179.

Izidoro, A., Raymond, S. N., Morbidelli, A., and Winter, O. C. (2015). Terrestrial planet formation constrained by Mars and the structure of the asteroid belt. *Monthly Notices of the Royal Astronomical Society*, 453:3619–3634.

Janson, M., Bonavita, M., Klahr, H., and Lafrenière, D. (2012). How do Most Planets Form? Constraints on Disk Instability from Direct Imaging. *Astrophysical Journal*, 745:4.

Jenkins, J. M., Chandrasekaran, H., McCauliff, S. D., Caldwell, D. A., Tenenbaum, P., Li, J., Klaus, T. C., Cote, M. T., and Middour, C. (2010). Transiting planet search in the Kepler pipeline. In *Software and Cyberinfrastructure for Astronomy*, volume 7740 of *Society of Photo-Optical Instrumentation Engineers (SPIE) Conference Series*, page 77400D.

Johnson, J. A., Aller, K. M., Howard, A. W., and Crepp, J. R. (2010). Giant Planet Occurrence in the Stellar Mass-Metallicity Plane. *Publications of the ASP*, 122:905–915.

Johnson, J. A. and Apps, K. (2009). On the Metal Richness of M Dwarfs with Planets. *The Astrophysical Journal*, 699:933–937.

Johnson, J. A., Butler, R. P., Marcy, G. W., Fischer, D. A., Vogt, S. S., Wright, J. T., and Peek, K. M. G. (2007). A New Planet around an M Dwarf: Revealing a Correlation between Exoplanets and Stellar Mass. *Astrophysical Journal*, 670:833–840.

Johnson, J. A., Gazak, J. Z., Apps, K., Muirhead, P. S., Crepp, J. R., Crossfield, I. J. M., Boyajian, T., von Braun, K., Rojas-Ayala, B., Howard, A. W., Covey, K. R., Schlawin, E., Hamren, K., Morton, T. D., Marcy, G. W., and Lloyd, J. P. (2012). Characterizing the Cool KOIs. II. The M Dwarf KOI-254 and Its Hot Jupiter. *Astronomical Journal*, 143:111.

Jones, D. J., Diddams, S. A., Ranka, J. K., Stentz, A., Windeler, R. S., Hall, J. L., and Cundiff, S. T. (2000). Carrier-Envelope Phase Control of Femtosecond Mode-Locked Lasers and Direct Optical Frequency Synthesis. *Science*, 288:635–640.

Joshi, M. (2003). Climate Model Studies of Synchronously Rotating Planets. *Astrobiology*, 3:415–427.

Jovanovic, N., Martinache, F., Guyon, O., Clergeon, C., Singh, G., Kudo, T., Garrel, V., Newman, K., Doughty, D., Lozi, J., Males, J., Minowa, Y., Hayano, Y., Takato, N., Morino, J., Kuhn, J., Serabyn, E., Norris, B., Tuthill, P., Schworer, G., Stewart, P., Close, L., Huby, E., Perrin, G., Lacour, S., Gauchet, L., Vievard, S., Murakami, N., Oshiyama, F., Baba, N., Matsuo, T., Nishikawa, J., Tamura, M., Lai, O., Marchis, F., Duchene, G., Kotani, T., and Woillez, J. (2015). The Subaru Coronagraphic Extreme Adaptive Optics System: Enabling High-Contrast Imaging on Solar-System Scales. *Publications of the Astronomical Society of the Pacific*, 127:890–910.

Kaiser, N., Aussel, H., Burke, B. E., Boesgaard, H., Chambers, K., Chun, M. R., Heasley, J. N., Hodapp, K.-W., Hunt, B., Jedicke, R., Jewitt, D., Kudritzki, R., Luppino, G. A., Maberry, M., Magnier, E., Monet, D. G., Onaka, P. M., Pickles, A. J., Rhoads, P. H. H., Simon, T., Szalay, A., Szapudi, I., Tholen, D. J., Tonry, J. L., Waterson, M., and Wick, J. (2002). Pan-STARRS: A Large Synoptic Survey Telescope Array. In Tyson, J. A. and Wolff, S., editors, *Survey and Other Telescope Technologies and Discoveries*, volume 4836 of *Society of Photo-Optical Instrumentation Engineers (SPIE) Conference Series*, pages 154–164.

Kalas, P., Graham, J. R., Chiang, E., Fitzgerald, M. P., Clampin, M., Kite, E. S., Stapelfeldt, K., Marois, C., and Krist, J. (2008). Optical Images of an Exosolar Planet 25 Light-Years from Earth. *Science*, 322:1345–.

Kaltenegger, L. and Traub, W. A. (2009). Transits of Earth-like Planets. *The Astrophysical Journal*, 698:519–527.

Kant, I. (1755). *Universal Natural History and Theory of the Heavens.*

Kargel, J. S., Kaye, J. Z., Head, J. W., Marion, G. M., Sassen, R., Crowley, J. K., Ballesteros, O. P., Grant, S. A., and Hogenboom, D. L. (2000). Europa's Crust and Ocean: Origin, Composition, and the Prospects for Life. *Icarus*, 148:226–265.

Kasting, J. F., Whitmire, D. P., and Reynolds, R. T. (1993). Habitable Zones around Main Sequence Stars. *Iokcarus*, 101:108–128.

Kipping, D. M. (2013). Parametrizing the exoplanet eccentricity distribution with the Beta distribution. *Monthly Notices of the Royal Astronomical Society*, 434:L51–L55.

Kley, W. and Nelson, R. P. (2012). Planet-Disk Interaction and Orbital Evolution. *Annual Review of Astronomy and Astrophysics*, 50:211–249.

Knutson, H. A., Charbonneau, D., Allen, L. E., Fortney, J. J., Agol, E., Cowan, N. B., Showman, A. P., Cooper, C. S., and Megeath, S. T. (2007). A map of the day-night contrast of the extrasolar planet HD 189733b. *Nature*, 447:183–186.

Kolbl, R., Marcy, G. W., Isaacson, H., and Howard, A. W. (2015). Detection of Stars Within 0.8 in of Kepler Objects of Interest. *The Astronomical Journal*, 149:18.

Kopparapu, R. K., Ramirez, R., Kasting, J. F., Eymet, V., Robinson, T. D., Mahadevan, S., Terrien, R. C., Domagal-Goldman, S., Meadows, V., and Deshpande, R. (2013). Habitable Zones around Main-sequence Stars: New Estimates. *The Astrophysical Journal*, 765:131.

Kopparapu, R. K., Ramirez, R. M., SchottelKotte, J., Kasting, J. F., Domagal-Goldman, S., and Eymet, V. (2014). Habitable Zones around Main-sequence Stars: Dependence on Planetary Mass. *The Astrophysical Journal Letters*, 787:L29.

Koppenhoefer, J., Afonso, C., Saglia, R. P., and Henning, T. (2009). Investigating the potential of the Pan-Planets project using Monte Carlo simulations. *Astronomy and Astrophysics*, 494:707–717.

Koppenhoefer, J., Saglia, R. P., and Riffeser, A. (2013). MDia and POTS. The munich difference imaging analysis for the pre-OmegaTranS project. *Experimental Astronomy*, 35:329–336.

Koshland, D. E. (2002). The seven pillars of life. *Science*, 295(5563):2215–2216.

Kosyra, R., Gössl, C., Hopp, U., Lang-Bardl, F., Riffeser, A., Bender, R., and Seitz, S. (2014). The 64 Mpixel wide field imager for the Wendelstein 2m telescope: design and calibration. *Experimental Astronomy*, 38:213–248.

Kotani, T., Tamura, M., Suto, H., Nishikawa, J., Sato, B., Aoki, W., Usuda, T., Kurokawa, T., Kashiwagi, K., Nishiyama, S., Ikeda, Y., Hall, D. B., Hodapp, K. W., Hashimoto, J., Morino, J.-I., Okuyama, Y., Tanaka, Y., Suzuki, S., Inoue, S., Kwon, J., Suenaga, T., Oh, D., Baba, H., Narita, N., Kokubo, E., Hayano, Y., Izumiura, H., Kambe, E., Kudo, T., Kusakabe, N., Ikoma, M., Hori, Y., Omiya, M., Genda, H., Fukui, A., Fujii, Y., Guyon, O., Harakawa, H., Hayashi, M., Hidai, M., Hirano, T., Kuzuhara, M., Machida, M., Matsuo, T., Nagata, T., Onuki, H., Ogihara, M., Takami, H., Takato, N., Takahashi, Y. H., Tachinami, C., Terada, H., Kawahara, H., and Yamamuro, T. (2014). Infrared Doppler instrument (IRD) for the Subaru telescope to search for Earth-like planets around nearby M-dwarfs. In *Ground-based and Airborne Instrumentation for Astronomy V*, volume 9147 of *Proceedings of the SPIE*, page 914714.

Kovács, G., Hodgkin, S., Sipőcz, B., Pinfield, D., Barrado, D., Birkby, J., Cappetta, M., Cruz, P., Koppenhoefer, J., Martín, E. L., Murgas, F., Nefs, B., Saglia, R., and Zendejas, J. (2013). A sensitivity analysis of the WFCAM Transit Survey for short-period giant planets around M dwarfs. *Monthly Notices of the RAS*, 433:889–906.

Kovács, G., Zucker, S., and Mazeh, T. (2002). A box-fitting algorithm in the search for periodic transits. *Astronomy and Astrophysics*, 391:369–377.

Kratter, K. M. and Murray-Clay, R. A. (2011). Fragment Production and Survival in Irradiated Disks: A Comprehensive Cooling Criterion. *The Astrophysical Journal*, 740:1.

Kraus, A. L. and Hillenbrand, L. A. (2007). The Stellar Populations of Praesepe and Coma Berenices. *The Astronomical Journal*, 134:2340–2352.

Kraus, A. L., Ireland, M. J., Martinache, F., and Lloyd, J. P. (2008). Mapping the Shores of the Brown Dwarf Desert. I. Upper Scorpius. *The Astrophysical Journal*, 679:762–782.

Kraus, A. L., Tucker, R. A., Thompson, M. I., Craine, E. R., and Hillenbrand, L. A. (2011). The Mass-Radius(-Rotation?) Relation for Low-mass Stars. *The Astrophysical Journal*, 728:48.

Kreidberg, L. (2015). batman: BAsic Transit Model cAlculatioN in Python. *Publications of the Astronomical Society of Pacific*, 127:1161–1165.

Lada, C. J. and Lada, E. A. (2003). Embedded Clusters in Molecular Clouds. *Annual Review of Astronomy and Astrophysics*, 41:57–115.

Lang-Bardl, F., Hodapp, K., Jacobson, S., Bender, R., Gössl, C., Fabricius, M., Grupp, F., Hopp, U., and Mitsch, W. (2010). 3kk: the Optical-NIR Multi-Channel Nasmyth Imager for the Wendelstein Fraunhofer Telescope. In *Ground-based and Airborne Instrumentation for Astronomy III*, volume 7735 of *Proceedings of the SPIE*, page 77353Q.

Laughlin, G., Bodenheimer, P., and Adams, F. C. (2004). The Core Accretion Model Predicts Few Jovian-Mass Planets Orbiting Red Dwarfs. *The Astrophysical Journal*, 612:L73–L76.

Law, N. M., Fors, O., Wulfken, P., Ratzloff, J., and Kavanaugh, D. (2014). The Evryscope: the first full-sky gigapixel-scale telescope. In *Ground-based and Airborne Telescopes V*, volume 9145 of *Proceedings of the SPIE*, page 91450Z.

Lee, J. W., Kim, S.-L., Kim, C.-H., Koch, R. H., Lee, C.-U., Kim, H.-I., and Park, J.-H. (2009). The sdB+M Eclipsing System HW Virginis and its Circumbinary Planets. *The Astronomical Journal*, 137:3181–3190.

Léger, A., Rouan, D., Schneider, J., Barge, P., Fridlund, M., Samuel, B., Ollivier, M., Guenther, E., Deleuil, M., Deeg, H. J., Auvergne, M., Alonso, R., Aigrain, S., Alapini, A., Almenara, J. M., Baglin, A., Barbieri, M., Bruntt, H., Bordé, P., Bouchy, F., Cabrera, J., Catala, C., Carone, L., Carpano, S., Csizmadia, S., Dvorak, R., Erikson, A., Ferraz-Mello, S., Foing, B., Fressin, F., Gandolfi, D., Gillon, M., Gondoin, P., Grasset, O., Guillot, T., Hatzes, A., Hébrard, G., Jorda, L., Lammer, H., Llebaria, A., Loeillet, B., Mayor, M., Mazeh, T., Moutou, C., Pätzold, M., Pont, F., Queloz, D., Rauer, H., Renner, S., Samadi, R., Shporer, A., Sotin, C., Tingley, B., Wuchterl, G., Adda, M., Agogu, P., Appourchaux, T., Ballans, H., Baron, P., Beaufort, T., Bellenger, R., Berlin, R., Bernardi, P., Blouin, D., Baudin, F., Bodin, P., Boisnard, L., Boit, L., Bonneau, F., Borzeix, S., Briet, R., Buey, J.-T., Butler, B., Cailleau, D., Cautain, R., Chabaud, P.-Y., Chaintreuil, S., Chiavassa, F., Costes, V., Cuna Parrho, V., de Oliveira Fialho, F., Decaudin, M., Defise, J.-M., Djalal, S., Epstein, G., Exil, G.-E., Fauré, C., Fenouillet, T., Gaboriaud, A., Gallic, A., Gamet, P., Gavalda, P., Grolleau, E., Gruneisen, R., Gueguen, L., Guis, V., Guivarc'h, V., Guterman, P., Hallouard, D., Hasiba, J., Heuripeau, F., Huntzinger, G., Hustaix, H., Imad, C., Imbert, C., Johlander, B., Jouret, M., Journoud, P., Karioty, F., Kerjean, L., Lafaille, V., Lafond, L., Lam-Trong, T., Landiech, P., Lapeyrere, V., Larqué, T., Laudet, P., Lautier, N., Lecann, H., Lefevre, L., Leruyet, B., Levacher, P., Magnan, A., Mazy, E., Mertens, F., Mesnager, J.-M., Meunier, J.-C., Michel, J.-P., Monjoin, W., Naudet, D., Nguyen-Kim, K., Orcesi, J.-L., Ottacher, H., Perez, R., Peter, G., Plasson, P., Plesseria, J.-Y., Pontet, B., Pradines, A., Quentin, C., Reynaud, J.-L., Rolland, G., Rollenhagen, F., Romagnan, R., Russ, N., Schmidt, R., Schwartz, N., Sebbag, I., Sedes, G., Smit, H., Steller, M. B., Sunter, W., Surace, C., Tello, M., Tiphène, D., Toulouse, P., Ulmer, B., Vandermarcq, O., Vergnault, E., Vuillemin, A., and Zanatta, P. (2009). Transiting exoplanets from the CoRoT space mission. VIII. CoRoT-7b: the first super-Earth with measured radius. *Astronomy and Astrophysics*, 506:287–302.

Lépine, S. and Simon, M. (2009). Nearby Young Stars Selected by Proper Motion. I. Four New Members of the β Pictoris Moving Group From The Tycho-2 Catalog. *The Astronomical Journal*, 137:3632–3645.

Lin, D. N. C. and Papaloizou, J. (1979). Tidal torques on accretion discs in binary systems with extreme mass ratios. *Monthly Notices of the Royal Astronomical Society*, 186:799–812.

Lineweaver, C. H., Fenner, Y., and Gibson, B. K. (2004). The Galactic Habitable Zone and the Age Distribution of Complex Life in the Milky Way. *Science*, 303:59–62.

Lissauer, J. J., Fabrycky, D. C., Ford, E. B., Borucki, W. J., Fressin, F., Marcy, G. W., Orosz, J. A., Rowe, J. F., Torres, G., Welsh, W. F., Batalha, N. M., Bryson, S. T., Buchhave, L. A., Caldwell, D. A., Carter, J. A., Charbonneau, D., Christiansen, J. L., Cochran, W. D., Desert, J.-M., Dunham, E. W., Fanelli, M. N., Fortney, J. J., Gautier, III, T. N., Geary, J. C., Gilliland, R. L., Haas, M. R., Hall, J. R., Holman, M. J., Koch, D. G., Latham, D. W., Lopez, E., McCauliff, S., Miller, N., Morehead, R. C., Quintana, E. V., Ragozzine, D., Sasselov, D., Short, D. R., and Steffen, J. H. (2011). A closely packed system of low-mass, low-density planets transiting Kepler-11. *Nature*, 470:53–58.

Lissauer, J. J., Marcy, G. W., Bryson, S. T., Rowe, J. F., Jontof-Hutter, D., Agol, E., Borucki, W. J., Carter, J. A., Ford, E. B., Gilliland, R. L., Kolbl, R., Star, K. M., Steffen, J. H., and Torres, G. (2014). Validation of Kepler's Multiple Planet Candidates. II. Refined Statistical Framework and Descriptions of Systems of Special Interest. *The Astrophysical Journal*, 784:44.

Lopez, E. D. and Fortney, J. J. (2016). Re-inflated Warm Jupiters around Red Giants. *The Astrophysical Journal*, 818:4.

Lovis, C. and Mayor, M. (2007). Planets around evolved intermediate-mass stars. I. Two substellar companions in the open clusters NGC 2423 and NGC 4349. *Astronomy and Astrophysics*, 472:657–664.

Lovis, C. and Pepe, F. (2007). A new list of thorium and argon spectral lines in the visible. *Astronomy and Astrophysics*, 468:1115–1121.

Lovis, C., Ségransan, D., Mayor, M., Udry, S., Benz, W., Bertaux, J.-L., Bouchy, F., Correia, A. C. M., Laskar, J., Lo Curto, G., Mordasini, C., Pepe, F., Queloz, D., and Santos, N. C. (2011). The HARPS search for southern extra-solar planets. XXVIII. Up to seven planets orbiting HD 10180: probing the architecture of low-mass planetary systems. *Astronomy and Astrophysics*, 528:A112.

Lubow, S. H. and Ida, S. (2010). Planet Migration. *arXiv, To appear in Exoplanets, ed. S. Seager*.

Lutz, R., Schuh, S., Silvotti, R., Bernabei, S., Dreizler, S., Stahn, T., and Hugelmeyer, S. D. (2009). The planet-hosting subdwarf B star V 391 Pegasi is a hybrid pulsator. *Astronomy and Astrophysics*, 496:469–473.

Maciejewski, G., Dimitrov, D., Neuhäuser, R., Niedzielski, A., Raetz, S., Ginski, C., Adam, C., Marka, C., Moualla, M., and Mugrauer, M. (2010). Transit timing variation in exoplanet WASP-3b. *Monthly Notices of the Royal Astronomical Society*, 407:2625–2631.

Madsen, S., Dravins, D., and Lindegren, L. (2002). Astrometric radial velocities. III. Hipparcos measurements of nearby star clusters and associations. *Astronomy and Astrophysics*, 381:446–463.

Magnier, E. (2006). The Pan-STARRS PS1 Image Processing Pipeline. In *The Advanced Maui Optical and Space Surveillance Technologies Conference*, page 50.

Magnier, E. A., Schlafly, E., Finkbeiner, D., Juric, M., Tonry, J. L., Burgett, W. S., Chambers, K. C., Flewelling, H. A., Kaiser, N., Kudritzki, R.-P., Morgan, J. S., Price, P. A., Sweeney, W. E., and Stubbs, C. W. (2013). The Pan-STARRS 1 Photometric Reference Ladder, Release 12.01. *The Astrophysical Journal Supplement*, 205:20.

Mahadevan, S., Ramsey, L., Bender, C., Terrien, R., Wright, J. T., Halverson, S., Hearty, F., Nelson, M., Burton, A., Redman, S., Osterman, S., Diddams, S., Kasting, J., Endl, M., and Deshpande, R. (2012). The habitable-zone planet finder: a stabilized fiber-fed NIR spectrograph for the Hobby-Eberly Telescope. In *Ground-based and Airborne Instrumentation for Astronomy IV*, volume 8446 of *Ground-based and Airborne Instrumentation for Astronomy IV. Proceedings of the SPIE*, page 84461S.

Majaess, D. J., Turner, D. G., Lane, D. J., and Krajci, T. (2011). Deep Infrared ZAMS Fits to Benchmark Open Clusters Hosting Delta Scuti Stars. *Journal of the American Association of Variable Star Observers (JAAVSO)*, 39:219.

Mamajek, E. E., Quillen, A. C., Pecaut, M. J., Moolekamp, F., Scott, E. L., Kenworthy, M. A., Collier Cameron, A., and Parley, N. R. (2012). Planetary Construction Zones in Occultation: Discovery of an Extrasolar Ring System Transiting a Young Sun-like Star and Future Prospects for Detecting Eclipses by Circumsecondary and Circumplanetary Disks. *The Astronomical Journal*, 143:72.

Mancini, L., Ciceri, S., Chen, G., Tregloan-Reed, J., Fortney, J. J., Southworth, J., Tan, T. G., Burgdorf, M., Calchi Novati, S., Dominik, M., Fang, X.-S., Finet, F., Gerner, T., Hardis, S., Hinse, T. C., Jørgensen, U. G., Liebig, C., Nikolov, N., Ricci, D., Schäfer, S., Schönebeck, F., Skottfelt, J., Wertz, O., Alsubai, K. A., Bozza, V., Browne, P., Dodds, P., Gu, S.-H., Harpsøe, K., Henning, T., Hundertmark, M., Jessen-Hansen, J., Kains, N., Kerins, E., Kjeldsen, H., Lund, M. N., Lundkvist, M., Madhusudhan, N., Mathiasen, M., Penny, M. T., Prof, S., Rahvar, S., Sahu, K., Scarpetta, G., Snodgrass, C., and Surdej, J. (2013). Physical properties, transmission and emission spectra of the WASP-19 planetary system from multi-colour photometry. *Monthly Notices of the Royal Astronomical Society*, 436:2–18.

Mandel, K. and Agol, E. (2002). Analytic Light Curves for Planetary Transit Searches. *The Astrophysical Journal*, 580:L171–L175.

Mann, A. W., Brewer, J. M., Gaidos, E., Lépine, S., and Hilton, E. J. (2013a). Prospecting in Late-type Dwarfs: A Calibration of Infrared and Visible Spectroscopic Metallicities of Late K and M Dwarfs Spanning 1.5 dex. *The Astronomical Journal*, 145:52.

Mann, A. W., Feiden, G. A., Gaidos, E., Boyajian, T., and von Braun, K. (2015). How to Constrain Your M Dwarf: Measuring Effective Temperature, Bolometric Luminosity, Mass, and Radius. *The Astrophysical Journal*, 804:64.

Mann, A. W., Gaidos, E., and Ansdell, M. (2013b). Spectro-thermometry of M Dwarfs and Their Candidate Planets: Too Hot, Too Cool, or Just Right? *The Astrophysical Journal*, 779:188.

Mann, A. W., Gaidos, E., Kraus, A., and Hilton, E. J. (2013c). Testing the Metal of Late-type Kepler Planet Hosts with Iron-clad Methods. *The Astrophysical Journal*, 770:43.

Mann, A. W., Gaidos, E., Lépine, S., and Hilton, E. J. (2012). They Might be Giants: Luminosity Class, Planet Occurrence, and Planet-Metallicity Relation of the Coolest Kepler Target Stars. *Astrophysical Journal*, 753:90.

Mann, A. W., Gaidos, E., Mace, G. N., Johnson, M. C., Bowler, B. P., LaCourse, D., Jacobs, T. L., Vanderburg, A., Kraus, A. L., Kaplan, K. F., and Jaffe, D. T. (2016a). Zodiacal Exoplanets in Time (ZEIT). I. A Neptune-sized Planet Orbiting an M4.5 Dwarf in the Hyades Star Cluster. *The Astrophysical Journal*, 818:46.

Mann, A. W., Newton, E. R., Rizzuto, A. C., Irwin, J., Feiden, G. A., Gaidos, E., Mace, G. N., Kraus, A. L., James, D. J., Ansdell, M., Charbonneau, D., Covey, K. R., Ireland, M. J., Jaffe, D. T., Johnson, M. C., Kidder, B., and Vanderburg, A. (2016b). Zodiacal Exoplanets in Time (ZEIT) III: A Neptune-sized planet orbiting a pre-main-sequence star in the Upper Scorpius OB Association. *ArXiv e-prints*.

Mapelli, M., Sigurdsson, S., Ferraro, F. R., Colpi, M., Possenti, A., and Lanzoni, B. (2006). The radial distribution of blue straggler stars and the nature of their progenitors. *Monthly Notices of the Royal Astronomical Society*, 373:361–368.

Marcy, G. W. and Butler, R. P. (2000). Planets Orbiting Other Suns. *The Publications of the Astronomical Society of the Pacific*, 112:137–140.

Marcy, G. W., Isaacson, H., Howard, A. W., Rowe, J. F., Jenkins, J. M., Bryson, S. T., Latham, D. W., Howell, S. B., Gautier, III, T. N., Batalha, N. M., Rogers, L., Ciardi, D., Fischer, D. A., Gilliland, R. L., Kjeldsen, H., Christensen-Dalsgaard, J., Huber, D., Chaplin, W. J., Basu, S., Buchhave, L. A., Quinn, S. N., Borucki, W. J., Koch, D. G., Hunter, R., Caldwell, D. A., Van Cleve, J., Kolbl, R., Weiss, L. M., Petigura, E., Seager, S., Morton, T., Johnson, J. A., Ballard, S., Burke, C., Cochran, W. D., Endl, M., MacQueen, P., Everett, M. E., Lissauer, J. J., Ford, E. B., Torres, G., Fressin, F., Brown, T. M., Steffen, J. H., Charbonneau, D., Basri, G. S., Sasselov, D. D., Winn, J., Sanchis-Ojeda, R., Christiansen, J., Adams, E., Henze, C., Dupree, A., Fabrycky, D. C., Fortney, J. J., Tarter, J., Holman, M. J., Tenenbaum, P., Shporer, A., Lucas, P. W., Welsh, W. F., Orosz, J. A., Bedding, T. R., Campante, T. L., Davies, G. R., Elsworth, Y., Handberg, R., Hekker, S., Karoff, C., Kawaler, S. D., Lund, M. N., Lundkvist, M., Metcalfe, T. S., Miglio, A., Silva Aguirre, V., Stello, D., White, T. R., Boss, A., Devore, E., Gould, A., Prsa, A., Agol, E., Barclay, T., Coughlin, J., Brugamyer, E., Mullally, F., Quintana, E. V., Still, M., Thompson, S. E., Morrison, D., Twicken, J. D., Désert, J.-M., Carter, J., Crepp, J. R., Hébrard, G., Santerne, A., Moutou, C., Sobeck, C., Hudgins, D., Haas, M. R., Robertson, P., Lillo-Box, J., and Barrado, D. (2014). Masses, Radii, and Orbits of Small Kepler Planets: The Transition from Gaseous to Rocky Planets. *The Astrophysical Journals*, 210:20.

Margot, J.-L. (2015). A Quantitative Criterion for Defining Planets. *ArXiv e-prints*.

Marion, G. M., Fritsen, C. H., Eicken, H., and Payne, M. C. (2003). The Search for Life on Europa: Limiting Environmental Factors, Potential Habitats, and Earth Analogues. *Astrobiology*, 3:785–811.

Marois, C., Macintosh, B., Barman, T., Zuckerman, B., Song, I., Patience, J., Lafrenière, D., and Doyon, R. (2008). Direct Imaging of Multiple Planets Orbiting the Star HR 8799. *Science*, 322:1348–.

Masset, F. S. (2002). The co-orbital corotation torque in a viscous disk: Numerical simulations. *Astronomy and Astrophysics*, 387:605–623.

Matsumura, S., Takeda, G., and Rasio, F. A. (2008). On the Origins of Eccentric Close-In Planets. *Astrophysical Journal*, 686:L29–L32.

Mautner, M. N. (1997). Directed Panspermia. 3. strategies and Motivation for Seeding Star-Forming Clouds. *Journal of the British Interplanetary Society*, 50:93–102.

Mayor, M., Pepe, F., Queloz, D., Bouchy, F., Rupprecht, G., Lo Curto, G., Avila, G., Benz, W., Bertaux, J.-L., Bonfils, X., Dall, T., Dekker, H., Delabre, B., Eckert, W., Fleury, M., Gilliotte, A., Gojak, D., Guzman, J. C., Kohler, D., Lizon, J.-L., Longinotti, A., Lovis, C., Megevand, D., Pasquini, L., Reyes, J., Sivan, J.-P., Sosnowska, D., Soto, R., Udry, S., van Kesteren, A., Weber, L., and Weilenmann, U. (2003). Setting New Standards with HARPS. *The Messenger*, 114:20–24.

Mayor, M. and Queloz, D. (1995). A Jupiter-mass companion to a solar-type star. *Nature*, 378:355–359.

Mayor, M., Udry, S., Lovis, C., Pepe, F., Queloz, D., Benz, W., Bertaux, J.-L., Bouchy, F., Mordasini, C., and Segransan, D. (2009). The HARPS search for southern extra-solar planets. XIII. A planetary system with 3 super-Earths (4.2, 6.9, and 9.2 M). *Astronomy and Astrophysics*, 493:639–644.

McLaughlin, D. B. (1924). Some results of a spectrographic study of the Algol system. *Astrophysical Journal*, 60.

Meibom, S., Torres, G., Fressin, F., Latham, D. W., Rowe, J. F., Ciardi, D. R., Bryson, S. T., Rogers, L. A., Henze, C. E., Janes, K., Barnes, S. A., Marcy, G. W., Isaacson, H., Fischer, D. A., Howell, S. B., Horch, E. P., Jenkins, J. M., Schuler, S. C., and Crepp, J. (2013). The same frequency of planets inside and outside open clusters of stars. *Nature*, 499:55–58.

Miller, S. L. (1953). A Production of Amino Acids under Possible Primitive Earth Conditions. *Science*, 117:528–529.

Mislis, D., Schröter, S., Schmitt, J. H. M. M., Cordes, O., and Reif, K. (2010). Multi-band transit observations of the TrES-2b exoplanet. *Astronomy and Astrophysics*, 510:A107.

Monet, D. G., Levine, S. E., Canzian, B., Ables, H. D., Bird, A. R., Dahn, C. C., Guetter, H. H., Harris, H. C., Henden, A. A., Leggett, S. K., Levison, H. F., Luginbuhl, C. B., Martini, J., Monet, A. K. B., Munn, J. A., Pier, J. R., Rhodes, A. R., Riepe, B., Sell, S., Stone, R. C., Vrba, F. J., Walker, R. L., Westerhout, G., Brucato, R. J., Reid, I. N., Schoening, W., Hartley, M., Read, M. A., and Tritton, S. B. (2003). The USNO-B Catalog. *Astronomical Journal*, 125:984–993.

Monnier, J. D. (2003). Optical interferometry in astronomy. *Reports on Progress in Physics*, 66(5):789.

Montalto, M., Gregorio, J., Boué, G., Mortier, A., Boisse, I., Oshagh, M., Maturi, M., Figueira, P., Sousa, S., and Santos, N. C. (2012). A new analysis of the WASP-3 system: no evidence for an additional companion. *Monthly Notices of the Royal Astronomical Society*, 427:2757–2771.

Montet, B. T., Crepp, J. R., Johnson, J. A., Howard, A. W., and Marcy, G. W. (2014). The TRENDS High-contrast Imaging Survey. IV. The Occurrence Rate of Giant Planets around M Dwarfs. *The Astrophysical Journal*, 781:28.

Mordasini, C., Alibert, Y., Benz, W., Klahr, H., and Henning, T. (2012). Extrasolar planet population synthesis . IV. Correlations with disk metallicity, mass, and lifetime. *Astronomy and Astrophysics*, 541:A97.

Morton, T. D. (2012). An Efficient Automated Validation Procedure for Exoplanet Transit Candidates. *The Astrophysical Journal*, 761:6.

Morton, T. D. (2015). VESPA: False positive probabilities calculator. Astrophysics Source Code Library.

Morton, T. D., Bryson, S. T., Coughlin, J. L., Rowe, J. F., Ravichandran, G., Petigura, E. A., Haas, M. R., and Batalha, N. M. (2016). False Positive Probabilities for all Kepler Objects of Interest: 1284 Newly Validated Planets and 428 Likely False Positives. *The Astrophysical Journal*, 822:86.

Morton, T. D. and Swift, J. (2014). The Radius Distribution of Planets around Cool Stars. *The Astrophysical Journal*, 791:10.

Mulders, G. D., Pascucci, I., and Apai, D. (2015a). A Stellar-mass-dependent Drop in Planet Occurrence Rates. *Astrophysical Journal*, 798:112.

Mulders, G. D., Pascucci, I., and Apai, D. (2015b). An Increase in the Mass of Planetary Systems around Lower-mass Stars. *The Astrophysical Journal*, 814:130.

Murphy, M. T., Udem, T., Holzwarth, R., Sizmann, A., Pasquini, L., Araujo-Hauck, C., Dekker, H., D'Odorico, S., Fischer, M., Hänsch, T. W., and Manescau, A. (2007). High-precision wavelength calibration of astronomical spectrographs with laser frequency combs. *Monthly Notices of the Royal Astronomical Society*, 380:839–847.

Muterspaugh, M. W., Lane, B. F., Kulkarni, S. R., Konacki, M., Burke, B. F., Colavita, M. M., Shao, M., Hartkopf, W. I., Boss, A. P., and Williamson, M. (2010). The Phases Differential Astrometry Data Archive. V. Candidate Substellar Companions to Binary Systems. *The Astronomical Journal*, 140:1657–1671.

Nefs, S. V., Birkby, J. L., Snellen, I. A. G., Hodgkin, S. T., Sipőcz, B. M., Kovács, G., Mislis, D., Pinfield, D. J., and Martin, E. L. (2013). A highly unequal-mass eclipsing M-dwarf binary in the WFCAM Transit Survey. *Monthly Notices of the Royal Astronomical Society*, 431:3240–3257.

Neuhäuser, R., Errmann, R., Berndt, A., Maciejewski, G., Takahashi, H., Chen, W. P., Dimitrov, D. P., Pribulla, T., Nikogossian, E. H., Jensen, E. L. N., Marschall, L., Wu, Z.-Y., Kellerer, A., Walter, F. M., Briceño, C., Chini, R., Fernandez, M., Raetz, S., Torres, G., Latham, D. W., Quinn, S. N., Niedzielski, A., Bukowiecki, Ł., Nowak, G., Tomov, T., Tachihara, K., Hu, S. C.-L., Hung, L. W., Kjurkchieva, D. P., Radeva, V. S., Mihov, B. M., Slavcheva-Mihova, L., Bozhinova, I. N., Budaj, J., Vaňko, M., Kundra, E., Hambálek, Ľ., Krushevska, V., Movsessian, T., Harutyunyan, H., Downes, J. J., Hernandez, J., Hoffmeister, V. H., Cohen, D. H., Abel, I., Ahmad, R., Chapman, S., Eckert, S., Goodman, J., Guerard, A., Kim, H. M., Koontharana, A., Sokol, J., Trinh, J., Wang, Y., Zhou, X., Redmer, R., Kramm, U., Nettelmann, N., Mugrauer, M., Schmidt, J., Moualla, M., Ginski, C., Marka, C., Adam, C., Seeliger, M., Baar, S., Roell, T., Schmidt, T. O. B., Trepl, L., Eisenbeiss, T., Fiedler, S., Tetzlaff, N., Schmidt, E., Hohle, M. M., Kitze, M., Chakrova, N., Gräfe, C., Schreyer, K., Hambaryan, V. V., Broeg, C. H., Koppenhoefer, J., and Pandey, A. K. (2011). The Young Exoplanet Transit Initiative (YETI). *Astronomische Nachrichten*, 332:547.

Neves, V., Bonfils, X., Santos, N. C., Delfosse, X., Forveille, T., Allard, F., and Udry, S. (2013). Metallicity of M dwarfs. III. Planet-metallicity and planet-stellar mass correlations of the HARPS GTO M dwarf sample. *Astronomy and Astrophysics*, 551:A36.

Newton, E. R., Charbonneau, D., Irwin, J., Berta-Thompson, Z. K., Rojas-Ayala, B., Covey, K., and Lloyd, J. P. (2014). Near-infrared Metallicities, Radial Velocities, and Spectral Types for 447 Nearby M Dwarfs. *The Astronomical Journal*, 147:20.

Newton, E. R., Charbonneau, D., Irwin, J., and Mann, A. W. (2015). An Empirical Calibration to Estimate Cool Dwarf Fundamental Parameters from H-band Spectra. *The Astrophysical Journal*, 800:85.

Obermeier, C., Koppenhoefer, J., Saglia, R. P., Henning, T., Bender, R., Kodric, M., Deacon, N., Riffeser, A., Burgett, W., Chambers, K. C., Draper, P. W., Flewelling, H., Hodapp, K. W., Kaiser, N., Kudritzki, R.-P., Magnier, E. A., Metcalfe, N., Price, P. A., Sweeney, W., Wainscoat, R. J., and Waters, C. (2016). Pan-Planets: Searching for hot Jupiters around cool dwarfs. *Astronomy and Astrophysics*, 587:A49.

Pál, A., Bakos, G. Á., Torres, G., Noyes, R. W., Latham, D. W., Kovács, G., Marcy, G. W., Fischer, D. A., Butler, R. P., Sasselov, D. D., Sipőcz, B., Esquerdo, G. A., Kovács, G., Stefanik, R., Lázár, J., Papp, I., and Sári, P. (2008). HAT-P-7b: An Extremely Hot Massive Planet Transiting a Bright Star in the Kepler Field. *The Astrophysical Journal*, 680:1450–1456.

Parviainen, H. and Aigrain, S. (2015). LDTK: Limb Darkening Toolkit. *Monthly Notices of the Royal Astronomical Society*, 453:3821–3826.

Pecaut, M. J. and Mamajek, E. E. (2013). Intrinsic Colors, Temperatures, and Bolometric Corrections of Pre-main-sequence Stars. *The Astrophysical Journals*, 208:9.

Perryman, M. (2011). *The Exoplanet Handbook*.

Perryman, M. A. C. (2000). Extra-solar planets. *Reports on Progress in Physics*, 63:1209–1272.

Petigura, E. A., Howard, A. W., and Marcy, G. W. (2013a). Prevalence of Earth-size planets orbiting Sun-like stars. *Proceedings of the National Academy of Science*, 110:19273–19278.

Petigura, E. A., Marcy, G. W., and Howard, A. W. (2013b). A Plateau in the Planet Population below Twice the Size of Earth. *The Astrophysical Journal*, 770:69.

Petigura, E. A., Schlieder, J. E., Crossfield, I. J. M., Howard, A. W., Deck, K. M., Ciardi, D. R., Sinukoff, E., Allers, K. N., Best, W. M. J., Liu, M. C., Beichman, C. A., Isaacson, H., Hansen, B. M. S., and Lépine, S. (2015). Two Transiting Earth-size Planets Near Resonance Orbiting a Nearby Cool Star. *The Astrophysical Journal*, 811:102.

Pfeiffer, M. J., Frank, C., Baumueller, D., Fuhrmann, K., and Gehren, T. (1998). FOCES - a fibre optics Cassegrain Echelle spectrograph. *Astronomy and Astrophysics Supplement*, 130:381–393.

Pollacco, D. L., Skillen, I., Collier Cameron, A., Christian, D. J., Hellier, C., Irwin, J., Lister, T. A., Street, R. A., West, R. G., Anderson, D. R., Clarkson, W. I., Deeg, H., Enoch, B., Evans, A., Fitzsimmons, A., Haswell, C. A., Hodgkin, S., Horne, K., Kane, S. R., Keenan, F. P., Maxted, P. F. L., Norton, A. J., Osborne, J., Parley, N. R., Ryans, R. S. I., Smalley, B., Wheatley, P. J., and Wilson, D. M. (2006). The WASP Project and the SuperWASP Cameras. *The Publications of the Astronomical Society of the Pacific*, 118:1407–1418.

Pollack, J. B., Hubickyj, O., Bodenheimer, P., Lissauer, J. J., Podolak, M., and Greenzweig, Y. (1996). Formation of the Giant Planets by Concurrent Accretion of Solids and Gas. *Icarus*, 124:62–85.

Prialnik, D. (2000). *An Introduction to the Theory of Stellar Structure and Evolution*.

Queloz, D., Eggenberger, A., Mayor, M., Perrier, C., Beuzit, J. L., Naef, D., Sivan, J. P., and Udry, S. (2000). Detection of a spectroscopic transit by the planet orbiting the star HD209458. *Astronomy and Astrophysics*, 359:L13–L17.

Quinn, S. N., White, R. J., Latham, D. W., Buchhave, L. A., Cantrell, J. R., Dahm, S. E., Fűrész, G., Szentgyorgyi, A. H., Geary, J. C., Torres, G., Bieryla, A., Berlind, P., Calkins, M. C., Esquerdo, G. A., and Stefanik, R. P. (2012). Two "b"s in the Beehive: The Discovery of the First Hot Jupiters in an Open Cluster. *The Astrophysical Journal*, 756:L33.

Quinn, S. N., White, R. J., Latham, D. W., Buchhave, L. A., Torres, G., Stefanik, R. P., Berlind, P., Bieryla, A., Calkins, M. C., Esquerdo, G. A., Fűrész, G., Geary, J. C., and Szentgyorgyi, A. H. (2014). HD 285507b: An Eccentric Hot Jupiter in the Hyades Open Cluster. *The Astrophysical Journal*, 787:27.

Quirrenbach, A., Amado, P. J., Caballero, J. A., Mundt, R., Reiners, A., Ribas, I., Seifert, W., Abril, M., Aceituno, J., Alonso-Floriano, F. J., Ammler-von Eiff, M., Antona Jiménez, R., Anwand-Heerwart, H., Azzaro, M., Bauer, F., Barrado, D., Becerril, S., Béjar, V. J. S., Benítez, D., Berdiñas, Z. M., Cárdenas, M. C., Casal, E., Claret, A., Colomé, J., Cortés-Contreras, M., Czesla, S., Doellinger, M., Dreizler, S., Feiz, C., Fernández, M., Galadí, D., Gálvez-Ortiz, M. C., García-Piquer, A., García-Vargas, M. L., Garrido, R., Gesa, L., Gómez Galera, V., González Álvarez, E., González Hernández, J. I., Grözinger, U., Guàrdia, J., Guenther, E. W., de Guindos, E., Gutiérrez-Soto, J., Hagen, H.-J., Hatzes, A. P.,

Hauschildt, P. H., Helmling, J., Henning, T., Hermann, D., Hernández Castaño, L., Herrero, E., Hidalgo, D., Holgado, G., Huber, A., Huber, K. F., Jeffers, S., Joergens, V., de Juan, E., Kehr, M., Klein, R., Kürster, M., Lamert, A., Lalitha, S., Laun, W., Lemke, U., Lenzen, R., López del Fresno, M., López Martí, B., López-Santiago, J., Mall, U., Mandel, H., Martín, E. L., Martín-Ruiz, S., Martínez-Rodríguez, H., Marvin, C. J., Mathar, R. J., Mirabet, E., Montes, D., Morales Muñoz, R., Moya, A., Naranjo, V., Ofir, A., Oreiro, R., Pallé, E., Panduro, J., Passegger, V.-M., Pérez-Calpena, A., Pérez Medialdea, D., Perger, M., Pluto, M., Ramón, A., Rebolo, R., Redondo, P., Reffert, S., Reinhardt, S., Rhode, P., Rix, H.-W., Rodler, F., Rodríguez, E., Rodríguez-López, C., Rodríguez-Pérez, E., Rohloff, R.-R., Rosich, A., Sánchez-Blanco, E., Sánchez Carrasco, M. A., Sanz-Forcada, J., Sarmiento, L. F., Schäfer, S., Schiller, J., Schmidt, C., Schmitt, J. H. M. M., Solano, E., Stahl, O., Storz, C., Stürmer, J., Suárez, J. C., Ulbrich, R. G., Veredas, G., Wagner, K., Winkler, J., Zapatero Osorio, M. R., Zechmeister, M., Abellán de Paco, F. J., Anglada-Escudé, G., del Burgo, C., Klutsch, A., Lizon, J. L., López-Morales, M., Morales, J. C., Perryman, M. A. C., Tulloch, S. M., and Xu, W. (2014). CARMENES instrument overview. In *Ground-based and Airborne Instrumentation for Astronomy V*, volume 9147 of *Proceedings of the SPIE*, page 91471F.

Raghavan, D., McAlister, H. A., Henry, T. J., Latham, D. W., Marcy, G. W., Mason, B. D., Gies, D. R., White, R. J., and ten Brummelaar, T. A. (2010). A Survey of Stellar Families: Multiplicity of Solar-type Stars. *The Astrophysical Journal Supplement*, 190:1–42.

Ramsey, L. W., Adams, M. T., Barnes, T. G., Booth, J. A., Cornell, M. E., Fowler, J. R., Gaffney, N. I., Glaspey, J. W., Good, J. M., Hill, G. J., Kelton, P. W., Krabbendam, V. L., Long, L., MacQueen, P. J., Ray, F. B., Ricklefs, R. L., Sage, J., Sebring, T. A., Spiesman, W. J., and Steiner, M. (1998). Early performance and present status of the Hobby-Eberly Telescope. In Stepp, L. M., editor, *Advanced Technology Optical/IR Telescopes VI*, volume 3352 of *Society of Photo-Optical Instrumentation Engineers (SPIE) Conference Series*, pages 34–42.

Rauer, H., Catala, C., Aerts, C., Appourchaux, T., Benz, W., Brandeker, A., Christensen-Dalsgaard, J., Deleuil, M., Gizon, L., Goupil, M.-J., Güdel, M., Janot-Pacheco, E., Mas-Hesse, M., Pagano, I., Piotto, G., Pollacco, D., Santos, Ċ., Smith, A., Suárez, J.-C., Szabó, R., Udry, S., Adibekyan, V., Alibert, Y., Almenara, J.-M., Amaro-Seoane, P., Eiff, M. A.-v., Asplund, M., Antonello, E., Barnes, S., Baudin, F., Belkacem, K., Bergemann, M., Bihain, G., Birch, A. C., Bonfils, X., Boisse, I., Bonomo, A. S., Borsa, F., Brandão, I. M., Brocato, E., Brun, S., Burleigh, M., Burston, R., Cabrera, J., Cassisi, S., Chaplin, W., Charpinet, S., Chiappini, C., Church, R. P., Csizmadia, S., Cunha, M., Damasso, M., Davies, M. B., Deeg, H. J., Díaz, R. F., Dreizler, S., Dreyer, C., Eggenberger, P., Ehrenreich, D., Eigmüller, P., Erikson, A., Farmer, R., Feltzing, S., de Oliveira Fialho, F., Figueira, P., Forveille, T., Fridlund, M., García, R. A., Giommi, P., Giuffrida, G., Godolt, M., Gomes da Silva, J., Granzer, T., Grenfell, J. L., Grotsch-Noels, A., Günther, E., Haswell, C. A., Hatzes, A. P., Hébrard, G., Hekker, S., Helled, R., Heng, K., Jenkins, J. M., Johansen, A., Khodachenko, M. L., Kislyakova, K. G., Kley, W., Kolb, U., Krivova, N., Kupka, F., Lammer, H., Lanza, A. F., Lebreton, Y., Magrin, D., Marcos-Arenal, P., Marrese, P. M., Marques, J. P., Martins, J., Mathis, S., Mathur, S., Messina, S., Miglio, A., Montalban, J., Montalto, M., Monteiro, M. J. P. F. G., Moradi, H., Moravveji, E., Mordasini, C., Morel, T., Mortier, A., Nascimbeni, V., Nelson, R. P., Nielsen, M. B., Noack, L., Norton, A. J.,

Ofir, A., Oshagh, M., Ouazzani, R.-M., Pápics, P., Parro, V. C., Petit, P., Plez, B., Poretti, E., Quirrenbach, A., Ragazzoni, R., Raimondo, G., Rainer, M., Reese, D. R., Redmer, R., Reffert, S., Rojas-Ayala, B., Roxburgh, I. W., Salmon, S., Santerne, A., Schneider, J., Schou, J., Schuh, S., Schunker, H., Silva-Valio, A., Silvotti, R., Skillen, I., Snellen, I., Sohl, F., Sousa, S. G., Sozzetti, A., Stello, D., Strassmeier, K. G., Švanda, M., Szabó, G. M., Tkachenko, A., Valencia, D., Van Grootel, V., Vauclair, S. D., Ventura, P., Wagner, F. W., Walton, N. A., Weingrill, J., Werner, S. C., Wheatley, P. J., and Zwintz, K. (2014). The PLATO 2.0 mission. *Experimental Astronomy*, 38:249–330.

Rayner, J. T., Toomey, D. W., Onaka, P. M., Denault, A. J., Stahlberger, W. E., Vacca, W. D., Cushing, M. C., and Wang, S. (2003). SpeX: A Medium-Resolution 0.8-5.5 Micron Spectrograph and Imager for the NASA Infrared Telescope Facility. *Publications of the Astronomical Society of Pacific*, 115:362–382.

Reichert, J., Holzwarth, R., Udem, T., and Hänsch, T. W. (1999). Measuring the frequency of light with mode-locked lasers. *Optics Communications*, 172:59–68.

Rice, K., Lopez, E., Forgan, D., and Biller, B. (2015). Disc fragmentation rarely forms planetary-mass objects. *Monthly Notices of the Royal Astronomical Society*, 454:1940–1947.

Ricker, G. R., Winn, J. N., Vanderspek, R., Latham, D. W., Bakos, G. Á., Bean, J. L., Berta-Thompson, Z. K., Brown, T. M., Buchhave, L., Butler, N. R., Butler, R. P., Chaplin, W. J., Charbonneau, D., Christensen-Dalsgaard, J., Clampin, M., Deming, D., Doty, J., De Lee, N., Dressing, C., Dunham, E. W., Endl, M., Fressin, F., Ge, J., Henning, T., Holman, M. J., Howard, A. W., Ida, S., Jenkins, J. M., Jernigan, G., Johnson, J. A., Kaltenegger, L., Kawai, N., Kjeldsen, H., Laughlin, G., Levine, A. M., Lin, D., Lissauer, J. J., MacQueen, P., Marcy, G., McCullough, P. R., Morton, T. D., Narita, N., Paegert, M., Palle, E., Pepe, F., Pepper, J., Quirrenbach, A., Rinehart, S. A., Sasselov, D., Sato, B., Seager, S., Sozzetti, A., Stassun, K. G., Sullivan, P., Szentgyorgyi, A., Torres, G., Udry, S., and Villasenor, J. (2015). Transiting Exoplanet Survey Satellite (TESS). *Journal of Astronomical Telescopes, Instruments, and Systems*, 1(1):014003.

Ries, J. and Riddle, A. (2014). Reviving astrometry on the McDonald observatory 2.1-m Otto Struve telescope. In Muinonen, K., Penttilä, A., Granvik, M., Virkki, A., Fedorets, G., Wilkman, O., and Kohout, T., editors, *Asteroids, Comets, Meteors 2014*, page 446.

Robin, A. C., Reylé, C., Derrière, S., and Picaud, S. (2003). A synthetic view on structure and evolution of the Milky Way. *Astronomy and Astrophysics*, 409:523–540.

Rogers, L. A. (2015). Most 1.6 Earth-radius Planets are Not Rocky. *The Astrophysical Journal*, 801:41.

Rojas-Ayala, B., Covey, K. R., Muirhead, P. S., and Lloyd, J. P. (2012). Metallicity and Temperature Indicators in M Dwarf K-band Spectra: Testing New and Updated Calibrations with Observations of 133 Solar Neighborhood M Dwarfs. *The Astrophysical Journal*, 748:93.

Roldan, A., Hollingsworth, N., Roffey, A., Islam, H.-U., Goodall, J. B. M., Catlow, C. R. A., Darr, J. A., Bras, W., Sankar, G., Holt, K. B., Hogarth, G., and de Leeuw, N. H. (2015). Bio-inspired co2 conversion by iron sulfide catalysts under sustainable conditions. *Chem. Commun.*, 51:7501–7504.

Rosenblatt, F. (1971). A Two-Color Photometric Method for Detection of Extra solar Planetary Systems. *Icarus*, 14:71–93.

Rossiter, R. A. (1924). On the detection of an effect of rotation during eclipse in the velocity of the brigher component of beta Lyrae, and on the constancy of velocity of this system. *Astrophysical Journal*, 60:15–21.

Rousset, G., Fontanella, J. C., Kern, P., Gigan, P., and Rigaut, F. (1990). First diffraction-limited astronomical images with adaptive optics. *Astronomy and Astrophysics*, 230:L29–L32.

Rowe, J. F., Bryson, S. T., Marcy, G. W., Lissauer, J. J., Jontof-Hutter, D., Mullally, F., Gilliland, R. L., Issacson, H., Ford, E., Howell, S. B., Borucki, W. J., Haas, M., Huber, D., Steffen, J. H., Thompson, S. E., Quintana, E., Barclay, T., Still, M., Fortney, J., Gautier, III, T. N., Hunter, R., Caldwell, D. A., Ciardi, D. R., Devore, E., Cochran, W., Jenkins, J., Agol, E., Carter, J. A., and Geary, J. (2014). Validation of Kepler's Multiple Planet Candidates. III. Light Curve Analysis and Announcement of Hundreds of New Multi-planet Systems. *The Astrophysical Journal*, 784:45.

Rowe, J. F., Matthews, J. M., Seager, S., Miller-Ricci, E., Sasselov, D., Kuschnig, R., Guenther, D. B., Moffat, A. F. J., Rucinski, S. M., Walker, G. A. H., and Weiss, W. W. (2008). The Very Low Albedo of an Extrasolar Planet: MOST Space-based Photometry of HD 209458. *The Astrophysical Journal*, 689:1345–1353.

Salpeter, E. E. (1955). The Luminosity Function and Stellar Evolution. *The Astrophysical Journal*, 121:161.

Santos, N. C., Israelian, G., and Mayor, M. (2001). The metal-rich nature of stars with planets. *Astronomy and Astrophysics*, 373:1019–1031.

Scalo, J., Kaltenegger, L., Segura, A. G., Fridlund, M., Ribas, I., Kulikov, Y. N., Grenfell, J. L., Rauer, H., Odert, P., Leitzinger, M., Selsis, F., Khodachenko, M. L., Eiroa, C., Kasting, J., and Lammer, H. (2007). M Stars as Targets for Terrestrial Exoplanet Searches And Biosignature Detection. *Astrobiology*, 7:85–166.

Scheeres, D., Hartzell, C., Sánchez, P., and Swift, M. (2010). Scaling forces to asteroid surfaces: The role of cohesion. *Icarus*, 210:968–984.

Schlafly, E. F. and Finkbeiner, D. P. (2011). Measuring Reddening with Sloan Digital Sky Survey Stellar Spectra and Recalibrating SFD. *The Astrophysical Journal*, 737:103.

Schlegel, D. J., Finkbeiner, D. P., and Davis, M. (1998). Maps of Dust Infrared Emission for Use in Estimation of Reddening and Cosmic Microwave Background Radiation Foregrounds. *Astrophysical Journal*, 500:525.

Schlesinger, F. (1910). The Algol-variable [delta] Librae. *Publications of the Allegheny Observatory of the University of Pittsburgh*, 1:123–134.

Schlieder, J. E., Crossfield, I. J. M., Petigura, E. A., Howard, A. W., Aller, K. M., Sinukoff, E., Isaacson, H. T., Fulton, B. J., Ciardi, D. R., Bonnefoy, M., Ziegler, C., Morton, T. D., Lépine, S., Obermeier, C., Liu, M. C., Bailey, V. P., Baranec, C., Beichman, C. A., Defrère,

D., Henning, T., Hinz, P., Law, N., Riddle, R., and Skemer, A. (2016). Two Small Temperate Planets Transiting Nearby M Dwarfs in K2 Campaigns 0 and 1. *The Astrophysical Journal*, 818:87.

Schneider, J., Dedieu, C., Le Sidaner, P., Savalle, R., and Zolotukhin, I. (2011). Defining and cataloging exoplanets: the exoplanet.eu database. *Astronomy and Astrophysics*, 532:A79.

Shan, Y., Johnson, J. A., and Morton, T. D. (2015). Measuring the Number of M Dwarfs per M Dwarf Using Kepler Eclipsing Binaries. *The Astrophysical Journal*, 813:75.

Shen, Y. and Turner, E. L. (2008). On the Eccentricity Distribution of Exoplanets from Radial Velocity Surveys. *The Astrophysical Journal*, 685:553–559.

Shkolnik, E. L. and Barman, T. S. (2014). HAZMAT. I. The Evolution of Far-UV and Near-UV Emission from Early M Stars. *The Astronomical Journal*, 148:64.

Silburt, A., Gaidos, E., and Wu, Y. (2015). A Statistical Reconstruction of the Planet Population around Kepler Solar-type Stars. *Astrophysical Journal*, 799:180.

Silvotti, R., Schuh, S., Janulis, R., Solheim, J.-E., Bernabei, S., Østensen, R., Oswalt, T. D., Bruni, I., Gualandi, R., Bonanno, A., Vauclair, G., Reed, M., Chen, C.-W., Leibowitz, E., Paparo, M., Baran, A., Charpinet, S., Dolez, N., Kawaler, S., Kurtz, D., Moskalik, P., Riddle, R., and Zola, S. (2007). A giant planet orbiting the 'extreme horizontal branch' star V391 Pegasi. *Nature*, 449:189–191.

Skrutskie, M. F., Cutri, R. M., Stiening, R., Weinberg, M. D., Schneider, S., Carpenter, J. M., Beichman, C., Capps, R., Chester, T., Elias, J., Huchra, J., Liebert, J., Lonsdale, C., Monet, D. G., Price, S., Seitzer, P., Jarrett, T., Kirkpatrick, J. D., Gizis, J. E., Howard, E., Evans, T., Fowler, J., Fullmer, L., Hurt, R., Light, R., Kopan, E. L., Marsh, K. A., McCallon, H. L., Tam, R., Van Dyk, S., and Wheelock, S. (2006). The Two Micron All Sky Survey (2MASS). *Astronomical Journal*, 131:1163–1183.

Smiley, C. H. (1936). The Schmidt camera. *Popular Astronomy*, 44:415.

Smith, A., Bailey, J., Hough, J. H., and Lee, S. (2009). An investigation of lucky imaging techniques. *Monthly Notices of the Royal Astronomical Society*, 398:2069–2073.

Snellen, I. A. G., de Mooij, E. J. W., and Albrecht, S. (2009). The changing phases of extrasolar planet CoRoT-1b. *Nature*, 459:543–545.

Soares, D. S. L. (2005). Newtonian gravitational deflection of light revisited. *ArXiv Physics e-prints*.

Soter, S. (2006). What Is a Planet? *The Astronomical Journal*, 132:2513–2519.

Southworth, J., Mancini, L., Maxted, P. F. L., Bruni, I., Tregloan-Reed, J., Barbieri, M., Ruocco, N., and Wheatley, P. J. (2012). Physical properties and radius variations in the HAT-P-5 planetary system from simultaneous four-colour photometry. *Monthly Notices of the Royal Astronomical Society*, 422:3099–3106.

Southworth, J., Tregloan-Reed, J., Andersen, M. I., Calchi Novati, S., Ciceri, S., Colque, J. P., D'Ago, G., Dominik, M., Evans, D. F., Gu, S.-H., Herrera-Cordova, A., Hinse, T. C., Jørgensen, U. G., Juncher, D., Kuffmeier, M., Mancini, L., Peixinho, N., Popovas, A., Rabus, M., Skottfelt, J., Tronsgaard, R., Unda-Sanzana, E., Wang, X.-B., Wertz, O., Alsubai, K. A., Andersen, J. M., Bozza, V., Bramich, D. M., Burgdorf, M., Damerdji, Y., Diehl, C., Elyiv, A., Figuera Jaimes, R., Haugbølle, T., Hundertmark, M., Kains, N., Kerins, E., Korhonen, H., Liebig, C., Mathiasen, M., Penny, M. T., Rahvar, S., Scarpetta, G., Schmidt, R. W., Snodgrass, C., Starkey, D., Surdej, J., Vilela, C., Essen, C. v., and Wang, Y. (2016). High-precision photometry by telescope defocussing - VIII. WASP-22, WASP-41, WASP-42 and WASP-55. *Monthly Notices of the Royal Astronomical Society*, 457:4205–4217.

Spiegel, D. S. and Burrows, A. (2013). Thermal Processes Governing Hot-Jupiter Radii. *The Astrophysical Journal*, 772:76.

Spitoni, E., Matteucci, F., and Sozzetti, A. (2014). The galactic habitable zone of the Milky Way and M31 from chemical evolution models with gas radial flows. *Monthly Notices of the Royal Astronomical Society*, 440:2588–2598.

Spurzem, R., Giersz, M., Heggie, D. C., and Lin, D. N. C. (2009). Dynamics of Planetary Systems in Star Clusters. *The Astrophysical Journal*, 697:458–482.

Sterken, C. (2005). The O-C Diagram: Basic Procedures. In Sterken, C., editor, *The Light-Time Effect in Astrophysics: Causes and cures of the O-C diagram*, volume 335 of *Astronomical Society of the Pacific Conference Series*, page 3.

Stevenson, K. B., Désert, J.-M., Line, M. R., Bean, J. L., Fortney, J. J., Showman, A. P., Kataria, T., Kreidberg, L., McCullough, P. R., Henry, G. W., Charbonneau, D., Burrows, A., Seager, S., Madhusudhan, N., Williamson, M. H., and Homeier, D. (2014). Thermal structure of an exoplanet atmosphere from phase-resolved emission spectroscopy. *Science*, 346:838–841.

Street, R. A., Pollaco, D. L., Fitzsimmons, A., Keenan, F. P., Horne, K., Kane, S., Collier Cameron, A., Lister, T. A., Haswell, C., Norton, A. J., Jones, B. W., Skillen, I., Hodgkin, S., Wheatley, P., West, R., and Brett, D. (2003). SuperWASP: Wide Angle Search for Planets. In Deming, D. and Seager, S., editors, *Scientific Frontiers in Research on Extrasolar Planets*, volume 294 of *Astronomical Society of the Pacific Conference Series*, pages 405–408.

Struve, O. (1952). Proposal for a project of high-precision stellar radial velocity work. *The Observatory*, 72:199–200.

Sudarsky, D., Burrows, A., and Hubeny, I. (2003). Theoretical Spectra and Atmospheres of Extrasolar Giant Planets. *Astrophysical Journal*, 588:1121–1148.

Sudarsky, D., Burrows, A., and Pinto, P. (2000). Albedo and Reflection Spectra of Extrasolar Giant Planets. *The Astrophysical Journal*, 538:885–903.

Swedenborg, E. (1734). *Philosophical and Mineralogical Works*.

Swift, J. J., Johnson, J. A., Morton, T. D., Crepp, J. R., Montet, B. T., Fabrycky, D. C., and Muirhead, P. S. (2013). Characterizing the Cool KOIs. IV. Kepler-32 as a Prototype for the Formation of Compact Planetary Systems throughout the Galaxy. *The Astrophysical Journal*, 764:105.

Tamuz, O., Mazeh, T., and Zucker, S. (2005). Correcting systematic effects in a large set of photometric light curves. *Monthly Notices of the RAS*, 356:1466–1470.

Thommes, E. W., Duncan, M. J., and Levison, H. F. (2002). The Formation of Uranus and Neptune among Jupiter and Saturn. *The Astronomical Journal*, 123:2862–2883.

Tomaney, A. B. and Crotts, A. P. S. (1996). Expanding the Realm of Microlensing Surveys with Difference Image Photometry. *Astronomical Journal*, 112:2872.

Tonry, J. and Onaka, P. (2009). The Pan-STARRS Gigapixel Camera. In *Advanced Maui Optical and Space Surveillance Technologies Conference*, page 40.

Tonry, J. and Pan-STARRS Team (2005). The 1.4 Gigapixel Camera for Pan-STARRS. In *American Astronomical Society Meeting Abstracts*, volume 37 of *Bulletin of the American Astronomical Society*, page 121.01.

Tonry, J. L., Stubbs, C. W., Lykke, K. R., Doherty, P., Shivvers, I. S., Burgett, W. S., Chambers, K. C., Hodapp, K. W., Kaiser, N., Kudritzki, R.-P., Magnier, E. A., Morgan, J. S., Price, P. A., and Wainscoat, R. J. (2012). The Pan-STARRS1 Photometric System. *Astrophysical Journal*, 750:99.

Torres, G., Fressin, F., Batalha, N. M., Borucki, W. J., Brown, T. M., Bryson, S. T., Buchhave, L. A., Charbonneau, D., Ciardi, D. R., Dunham, E. W., Fabrycky, D. C., Ford, E. B., Gautier, III, T. N., Gilliland, R. L., Holman, M. J., Howell, S. B., Isaacson, H., Jenkins, J. M., Koch, D. G., Latham, D. W., Lissauer, J. J., Marcy, G. W., Monet, D. G., Prsa, A., Quinn, S. N., Ragozzine, D., Rowe, J. F., Sasselov, D. D., Steffen, J. H., and Welsh, W. F. (2011). Modeling Kepler Transit Light Curves as False Positives: Rejection of Blend Scenarios for Kepler-9, and Validation of Kepler-9 d, A Super-earth-size Planet in a Multiple System. *The Astrophysical Journal*, 727:24.

Torres-Dodgen, A. V. and Weaver, W. B. (1993). An atlas of low-resolution near-infrared spectra of normal stars. *Publications of the ASP*, 105:693–720.

Triaud, A. H. M. J., Anderson, D. R., Collier Cameron, A., Doyle, A. P., Fumel, A., Gillon, M., Hellier, C., Jehin, E., Lendl, M., Lovis, C., Maxted, P. F. L., Pepe, F., Pollacco, D., Queloz, D., Ségransan, D., Smalley, B., Smith, A. M. S., Udry, S., West, R. G., and Wheatley, P. J. (2013). WASP-80b: a gas giant transiting a cool dwarf. *Astronomy and Astrophysics*, 551:A80.

Trumpler, R. J. (1930). Preliminary results on the distances, dimensions and space distribution of open star clusters. *Lick Observatory Bulletin*, 14:154–188.

Tsokolov, S. A. (2009). Why is the definition of life so elusive? epistemological considerations. *Astrobiology*, 9(4):401–412.

Udalski, A., Jaroszyński, M., Paczyński, B., Kubiak, M., Szymański, M. K., Soszyński, I., Pietrzyński, G., Ulaczyk, K., Szewczyk, O., Wyrzykowski, Ł., OGLE Collaboration, Christie, G. W., DePoy, D. L., Dong, S., Gal-Yam, A., Gaudi, B. S., Gould, A., Han, C., Lépine, S., McCormick, J., Park, B.-G., Pogge, R. W., μFUN Collaboration, Bennett, D. P., Bond, I. A., Muraki, Y., Tristram, P. J., Yock, P. C. M., MOA Collaboration, Beaulieu, J.-P., Bramich, D. M., Dieters, S. W., Greenhill, J., Hill, K., Horne, K., Kubas, D., and PLANET/ROBONET Collaboration (2005). A Jovian-Mass Planet in Microlensing Event OGLE-2005-BLG-071. *The Astrophysical Journal*, 628:L109–L112.

Udem, T., Holzwarth, R., and Hänsch, T. W. (2002). Optical frequency metrology. *Nature*, 416:233–237.

Udry, S. and Santos, N. C. (2007). Statistical Properties of Exoplanets. *Annual Review of Astronomy and Astrophysics*, 45:397–439.

Vacca, W. D., Cushing, M. C., and Rayner, J. T. (2003). A Method of Correcting Near-Infrared Spectra for Telluric Absorption. *Publications of the Astronomical Society of Pacific*, 115:389–409.

Van Eylen, V. and Albrecht, S. (2015). Eccentricity from Transit Photometry: Small Planets in Kepler Multi-planet Systems Have Low Eccentricities. *The Astrophysical Journal*, 808:126.

van Leeuwen, F. (2009). Parallaxes and proper motions for 20 open clusters as based on the new Hipparcos catalogue. *Astronomy and Astrophysics*, 497:209–242.

van Saders, J. L. and Gaudi, B. S. (2011). Ensemble Analysis of Open Cluster Transit Surveys: Upper Limits on the Frequency of Short-period Planets Consistent with the Field. *The Astrophysical Journal*, 729:63.

Vanderburg, A. and Johnson, J. A. (2014). A Technique for Extracting Highly Precise Photometry for the Two-Wheeled Kepler Mission. *Publications of the Astronomical Society of Pacific*, 126:948–958.

Vanderburg, A., Johnson, J. A., Rappaport, S., Bieryla, A., Irwin, J., Lewis, J. A., Kipping, D., Brown, W. R., Dufour, P., Ciardi, D. R., Angus, R., Schaefer, L., Latham, D. W., Charbonneau, D., Beichman, C., Eastman, J., McCrady, N., Wittenmyer, R. A., and Wright, J. T. (2015). A disintegrating minor planet transiting a white dwarf. *Nature*, 526:546–549.

Veras, D. and Raymond, S. N. (2012). Planet-planet scattering alone cannot explain the free-floating planet population. *Monthly Notices of the Royal Astronomical Society*, 421:L117–L121.

Vogt, S. S., Allen, S. L., Bigelow, B. C., Bresee, L., Brown, B., Cantrall, T., Conrad, A., Couture, M., Delaney, C., Epps, H. W., Hilyard, D., Hilyard, D. F., Horn, E., Jern, N., Kanto, D., Keane, M. J., Kibrick, R. I., Lewis, J. W., Osborne, J., Pardeilhan, G. H., Pfister, T., Ricketts, T., Robinson, L. B., Stover, R. J., Tucker, D., Ward, J., and Wei, M. Z. (1994). HIRES: the high-resolution echelle spectrometer on the Keck 10-m Telescope. In Crawford, D. L. and Craine, E. R., editors, *Instrumentation in Astronomy VIII*, volume 2198 of *Proceedings of the SPIE*, page 362.

Vukotić, B., Steinhauser, D., Martinez-Aviles, G., Ćirković, M. M., Micic, M., and Schindler, S. (2016). "Grandeur in this view of life": N-body simulation models of the Galactic habitable zone. *Monthly Notices of the Royal Astronomical Society*, 459:3512–3524.

Wachtershauser, G. (1990). Evolution of the First Metabolic Cycles. *Proceedings of the National Academy of Science*, 87:200–204.

Walker, G. A. H. (2012). The first high-precision radial velocity search for extra-solar planets. *New Astronomy Reviews*, 56:9–15.

Walton, N. A., Walsh, J. R., and Pottasch, S. R. (1993). Imaging and Spectroscopy of ABELL:63 Uu-Sagittae. *Astronomy and Astrophysics*, 275:256.

Weiss, L. M. and Marcy, G. W. (2014). The Mass-Radius Relation for 65 Exoplanets Smaller than 4 Earth Radii. *The Astrophysical Journal*, 783:L6.

Weldrake, D. T. F., Sackett, P. D., Bridges, T. J., and Freeman, K. C. (2005). An Absence of Hot Jupiter Planets in 47 Tucanae: Results of a Wide-Field Transit Search. *The Astrophysical Journal*, 620:1043–1051.

West, A. A., Morgan, D. P., Bochanski, J. J., Andersen, J. M., Bell, K. J., Kowalski, A. F., Davenport, J. R. A., Hawley, S. L., Schmidt, S. J., Bernat, D., Hilton, E. J., Muirhead, P., Covey, K. R., Rojas-Ayala, B., Schlawin, E., Gooding, M., Schluns, K., Dhital, S., Pineda, J. S., and Jones, D. O. (2011). The Sloan Digital Sky Survey Data Release 7 Spectroscopic M Dwarf Catalog. I. Data. *Astronomical Journal*, 141:97.

Wheatley, P. J., Pollacco, D. L., Queloz, D., Rauer, H., Watson, C. A., West, R. G., Chazelas, B., Louden, T. M., Walker, S., Bannister, N., Bento, J., Burleigh, M., Cabrera, J., Eigmüller, P., Erikson, A., Genolet, L., Goad, M., Grange, A., Jordán, A., Lawrie, K., McCormac, J., and Neveu, M. (2013). The Next Generation Transit Survey (NGTS). In *European Physical Journal Web of Conferences*, volume 47 of *European Physical Journal Web of Conferences*, page 13002.

Williams, S. D., Stauffer, J. R., Prosser, C. F., and Herter, T. (1994). Spectroscopy and photometry for low-mass stars in Praesepe. *Publications of the Astronomical Society of Pacific*, 106:817–821.

Wilson, R. N. (1991). Active optics and the New Technology Telescope (NTT): the key to improved optical quality at lower cost in large astronomical telescopes. *Contemporary Physics*, 32:157–172.

Winn, J. N., Johnson, J. A., Albrecht, S., Howard, A. W., Marcy, G. W., Crossfield, I. J., and Holman, M. J. (2009). HAT-P-7: A Retrograde or Polar Orbit, and a Third Body. *The Astrophysical Journal Letters*, 703:L99–L103.

Winters, J. G., Henry, T. J., Lurie, J. C., Hambly, N. C., Jao, W.-C., Bartlett, J. L., Boyd, M. R., Dieterich, S. B., Finch, C. T., Hosey, A. D., Ianna, P. A., Riedel, A. R., Slatten, K. J., and Subasavage, J. P. (2015). The Solar Neighborhood. XXXV. Distances to 1404 m Dwarf Systems Within 25 pc in the Southern Sky. *The Astronomical Journal*, 149:5.

Wolfgang, A. and Lopez, E. (2015). How Rocky Are They? The Composition Distribution of Kepler's Sub-Neptune Planet Candidates within 0.15 AU. *The Astrophysical Journal*, 806:183.

Wolfgang, A., Rogers, L. A., and Ford, E. B. (2016). Probabilistic Mass-Radius Relationship for Sub-Neptune-Sized Planets. *The Astrophysical Journal*, 825:19.

Wolszczan, A. and Frail, D. A. (1992). A planetary system around the millisecond pulsar PSR1257 + 12. *Nature*, 355:145–147.

Wordsworth, R. D., Forget, F., Selsis, F., Madeleine, J.-B., Millour, E., and Eymet, V. (2010). Is Gliese 581d habitable? Some constraints from radiative-convective climate modeling. *Astronomy and Astrophysics*, 522:A22.

Wright, E. L., Eisenhardt, P. R. M., Mainzer, A. K., Ressler, M. E., Cutri, R. M., Jarrett, T., Kirkpatrick, J. D., Padgett, D., McMillan, R. S., Skrutskie, M., Stanford, S. A., Cohen, M., Walker, R. G., Mather, J. C., Leisawitz, D., Gautier, III, T. N., McLean, I., Benford, D., Lonsdale, C. J., Blain, A., Mendez, B., Irace, W. R., Duval, V., Liu, F., Royer, D., Heinrichsen, I., Howard, J., Shannon, M., Kendall, M., Walsh, A. L., Larsen, M., Cardon, J. G., Schick, S., Schwalm, M., Abid, M., Fabinsky, B., Naes, L., and Tsai, C.-W. (2010). The Wide-field Infrared Survey Explorer (WISE): Mission Description and Initial On-orbit Performance. *Astronomical Journal*, 140:1868–1881.

York, D. G., Adelman, J., Anderson, Jr., J. E., Anderson, S. F., Annis, J., Bahcall, N. A., Bakken, J. A., Barkhouser, R., Bastian, S., Berman, E., Boroski, W. N., Bracker, S., Briegel, C., Briggs, J. W., Brinkmann, J., Brunner, R., Burles, S., Carey, L., Carr, M. A., Castander, F. J., Chen, B., Colestock, P. L., Connolly, A. J., Crocker, J. H., Csabai, I., Czarapata, P. C., Davis, J. E., Doi, M., Dombeck, T., Eisenstein, D., Ellman, N., Elms, B. R., Evans, M. L., Fan, X., Federwitz, G. R., Fiscelli, L., Friedman, S., Frieman, J. A., Fukugita, M., Gillespie, B., Gunn, J. E., Gurbani, V. K., de Haas, E., Haldeman, M., Harris, F. H., Hayes, J., Heckman, T. M., Hennessy, G. S., Hindsley, R. B., Holm, S., Holmgren, D. J., Huang, C.-h., Hull, C., Husby, D., Ichikawa, S.-I., Ichikawa, T., Ivezić, Ž., Kent, S., Kim, R. S. J., Kinney, E., Klaene, M., Kleinman, A. N., Kleinman, S., Knapp, G. R., Korienek, J., Kron, R. G., Kunszt, P. Z., Lamb, D. Q., Lee, B., Leger, R. F., Limmongkol, S., Lindenmeyer, C., Long, D. C., Loomis, C., Loveday, J., Lucinio, R., Lupton, R. H., MacKinnon, B., Mannery, E. J., Mantsch, P. M., Margon, B., McGehee, P., McKay, T. A., Meiksin, A., Merelli, A., Monet, D. G., Munn, J. A., Narayanan, V. K., Nash, T., Neilsen, E., Neswold, R., Newberg, H. J., Nichol, R. C., Nicinski, T., Nonino, M., Okada, N., Okamura, S., Ostriker, J. P., Owen, R., Pauls, A. G., Peoples, J., Peterson, R. L., Petravick, D., Pier, J. R., Pope, A., Pordes, R., Prosapio, A., Rechenmacher, R., Quinn, T. R., Richards, G. T., Richmond, M. W., Rivetta, C. H., Rockosi, C. M., Ruthmansdorfer, K., Sandford, D., Schlegel, D. J., Schneider, D. P., Sekiguchi, M., Sergey, G., Shimasaku, K., Siegmund, W. A., Smee, S., Smith, J. A., Snedden, S., Stone, R., Stoughton, C., Strauss, M. A., Stubbs, C., SubbaRao, M., Szalay, A. S., Szapudi, I., Szokoly, G. P., Thakar, A. R., Tremonti, C., Tucker, D. L., Uomoto, A., Vanden Berk, D., Vogeley, M. S., Waddell, P., Wang, S.-i., Watanabe, M., Weinberg, D. H., Yanny, B., Yasuda, N., and SDSS Collaboration (2000). The Sloan Digital Sky Survey: Technical Summary. *The Astronomical Journal*, 120:1579–1587.

Youdin, A. N. and Shu, F. H. (2002). Planetesimal Formation by Gravitational Instability. *Astrophysical Journal*, 580:494–505.

Zendejas, J., Koppenhoefer, J., Saglia, R. P., Birkby, J. L., Hodgkin, S. T., Kovács, G., Pinfield, D. J., Sipőcz, B., Barrado, D., Bender, R., del Burgo, C., Cappetta, M., Martín, E. L., Nefs, S. V., Riffeser, A., and Steele, P. (2013). Searching for transits in the Wide Field Camera Transit Survey with difference-imaging light curves. *Astronomy and Astrophysics*, 560:A92.

Zucker, S., Mazeh, T., and Alexander, T. (2007). Beaming Binaries: A New Observational Category of Photometric Binary Stars. *The Astrophysical Journal*, 670:1326–1330.

Acknowledgements

This research has made use of the NASA/ IPAC Infrared Science Archive, which is operated by the Jet Propulsion Laboratory, California Institute of Technology, under contract with the National Aeronautics and Space Administration.
The Pan-STARRS1 Surveys (PS1) have been made possible through contributions of the Institute for Astronomy, the University of Hawaii, the Pan-STARRS Project Office, the Max-Planck Society and its participating institutes, the Max Planck Institute for Astronomy, Heidelberg and the Max Planck Institute for Extraterrestrial Physics, Garching, The Johns Hopkins University, Durham University, the University of Edinburgh, Queen's University Belfast, the Harvard-Smithsonian Center for Astrophysics, the Las Cumbres Observatory Global Telescope Network Incorporated, the National Central University of Taiwan, the Space Telescope Science Institute, the National Aeronautics and Space Administration under Grant No. NNX08AR22G issued through the Planetary Science Division of the NASA Science Mission Directorate, the National Science Foundation under Grant No. AST-1238877, the University of Maryland, and Eotvos Lorand University (ELTE).
This publication contains data obtained with the 2m Fraunhofer Telescope of the Wendelstein observatory of the Ludwig-Maximilians University Munich.
We thank the staff of the Wendelstein observatory for technical help and strong support, including observing targets for us during the data acquisition.
This publication makes use of data products from the Two Micron All Sky Survey, which is a joint project of the University of Massachusetts and the Infrared Processing and Analysis Center/California Institute of Technology, funded by the National Aeronautics and Space Administration and the National Science Foundation.
This paper includes data taken at The McDonald Observatory of The University of Texas at Austin. The Hobby-Eberly Telescope (HET) is a joint project of the University of Texas at Austin, the Pennsylvania State University, Stanford University, Ludwig-Maximilians-Universität München, and Georg-August-Universität Göttingen. The HET is named in honor of its principal benefactors, William P. Hobby and Robert E. Eberly.
The Marcario Low Resolution Spectrograph is named for Mike Marcario of High Lonesome Optics who fabricated several optics for the instrument but died before its completion. The LRS is a joint project of the Hobby-Eberly Telescope partnership and the Instituto de Astronomia de la Universidad Nacional Autonoma de Mexico.
This research has made use of the Exoplanet Orbit Database and the Exoplanet Data Explorer at exoplanets.org.
Some of the data presented herein were obtained at the W.M. Keck Observatory (which is operated as a scientific partnership among Caltech, UC, and NASA) and at the Infrared Telescope Facility (IRTF, operated by UH under NASA contract NNH14CK55B). The authors wish to recognize and acknowledge the very significant cultural role and reverence that the summit of Maunakea has always had within the indigenous Hawaiian community. We are most fortunate to have the opportunity to conduct observations from this mountain.
Based on observations obtained at the Gemini Observatory, which is operated by the Association of Universities for Research in Astronomy, Inc., under a cooperative agreement with the NSF on behalf of the Gemini partnership: the National Science Foundation (United States), the National Research Council (Canada), CONICYT (Chile), Ministerio de Ciencia, Tecnología e Innovación Productiva (Argentina), and Ministério da Ciência, Tecnologia e Inovação (Brazil).

Personal Acknowledgements

There are so many people to thank, it is difficult to everyone in this list without forgetting anybody. I tried to compress it into one page but failed horribly.

The biggest thanks has to go out to Johannes Koppenhöfer. Johannes, you always placed your faith in me, never demanded more from me than you would have from yourself and I couldn't have done this PhD without your help. And we have become friends! I value that a lot.
Thomas Henning - you trusted me enough to make this PhD possible and I cannot be thankful enough for this. The year in Heidelberg, on which you insisted, has also been one of the most exciting years I probably will ever have lived through. Your insistence on letting me observe led to a new passion and a new field of photography. Roberto Saglia - you have been my thesis supervisor for many years and study courses, Bachelor, Master and now the PhD, and I have always valued your judgement. It is fair to say that my whole time at the LMU has been deeply linked to you and I never had the desire to switch. Ralf Bender - thank you for making my PhD possible and for all the support you have given over the years.
I want to thank my coworker Sabine Kretschmann and my Master student Anja Paula. The first year of my PhD would have been nowhere near as great without you.

My time was spent at three institutes - USM, MPIA, MPE - and I have met more amazing people than I would have ever thought and I will try to sum it up as best as I can. I also met many good people on my journeys across the world and I am very happy about that - just to sum up a few: John, Josh, Ian, Eyal, Ummi, Alessandro and many more.

The USM has always been my "home" institute and I met some of my closest friends here. Mihael - we are best friends and our coffee sessions have always been so much fun. Plus, you were the only one besides Johannes who could help when I had problems with my work. Pan-STARRS buddies! Max, Ralf, Natascha, Marcel - thank you for our P&P group, European Martial Arts, board game nights, smokeless "smoke" sessions outside...you made life enjoyable. Matthias - boy did we have fun on the Wendelstein or when trying to outdo each other with figuring out how to reduce noise! Or anything else, really. The people of the Wendelstein team - thank you for welcoming me in the observer's group. It is an amazing place and I have enjoyed any minute at that mountain.

It is fair to say that I didn't want to leave the USM for the MPIA, but the amazing people there convinced me otherwise. First and foremost - Chiara! You kept my mental sanity over the first months and I am so happy to have met you. Grazie di tutto! Wilma - thank you for all of our conversations, ranging from politics to Harry Potter. Come to Munich! Kalyan - thank you for our conversations and photo walks, I always had great fun. My office in general - thank you! Especially the discussions that always went off-topic, Tobias. Andreas - good times with good conversations, good food and good drinks. Simona - thank you for everything, really! And onwards to more great times in our collaboration. Vanja - for discussions about music, photography, foxes...and for organizing my very first art exhibition! Then all of the PhD/Master students - Michael, Paolo, Christine, Emer, Christina, Benjamin, Jakob, Miguel, Hektor, just to name a few. You threw the most outrageous parties.

The MPE has now overtaken the other institutes in time I spent there and I met people to not make me regret it. The amazing people in my office - thank you for all the fun discussions and the decidedly not-drinking we sometimes didn't do. I couldn't have wished for a better office. Siyi - for good conversations over tea. Anja - you were strictly speaking at the ESO but we met often enough regardless. The MPE band - we had some fun times and it felt good to have a break from work and just do music. The OPINAS group in general - good conversations about virtually any topic. Jenny - just met you but we already had great fun observing and roadtripping. Anita - first up, for all the lovely tea/"ratsch"-sessions and your support. And for finding a soul mate!

There are also many friends outside of science that I want to acknowledge. First and foremost my old friends from Landshut, Uhl, Yanic, Alexandra, Kathi. Thank you for putting up with my, let's say, rather strained schedule. I am so happy to have known you all for more than 15 years. My friends in Hamburg and Augsburg also have to mentioned here. Tina - strictly speaking we should have met during your USM time but I rather count you here. Towards many years full with joy! Paula - again, you should count towards MPIA but we just met last year. It has been a pleasure meeting you and we will travel at some point, promise!
My thanks go to all people from various orchestras and the summer academy. Evelyn - for your unshakeable (but probably still wrong) conviction that I am a genius. And everything else, really! Theresa - for science! And photography.
Bob Fosbury - you impacted me in many ways and I think I would have never gotten the scientific outlook on the real world I have now and my love for light beyond the visual spectrum without you. I am indebted to you for talking me into getting my first infrared camera.

Last but in no way least, my family. My thanks go to my parents, Alfons and Christine. My dear mother in particular inspired my love for astronomy. Thanks, Mum! My siblings, Bastian and Julia, who make me feel like being a physicist means being the normal person in our family - surrounded by lawyers. I am grateful to my new extended family as well, Waltraud, Jürgen, Johanna and Willi, who have fully embraced me into theirs.

The final acknowledgement is for my dear partner Lena who has stood by me during all of my adventures, travels and living in different cities for four years. We almost made the first decade together, onwards to many more! *Mau.*